Nanostructured Transition Metal Oxides and Sulfides for Catalytical and Energy Applications

Dissertation

zur Erlangung des Grades

„Doktor der Naturwissenschaften"

im Promotionsfach Chemie

am Fachbereich Chemie, Pharmazie und Geowissenschaften der

Johannes Gutenberg-Universität

in Mainz

vorgelegt von

Dmitri Spetter

geboren in Aleksejwka/Kasachstan

Mainz 2017

Dekan: XXX

Erster Berichterstatter: XXX

Zweiter Berichterstatter: XXX

Datum der mündlichen Prüfung: 11.01.2018

Die vorliegende Arbeit wurde von November 2014 bis November 2017 im Institut für Anorganische Chemie und Analytische Chemie der Johannes Gutenberg-Universität Mainz in der Arbeitsgruppe von XXX angefertigt.

Ich, Dmitri Spetter, erkläre hiermit, dass ich die vorliegende Arbeit selbstständig und ohne fremde Hilfe verfasst habe. Alle verwendeten Quellen und Hilfsmittel sind vollständig angegeben.

Mainz, 27.11.2017

Dmitri Spetter

Publications and Patents

1. **D. Spetter**, W. Tremel, "Process and Device for the Production of Nanoscale Metal Sulfides and after the Process Produced Metal Sulfides", *Ger. Offen.* DE 102015016878.9 (December 31, 2015).
2. D. Haba, A. J. Brunner, M. Barbezat, **D. Spetter**, W. Tremel, G. Pinter, "Correlation of Epoxy Material Properties with the Toughening Effect of Fullerene-Like WS_2 Nanoparticles", *Eur. Polym. J.* 2016, **84**, 125-136.
3. **D. Spetter**, W. Tremel, "Method and Device for Producing Metal Sulfides, and Metal Sulfides Produced According to the Method", *Ger. Offen.* DE 1020150106878 (December 19, 2016), *PCT Int. Appl.* WO 2017114588 A1 20170706.
4. **D. Spetter**, F. Hoshyargar, J. K. Sahoo, M. N. Tahir, R. Brandscheid, B. Barton, M. Panthöfer, U. Kolb, W. Tremel, "Surface Defects as Tools to Solubilize and Funtionalize WS_2 Nanotubes", *Eur. J. Inorg. Chem.* 2017, **15**, 2190-2194.
5. S. Hanif, B. Oschmann, **D. Spetter**, M. N. Tahir, W. Tremel, R. Zentel, "Block copolymers from ionic liquids for the preparation of thin carbonaceous shells", *Beilstein J. Org. Chem.* 2017, **13**, 1693-1701.
6. **D. Spetter**, M. N. Tahir, I. Khan, A. Qurashi, H. Lu, T. Weidner, W. Tremel, "Solvothermal Synthesis of Molybdenum-Tungsten-Oxides and Their Application as Photoelectrocatalysts in the Hydrogen Evolution Reaction", *J. Mater. Chem. A*, submitted 2017.
7. **D. Spetter**, J. Hilgert, A. Wahl, W. Tremel, „Einfache und kostengünstige Synthese von schichtartigen nanopartikulären Molybdänsulfiden, Wolframsulfiden, Molybdänoxy-sulfiden, Wolframoxysulfiden und deren Funktionalisierung für die Anwendung in tribologischen und katalytischen Prozessen**",** *patent application*, Johannes Gutenberg-University Mainz, September 2017.
8. K. Korschelt, **D. Spetter**, E. Schechtel, M. N. Tahir, M. Panthöfer, W. Tremel, "Oxidation of Thioanisol Catalysed by Various Transition Metal Oxide Nanoparticles with Hydrogen Peroxide as Harmless Oxidation Agent", *in preparation 2017*.
9. **D. Spetter**, J. Hilgert, E. Piras, F. Dassenoy, W. Tremel, "Tungsten Oxysulfide and Molybdenum Oxysulfide Nanoflakes as Superior Solid Lubricants", *in preparation 2017*.
10. **D. Spetter**, K. Korschelt, M. N. Tahir, S. Leukel, M. Mondeshki, W. Tremel, "Molybdenum-Tungsten-Oxides as new Catalysts for the Sulfoxidation Reaction", *in preparation 2017*.

Danksagung

In erster Linie gilt mein Dank Prof. Dr. XXX dafür, dass ich an diesem spannenden Thema arbeiten durfte. Sein Vertrauen in meine Arbeit, die stetige Bereitschaft, darüber zu diskutieren und seine Vorschläge und Lösungsansätze waren immer wieder ein zusätzlicher Ansporn und mit ein Grund dafür, dass die drei Jahre recht kurzweilig und unterhaltsam waren.
Ganz besonders herzlich danken möchte ich auch Dr. XXX, der meist die erste Anlaufstelle bei drängenden Fragen war und bei dem ich immer mit Freundlichkeit und einer offenen Tür, egal zu welcher Tageszeit, empfangen wurde. Fruchtbare wissenschaftliche Diskussionen, die Vermittlung wertvoller Kontakte und viele Anregungen, die die Qualität meiner Arbeit sehr positiv beeinflusst haben, werden mir stets in Erinnerung bleiben.
Ein großer Dank gebührt auch XXX dafür, dass sie mit ihrer unaufgeregten Art und Hilfsbereitschaft für einen reibungslosen organisatorischen Ablauf im AK sorgt.
Weiterhin bedanken möchte ich mich bei Prof. Dr. XXX für die Übernahme des Zweitgutachtens. So eine Arbeit entsteht natürlich nicht im Alleingang, schon garnicht bei der Verwendung der breiten Palette an analytischen Methoden, die hier zum Einsatz kamen. Deswegen möchte ich mich an dieser Stelle bei XXX für die Messung unzähliger (manchmal recht dürftig präparierter) XRD-Proben bedanken. Weiterhin gilt mein Dank Dr. XXX, der mir Zugang zum Raman-Gerät verschaffte und auch immer dafür Sorge trug, dass es ordentlich kalibriert war. Dr. XXX möchte ich auch recht herzlich für seine stets unkomplizierte und engagierte Art danken, mit welcher er auch vermeintlich komplexeste NMR-Fragestellungen durch einfache Tastaturbefehle in einfach nachzuvollziehende Sachverhalte verwandelt. Unserer TEM-Crew gebührt der Dank für die Unmengen an Proben, die in den drei Jahren gemessen wurden. Für die schnelle und kompetente Bearbeitung der HR-TEM-Proben möchte ich mich bei XXX bedanken. Auch die gezeigten XPS-Daten wären ohne die Hilfe von Dr. XXX aus dem XXX nicht zustande gekommen, danke! XXX und Dr. XXX sorgten dafür, dass meine Proben auch mit der Synchrotronstrahlung der *Diamond Light Source* interagieren durften. Vielen Dank euch beiden!
Weiterhin danken möchte ich meinen internationalen Kooperationspartnern von der KFUPM in Saudi-Arabien (XXX und Dr. XXX) für die Messungen und Auswertung der Photoelektrokatalyse und die in diesem Zusammenhang entstandene Veröffentlichung. Bei unseren französischen Kollegen Dr. XXX und Prof. Dr. XXX (LTDS, Lyon) bedanke ich mich für die Tribo-Messungen und die weitergehende Analyse mittels XPS. Diese Ergebnisse eröffneten ganz neue Sichtweisen auf das vermeintlich schon abgegraste Gebiet der Feststoffschmiermittel.
Die alltägliche Arbeit hätte natürlich nur halb so viel Spaß gemacht, hätte ich sie nicht in der angenehmen Atmosphäre meiner Arbeitsgruppe verrichtet. Deswegen geht an dieser Stelle ein ganz großes Dankeschön an alle Mitglieder des AK XXX und insbesondere an die Mitglieder des Durak-Clubs für viele nette, auflockernde Stunden und Runden im Kaffeeraum. Meinen beiden (Ex-)Outlaws-Kleingruppen-Kumpanen XXX und XXX danke ich ganz herzlich nicht nur für die fachliche Kooperation, sondern vor allem für viele lustige Aktivitäten außerhalb der Arbeit.
Nicht zuletzt geht mein allerherzlichster Dank an meine Eltern, meine Familie und meine Freunde für ihre Unterstützung, die Motivation und ihren Rückhalt in sämtlichen Lebenslagen. Ohne Euch wären die guten Zeiten nur halb so schön und die schlechten Zeiten doppelt so schwer.

Abstract

The aim of this work was the development of novel compounds for application in energy engineering and catalytic processes. The focus was placed on oxides and sulfides of molybdenum, tungsten and iron. In addition, it was important to establish a synthetic pathway, which is potentially easily scalable.

The first part of the work deals with the production of tungsten-molybdenum oxides (TMOs) by means of two different synthetic routes, but starting from the same precursor compounds. Thus, by a simple precipitation technique, nanoflakes of TMO were prepared at room temperature in almost quantitative yield. The elemental composition and morphology of the compounds can be easily controlled without the addition of a surfactant. The TMO nanoflakes are suitable for use in photocatalysis due to their strong absorbance of visible light.
If the same reaction was carried out under solvothermal conditions in the autoclave, microspheres of mixed TMOs were obtained. These novel particles were examined for their use in two major technical fields. It was found that the mixed oxides yield significantly better results as catalyst materials in water splitting reactions than the pure oxides of tungsten or molybdenum. Thus, a synergetic effect could be demonstrated, which was proposed by other publications for affecting the physico-chemical characteristics of the mixed compounds. Photoelectrocatalysts such as the developed TMO microspheres are elementary components of fuel cells, which are an immensely important alternative for future energy production besides fossil fuels.
Furthermore, the use of the same microspheres as catalysts in the oxidation of sulfides was investigated. This reaction is an important step on the route to many organic substrates, e.g. the preparation of active ingredients. The sulfoxidation was carried out in aqueous medium with hydrogen peroxide as oxidant, thus establishing a green chemistry set-up. Due to its chemical properties, this reagent is superior to other oxidizing agents in terms of toxicological and environmental properties. In the reaction of the TMO catalysts with various sulfides in the presence of hydrogen peroxide, significantly faster reactions than previously known to the corresponding sulfoxide or sulfone were achieved.

In the second part, a new synthesis of porous iron oxide particles was investigated. Starting from templates of mesoporous silica, iron oxide particles with a cellular structure were obtained by nucleation and growth on the silica particles. However, it was not possible to synthesize pure mesoporous hematite nanoparticles since a residual amount of silicon remained in the product. The investigation of these particles in the decomposition of Rhodamine B also showed that the mesoporous silica particles (remaining from the synthesis) strongly delayed the oxidative reaction. However, the product itself showed significantly higher conversion rates than in the

absence of a catalyst. Thus, the use of the silica-hematite particles in the field of wastewater treatment for the removal of dyes is essentially possible.

In the final part, various nanoparticulate compounds of tungsten and molybdenum sulfide were tested as friction-reducing additives in synthetic oil. The production of the particles was carried out partly using a novel wet-chemistry approach in benzyl alcohol, in which nanoflakes of molybdenum oxysulfide were obtained. In friction experiments, a significant reduction of both the friction coefficient and the wear on the components was found, especially for this product. To date, the pure sulfide materials have been regarded as the best additive, which is why the results of the oxysulfide offer a new approach for the development of better lubricant additives.

Kurzfassung

Das Ziel der vorliegenden Arbeit war die Entwicklung neuartiger Verbindungen für die Anwendung in energietechnischen und katalytischen Prozessen. Hierbei lag der Fokus auf Übergangsmetalloxiden und -sulfiden des Molybdäns, des Wolframs wie auch des Eisens. Außerdem war es wichtig, für die Herstellung einen Syntheseweg zu etablieren, welcher leicht aufskalierbar ist.

Der erste Teil der Arbeit behandelt die Herstellung von Wolfram-Molybdän-Oxiden (*engl.* TMOs) mittels zweier unterschiedlicher Synthesewege, ausgehend von den gleichen Vorläuferverbindungen. So wurden durch eine Fällungsreaktion in fast quantitativer Ausbeute Nanoflocken aus TMOs bei Raumtemperatur hergestellt. Hierbei kann die elementare Zusammensetzung und Morphologie der Verbindungen ohne den Zusatz eines Tensids leicht angepasst werden. Die TMO-Nanoflocken bieten sich aufgrund ihres hohen Absorptionsvermögens des sichtbaren Anteils des Lichtes besonders als Kandidaten für den Einsatz in der Photokatalyse an.
Wurde die genannte Umsetzung unter solvothermalen Bedingungen im Autoklaven durchgeführt, konnten Mikrokugeln der gemischten TMOs gewonnen werden. Diese neuartigen Partikel wurden im weiteren Verlauf für ihren Einsatz in zwei großen technischen Bereichen untersucht. Zum einen wurde gezeigt, dass die Mischoxide erheblich bessere Ergebnisse als Katalysatormaterialien in der Wasserspaltung liefern als die reinen Oxide des Wolframs oder Molybdäns. Somit konnte ein synergetischer Effekt nachgewiesen werden, welcher durch vorangegangene Publikationen für die Beeinflussung der Eigenschaften der Mischverbindungen prognostiziert wurde. Photoelektrokatalysatoren wie die entwickelten TMO-Mikrokugeln sind elementare Bestandteile von Brennstoffzellen, welchen für die zukünftige Energiegewinnung abseits fossiler Brennstoffe eine immense Bedeutung zugeschrieben wird.
Die Verwendung der gleichen Mikrokugeln als Katalysatoren in der Oxidation von Sulfiden wurde ebenfalls untersucht. Diese Reaktion stellt eine wichtige Stufe in vielen organischen Umsetzungen, z. B. zur Herstellung von Wirkstoffen, dar. Die Sulfoxidation wurde in dieser Arbeit in wässrigem Medium mit Wasserstoffperoxid durchgeführt. Dieses Reagenz ist in Hinsicht auf die toxikologischen und umweltspezifischen Eigenschaften anderen Oxidationsmitteln überlegen, weshalb es vermehrt im Rahmen der sogenannten Grünen Chemie Anwendung findet. Bei der Umsetzung der TMO-Katalysatoren mit diversen Sulfiden in Anwesenheit von Wasserstoffperoxid konnten deutlich schnellere Umsetzungen als bislang bekannt, zu den entsprechenden Sulfoxiden bzw. Sulfonen erreicht werden.

Im zweiten Teil der Arbeit wurde eine neuartige Synthese von porösen Eisenoxidpartikeln untersucht. Ausgehend von einem Templat aus mesoporösen Silicapartikeln wurden durch Nukleation an deren Oberfläche Partikel mit poröser Struktur erhalten. Allerdings gelang es hierbei nicht, reine Hämatitpartikel zu synthetisieren, da aufgrund des Aufwachsens des

Eisenoxides auf der Silicaoberfläche ein Rest Silicium im Produkt verblieb. Bei der Untersuchung dieser Partikel in Zersetzungsreaktionen von Rhodamin B zeigte sich auch, dass die aus der Synthese verbliebenen, mesoporösen Silicapartikel die oxidative Umsetzung stark verzögerten, bei der Zersetzung des Farbstoffes aber deutlich höhere Umsatzraten zeigten als in Abwesenheit eines Katalysators. Somit ist die Anwendung der Silica-Hämatit-Partikel im Bereich der Abwasserbehandlung zur Entfernung von Farbstoffen prinzipiell möglich.

Im abschließenden Teil wurden diverse nanopartikuläre Verbindungen des Wolfram- und Molybdänsulfids als reibungsvermindernde Additive in synthetischen Ölen untersucht. Die Herstellung der verschiedenen Partikel erfolgte teilweise über eine neuartige Synthese, wobei durch die Präparation in Benzylakohol Nanoflocken von Molybdänoxysulfid erhalten wurden. In Reibungsexperimenten zeigte sich insbesondere für dieses Produkt eine erhebliche Erniedrigung des Koeffizienten und auch des Verschleißes an den untersuchten Komponenten. Bisher wurden die reinen sulfidischen Materialien als bestes Additiv angesehen, weshalb die Ergebnisse des Oxysulfides einen neuen Ansatz für die Entwicklung besserer Schmierstoffadditive bieten.

List of Contents

List of Figures

List of Figures

List of Figures

List of Figures

List of Tables

1. Introduction

1.1. Central Issues

Metal Oxides. Shrinking reserves of fossil fuels urge us to find new methods to produce clean and renewable energy, the need for developing new sources of energy and storage is becoming increasingly important. Wind power is a clean alternative but depends on strong wind currents. Another green source of energy are solar cells, which nowadays can convert up to 30% of the incident solar radiation into electricity.[1-4] However, compared to brown or hard coal, they are relatively expensive and deliver electricity only when the sun is shining. The sun is the most powerful known source of renewable energy, every second radiation with an energy content of approx. $1.2 \cdot 10^{14}$ kJ hits the earth's surface.[5] Therefore, a feasible permanent conversion of solar energy into electricity would be a significant step away from fossil fuels. The coupling of different methods with energy generated by solar radiation is increasingly moving into the focus of science. The production of hydrogen fuel from water using photo- and photo-electrocatalysts is another and the most promising solution among these sustainable sources due to its natural abundance, economic reasonableness and environmental compatibility. However, the synthesis of new photocatalytically active materials, which are electrically and chemically stable and able to generate a high flux of charge carriers, with suitable band-edge potentials to split water and (especially) cost effective, still remains a challenge. Many different catalysts with a variety of compositions ranging from metals, metal alloys, metal oxides, or metal chalcogenides are employed as catalysts but not a single semiconductor has yet been identified that meets all the above mentioned necessary criteria.[6-8] Therefore, multifunctional approaches based on the integration of different semiconductor materials in a single particle or doping of semiconductors to engineer the bandgap, were developed to achieve the maximum efficiency.[9-11] Among these semiconductors MoO_3 or WO_3 are low cost, naturally abundant and environmentally friendly transition metals with high chemical stability that have been widely used in heterogeneous catalysis, electrocatalysis, and lithium-ion batteries research.[12, 13] Therefore, studies combining both these oxides to achieve new, high-performing compounds are conducted by materials researchers for years.

One of the most common approaches of energy saving in production is catalysis. It is estimated that about 90% of all chemical production processes worldwide are catalyzed.[14] Most of them are catalyzed heterogeneously, i.e. they occur on the surface of solids whereas the others are used in the same phase, hence called homogeneous catalysis. In addition, numerous other technical processes, e.g. exhaust gas purification, depend on catalysts too. In addition to large-scale processes, the conversion of organic substrates using catalysis can also be specifically controlled and accelerated. Furthermore, their yields can be optimized and the number of by-products can

be reduced.[15] This allows to produce valuable intermediate products of pharmaceuticals and medicines and to make manufacturing more cost-effectively, without forfeiting any product quality. The oxidation of substrates using cheap oxidants and highly-effective catalysts offers a particularly elegant and environmentally friendly method to achieve high turnover rates.[16] Accurate control of the catalyst composition provides further possibilities for producing novel catalysts for heterogeneous sulfoxidation processes and, thus, is a research field of particular interest.

As one of the major environmental problems, wastewater treatment is significantly gaining importance due to the shortage of clean drinking water in some developing countries. Although 70% of our planet is covered with water, just three percent of these huge quantities is potable fresh water, and only one third of those is available for human use.[17] As the contamination of the water with hardly decomposable pollutants surges, the development of proper methods and techniques to face this task will be paramount. Heterogeneous catalysis in the he decomposition of impurities such as colorants can be considerably accelerated by various catalytic processes. Photocatalysis enables easy degradation of dye by simple UV-light irradiation, whereas oxidation processes require additional oxidizing agents.[18-20] In either case, the development of highly active catalysts, which can be utilized under most diverse conditions, is nowhere near exhausted. Hematite is one of the best-studied and most prominent material that has been applied as a photo-catalyst in waste-water treatment due to its abundance, low toxicity and high degradation efficiency. Combining hematite with other materials or preparing novel morphologies would be one step further to obtain dye-degradation catalysts of better quality.

Metal Sulfides. With the already established systems and production machines employed in the running technology, reducing energy consumption is not an easy task. A possible approach here could be to shrink the running costs by reducing the friction and the wearing of the individual components by adding or improving the quality of the lubricants. Friction and wear are estimated to cause annual losses of between 2% and 7% of the gross national product to the respective economies of the industrialized countries.[21] The increased consideration of tribological knowledge can lead to considerable savings in the use of energy and materials as well as in the production and maintenance. In this way, the energy and raw material resources can be spared, environmental damage be avoided, and occupational safety and health can be improved. For this reason, new lubricants are continually being developed and improved. Facing the fact that in every industrial branch machinery and engines are needed to provide and maintain a certain level of productivity, a wide range of application possibilities for novel lubricant additives is obtained. In principle, all known solid lubricants, e.g. graphite or polytetrafluoroethylene (PTFE) can be used as additives.[22] In areas of particularly high physical load, ceramic dusts or molybdenum as well as tungsten sulfide nanoparticles are preferentially used as solid lubricants.[23-25] Because of the relatively high price, these nanoparticles are mainly used as additives to conventional synthetic

oils.[26] In this respect, it is of major interest to develop procedures and synthetic approaches which allow for high yield of MoS_2/WS_2 particles.

In the following, **chapter 2** provides general insights on the basic theoretical concepts of heterogeneous and photoelectrochemical catalysis, which is a major part of the thesis. Futhermore, the field of tribology is introduced by illustrating the relevant physico-chemical parameters and their correlation. In **chapter 3**, the focus is on experimental methods such as the solvothermal technique and all chemicals and analytical equipment used in this work is enlisted. **Chapter 4** reports on the synthesis of molybdenum-doped tungsten oxide nanoflakes and tungsten-doped molybdenum oxide microspheres, respectively. Both the products are investigated on their catalytical performances in photocatalysis, photoelectrocatalysis and sulfoxidation reactions. While the results of the nanoflakes for the degradation of RB are indifferent, the Mo/W-microspheres show considerable catalytic ability in water splitting reactions as well as high conversion rates for the oxidation of sulfidic reagents. In **chapter 5** a novel route to porous silica-hematite nanoparticles is presented. Mesoporous silica nanoparticles are used as templates to promote the growth of a hematite phase, while NaF is used as *in-situ* etching agent. However, the performance of as-obtained silica-hematite nanoparticles in the degradation of RB are only slightly better compared to pristine silica-particles and inferior with regard to pure hematite nanoparticles. **Chapter 6** demonstrates the friction-reducing ability of different sulfidic nanoparticles, whereas novel oxysulfidic particles of tungsten and molybdenum provide the best results. The friction coefficients measured for the oxysulfides are significantly lower compared to known inorganic fullerene-like particles and nanotubes of WS_2. It is proposed, that due to the incorporation of oxide into the sulfide lattice the van-der-Waals gap between the distinct layers is expanded and, thus, facilitates delamination of the MoO_xS_{2-x} layers. **Chapter 7** includes a brief summary of the complete thesis. Additional data for all chapters of the thesis are presented in **chapter 8**.

1.2. References of Chapter 1

[1] A. Reinders, P. Verlinden, W. van Sark, A. Freundlich, *Photovoltaic Solar Energy: From Fundamentals to Applications*, John Wiley & Sons, Ltd., West Sussex, UK, 2017.

[2] M. Freitag, J. Teuscher, Y. Saygili, X. Zhang, F. Giordano, P. Liska, J. Hua, S. M. Zakeeruddin, J.-E. Moser, M. Grätzel, A. Hagfeldt, *Nat. Photonics* 2017, **11**, 372-378.

[3] K. Fan, J. Yu, W. Ho, *Mater. Horiz.* 2017, **4**, 319-344.

[4] D. Baran, R. S. Ashraf, D. A. Hanifi, M. Abdelsamie, N. Gasparini, J. A. Röhr, S. Holliday, A. Wadsworth, S. Lockett, M. Neophytou, C. J. M. Emmott, J. Nelson, C. J. Brabec, A. Amassian, A. Salleo, T. Kirchartz, J. R. Durrant, I. McCulloch, *Nat. Mater.* 2017, **16**, 363-369.

[5] J. Tsao, N. Lewis, G. Crabtree, *Solar FAQs*, US Department of Energy, 2006.

[6] V. Augugliaro, G. Camera-Roda, V. Loddo, G. Palmisano, L. Palmisano, J. Soria, S. Yurdakal, *J. Phys. Chem. Lett.* 2015, **6**(10), 1968-1981.

[7] J. Z. Bloh, *J. Phys. Chem. C* 2017, **121**(1), 844-851.

[8] A. Grimaud, O. Diaz-Morales, B. Han, W. T. Hong, Y. L. Lee, L. Giordano, K. A. Stoerzinger, M. T. M. Koper, Y. Shao-Horn, *Nat. Chem.* 2017, **9**, 457-465.

[9] F. Opoku, K. K. Govender, C. G. C. E. van Sittert, P. P. Govender, *Adv. Sustainable Syst.* 2017, **1**, 1700006.

[10] A. B. Djurisic, Y. H. Leung, A. M. C. Ng, *Mater. Horiz.* 2014, **1**, 400-410.

[11] J. Li, N. Wu, *Catal. Sci. Technol.* 2015, **5**, 1360-1384.

[12] T. Zhu, M. N. Chong, E. S. Chan, *ChemSusChem* 2014, **7**(11), 2974-2997.

[13] J. Zhang, Z. Liu, Z. Liu, *ACS Appl. Mater. Interfaces* 2016, **8**(15), 9684-9691.

[14] C. M. Friend, B. Xu, *Acc. Chem. Res.* 2017, **50**(3), 517-521.

[15] R. A. Sheldon, H. van Bekkum, *Fine Chemicals through Heterogeneous Catalysis*, Wiley-VCH, Weinheim, 2002.

[16] G. Centi, F. Cavani, F. Trifiro, *Selective Oxidation by Heterogeneous Catalysis*, Springer Science & Business Media, 2012.

[17] P. Dickie, *WWF Freshwater Program*, http://www.wwf.de/fileadmin/fm-wwf/Publikationen-PDF/richcountriespoorwaterfinal170706.pdf; retrieved on 07.09.2017

[18] S. ul-Islam (Ed.), *Advanced Materials for Wastewater Treatment*, John Wiley & Sons, Hoboken, 2017.

[19] M. Mehrjouei, S. Müller, D. Möller, *Chem. Eng. J.* 2015, **263**, 209-219.

[20] A. Ghosh, A. K. Nayak, A. Pal, *Curr. Polluttion Rep.* 2017, **3**(1), 17-30.

[21] I. Hutchings, P. Shipway, *Tribology: Friction and Wear of Engineering Materials*, Butterworth-Heinemann, Elsevier, Cambridge, 2017.

[22] T. W. Scharf, S. V. Prasad, *J. Mater. Sci.* 2013, **48**(2), 511-531.

[23] Z. A. Khan, V. Chacko, H. Nazir, *Friction* 2017, **5**(1), 1-22.

[24] H. Il, P. Tian, H. Lu, W. Jia, H. Du, X. Zhang, Q. Li, Y. Tian, *ACS Appl. Mater. Interfaces* 2017, **9**(6), 5638-5644.

[25] M. Ratoi, V. B. Niste, J. WaJ. Zekonyte, *Tribol. Lett.* 2013, **52**(1), 81-91.

[26] H. Xiao, S. Liu, *Mater. Des.* 2017, **135**, 319-332.

2. Theoretical Background

2.1. Heterogeneous Catalysis

Many chemical reactions might be thermodynamically possible, but do not proceed owing to some kinetic reasons. Therefore, it is necessary to provide a certain amount of energy to initiate the reaction. The activation energy to be supplied can be reduced by means of a catalyst. With regards to catalysis systems, a distinction is made based on the physical states of catalyst and reactants such as homogeneous catalysis (catalyst and starting materials present in the same phase) and heterogeneous catalysis (the reactants and the catalyst are located in at least two separate phases).

In many cases, the system of a heterogeneously catalyzed reaction consists of three phases in different combinations. Usually, the catalyst is in the solid state and the reagents are in gaseous or liquid phase. Heterogeneously catalyzed processes are predominantly carried out on solid catalysts. The catalysis takes place on the outer and/or inner surface of the catalyst, which gives rise to the terms surface catalysis and contact catalysis. Diffusion as well as adsorption and desorption processes of the reactants on the catalyst surface activate the molecules by weakening the bonds within the molecule or even splitting them. Hence, this allows the subsequent reactions to proceed more easily.

The majority of economically relevant reactions is performed with the aid of catalysts, whereby heterogeneous catalysis is the driving force of several famous large-scale conversions, such as:

- Haber-Bosch process (ammonia production),
- Fischer-Tropsch process (hydrocarbon synthesis),
- Ostwald process (nitric acid),
- steam reforming (hydrogen production),
- water-gas shift (hydrogen production, carbon dioxide),
- ethylbenzene dehydrogenation (styrene monomers),
- contact process (sulfuric acid),
- water-splitting (hydrogen production),
- aerobic oxidation of organics (intermediates/products for fine chemicals).

There is no unanimous theory of catalysis since different models exist for certain classes of catalytic reactions. Nonetheless, catalytic effects are always caused by intense interactions between the reactants and the catalyst. Chemical bonds between the reacting molecules and the catalyst may be formed, creating an intermediate species. This intermediate then decomposes to the final product and the regenerated catalyst. Thus, only relatively low, non-stoichiometric concentration of the catalyst is required.

In Figure 1 a simplified scheme of the catalytic effect is shown. Here, two reaction curves coincide on one x-axis, which normally does not apply for both reactions at the same time. Since the potential energy surface of both reactions strongly differ, the coordinates for both the reactions exhibit fundamental differences. Notwithstanding the actual reaction, the catalyst affects only the reaction rate of equilibrium, but not the position of the equilibrium of the reaction itself and therefore cannot trigger a thermodynamically impossible reaction. Both the forward chemical process and back reaction are affected likewise.

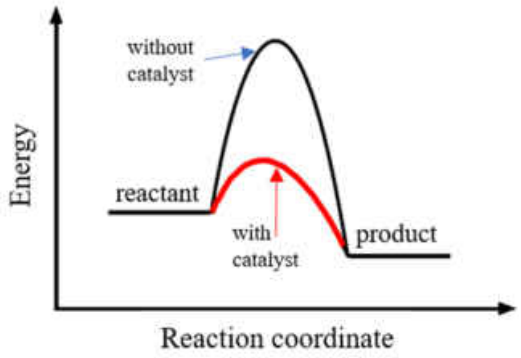

Figure 1. Schematic illustration of the two different energetic pathways for conventional reactions and catalysed reactions.

As mentioned above, heterogeneously catalyzed processes proceed on the surface of solids. Therefore, the properties of the solid's surface substantially determine the performance characteristics of a catalyst, such as activity, selectivity or deactivation behavior. In the simplest case, a larger specific surface area (active surface area per unit mass of the catalyst) provides a higher activity of the catalyst. In order to promote the catalytically most active compound with high levels of activity, great efforts are made to obtain stable particles with the lowest possible diameter.[1-4] This allows to reduce the size of the reactors and investment costs, in particular if expensive precious metals (e.g. rhodium or platinum) are used as catalyst. Since, with decreasing particle size, the relative number of surface atoms (and thus also reaction centers) increases, i. e. nanoparticles are usually clearly superior to smooth continuous surfaces of the same material in terms of reactivity. Catalysts, which are extremely expensive, are usually prepared as thin films or coatings on supporting materials.

Due to the electronic and coordinative characteristics, especially transition metals are promising materials for efficient catalysts. Metal oxide nanoparticles (NPs) or microparticles (MPs) are known as catalysts in heterogeneous catalysis.[5-7] Metals like copper,[8, 9] nickel,[10, 11] iron,[12] molybdenum[13, 14] and manganese[15, 16] are distinguished by being earth abundant and by their functionality in various biological reactions.

A measure of the fraction of catalytically active atoms, so-called **dispersion**, is defined as the number of surface atoms of the catalytically active substance divided by the total number of atoms

present in that substance. A dispersion of 1 means that all atoms of the material are on its surface. For typical catalytic materials with particle sizes < 1 nm the dispersion is above 0.5. The exact values are affected by atomic radii and particle morphology.

The **catalyst activity** can be expressed by the reaction rate *r*, the rate constant k and the activation energy E_A. The reaction rate is a function of the time change (t) of the mass quantity n_E of a reactant E based on the reaction volume V or the catalyst mass m_C:

$$r = n_E/(m_C \cdot t). \quad (1)$$

The rate constant k results from the decomposition law:

$$d[E]/dt = k[E]. \quad (2)$$

However, if different catalysts are compared for a reaction, it is necessary to define other comparative parameters, since each catalyst requires different operating conditions. In this context, it is more useful to consider measurements such as conversion at constant reaction conditions, space velocity for a specific, constant turnover or a space-time yield. The **turnover rate** (TR) or **turnover frequency** (TOF) is defined as the number of revolutions of the catalytic cycle per unit time. Though, it is a chemical reaction rate in terms of a differential quantity, which depends on the concentration, temperature and pressure.

Technical realizations of the chemical reactions are often complex processes in which, apart from the actual reaction, its outcome can be significantly affected by temperature, pressure, concentrations and transport phenomenona (heat, matter and impulse).

2.2. Catalytical Sulfoxidation

Sulfoxidation is one of the most fundamental reactions among organic chemistry conversions.[17] Many sulfoxides and sulfones are intermediates in organic reactions and constituents of important pharmaceutical products.[18] Most of the processes currently used for carrying out sulfoxidations rely on the utilization of peracids or halogen derivatives as oxidizing agents, such as *meta*-chloro-peroxybenzoic acid (*m*-CPBA),[19] perborate in acetic acid[20] or *tert*-butylnitrite.[21] This leads to the production of eco-unfriendly by-products.

In recent years, the transfer of known and establishing the new processes in the field of green chemistry has become increasingly important. Therefore, agents that are comparatively easy and safely to handle have preferably to be used to avoid or reduce undesired byproducts. The utilization of a heterogeneous catalyst in combination with hydrogen peroxide provides an alternative green chemistry approach. Hydrogen peroxide is a cheap, non-toxic and large-scale industrial chemical, which is primarily used in detergents as bleaching agent.[22] It offers simple control of the reaction, to selectively oxidize various sulfides into sulfoxides (RSOR) or sulfones

(RSO_2R) under mild conditions and less extensive product purification.[23-25] As a result, the oxidation of the organic compounds with hydrogen peroxide (H_2O_2) is of high interest, in especially as the reaction products, oxygen (O_2) and water (H_2O), are completely harmless and biocompatible:

$$2\ H_2O_2 \rightarrow 2\ H_2O + O_2. \qquad (3)$$

There are some elemental requirements to achieve high conversion efficiencies with metal containing catalysts: a) the metal center can easily change the oxidation states by providing a sufficient stability, b) the possibility of the reoxidation into the initial state and c) the reversible formation of bonds during the catalysis.

It is well known that tungsten as well as molybdenum forms stable bonds with oxygen and sulfur in high oxidation states.[26] In particular, the affinity to sulfur and its ability to catalyze oxidation reactions make both tungsten and molybdenum ideal candidates for catalysts in sulfoxidation reactions. Besides these two metals, sulfoxidation catalyzed by many other transition metals (Ti, Fe, V, Re or Ru) is already reported.[27-30]

While oxidations catalyzed by various metal complexes like ammonium or sodium metavanadate (NH_4VO_3, $NaVO_3$),[31, 32] vanadyl diacetylacetonate ($VO(acac)_2$),[33, 34] titanium chloride ($TiCl_3$),[35] molybdyl diacetylacetonate ($MoO_2(acac)_2$)[36] and other molybdenum complexes[37-39] have been reported in organic solvents, reactions in aqueous solutions are rare.[40, 41] In addition to metal complexes also natural enzymes like the vanadium haloperoxidase[42, 43] and other metal containing model complexes are able to catalyze the selective oxidation of organic sulfides and further substrates,[44, 45] but are too expensive for large-scale industrial applications.

2.3. Photocatalysis and Photoelectrocatalytical Water Splitting (PEC)

2.3.1. Principles of Photocatalysis and PEC

The efficient use of different systems and strategies to explore renewable or inexhaustible resources (wind energy, solar cells, bio mass or global thermal energy) could be the only way forward to generate carbon free alternative sources of energy. As the most promising method for producing renewable energy, the cleavage of water into its molecular constituents oxygen and hydrogen (equation 4), is increasingly gaining importance because of its eco-friendliness and cost effectiveness:[46-49]

$$2\ H_2O \rightarrow O_2 + 2\ H_2. \qquad (4)$$

The hydrogen produced can be stored as an energy carrier and thus can be used for energy generation if required. During combustion in air or in fuel cells, only water is produced as a by-product, the liberated energy being stored in a targeted manner. In addition, the entire process is carbon neutral, which is of great importance in terms of global warming. The reaction shown in equation 4 is an endothermic process, to which energy of 237.2 kJ/mol must be supplied (at room temperature and 1 atm pressure), corresponding to a potential of $\Delta E^0 = 1.23$ V per electron transferred.

Water cleavage can be carried out not only by externally applied voltage by means of electrolysis. In the photoelectrocatalysis, materials with bandgap values exceeding 1.23 eV are used. For the actual water cleavage, the material must also be able to overcome the overpotential and to be able to compensate for further (electron-transfer-induced) losses.[50] Therefore, in the normal case, compounds are used whose band gaps (E_g) exhibit values between 1.6 and 2.4 eV. These E_g values correspond to a wavelength between 800 and 400 nm, i.e. the visible range.

In principle, water-splitting takes place in conventional electrolysis cells, in which water is oxidized under acidic conditions. This process, also known as **oxygen evolution reaction** (OER), occurs at the anode:

$$2\ H_2O \rightarrow O_2 + 4\ e^- + 4\ H^+. \qquad (5)$$

The released electrons (e^-) are extracted via an external circuit, while the protons (H^+) migrate through the permeable membrane into the cathode compartment. There, electrons and protons recombine with the emergence of hydrogen (**hydrogen evolution reaction**, HER):

$$4\ e^- + 4\ H^+ \rightarrow 2\ H_2. \qquad (6)$$

The process described above can also be carried out in basic medium, the reactions of hydrogen and oxygen generation being:

$$4\ H_2O + 4\ e^- \rightarrow 2\ H_2 + 4\ OH^- \text{ (HER)}, \qquad (7)$$

$$4\ OH^- \rightarrow O_2 + 2\ H_2O + 4\ e^- \text{ (OER)}. \qquad (8)$$

In acidic medium, precious metals (platinum cathodes) represent the best materials known to date. Under basic conditions, transition metals of the first series and their appropriate oxides are the most effective catalysts.

An important parameter in this context is the **current density**, which is defined as the charge flow per unit area of the electrode per unit time and, ultimately, allows a statement about the rate of water cleavage. However, for faster rates the system must also be supplied with a larger amount of activation energy. This additional energy is a necessary prerequisite for the potential bias above 1.23 V. The amount of additional voltage to be supplied to achieve a particular current density is

referred to as **overvoltage**. The actual task of the electrocatalyst is therefore to reduce the overvoltage as much as possible.

A general set-up of a water-splitting cell operated with a tungsten oxide anode and platinum cathode is illustrated in Figure 2. Incoming light is absorbed by the photocatalyst-containing photoanode, which usually is applied on a conductive material such as FTO or ITO. The photocatalyst absorbs photon energy greater than the bandgap energy, promoting an electron from the valence band to the conduction band. This electron and the remaining hole in the valence band form a so-called exciton. These photo-excited carriers separate and migrate to the surface without recombination. The adsorbed species (water) is subsequently oxidized by the photo-generated holes to produce O_2. At the Pt as counter electrode, a recombination of e^- and H^+ to hydrogen takes places to produce hydrogen. The electrodes are electrically connected to maintain a constant electron transfer.

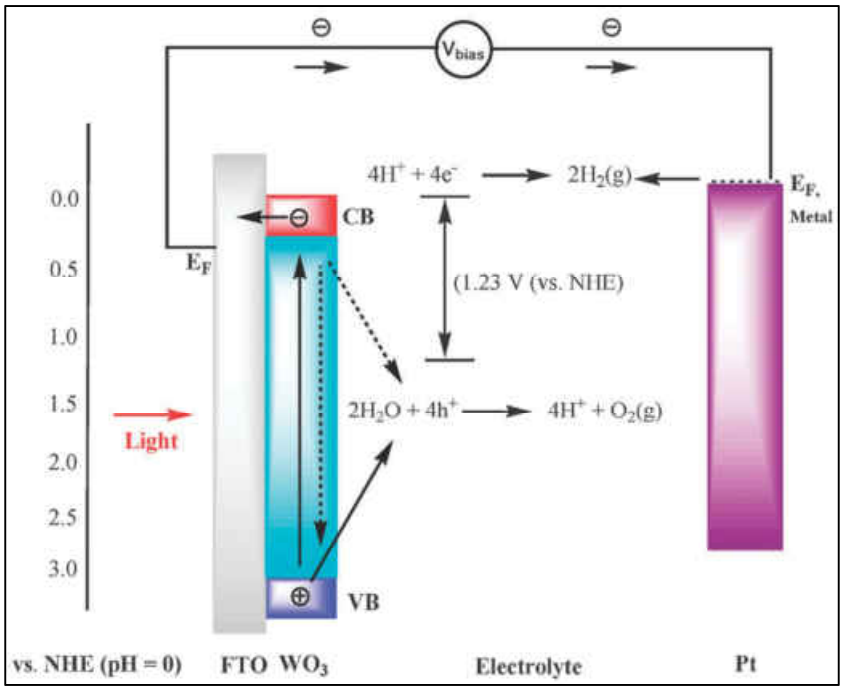

Figure 2. Schematic representation of the fundamental principles of photoelectrocatalytic water splitting with WO_3-based n-type semiconductor and Pt as the counter electrode.[51]

In general, solar-aided electrochemical water splitting can be achieved by two different approaches (Figure 3). On the direct route, the solar energy is absorbed by the module which also catalyzes the water cleavage (Figure 3 a); on the indirect route, energy absorption and water cleavage are carried out in two separate steps (Figure 3 b). The latter offers the possibility to use known materials and technologies, but provides significantly smaller efficiencies due to the additional step. To this extent, the endeavor to take the direct path to water cleavage has become increasingly important in recent years.

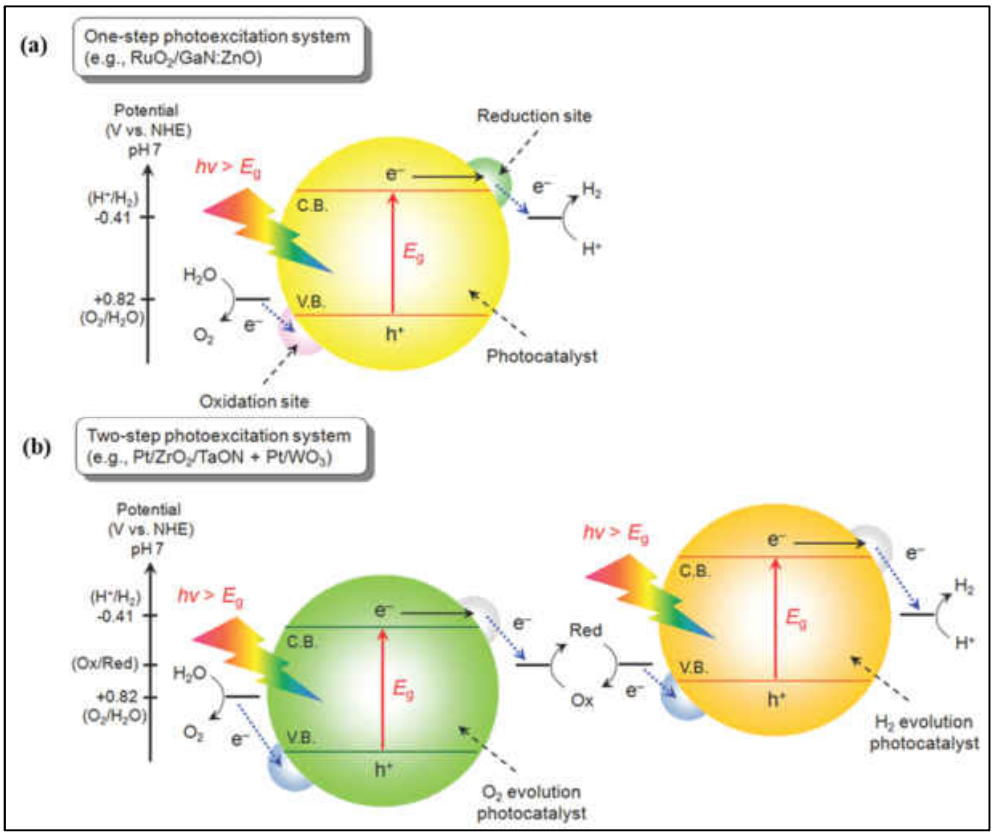

Figure 3. Schematic showing the energy diagrams of photocatalytic water splitting by (a) one-step system with oxidation and reduction site provided by photocatalyst with co-catalyst support and (b) two-step photoexcitation system using two different photocatalysts at separated locations.[52]

A major problem of all semiconductors suitable for photoelectrocatalysis is their chemical resistance under strongly acidic or strongly basic environments, which is decisive for the maximum possible concentration of charge carriers (H^+ or OH^-). With regard to the longevity, safety and economic utility of the cells, it would be more advantageous to operate under milder conditions. In addition, the use of abundant materials is another important factor for the viability of this technology.

In order to quantify the effectiveness of different catalysts for the HER, so-called **volcano plots** according to Trasatti can be considered (Figure 4). Here, the energy of the chemisorption of hydrogen on a particular material is correlated with the HER **exchange current density** (ECD) of the corresponding material. The ECD is the intrinsic rate of electron transfer between the analyte in solution and the electrode under a particular set of conditions. In general, a larger ECD is associated with a greater activity of the catalyst. For example, it was shown that molybdenum sulfide, actually known as a poor HER catalyst, would be an excellent candidate for use in water cleavage. As described by Jaramillo et al. and Kibsgaard et al.,[53, 54] the reason for this is the pronounced defect structure of MoS_2: the more edges of the material exhibit the more pronounced activity in terms of hydrogen evolution. The reactivity of the basal planes compared to the edges, on the other hand, is almost negligible. It has also been shown that a new compound with

improved hydrogen bonding properties can be created by combining two elements that are found on different sides of the volcano plot.[55] For many other compounds, excellent HER values were obtained,[56-59] while their long-term stability (up to many thousands of hours operating time) remains to be validated.

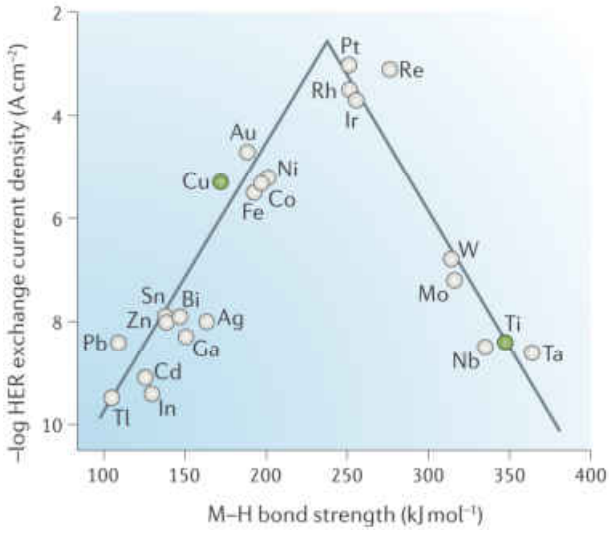

Figure 4. Trasatti's HER volcano plot.[60]

For the OER in basic medium, as already mentioned above, oxides of transition metals or transition metal alloys are usually employed. Currently, NiFe oxides are compounds requiring the smallest overvoltage (~ 30 mV at 1 mA/cm^{-2}) to provide excellent OER results in strongly basic media. Other mixed oxides of nickel and cobalt[61] or nickel and molybdenum[62] are also particularly suitable catalysts for OER. Trotochaud et al. showed that traces of nickel introduced into the cell by contaminated electrolytes can significantly reduce the overvoltage even in the absence of an additional catalyst.[63, 64] It was only recently that Zhang et al. showed W(VI)-doped FeCo oxides to yield outstanding results in the OER.[65] This is attributed to the fact that the intermediates formed in the OER can attach optimally to the catalyst surface. However, the OER can also be carried out in neutral buffer medium, as presented by Nocera et al.[66] The active sites are presumably provided by cobalt oxo cubanes, whereby cobalt is oxidized from its oxidation state (III) to the reactive (IV) species, which in turn is responsible for the oxidation of the water. During this process, Co (IV) is reduced to the soluble Co (II), which is subsequently oxidized to the Co (III) by anodic stress. It is particularly interesting that these catalysts not necessarily require high-purity water for the electrolyte's solvatation.[67]

2.3.2. Challenges and Optimization Strategies for PEC

Hydrogen evolution by water-splitting is a promising technique to achieve sustainability in energy production and much progress have already been made. Currently, the most efficient

electrocatalysts with significant incident photon-to-current conversion efficiencies (IPCE) are made of expensive and scarce noble metals, such as Pt,[68] Pt-Au,[69] Pd,[70] or Pd-Au.[71] Therefore, the development of new materials, which are cheap and efficient is highly desirable. These new materials have to meet a number of requirements to provide efficient visible light water splitting:

(i) absorption of a maximum amount of solar photon energy, especially the visible part of the solar spectrum (400–800 nm), implies the semiconductor band gap to be higher than 1.23 eV (hydrogen generation potential),

(ii) the reduction potential of water should be higher than the conduction band edge of the semiconducting material, whereas, in the case of the valence band it should be at a more positive potential than the oxidation reaction of water,

(iii) flat-band potentials, which determine the driving forces of all electron transfer reactions, should be adequately negative,[72]

(iv) stability against photocorrosion under operation in neutral or alkaline environment.

In addition, further increase in the complexity of the device's technological dimensions (especially the catalytical active areas) have to be accomplished. Arrays with a few square centimeters area are useful for demonstration purposes, but a scale-up to at least multiple square meters is required to even approximately meet future demands.

Though it is concomitant with the use of inexpensive components (electrolyte, electrocatalyst, membrane and light-absorber), which should also provide a stable performance with a long service life. Whether or not it is possible to separate the generated hydrogen safely from the material is still an open question which needs to be answered. A major drawback of the water splitting cells is that the permeability of oxygen and hydrogen through the membrane at high current densities can lead to dangerous mixtures of the two gases. Methods for preventing this gas evolution already exist, but most of them tend to potentially reduce the performance of the fuel cells. In order to strike a balance for this technical dilemma, further engineering development is necessary.

Decoupling the OER and HER reactions using electron-coupled-proton buffers (ECPB) might offer a meaningful and feasible solution for that problem, as has already been demonstrated by Cronin et al.[73-75] Here, the buffer is reduced and then protonated to be subsequently regenerated by the electrochemical oxidation to release hydrogen. In a large-scale device, hydrogen could be produced in a separated compartment using a conventional electrolyzer to achieve higher current densities. Thus, this would allow for an easier handling, storage and distribution of the gaseous products.

2.4. Tribology

2.4.1. Basic Principles of Tribology

According to the (withdrawn) DIN 50323 “Tribology is the science and technology of interacting surfaces in relative motion. It covers the entire range of **friction** and **wear**, including lubrication, and includes appropriate interfacial effects between both solids and between solids and liquids or gases.” Ultimately, friction processes lead to extensive and faster wear at the affected components, which result in high operating costs. An important task area of tribology is the functional, economical and ecological optimization of systems easing the movement. The use of tribology in technology covers all areas of development, design, manufacture and maintenance of mechanical motion systems in various industries and economic sectors.

In qualitative terms, tribological research is concerned with the study of tribological processes and laws by examination of the phenomena according to the type (characterized by tribological stress), the form (characterized by macroscopically detectable processes) and states and effects (with regard to the basic processes underlying the phenomena). The so-called tribometry represents a quantitative viewpoint, in which the measurement-technical determination of the characteristic quantities, their interdependence and underlying physical principles are in the foreground.

While examining tribological phenomena, the following specifications are significant:

a) the complex collective of stress factors comprising the course and duration of the load, the speed and temperature, the type of movement (e.g. sliding, rolling, bumping or flowing) and movement pattern (continuous, oscillating or intermittent),
b) the structure of the tribo-system (interfaces, lubricant and ambient medium),
c) energy dissipation (e.g. frictional heat or sound radiation),
d) material damage and loss (peeled particles, wear),
e) geometric conditions in the contact zone (e.g. surface geometry, contact areas or gap height),
f) changes in materials and lubricants (composition, built-up or removal of surface layers, transformations).

The two main subjects of tribological research are subdivided into **tribophysics** and **tribochemistry**. While the tribophysics is dealing with physical appearance, e.g. tribo-mechanics, -eletricity or -luminescence, tribochemistry considers the physico-chemical aspects such as tribocorrosion, oxidation, absorption or the triboreaction. Regarding a real system, friction and wear are complex phenomena, in which different tribophysical and tribochemical processes are usually involved.

The term **wear** is used to describe the progressive loss of material from the surface of a solid body caused by mechanical stress (or tribological stress), i.e. by contact and relative movement of a solid, liquid or gaseous counterpart (Figure 5). Tribological stress is the totality of the load factors acting on the elements of the wear system from the outside. Hence, wear is normally undesirable and provokes impairment. In exceptional cases, such as, e.g. during running-in operations, wear processes can also be technically desired. Heavy machinery is frequently subjected running-in cycles, where the severity is increased stepwise. This procedure is performed to reduce the danger of scuffing that might occur due to localized overloading in new components.

The main wear mechanisms are adhesion, abrasion, surface destruction (fatigue) and tribochemical reactions (tribooxidation). The measured variables directly or indirectly characterize the change in the shape or mass of a body by wear, such as abrasion depth or composition of the residual film on the material surface.

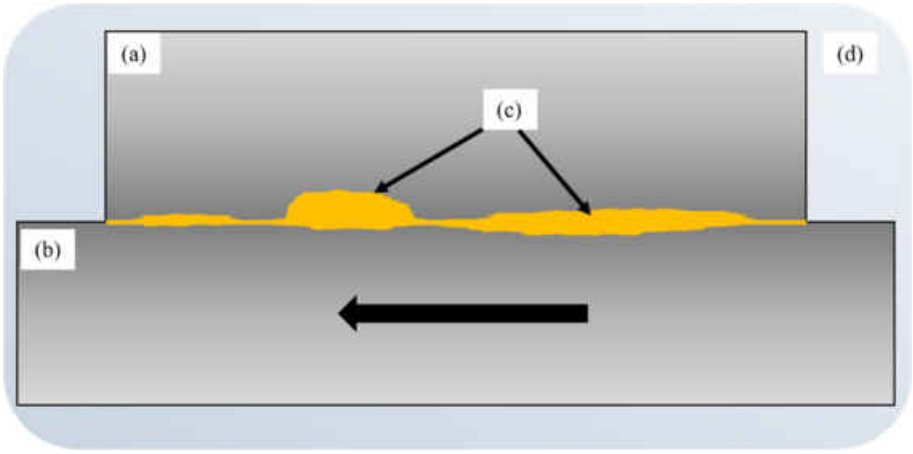

Figure 5. Schematic of a tribological system: (a) basic body, (b) moving counter body, (c) contact zone with lubricant and (d) surrounding medium.

Wear occurs on components whose technical function is associated with tribological stresses. In contrast to the strength properties (tensile strength, compressive strength, etc.), which are regarded as material-related characteristics, the wear occurring under tribological stress results from the interaction of all parts of a technical array involved in the wear process and can only be described by wear characteristics directly related to the examined system.

The technical-physical **stress parameters** during a wear process are given by the following four variables: normal force $F_{N,}$ velocity v, temperature T and load time t_L. Consequently, if the F_N and the size of the geometric contact surface between the basic body and the counter body (tribocontact surface area, TSA) is known, the mean surface pressure p can be calculated:

$$p = F_N/TSA. \qquad (9)$$

The speed v, which is decisive for a wear process, is the relative speed between the two wear partners. The temperature T refers to the respective thermal equilibrium state of the entire

tribological system. In thermal imbalances, e.g. at different temperatures of the basic body and the counter body, several temperatures or temperature functions have to be considered. The stress duration t_L indicates the period of time in which the tribological stresses leading to the wear are effective. From the knowledge of t_L and the velocity v, the stress path can be calculated.
Depending on the situation or knowledge of the tribosystem, the **types of wear** are classified according to the tribological load, the form of movement (sliding wear, rolling wear, impact wear, vibration wear, etc.) or the substances involved (grain sliding wear, solid body wear, particle sliding wear, jet wear, liquid erosion, etc.). As mentioned above, four different types of interactions or mechanisms can be distinguished:

a) adhesion (formation of interface bonding and subsequent material transfer by separation of adhesive bonds),
b) abrasive wear (material removement through furrowing and scratching stress),
c) fatigue wear (strength reduction and crack formations in surface areas due to alternating tribological stresses) and
d) tribo-oxidation (chemical reactions, initiated or promoted by tribological stress between the basic body, counterparts and surrounding medium leading to formation of layers with different composition compared to the origin material).

The type of tribological stress in the appropriate set-up ultimately affects the type of mechanism.

2.4.2. Nanoparticles as Friction Reducing Agents

Since the roughness of the materials subjected to tribological stress results from unevenness on the material's surface, it is possible to reduce friction by adding nano-/microparticles of any composition. The tribological performance of nanoparticle-based lubricants strongly depends upon the characteristics of the nanoparticles, such as shape, size and concentration within the lubricant. Practically, many other aspects have to be considered to explain why layered transition metal dichalcogenides are far superior to other particles as additives in lubricants.
Due to weak van-der-Waals interactions between two chalcogen (Q = S, Se, Te) layers, easy sliding of the chalcogenide layers on one another can be induced.[76] Depending on how the Q-layers are stacked in the unit cell, three main allotropes can be distinguished: 1T-MQ_2 with tetragonal stacking, 2H-MQ_2 with hexagonal (anti-parallel) and 3R-MQ_2 with a rhombohedral (parallel) arrangement of the trigonal prisms (Figure 6).

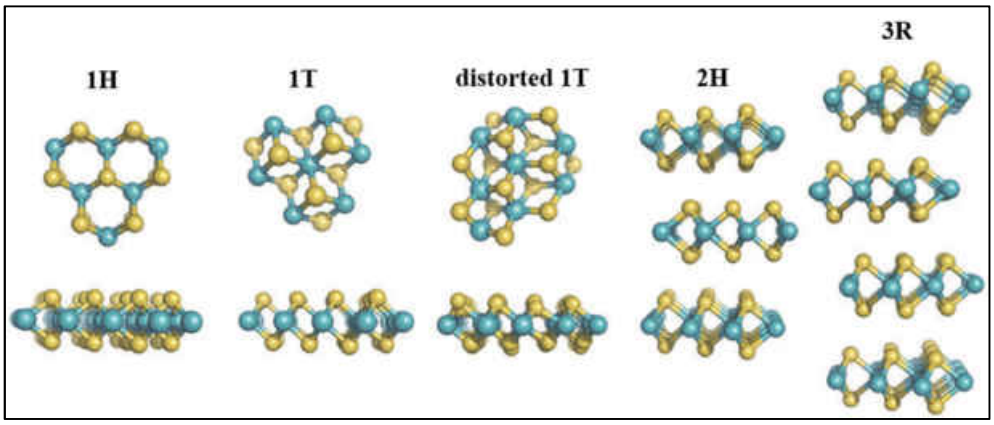

Figure 6. Structural arrangement in the allotropes of MS_2 layered chalcogenides; Mo or W as turquoise balls and S as yellow balls.[77]

Hence, layered chalcogenides are excellent lubricants. In particular, the molybdenum disulfide and tungsten disulfide exhibit superior temperature stability and inert behavior as high-performance lubricants and can withstand temperatures up to 400 °C (MoS_2) and 650 °C (WS_2), respectively.[78, 79] Due to this, solid lubricants can perform specific tasks in cases where liquid lubricants are not usable or have inadequate lubricating properties, such as under vacuum, in space, in highly stressed machine parts or in the automotive industry. In these cases molybdenum or tungsten sulfide (rarely graphite) are frequently used.

The advantage of MS_2 nanosheets and nanoflakes compared to the corresponding commercially available bulk material is their significantly reduced particle size, which allows penetration into the smallest cavities of the components.[80, 81] It is also possible to coat individual components of heavy-duty machinery with MS_2 in order to protect them even against abrasion and wear.

Due to the spherical structure of their building blocks, fullerene analogous compounds show considerably better lubricating properties than their crystalline counterparts. As Tenne and coworkers already showed, this behavior can be explained by the shear resistance between the elastic fullerene building blocks of IF-MS_2, which is caused by rolling friction in the first place. This model only applies for relatively small pressures (< 1.1 GPa), because exceeding a critical physical stress forces the spherical structure to collapse.[82, 83] In that case, the shear resistance is based on sliding friction between the layers and corresponds to that of crystalline 2H-MS_2 compounds.

The behavior of MS_2 particles with different morphologies is illustrated in Figure 7.

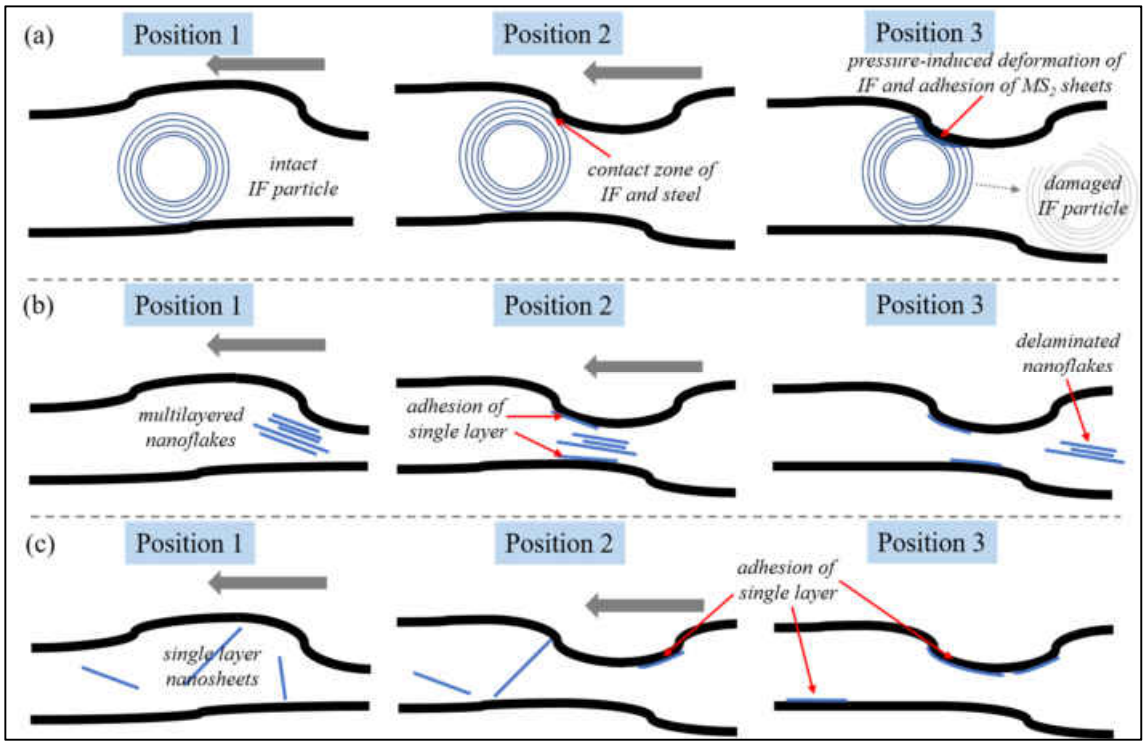

Figure 7. Scheme illustrating the behaviour of MS_2 particles with different morphologies between two sliding metallic surfaces at three different times: (a) inorganic fullerenes, (b) multi-layer nanoflakes and (c) single-layer nanosheets.

If the pressure exerted on the fullerene-like particles is further increased, the outermost layers are delaminated. These peeled layers then penetrate into the unevenness of the surrounding surfaces and flatten the irregularities. This in turn facilitates the sliding of the remaining particles on the material surfaces. The mechanism was shown by in-situ TEM measurements during a sliding test, as shown in Figure 8.

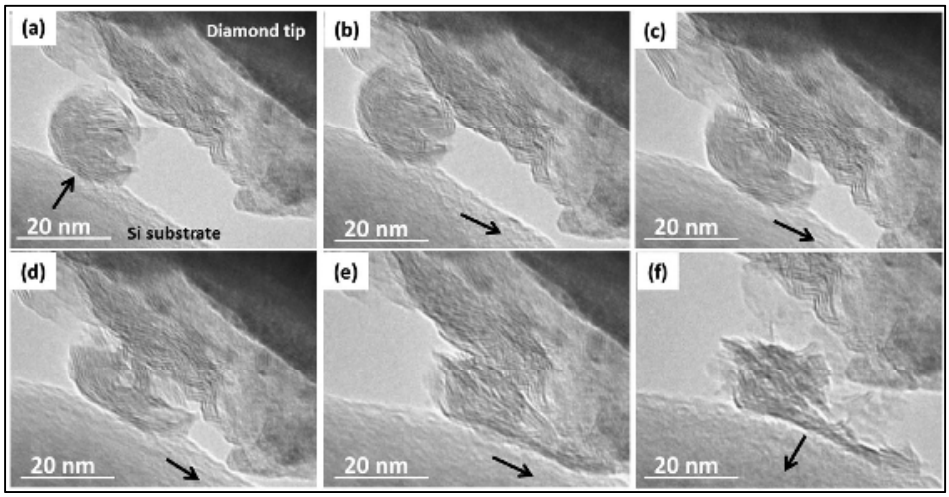

Figure 8. Images captures from a video recording during a sliding experiment carried out with a single crystallised IF-MoS_2 nanoparticle demonstrating exfoliation of the layered structure.[84]

Studies conducted by our working group suggested two possible mechanisms for the tribochemistry taking place on the steel surface.[85] As XPS analysis of the worn surfaces shows not only S-O and Mo-O bonds, but also the presence of Fe-S bonds, it was deduced that the delaminated MoS_2 layers could incorporate oxygen from the native iron oxide layer of the steel. Another explanation is that the tribofilm might be subsequently oxidized by air.

2.5. References of Chapter 2

[1] R. Narayanan, M. A. El-Sayed, *Nano Letters* 2004, **4**(7), 1343-1348.

[2] X. Zhou, W. Xu, G. Liu, D. Panda, P. Chen, *J. Am. Chem. Soc.* 2010, **132**(1), 138-146.

[3] H. Tsunoyama, H. Sakurai, Y. Negishi, T. Tsukuda, *J. Am. Chem. Soc.* 2005, **127**(26), 9374-9375.

[4] C. N. R. Rao, G. U. Kulkarni, P. J. Thomas, P. P. Edwards, *Chem. Eur. J.* 2002, **8**(1), 28-35.

[5] D. Koziej, A. Lauria, M. Niederberger, *Adv. Mater.* 2014, **26**(2), 235-257.

[6] J. Pal, T. Pal, *Nanoscale* 2015, **7**, 14159-14190.

[7] E. W. McFarland, H. Metiu, *Chem. Rev.* 2013, **113**(6), 4391-4427.

[8] L. Que Jr., W. B. Tolman, *Nature* 2008, **455**, 333-340.

[9] V. V. Rostovtsev, L. G. Green, V. V. Fokin, K. B. Sharpless, *Angew. Chem.* 2002, **114**(14), 2708-2711.

[10] F. S. Han, *Chem. Soc. Rev.* 2013, **42**, 5270-5298.

[11] J. Zhou, G. C. Fu, *J. Am. Chem. Soc.* 2003, **125**(48), 14726-14727.

[12] B. Plietker (Ed.), *Iron Catalysis in Organic Chemistry: Reactions and Applications*, Wiley-VCH, Weinheim, 2008.

[13] D. V. Yandulov, R. R. Schrock, *Science* 2003, **301**(5629), 76-78.

[14] S. J. Malcolmson, S. J. Meek, E. S. Sattely, R. B. Schrock, A. H. Hoveyda, *Nature* 2008, **456**(7224), 933-937.

[15] J. O. Bauer, S. Chakraborty, D. Milstein, *ACS Catal.* 2017, **7**(7), 4462-4466.

[16] A. Mukherjee, A. Nerush, G. Leitust, L. J. W. Shimon, Y. B. David, N. Angel, E. Jalapa, D. Milstein, *J. Am. Chem. Soc.* 2016, **138**(13), 4298-4301.

[17] E. N. Prilezhaeva, *Russ. Chem. Rev.* 2007, **69**, 367–408.

[18] S. Caron, R. W. Dugger, S. G. Ruggeri, J. A. Ragan, D. H. Brown Ripin, *Chem. Rev.* 2006, **106**, 2943-2989.

[19] N. K. Jana, J. G. Verkade, *Org. Lett.* 2003, **5**, 3787-3790.

[20] C. Karunakaran, R. Kamalam, *Eur. J. Org. Chem.* 2000, 3261-3263.

[21] B. Yu, Z.-F. Diao, A.-H. Liu, X. Han, B. Li, L.-N. He, X.-M. Liu, *Curr. Org. Syn.* 2014, **11**, 156-160.

[22] K. Kaczorowska, Z. Kolarska, K. Mitka, P. Kowalski, *Tetrahedron* 2005, **61**, 8315-8327.

[23] R. Noyori, M. Aoki, K. Sato, *Chem. Commun.* 2003, 1977-1986.

[24] J. M. Fraile, J. I. Garcia, B. Lazaro, J. A. Mayoral, *Chem. Commun.* 1998, 1807-1808.

[25] V. Hulea, F. Fajula, J. Bousquet, *J. Catal.* 2001, **198**, 179-186.

[26] P. C. H. Mitchell, *J. Inorg. Biochem*. 1986, **123**, 107–123.

[27] O. Bortolini, F. Di Furia, G. Modena, R. Seraglia, *J. Org. Chem.* 1985, **50**, 2688-2690.

[28] M. R. Berenguer, P. J. Campon, L. Coppi, *Chem. Abstr.* 2003, **135**, 242230.

[29] J. Oguma, K. Hagiya, T. Miyawaki, *Chem. Abstr.* 2002, **136**, 164701.

[30] H. Cotton, *Chem. Abstr.* 2000, **131**, 5258y.

[31] K. Masayasu, T. Yoshio, I. Norio, *Chem. Abstr.* 1989, **111**, 39369n.

[32] A. V. Anisimow, E. V. Fedorova, A. Z. Lesnugin, V. M. Senyavin, L. A. Aslanov, V. B. Rybakov, A. V. Tarakanova, *Catal. Today* 2003, **78**, 319-325.

[33] J. Skarzewski, E. Wojaczynska, I. Turowska-Tyrk, *Tetrahedron: Asymmetry* 2002, **13**, 369-375.

[34] C. Slemon, B. Macel, *Chem. Abstr.* 1995, **122**, 133189c.

[35] Y. Watanabe, T. Numata, S. Oae, *Synthesis* 1981, 204.

[36] A. Buxade Vinas, *Chem. Abstr.* 1995, **123**, 228183f.

[37] W. Winter, C. Mark, V. Schurig, *Inorg. Chem.* 1980, **19**, 2045-2048.

[38] M. Bonchio, T. Carofiglio, F. Di Furia, R. J. Fornasier, *Org. Chem.* 1995, **60**, 5986-5988.

[39] O. Bortolino, F. Di Furia, G. Modena, C. Scardellato, *J. Mol. Catal.* 1981, **11**, 107.

[40] L. Dai, A. M. Klibanov, *Biotechnol. Bioeng.* 2000, **70**(3), 353-357.

[41] P. Dixneuf, V. Cadierno, *Metal-Catalyzed Reactions in Water*, Wiley-VCH, Weinheim, 2013.

[42] A. Butler, J. N. Carter-Franklin, *Nat. Prod. Rep.* 2004, **21**, 180-188.

[43] H. B. ten Brink, H. L. Holland, H. E. Schoemaker, H. van Lingen, R. Wever, *Tetrahedron: Asymmetry* 1999, **10**, 4563-4572.

[44] D. Wischang, M Radlow, J. Hartung, *Dalton Trans.* 2013, **42**, 11926-11940.

[45] R. Ragg, F. Natalio, M. N. Tahir, H. Janssen, A. Kashyap, D. Strand, S. Strand, W. Tremel, *ACS Nano* 2014, **8**(5), 5182-5189.

[46] A. J. Bard, *Science* 1980, **207**, 4427.

[47] A. Turner, *Science* 2004, **305**, 972.

[48] N. S. Lewis, D. G. Nocera, *Proc. Natl. Acad. Sci.* 2006, **103**, 15729.

[49] H. B. Gray, *Nat. Chem.* 2009, **1**, 7.

[50] J. Chen, D. Yang, D. Song, J. Jiang, A. Ma, M. Z. Hu, C. Ni, *J. Power Sources* 2015, **280**, 649-666.

[51] X. Liu, F. Wang, Q. Wang, *Phys. Chem. Chem. Phys.* 2012, **14**, 7894-7911.

[52] K. Maeda, K. Domen, *J. Phys. Chem. Lett.* 2010, **1**, 2655-2661.

[53] T. F. Jaramillo, K. P. Jorgensen, J. Bonde, J. H. Nielsen, S. Horch, I. Chorkendorff, *Science* 2007, **317**, 100-102.

[54] J. Kibsgaard, Z. Chen, B. N. Reinecke, T. F. Jaramillo, *Nat. Mater.* 2012, **11**, 963-969.

[55] S. Trasatti, *J. Electroanal. Chem.* 1972, **39**, 163-184.

[56] J. Wang, W. Cui, Q. Liu, Z. Xing, A. M. Asiri, X. Sun, *Adv. Mater.* 2016, **28**(2), 215-230.

[57] C. G. Morales-Guio, L.-A. Stern, X. Hu, *Chem. Soc. Rev.* 2014, **43**, 6555-6569.

[58] X. Zou, Y. Zhang, *Chem. Soc. Rev.* 2015, **44**, 5148-5180.

[59] P. C. K. Vesborg, B. Seger, I. Chorkendorff, *J. Phys. Chem. Lett.* 2015, **6**(6), 951-957.

[60] I. Roger, M. A. Shipman, M. D. Symes, *Nat. Rev. Chem.* 2017, **1**(3), 1-13.

[61] T. N. Lambert, J. A. Vigil, S. E. White, D. J. Davis, S. J. Limmer, P. D. Burton, E. N. Coker, T. E. Beechem, M. T. Brumbach, *Chem. Commun.* 2015, **51**(46), 9511-9514.

[62] J. Tian, N. Cheng, Q. Liu, X. Sun, Y. He, A. M. Asin, *J. Mater. Chem. A* 2015, **3**, 20056-20059.

[63] L. Trotochaud, S. L. Young, J. K. Ranney, S. W. Boettcher, *J. Am. Chem. Soc.* 2014, **136**, 6744-6753.

[64] A. M. Smith, L. Trotochaud, M. S. Burke, S. W. Boettcher, *Chem. Commun.* 2015, **51**, 5261-5263.

[65] B. Zhang, X. Zheng, O. Voznyy, R. Comin, M. Bajdich, M. Garcia-Melchor, L. Han, J. Xu, M. Liu, L. Zheng, F. P. Garcia de Arquer, C. T. Dinh, F. Fan, M. Yuan, E. Yassitepe, N. Chen, T. Regier, P. Liu, Y. Li, P. De Luna, A. Janmohamed, H. L. Xin, H. Yang, A. Vojvodic, E. H. Sargent, *Science* 2016, **352**, 33-337.

[66] M. W. Kanan, D. G. Nocera, *Science* 2008, **321**, 1072-1075.

[67] A. J. Esswein, Y. Surendranath, S. Y. Reece, D. G. Nocera, *Energy Environ. Sci.* 2011, **4**, 499-504.

[68] R. Subbaraman, D. Tripkovic, D. Strmcnik, K. C. Chang, M. Uchimura, A. P. Paulikas, V. Stamenkovic, N. M. Markovic, *Science* 2011, **334**, 1256.

[69] J. Kye, M. Shin, B. Lim, J. W. Jang, I. Oh, S. Hwang, *ACS Nano* 2013, **7**(7), 6017.

[70] Y.-X. Huang, X.-W. Liu, X.-F. Sun, *Int. J. Hydr. Energy* 2011, **36**(4), 2773.

[71] E. Chorbadzhiyska, M. Miltov, G. Hristov, N. Dimcheva, L. Nalbandian, A. Evdou, Y. Hubenova, *Int. J. Electrochemistry* 2014, 239270.

[72] P. Xu, T. J. Milstein, T. E. Mallouk, *ACS Appl. Mater. Interf.* 2016, **8**, 11539.

[73] M. D. Symes, L. Cronin, *Nat. Chem.* 2013, **5**, 403-409.

[74] B. Rausch, M. D. Symes, L. A. Cronin, *J. Am. Chem. Soc.* 2013, **135**, 13656-13659.

[75] B. Rausch, M. D. Symes, G. Chisholm, L. Cronin, *Science* 2014, **345**, 1326-1330.

[76] A. A. Tedstone, D. J. Lewis, P. O'Brien, *Chem. Mater.* 2016, **28**, 1965-1974.

[77] D. Voiry, A. Mohite, M. Chhowalla, *Chem. Soc. Rev.* 2015, **44**, 2702-2712.

[78] S. Watanabe, J. Noshiro, S. Miyake, *Surf. Coat. Technol.* 2004, **188-189**, 644-648.

[79] A. A. Voevodin, J. P. O'Neill, J. S. Zabinski, *Surf. Coat. Technol.* 1999, **116-119**, 36-45.

[80] S. Brown, J. L. Musfeldt, I. Mihut, J. B. Betts, A. Migliori, A. Zak, R. Tenne, *Nano Lett.* 2007, **7**(8), 2365-2369.

[81] L. Rapoport, N. Fleischer, R. Tenne, *J. Mater. Chem.* 2005, **15**, 1782-1788.

[82] L. Cizaire, B. Vacher, T. Le Mogne, J. M. Martin, L. Rapoport, A. Margolin, R. Tenne, *Surf. Coat. Technol.* 2002, **160**, 282–287.

[83] O. Tevet, P. Von-Huth, R. Popovitz-Biro, R. Rosentsveig, H. D. Wagner, R. Tenne, *PNAS* 2011, **108**(50), 19901-19906.

[84] I. Lahouij, B. Vacher, F. Dassenoy, *Lubr. Sci.* 2014, **26**, 163-173.

[85] J. Tannous, F. Dassenoy, I. Lahouij, T. Le Mogne, B. Vacher, A. Bruhács, W. Tremel, *Tribol. Lett.* 2011, **41**, 55-64.

3. Experimental Methods

3.1. Solvothermal Reactions

Hydrothermal and solvothermal methods are commonly used for the preparation of versatile materials for a broad range of applications. From a formal point of view, hydrothermal reactions are special cases of solvothermal reactions, whereby the process takes place in an aqueous medium. Within a solvothermal process, precursors (reactants such as solutions, suspensions, gels or solids) are treated in a closed reaction vessel in the presence of a solvent at a temperature higher than the boiling temperature of the used solvent. Besides the reaction temperature, the second thermodynamical variable is the pressure, which can be imposed (by initially compressing the reaction medium at values far exceeding ambient pressure) or autogenous (the pressure depends on the filling volume and gaseous decomposition products, such as CO_2, O_2, etc.).
The most common high-pressure bombs are made of metals or alloys, with an additional Teflon® container (beaker, can) to protect the metal body from corrosive substances (Figure 9).

Figure 9. Photograph of a typical Morey-type autoclave, which was used in this work, with its single components: (a) stainless steel lid with plunger, (b) seal and bursting disc, (c) cylindrical pin, (d) stainless steel case, (e) Teflon®-lid and (f) Teflon®-lined vessel.

More unusual variations, which may be needed for extremely high-pressure or high-temperature purposes, can combine gold or silver beakers inside, or may even be built of diamond anvil cells. An overview of different reactors for solvothermal processes is given in Table 1.

Table 1. Most commonly used autoclaves, their maximum operating temperature and pressure.[1]

Autoclave type	Temperature (°C)	Pressure (bar)
quartz tube	250	6
Morey stainless steel	270	1500
delta ring, unsupported area	400	2300
welded Walker-Buehler closure	480	2000
modified Bridgman	500	3700
continuous flow reactors	600	2000
full Bridgeman	750	3700
Tuttle-Roy type cone closure	750-1150	4000-13000
piston cylinder	1000	40000
Belt apparatus	>1500	100000
opposed anvil	>1500	200000
opposed diamond anvil	>2000	500000

As the term already indicates, one of the main factors of solvothermal processes is the solvent, i.e. its physico-chemical properties. The solubility of the precursor affects the concentration of the relevant species and the reactivity of the compounds under high temperature and high pressure conditions. Thus, the solvent has a direct effect on the reaction kinetics. Furthermore, the choice of the solvent can dictate the preference for specific structures and morphologies due to the modification of the solvated species through its coordination. Many studies have already been published, where the effect of the solvent's properties such as polarity,[2] viscosity,[3] or its ability to form coordinative bonds[4] were described. The characteristics of the products are also affected by the interactions of reactants and solvents where, for example, the formation of intermediate species or metastable structures can be induced.[5-7] Table 2 summarizes the properties of common solvents used in autoclave syntheses.

One of the main advantages of organic solvents in comparison to water is the possibility to use precursors, which are sensitive to water. Furthermore, most of the solvothermal reactions can be conducted at lower temperatures and pressures in non-aqueous organics.

Table 2. Physico-chemical properties of solvents used in solvothermal reactions. All values were taken from [8].

Solvent (Formula)	Critical Temperature (°C)	Critical Pressure (MPa)
Water (H_2O)	374	22.1
Methanol (CH_3OH)	240	7.9
Ethanol (CH_3CH_2OH)	243	6.4
1-Propanol ($CH_3CH_2CH_2OH$)	264	5.2
2-Propanol (C_3H_7OH)	235	4.8
Benzyl alcohol (C_7H_7OH)	403	4.6
Cyclohexanol ($C_6H_{11}OH$)	352	3.8
Ethylendiamine ($H_2NCH_2CH_2NH_2$)	320	6.5
Ethanolamine ($HOCH_2CH_2NH_2$)	341	4.5
Toluene (C_7H_8)	319	4.1

During solvothermal processes, crystallisation occurs directly from the solution via consecutive crystal nucleation and crystal growth (resulting from supersaturation). Irreversible precipitation into clusters is followed by continuous growth up to microscopic sized crystals (Figure 10). The mechanism of crystal growth under solvothermal conditions can be described by four intersecting stages:

i) transport of solute molecules through bulk solution,
ii) attachment of nuclei to the surface,
iii) migration of growth units on the surface and
iv) incorporation of growth units into crystal entities.

Although this mechanism may be widely recognized, it is inadequate concerning the arrangement of growth units on the crystal's surface or other relevant steps of crystallization.

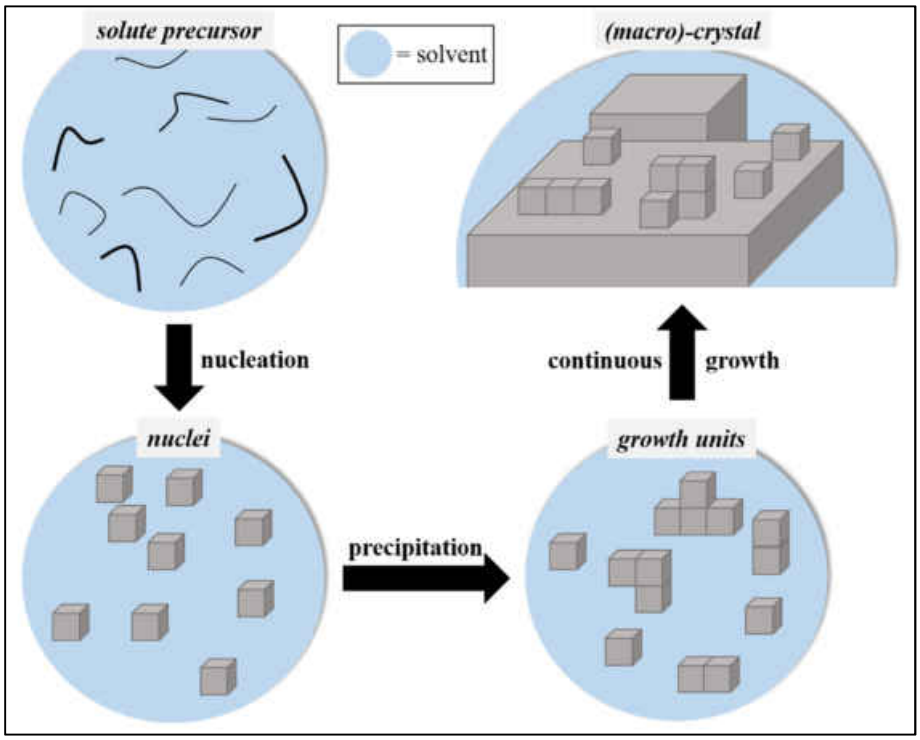

Figure 10. Schematic representation of the proposed crystallization process taking place under solvothermal conditions.

Several thermodynamic models have been proposed to describe the reaction equilibria in solution, whereby the Helgeson-Kirkham-Flowers (HKF) model provides the basis for more or less precise calculations of the solubility of different species in solvothermal systems.[9-12]

There are also many other factors, which can play a key role in solvothermal processes. Pressure and temperature are the two most easily adjustable and thus many screening experiments begin with varying these two parameters. An example of pressure-controlled particles formation is described by Yang et al.[13] Hence, the chemical reactivity and the kinetics of the reactions involved can significantly be enhanced by pressure changes. An enlargement of the thermal stability domain of the reactants can also take place, possibly concomitant with a stabilization of denser product structures.

Solvothermal processes can easily be combined with other techniques, both to enhance the chemical reactivity of the reactants and the reaction kinetic. These technologies can be electrochemistry,[14] mechanical mixing,[15] high-temperature mixing,[16] sonochemistry[17] or microwaves assistance.[18] For example, microwave assisted heating not only can provide for a better crystalline quality compared to conventional heating, but also for a faster reaction and a better yield of product.[19] Naturally, different methods can be combined to achieve unique preparation of nanocrystalline products[20] or metal organic frameworks.[21] The combination of solvothermal processes with different assistant techniques offers manifold opportunities for production of particles with controllable size, shape and chemical composition. A short overview of associated methods for the preparation of reaction media is enlisted in Table 3.

Table 3. Methods associated with solvothermal techniques.

Method	Product	Reference No.
hydrothermal process (assisted by microemulsion technique)	spherical ZnS nanoparticles (5-10 nm)	[22]
solvothermal pressure-relief (gas produced in high-pressure vessel is controlled)	La_2O_2S	[23]
solvothermal scission-template-transportation (intermediate compounds acts as template)	$CdIn_2S_4$ nanorods (25-700 nm)	[24]
sol-solvothermal process (sol as precursor mixture)	nanostructured TiO_2 (various morphologies)	[25]
extraction solvothermal method	CdS nanowires (70-200 nm) Bi_2S_3 nanorods	[26]
phase-transfer catalysis	monodispersed FePt nanoparticles (14-20 nm)	[27]

3.2. Chemicals

The following chemicals were used as received without further purification: molybdenum pentachloride ($MoCl_5$, anhydrous, 99.6%; ABCR), tungsten hexachloride (WCl_6, 99.9%; ABCR), ethanol (≥ 99.8%; Honeywell), benzyl alcohol (99% pure; Acros Organics), acetone (≥ 99.5%; Sigma-Aldrich), 2-propanol (≥ 99.8%; Sigma-Aldrich), methanol (99.8%; Sigma-Aldrich), cyclohexanol (99%; ABCR), *tert*-butanol (99%; ABCR), hexane (≥ 95%; Fischer Chemical), carbon disulphide (CS_2, 99%, Sigma-Aldrich), ammonium hydroxide solution (NH_4OH; 33%; Sigma-Aldrich), dimethyl formamide (analytical grade; Fischer Chemical), toluene (puriss; Sigma-Aldrich), diethyl ether (99.8%; Sigma-Aldrich), hydrochloric acid (HCl, ≥ 37%; Fluka), nitric acid (HNO_3, ≥ 65%; Sigma-Aldrich), ammonium polysulfide solution (NH_4S_x; Fischer Chemical), Rhodamine B (analytical standard; Sigma-Aldrich), Pluronic F127 (BASF), cetyl trimethylammonium bromide (CTAB, ≥ 99%; Sigma-Aldrich), oleylamine (≥ 50%; TCI), iron nitrate ($Fe(NO_3)_3$; Fischer Chemical), iron chloride hexahydrate ($FeCl_3 \cdot 6\ H_2O$, ACS grade; ABCR), tungstic acid (H_2WO_4, 98%; Alfa Aesar), sodium fluoride (NaF, ≥ 99%; Sigma-Aldrich), hydrogen peroxide (H_2O_2, 30%; Honeywell), ammonium heptamolybdate ($(NH_4)_6Mo_7O_{24} \cdot 4\ H_2O$; Sigma-Aldrich), vanadium oxide sulfate hydrate ($VOSO_4 \cdot x\ H_2O$, 97%; Sigma-Aldrich), ammonium metatungstate ($(NH_4)_6H_2W_{12}O_{40}$, 99.99%; Sigma-Aldrich), oxalic acid dihydrate ($HO_2CCO_2H \cdot 2\ H_2O$, ≥ 99%; Sigma-Aldrich), hydrogen sulphide (H_2S, 99.7%; Westfalen), hydrogen 4.6 (H_2, Westfalen), argon 3.0 (Ar, Westfalen).

3.3. Materials Characterization

Transmission Electron Microscopy (TEM), nanoparticle solution was diluted with ethanol, then 3-5 drops of the solution (depending on the concentration) were placed onto a carbon coated copper grid. The sample grid was left drying overnight. The images were captured with a Tecnai G2 Spirit transmission electron microscope with an acceleration voltage of 120 kV. **High resolution TEM (HR-TEM)** measurements were conducted on a FEI Tecnai F20 with an acceleration voltage of 200 kV. The size and diameter of the particles was measured using the software *Image J*.

Scanning Electron Microscopy (SEM) images were taken using a FEI Nova NanoSEM 600, equipped with an Everhart-Thornley detector (ETD) and a low-voltage high-contrast detector (vCD), operated under the high vacuum mode with an acceleration voltage of 5-10 kV. The powdered samples were drop casted on an aluminium stub using an adhesive conductive carbon tape. A built-in EDAX-Genesis detector was used to confirm the chemical composition on the non-sputtered samples with **Energy-Dispersive X-ray Spectroscopy (EDS/EDX).**

Powder X-ray diffraction (**PXRD**) patterns of the oxidic products were recorded with a Bruker AXS D8 discover diffractometer equipped with a HiStar detector using graphite monochromated Cu Kα radiation. The samples were attached to a glass substrate without using an adhesive. Individual frames were typically recorded at 2θ = 24, 34, 44, 54, 64, 74, and 84 (detector distance 150 mm, detector range D(2q) = 358) in 0.028 steps covering a 2θ range from 5 to 85 °. XRD analysis of the sulfidic products were conducted on a Siemens D5000 powder diffractometer in transmission geometry, equipped with a Braun M50 position-sensitive detector, Cu Kα radiation with a Ge (111) monochromator (Huber 615 002) and a step size of 0.0078 ° in 2θ. All X-ray diffraction patterns were integrated from individual frames by using the Bruker AXS GADDS software package and merged using Bruker AXS EVA. Crystalline phases were identified using the PDF-2 database and the Bruker AXS EVA program suite.[28]

X-ray Photoelectron Spectroscopy (XPS) samples were prepared by drop-casting a suspension of the particles on a gold-sputtered surface multiple times, until a homogeneous thin film was obtained. The XPS measurements were then conducted on a Kratos Axis Ultra^{DLD} spectrometer (Kratos, Manchester, England) using an Al Kα excitation source with a photon energy of 1487 eV. The data was acquired in the hybrid mode using a 0 ° take-off angle, defined as the angle between the surface normal and the axis of the analyser lens. The spectra were collected with setting the pass energy of the analyser at 20 eV. A neutralizer was always used during spectra collection to compensate charge build-up on the samples. The binding energy (BE) scale was calibrated according to Au $4f_{7/2}$ emission peak at 84 eV.[29]

Raman spectra were recorded with a Horiba Yvon Lab RAM HR 800 spectrometer equipped with a microscope (Olympus BX41) and a CCD detector. The entrance slit was set to 100 µm, the laser focal spot was 2·2 µm. A Nd:YAG laser (532.12 nm) with a laser power 2 mW was used

for excitation. The laser light was focused onto the fine powder sample using a 50x long working distance objective. All Raman spectra were recorded in backscattering geometry at a resolution of 0.5 cm^{-1} in the range between 150 and 1200 cm^{-1}, wherein at least 5 spectra for each sample where measured to improve the statistics.

Attenuated total reflection infrared (ATR-IR) spectroscopy was performed at a Nicolet iS10 spectrometer manufactured by Thermo Scientific. The spectra were recorded in a frequency range of 500 and 3500 cm^{-1} with a resolution of 1.4 cm^{-1} per data point.

The **optical absorption (UV-VIS)** spectra were recorded with a Cary Varian 5G UV-Vis-NIR spectrometer using a 1 mL micro-cuvette with a size of 12.5·12.5·45 mm from Brand, filled with a 1 mg/mL solution of the appropriate product.

Surface areas (Brunauer–Emmett–Teller, **BET**), pore volumes, and pore sizes (Barrett–Joyner–Halenda, BJH) of DMSN were determined by N_2-sorption measurements.

All **nuclear magnetic resonance (NMR)** experiments in solution were performed on a Bruker ARX 400 spectrometer with a ^1H frequency of 399.83 MHz. Samples were dissolved in D_2O or $CDCl_3$ and the spectra were analyzed with Mnova NMR software.[30]

X-ray total scattering measurements were conducted on beamline I15 at the Diamond Light Source Inc. using a wavelength of 0.1707 Å (72.7 keV) and a 2D MAR 345 detector. CeO_2 was used to calibrate the experimental setup. Data were processed using DAWN,[31] the PDF calculations were performed GUDRUN4.[32]

3.4. References of Chapter 3

[1] A. Rabenau, *Angew. Chem. Int. Ed.* 1985, **24**, 1026-1040.

[2] J. Mu, Z. Gu, L. Wang, Z. Zhang, H. Sun, S. Z. Kang, *J. Nanopart. Res.* 2008, **10**, 197-201.

[3] J. S. Lee, S. C. Choi, *J. Europ. Ceram. Soc.* 2005, **25**, 3307-3314.

[4] Z. X. Deng, L. Li, Y. Li, *Inorg. Chem.* 2003, **42**, 2331-2341.

[5] F. Li, W. Bi, T. Kong, C. Wang, Z. Li, X. Huang, *J. Alloys Compd.* 2009, **479**, 707-710.

[6] K. Eda, Y. Uno, N. Nagai, N. Sotani, C. Chen, S. Whittingham, *J. Solid State Chem.* 2006, **179**, 1453-1458.

[7] Y. Liu, J. Cao, C. Li, J. Zeng, K. Tang, Y. Qian, W. Zhang, *J. Am. Ceram. Soc.* 2006, **89**, 2926-2928.

[8] www.camechemicals.noaa.gov, retrieved on 23.08.2017

[9] E. L. Shock, E. H. Oelkers, J. W. Johnson, D. A. Sverjensky, H. C. Helgeson, *J. Chem. Soc. Faraday Trans.* 1992, **88**, 803.

[10] H. C. Helgeson, D. H. Kirkham, *Am. J. Sci.* 1974, **274**, 1089.

[11] H. C. Helgeson, D. H. Kirkham, *Am. J. Sci.* 1976, **276**, 97.

[12] H. C. Helgeson, D. H. Kirkham, G. C. Flowers, *Am. J. Sci.* 1981, **281**, 1249.

[13] J. Yang, J. H. Zeng, S. H. Yu, L. Wang, Y. H. Zhang, Q. T. Qian, *Chem. Mater.* 2000, **12**, 2924-2929.

[14] R. Roy, *J. Solid State Chem.* 1994, **111**, 11-17.

[15] R. M. Piticescu, P. Vilarnho, L. M. Popescu, R. Piticescu, *J. Europ. Ceram. Soc.* 2006, **26**, 2945-2949.

[16] J. Wang, Q. W. Chen, C. Zeng, B. Y. Hou, *Adv. Mater.* 2004, **16**, 137-140.

[17] S. Kormarneni, R. Roy, Q. H. Li, *Mater. Res. Bull.* 1992, **27**, 1393-1405.

[18] S. K. Park, J. H. Park, K. Y. Ko, S. Yoon, K. S. Chu, W. Kim, Y. R. Do, *Crystal Growth & Design* 2009, **9**, 3615-3620.

[19] T. C. Stamatatos, D. Foguet-Albiol, S. C. Lee, C. C. Stoumpos, C. P. Raptopoulou, A. Terzis, W. Wernsdorfer, S. O. Hill, S. P. Perlepes, G. Christou, *J. Am. Chem. Soc.* 2007, **129**, 9484-9499.

[20] W. J. Son, J. Kim, W.-S. Ahn, *Chem. Commun.* 2008, **47**, 6336-6338.

[21] T. Nathan, M. Cloke, S. R. S. Prabaharan, *J. Nanomater.* 2008, ArticleID 94813.

[22] J. Liu, J. Ma, Y. Liu, Z. Song, Y. Sung, J. Fang, Z. Liu, *J. Alloys & Compd.* 2009, **486**, L40-L43.

[23] C. H. Yu, Z. H. Han, J. Yang, H. Q. Zhao, R. Y. Yang, Y. Xie, Y. T. Qian, Y. H. Zhang, *Chem. Mater.* 1999, **11**, 192-194.

[24] J. Lu, Y. Xie, G. Du, X. Jiang, L. Zhu, X. Wang, Y. Qian, *J. Mater. Chem.* 2002, **12**, 103-106.

[25] S. Yang, L. Gao, *Mater. Chem. Phys.* 2006, **99**, 437-440.

[26] S. Huaquiang, Z. Xiaodong, X. Fu, W. Deabo, H. Zhengsdui, *Mater. Lett.* 2006, **60**, 1793-1795.

[27] M. Wen, H. Qi, W. Zhao, J. Chen, L. Li, Q. Wu, *Colloids Surf. A: Physicochem. Eng. Asp.* 2008, **312**, 73-78.

[28] PDF-2, Release2004, *JCPDS -International Center for Diffraction Data*, Newton Square (PA) USA, 2004.

[29] J. F. Moulder, J. Chastain, P. E. Sobol, K. D. Bomben, *Handbook of X-ray Photoelectron Spectroscopy*; Perkin-Elmer: Eden Prairie, MN, USA, 1992.

[30] Mestrenova Version 11.0.4-18998, Mestrelab Research S. L., 2017.

[31] M. Basham, J. Filik, M.T. Wharmby, P. C. Y. Chang, B. El Kassaby, M. Gerring, J. Aishima, K. Levik, B. C. A. Pulford, I. Sikharulidze, D. Sneddon, M. Webber, S. S. Dhesi, F. Maccherozzi, O. Svensson, S. Brockhauser, G. Naray, A. W. Ashton, *J. Synchrotron Rad.* 2015, **22**, 853-858.

[32] S. E. McLain, D. T. Bowron, A. C. Hannon, A. K. Soper, *Gudrun-A computer program developed for analysis of neutron diffraction data*, ISIS Facility, Rutherford Appleton Laboratory, UK.

4. Pure and Mixed Transition Metal Oxides (TMOs)

4.1. Introduction to TMOs

4.1.1. Magnéli Phases and Mixed Oxides of Molybdenum and Tungsten

Compounds of tungsten and molybdenum within the range of stoichiometric and non-stoichiometric composition were described more than 60 years ago.[1, 2] These reduced W/Mo oxides exhibit recurrent dislocations of atoms, with M^{6+} ions partly being reduced to M^{5+} ions (M = W, Mo). Nowadays, many non-stoichiometric compounds such as vanadium or titanium oxides are summarized under the superordinate term of Magnéli phases.[3, 4] All compositions and structures can be described as shear structures of ReO_3, where M is always located in octahedral coordination. ReO_3 can be extended by introducing crystallographic shear along certain directions and at certain distances. The number of common edges between the MO_6 octahedrons can explain a great variety for this type of composition, ranging from TiO (NaCl type, with eight common edges) to anatase (TiO_2, four common edges), V_2O_5 (two common edges) and ReO_3 (no common edges). The oxides of W, Mo and Nb are situated halfway between the two latter compositions M_2O_5 and MO_3. In general, the more edges are linked, the lower the oxygen content of the composition gets and the more M^{5+} species can be found.

The pure phases of WO_3 and MoO_3 have been widely studied for a long time because of their interesting dielectric, electrochromic and structural properties. Some of these properties strongly depend on the impurities and thus can be manipulated by doping the pristine oxides with other elements. The bonds in the stoichiometric compounds have mainly ionic character with a significant covalent part.[5, 6] In the case of sub-stoichiometric tungsten oxide the most common defect is the oxygen vacancy. Further distinction is made by the charge of the vacancy, which can be neutral (± 0), singly charged (+1) or doubly charged (+2). A neutral vacancy exhibits an electron configuration similar to the stoichiometric compound. Singly charged vacancies can be schematically depicted as occupied with one electron that forms a bond with one of the W^{6+} ions, resulting in an oxidation state change of the neighbouring tungsten ion to W^{5+}. In the latter case, the electron transfer into the conduction band gives rise to optical absorption. If electron transfer proceeds to one or two of the neighbouring W ions, the vacancy then becomes doubly charged. Since the occurrence of a W^{4+} species is energetically unfavourable, it would be more advantageous to form a doubly charged vacancy between two W^{5+} ions.[7] Charge insertion or separation is the basic physicochemical process from which the properties of so-called chromogenic (such as photochromic, electrochromic or thermochromic) materials originate.[8]

Electrochromic materials, which are able to change their optical properties reversibly by applying electrical voltage, are used in smart windows.[9] The same colour-changing effect can be induced upon bandgap photoexcitation (photochromism) or changes in temperature

(thermochromism).[10, 11] In general, electrochromic device applications require low conducting specimens. Creating additional electron traps (e.g. holes or defects) by replacing tungsten by molybdenum (or vice versa) is the most straightforward approach.

Within tungsten bronzes both the heavy metal atoms reveal octahedral environments but different octahedral networks. Salje et al. examined the phase transition in mixed crystals of $W_xMo_{1-x}O_3$ already in 1978.[12] They proposed a phase diagram for the mixed oxides, in which 12 distinct phases can be found. According to that, all structures of the WO_3–MoO_3 system (except nearly pure MoO_3) reveal perovskite-like arrangements of corner-sharing octahedral networks. The differences observed stem from characteristic deformations (tilts of octahedra or off-centering of the heavy metal atom) of these networks. Additional symmetry reduction can also be caused by partial ordering of W-Mo atoms. Figure 11 illustrates the crystal structures of WO_3 and MoO_3, accompanied by the structures of their thermodynamically most stable sub-stoichiometric representatives $W_{18}O_{49}$ and Mo_4O_{11}.

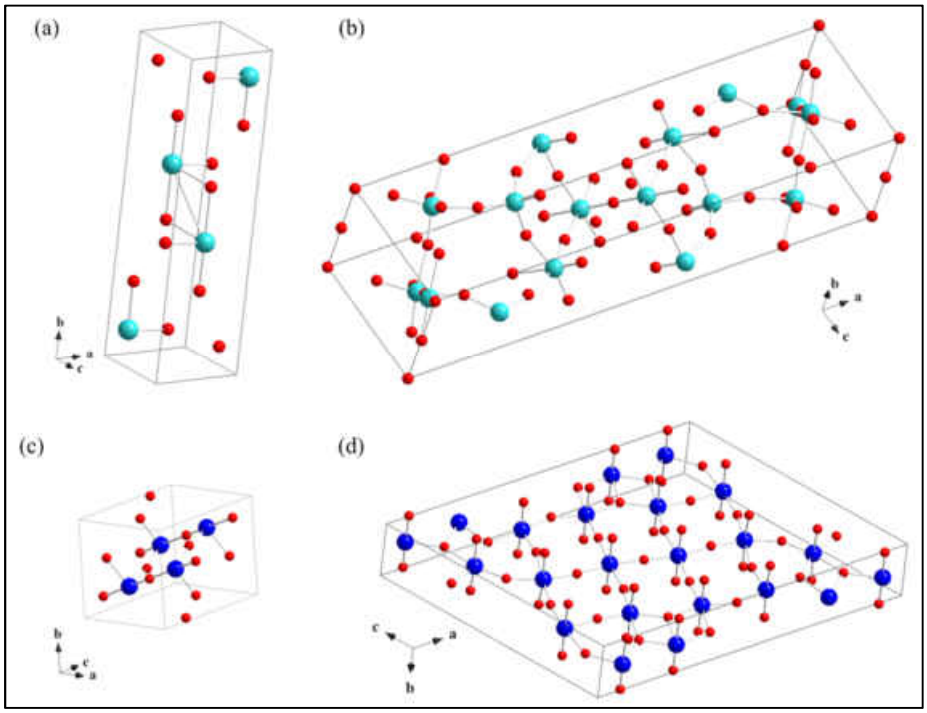

Figure 11. Ball-and-stick model of the crystal structures of (a) MoO_3, (b) Mo_4O_{11}, (c) WO_3 and (d) $W_{18}O_{49}$. Red balls represent oxygen, turquoise balls molybdenum and blue balls tungsten.

The easiest way to prepare sub-stoichiometric compounds is reduction of the appropriate trioxide (MO_3) either by the reaction with the pure metal or by annealing of MO_3 in hydrogen atmosphere. Herein, the composition of the reaction product can simply be controlled by oxygen pressure and temperature. Pure phase single crystals can be prepared by transport reactions[13] or by crystallization from molten material,[14] while thin films are obtained via CVD processes.[15]

The semiconducting transition metal oxides such as WO_3 or MoO_3, or WO_3/MoO_3 and their respective sub-oxides (WO_{3-x} or MoO_{3-x} or WO_{3-x}/MoO_{3-x}) are n-type/p-type semiconductors,

abundant in earth crust, low cost, with relatively large band gaps of 2.6–2.8 eV, concomitant good Hall mobility and long diffusion length, thus, fulfil all necessary conditions as potential candidates for photoelectrocatalysis.[16, 17] However, one of the main drawbacks of MoO_3 or WO_3 is their low conduction band levels (Figure 12), which significantly impede sufficient absorption of the solar spectrum and result in low photo-conversion efficiencies.[18]

Multifuncional approaches have been pursued to achieve maximum efficiency. This includes tuning the band gap via doping, the integration of different semiconductors in a single particle as well as the integration of electrocatalysts with semiconductor surfaces.[19, 20] Synthesizing binary oxides of molybdenum/tungsten ($Mo_xW_{1-x}O_y$) provides an appropriate opportunity to benefit from synergistic effects. Many approaches to prepare Mo/W-oxides have already been reported,[21-27] as well as studies of the formation mechanism[28, 29] and the investigation of characteristics of these composites.[30-37]

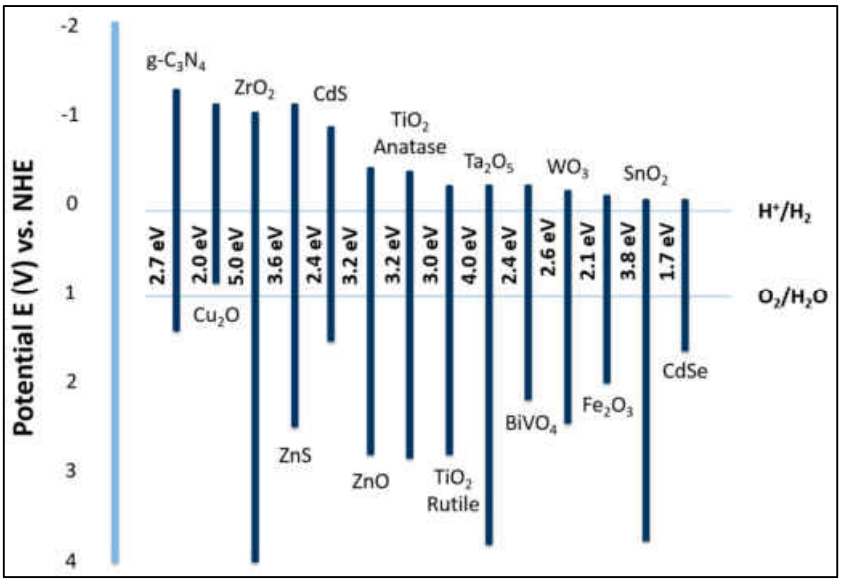

Figure 12. Schematic band structure illustration for various semiconductors with respect to the redox potentials of water splitting.[38]

In general, atomic doping is an effective way to modify the electronic structure of TMOs. [39-41] Since the radii of tungsten- and molybdenum-ions are nearly the same,[42] the incorporation of W into the Mo-lattice (and vice versa) is taking place without affecting the crystal structure. As Zhou et al. reported, the band-gaps in the mixed oxides of $Mo_xW_{1-x}O_3 \cdot 0.33\ H_2O$ can therefore easily be tuned, e.g. by using a hydrothermal approach.[43] Moreover, Li et al. highlighted the enhanced properties of Mo-doped tungsten oxides, in particular regarding the performance in photocatalysis and HERs.[44] Most recently, Jin et al. presented amorphous oxygen-deficient MoO_{3-x} spheres as highly active photoanodes in water oxidation.[45]

4.1.2. Synthesis Methods of TMOs

Nanoscaled TMOs of tungsten and molybdenum have already been prepared by different methods as well as they were examined for various applications. Given the multitude of publications, it is impossible for this work to render an exhaustive account. Therefore, Table 4 shall provide only a short overview of some outstanding results of molybdenum/tungsten oxides materials for photocatalytic and photoelectrocatalytic applications.

*Table 4. Photoelectrodes based on W/Mo oxides, their preparation methods and photocurrents (with *reference hydrogen electrode; #standard calomel electrode).*

Compound	Preparation Method	Current Density ($mA \cdot cm^{-2}$)	Reference
Mo-doped $W_{18}O_{49}$ (urchins)	hydrothermal	4.5 (0.3 V vs. RHE)*	[46]
MoO_{3-x} (microspheres)	solvothermal, CTAB-assisted	3.8 (1.23 V vs. RHE)	[45]
MoO_2@reduced graphene oxide	precipitation, polymer decomposition	4.8 (0.3 V vs. RHE)	[50]
WO_3/Mo (thin film)	co-sputtering	1.91 (1.6 V *vs.* SCE)#	[51]
WO_3 (nanoporous films)	anodization	3.45 (1.6 V *vs.* Ag/AgCl)	[52]
WO_3 (platelets)	sol-gel route, microwave-assisted	2.7 (1 V *vs.* RHE)	[53]
WO_3 (columns)	sputtering	2.7 (1.6 V *vs.* SCE)	[54]
WO_3 (nanostructured platelets)	sol-gel	3.7 (1.2 V *vs.* SCE)	[55]
WO_3 (sphere-like nanoparticles)	sol-gel	3.7 (1.3 V *vs.* Ag/AgCl)	[56]
WO_3 (plate-like films)	hydrothermal	4.0 (1.2 V *vs.* Ag/AgCl)	[57]
WO_3/Ag (porous films)	screen-printing	2.63 (1.23 V *vs.* SCE)	[58]

The content oft he following chapter is partially taken and adapted from D. Spetter, W. Tremel, “Process and Device for the Production of Nanoscale Metal Sulfides and after the Process Produced Metal Sulfides”, *Ger. Offen.* DE 102015016878.9 (December 31, 2015). Taken parts are delimited by single quotation marks (“”).

Authorship contributions

Category 1

Conception and design of study:

D. Spetter

Acquisition of data:

D. Spetter

Analysis and/or interpretation of data:

D. Spetter

Category 2

Drafting the manuscript:

D. Spetter

Revising the manuscript critically for important intellectual content:

W. Tremel

Category 3

Approval of the version of the manuscript to be published:

D. Spetter, W. Tremel

Figure 33-36: Prepared by D. Spetter

4.2. WO_{3-x} and $W_xMo_{1-x}O_{3-y}$ Nanoflakes

4.2.1. Synthesis and Characterization

The nanoflakes of tungsten and molybdenum oxide were synthesized using a simple precipitation technique. Briefly, 0.25 mmol of tungsten hexachloride (WCl_6) or molybdenum pentachloride ($MoCl_5$) were directly weighted in a centrifuge vial (100 mg or 63 mg). After adding 20 mL of alcohol or water, the as-prepared solutions were allowed to stand over night with the vial lid open. The products slowly precipitated and a dark-blue solid (in the case of tungsten as precursor) or a blue-greyish solid (molybdenum as precursor) was separated by centrifugation.

To significantly accelerate the process, a slight variation was utilized. After dissolving the precursors in the appropriate amount of alcoholic solvent, 25*vol*% of water was added to the solution. This caused a precipitation of the solids within 5 min after addition. Regardless of the approach for preparation (slow or fast precipitation), the yield of the products was practically quantitative. A scheme of the different routes for preparation of WO_{3-x} nanoflakes is shown in Figure 13.

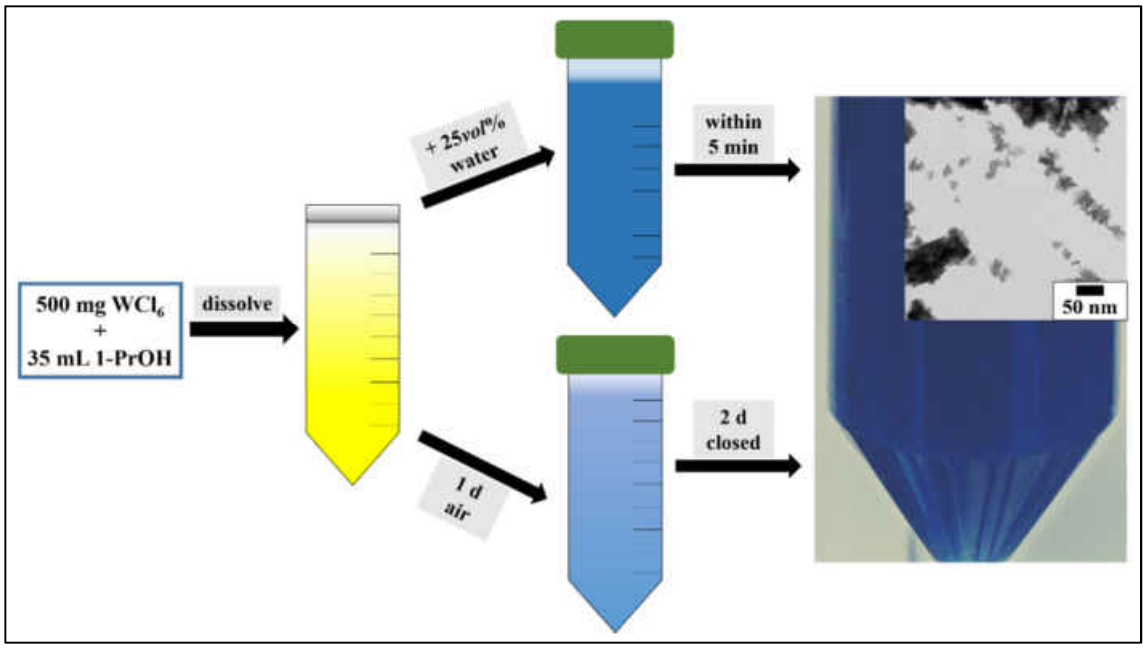

Figure 13. Scheme of the two different pathways to produce tungsten oxide nanoflakes, using tungsten hexachloride as precursor and 1-propanol as solvent. The inset shows a TEM image of the obtained WO_{3-x} nanoflakes.

The same procedure was used to obtain mixed tungsten-molybdenum oxide nanoflakes. For that, 100 mg (0.252 mmol) WCl_6 was mixed with the appropriate amount of $MoCl_5$ to achieve the desired composition. In the following, the samples are referred to as NF1 (pure WO_{3-x}), NF2 (5.7 mg; 0.021 mmol $MoCl_5$), NF3 (11.5 mg; 0.042 mmol $MoCl_5$), NF4 (22.9 mg; 0.084 mmol $MoCl_5$), NF5 (45.9 mg; 0.168 mmol $MoCl_5$), NF6 (68.8 mg; 0.252 mmol $MoCl_5$) and

NF7 (pure MoO_{3-x}). For the doping series 1-propanol was chosen as solvent due to the morphology obtained in the previous experiments.

Tungsten oxides from different solvents. The morphology of as-obtained products from different solvents was examined with TEM and SEM. As it can be seen from Figure 14 (a, b), the flake-like nanoparticles prepared in methanol are strongly agglomerated and show a defect-rich structure. The smallest flakes observed are ~7 nm in diameter, whereas the majority exhibits lateral sizes of ~11 nm. The SEM images in Figure 14 (c, d) reveal that besides the nanoflakes a large amount of bulk is obtained as by-product from the simple precipitation method.

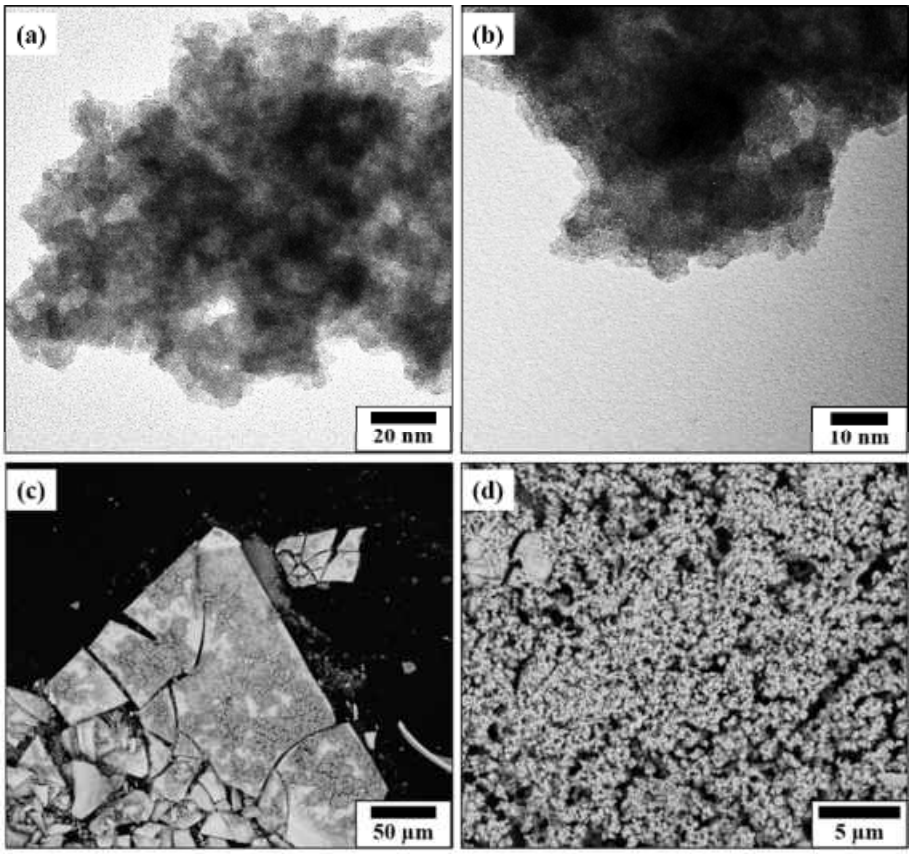

Figure 14. (a, b) High-magnification TEM images and (c, d) SEM images of WO_{3-x} nanoflakes obtained from the simple syntheses in methanol.

Conducting the same experiment with ethanol as a solvent also yields strongly agglomerated nanoflakes, but rather round shaped (Figure 15). The mean diameter of the flakes is ~10 nm, whereby no well-separated, single nanoflakes could be observed. The HR-TEM image in Figure 15 (d) shows lattice fringes of single crystals of the tungsten oxide product, with spacing of 0.3778 nm. This lattice spacing corresponds to the (001) crystalline plane of the non-stoichiometric hexagonal $WO_{2.8}$ phase.[59]

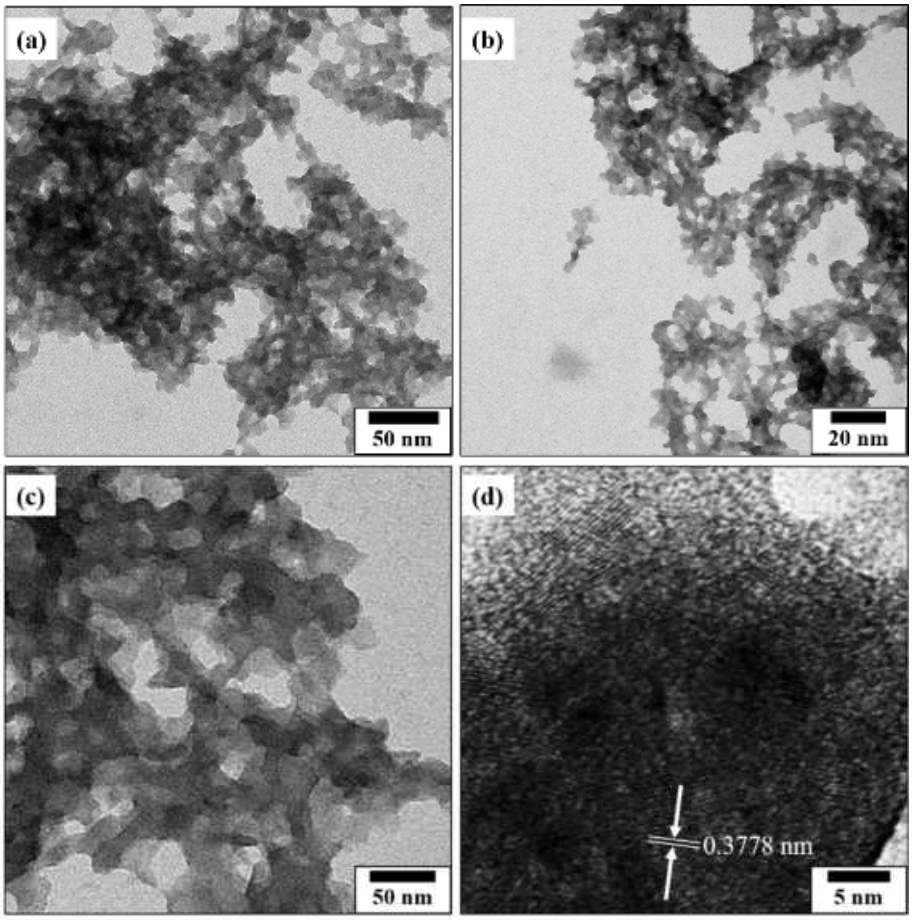

Figure 15. (a, b) Low- and (c, d) high-magnification TEM images of WO_{3-x} nanoflakes obtained from the simple syntheses in ethanol.

The nanoflakes obtained from the precipitation in 1-propanol are not round-shaped and of bigger lateral size (~16–18 nm), as presented in Figure 16. Furthermore, many distinct single nanoflakes and nanosheets can be observed besides bigger agglomerates already known from the other solvents. The SEM images in Figure 16 (c, d) clearly indicate that bulk material, decorated with nanoflakes of WO_{3-x}, was formed during the reaction.

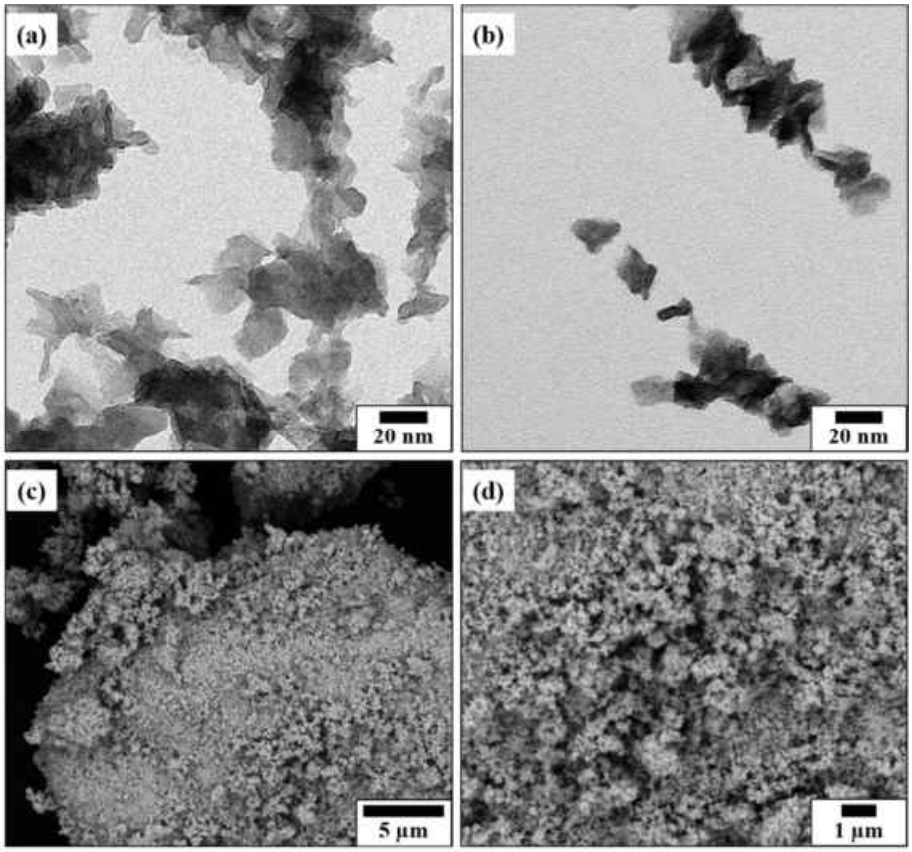

Figure 16. (a, b) Low-magnification TEM images and (c, d) SEM images of WO_{3-x} nanoflakes obtained from the simple syntheses in 1-propanol.

Cyclohexanol was expected to be an inappropriate solvent for the precipitation, because the WCl_6 did not completely dissolve. Figure 17 shows TEM images of the product. Hence, no nanoflakes can be observed and the bulky material consists of non-uniform nanoparticles such as elongated, round or single sheets.

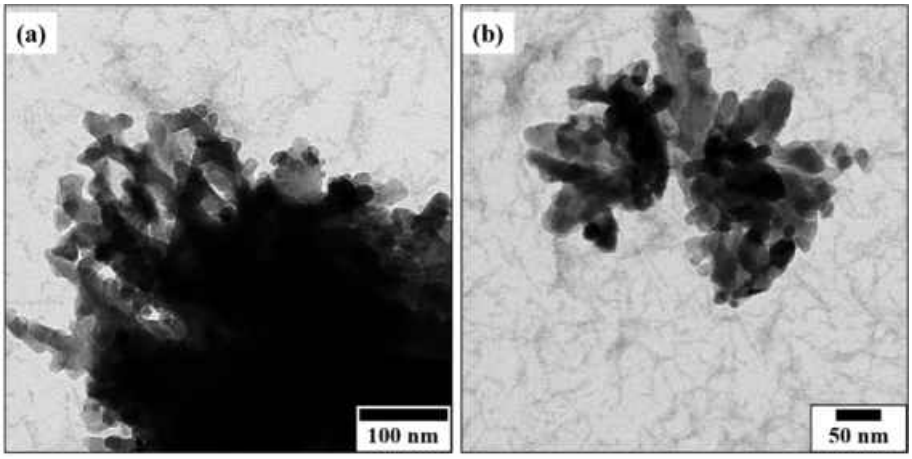

Figure 17. (a, b) Low-magnification TEM images of WO_{3-x} nanoflakes obtained from the simple syntheses in cyclohexanol.

The product prepared in water was the only one to yield a bright yellow colour. As it is well-known, nanoparticles of pure WO_3 phase and sub-stoichiometric species of WO_{3-x}, which are

treated with oxidizing agents, usually feature pronounced yellow colours. In general, the colour change in tungsten oxides is a result of a slight loss of oxygen with concomitant generation of an additional valence state in the WO_3 host structure either being W^{5+} or W^{4+}. The reduction of the W^{6+} species can further affect changes of the ideal cubic ReO_3 structure by distortions or tilting, giving rise to a series of lower symmetry structures. Such predominant distortion mechanisms are responsible for phase transformation and include tilting of the WO_6 octahedra, W atom displacements from the octahedral center or distortions of the octahedra. The cation-to-cation charge transfer between the parent W^{6+} and a reduced ion provides the colour change from dark-blue (substoichiometric) to yellow (stoichiometric). An increased amount of oxygen vacancies is believed to serve as shallow electron donor for WO_3, which e.g. can enhance its photoactivity.[60 61]

The nanoflakes produced in water show the biggest variety of dimension, ranging from 20 nm to few hundred nanometers of lateral size (Figure 18). Besides roughly quadrangular particles, also quasi-spherical particulates can be observed. Using the HR-TEM image in Figure 18 (b) it is possible to determine the d-spacing due to the lattice fringes observed. The measured distances of 0.3628 nm and 0.3153 nm can be attributed to (110) and (200) crystallographic planes of WO_3.[62] The SEM images are equally conclusive as for the other products, namely formation of large bulky material.

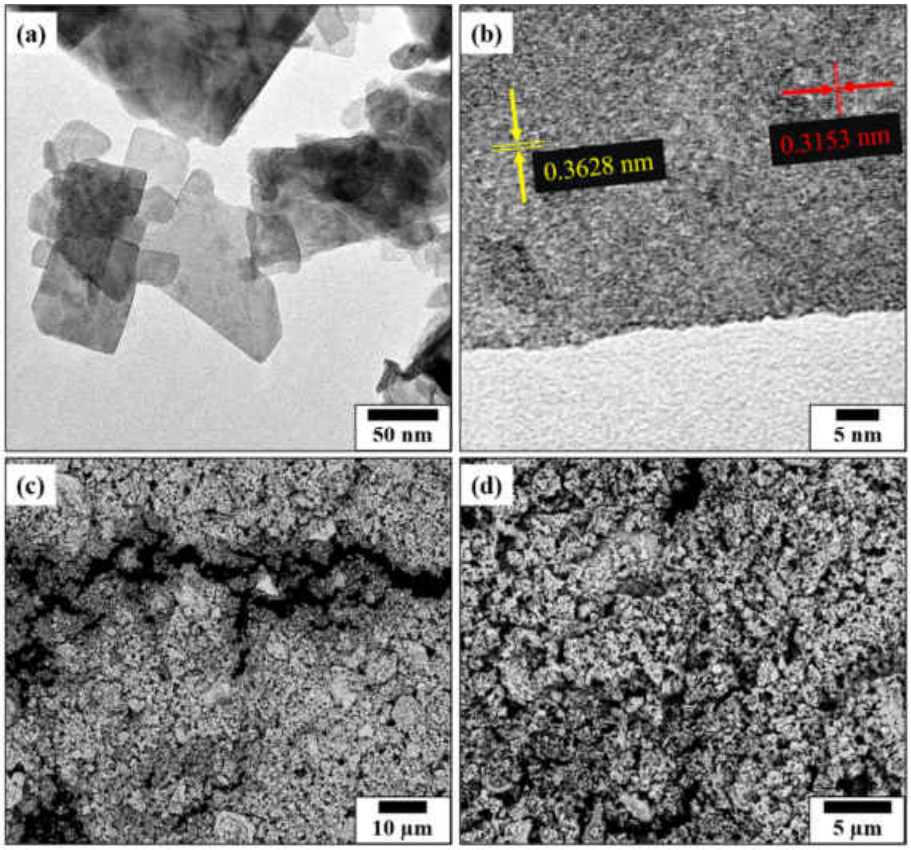

Figure 18. (a) Low-magnification TEM image, (b) HR-TEM image and (c, d) SEM images of WO_3 nanoflakes obtained from the simple syntheses in water.

Using $MoCl_5$ as a precursor for the reaction yields less precipitated product and more blue supernatant. Therefore, 20*wt*% more water had to be added to the supernatant to complete precipitation. The as-prepared product hardly reveals any morphological similarity with its tungsten counterpart. The formation of flake-like particles can only be seen in the approach. The majority is a non-distinctive amorphous substance without any definite morphology.

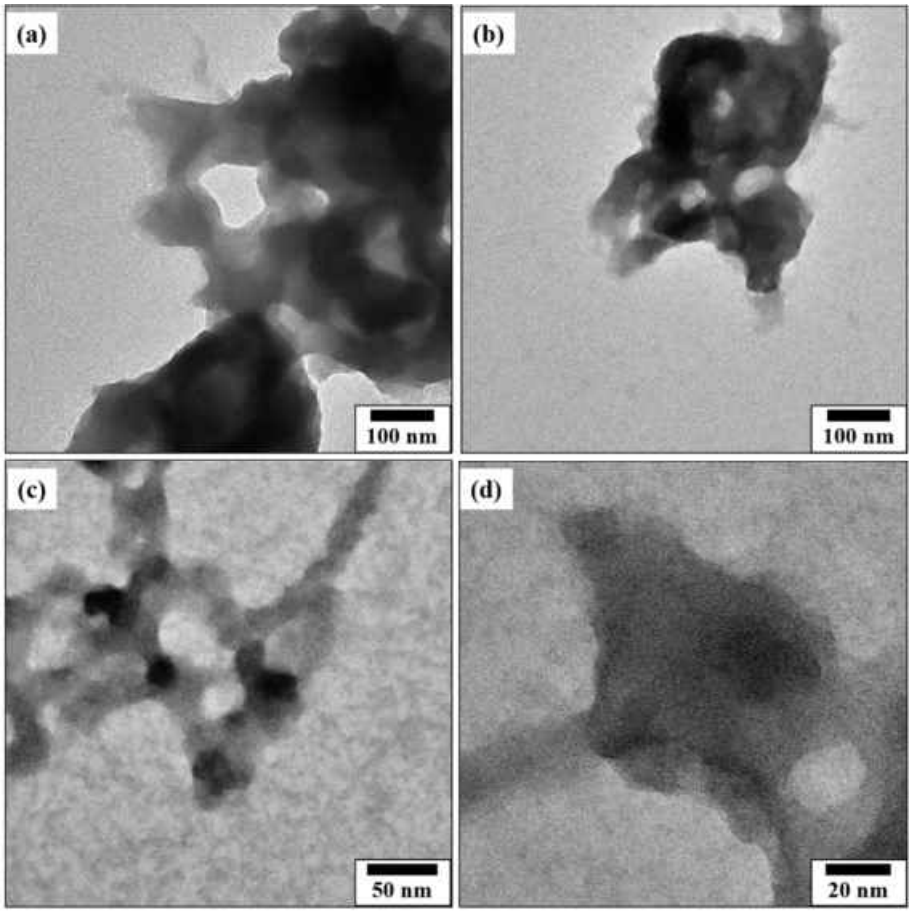

Figure 19. Low-magnification TEM images (a-d) of MoO_{3-x} nanoflakes obtained from the simple syntheses in 1-propanol.

Preparation with addition of Pluronic-F127. To examine whether the particles morphology can be tuned by a surfactant, two precipitation experiments were performed. For this purpose the precursor and a soft template were dissolved in 1-propanol. This method is part of the typical synthesis routes to mesoporous silica, but it was also successfully adapted for other mesoporous metal oxides.[63] During the process, soft templating agents such as cetyltrimethylammonium bromide (CTAB), alkylamines or Pluronic (a block-copolymer) form micelles in which both the nucleation and growth of the particles preferably occurs.[64-70] In this work, Pluronic-F127 was used as a surfactant in two different mass concentrations.

Figure 20 presents TEM images of WO_{3-x} nanoflakes prepared from a precursor solution in 1-propanol containing 100*wt*% Pluronic-F127 (in comparison to the mass of tungsten chloride in the solution). As it was expected, the nanoflakes obtained are less agglomerated than the ones from the surfactant-free synthesis. Hence, it seems that the concentration of micelles in the

solution was not sufficient to provide sufficient reaction space for all nucleation seeds, because most of the particles are fused. The mean particle dimension is ~17·17 nm (square-like flakes) and ~10 nm diameter (quasi-spherical particles).

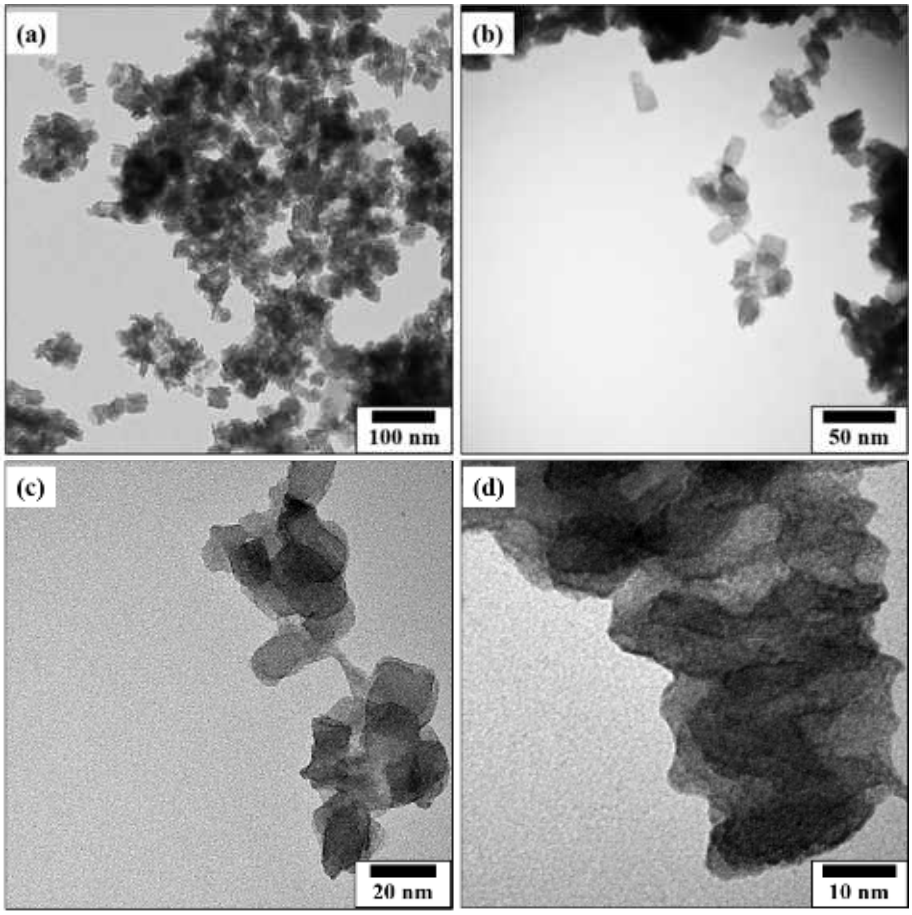

Figure 20. (a, b) Low- and (c, d) high-magnification TEM images of WO_{3-x} nanoflakes obtained from the simple syntheses in 1-propanol with the addition of 100wt% Pluronic F-127.

In the next step, the concentration of Pluronic was doubled to 200*wt*%. The particles obtained in that case are more uniform than the ones with 100*wt*% surfactant, showing that the quantity of micelles is closer to the optimum here (Figure 21). At the same time, some smaller agglomerates (~200·150 nm) are formed as flocculates of few nanoflakes. The mean lateral size of the flakes is measured to be ~30 nm.

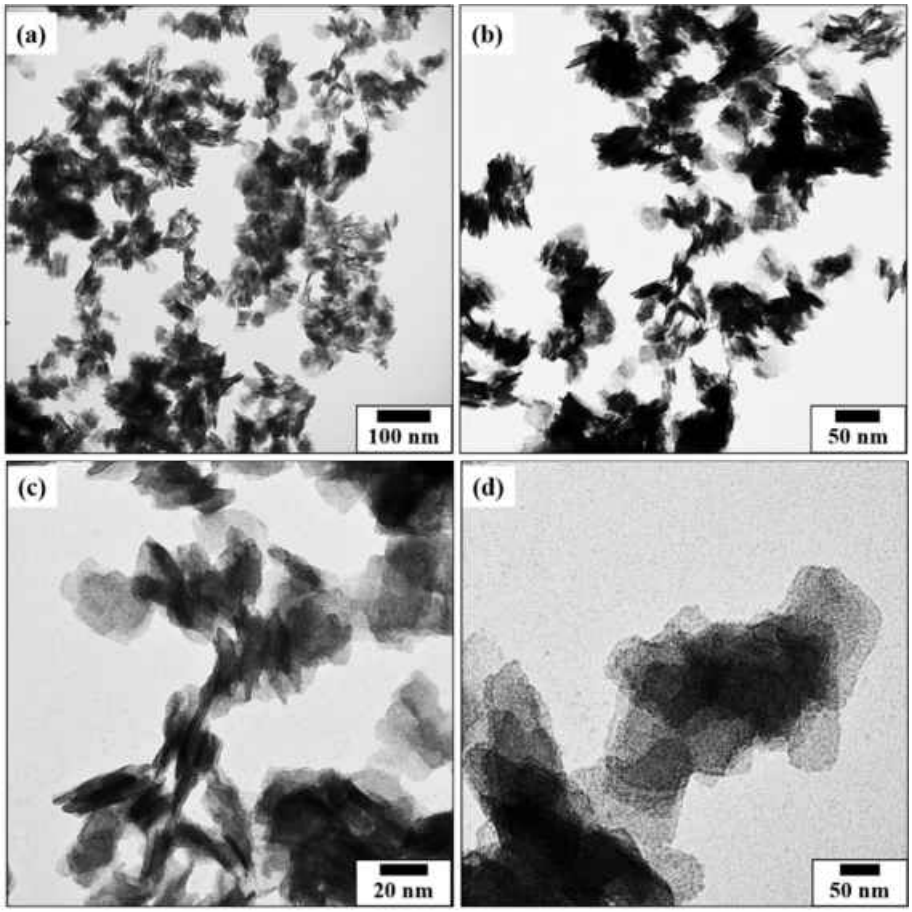

Figure 21. (a, b) Low- and (c, d) high-magnification TEM images of WO_{3-x} nanoflakes obtained from the simple syntheses in 1-propanol with the addition of 200wt% Pluronic F-127.

XRD patterns of all WO_{3-x} samples prepared in different alcohols or water are shown in Figure 22. The product in water can be identified as WO_3, all Bragg reflexes can be assigned to the hexagonal phase. Following this, a trend can be deduced: the better the miscibility of the solvent with water (MeOH > EtOH > 1-PrOH > CyOH), the sharper reflections in the respective diffractograms can be observed. This suggests that aqueous or water-containing solvent affects a pronounced crystallization of the product. However, the solubility of the WCl_6 plays an important role here, since in the case of a completely dissolved precursor theoretically more nucleation seeds shall be available. In the product from methanol, the reflections known from WO_3 are greatly broadened, yet this material obviously has the best-ordered structure regarding the materials prepared from different alcohols. In the transition to ethanol, only the widened (111)-reflection remains at $2\theta = 25$ °. The two other longer-chain alcohols yield completely amorphous material.

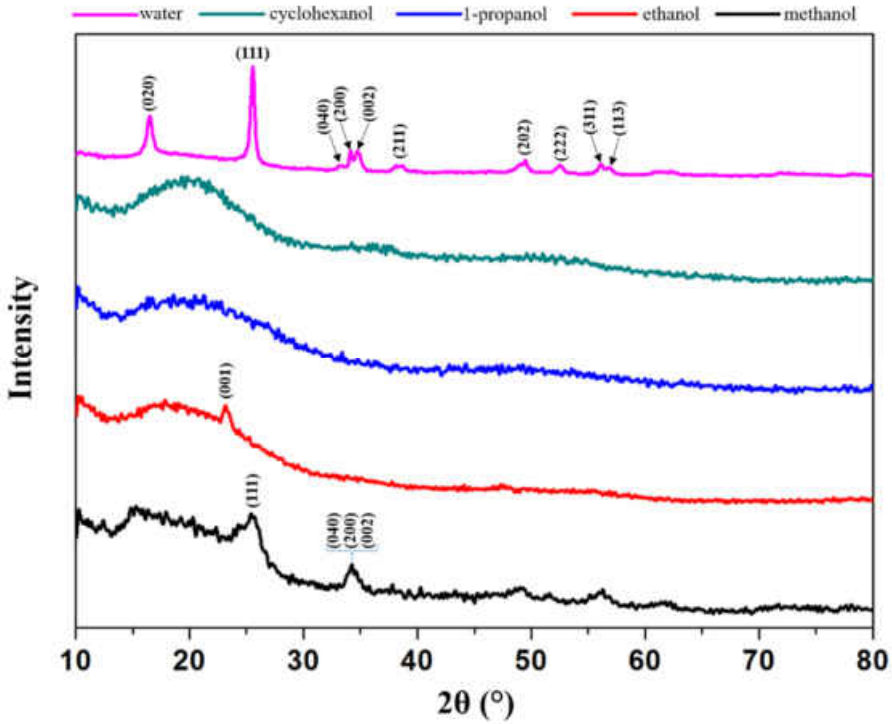

Figure 22. XRD patterns of the WO_{3-x} nanoflakes synthesized in different solvents.

The Raman spectra of tungsten oxides exhibits four main peaks (Figure 23). Usually the two bands with highest intensity, located at 806 and 710 cm^{-1} represent the stretching mode of the terminal ν(W=O) bond and stretching vibrations of bridging oxygen atoms ν(O-W-O), respectively. Two additional bands with intermediate intensity in the low wavenumber region (at 260 and 329 cm^{-1}) can be attributed to δ(O-W-O) deformation modes. The width of the bands is a strong indicator for the degree of structural order: the narrower the peaks the less oxygen deficiency and the less reduced W^{6+} ions are contained. Therefore, perfect crystalline materials exhibit narrow bands and amorphous compounds show significant peak broadening, respectively. This fact can be confirmed by the measured Raman spectra, where the trend derived from the diffractograms is also recognizable. Methanol yields, after water, the product with the best ordered structure, followed by ethanol and the other two alcohols.

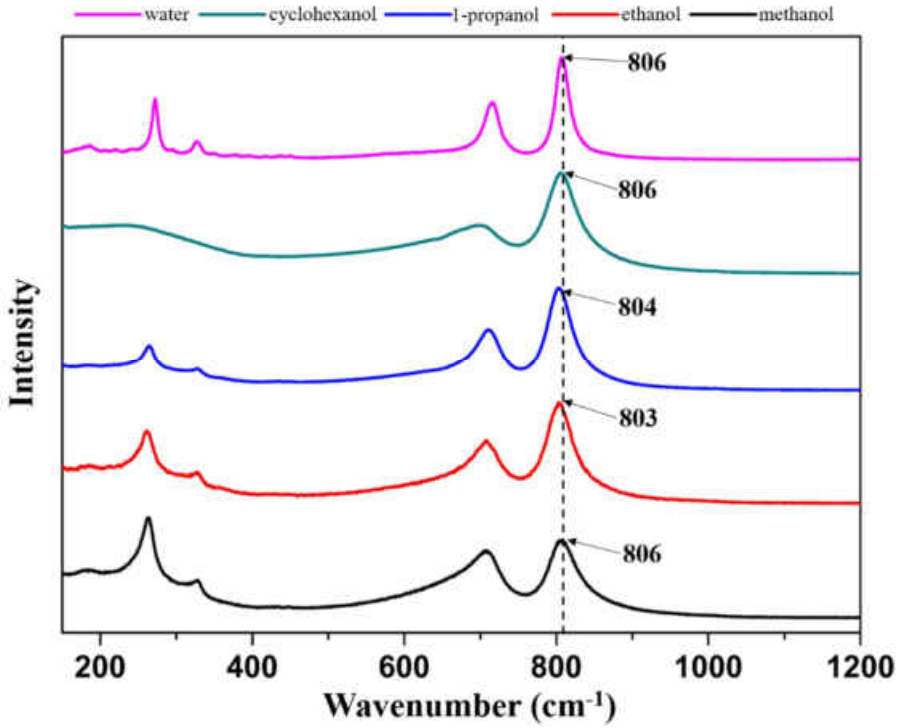

Figure 23. Raman spectra of the WO_{3-x} nanoflakes synthesized in different solvents.

Optical absorption spectra of all samples dissolved in water were recorded at room temperature in the wavelength range of 300–800 nm. Figure 24 reveals that for all nanoflakes samples the absorption onset is at ~450 nm. A steady decline in the absorption intensity can be observed for all samples, whereby the materials with the best-ordered structures (from water and methanol) show a steeper decrease. Another trend can be deduced from the colour of the solutions, which starts from dark-blue (for 1-propanol nanoflakes), proceeds over greyish-green (ethanol) to yellow for the WO_3.

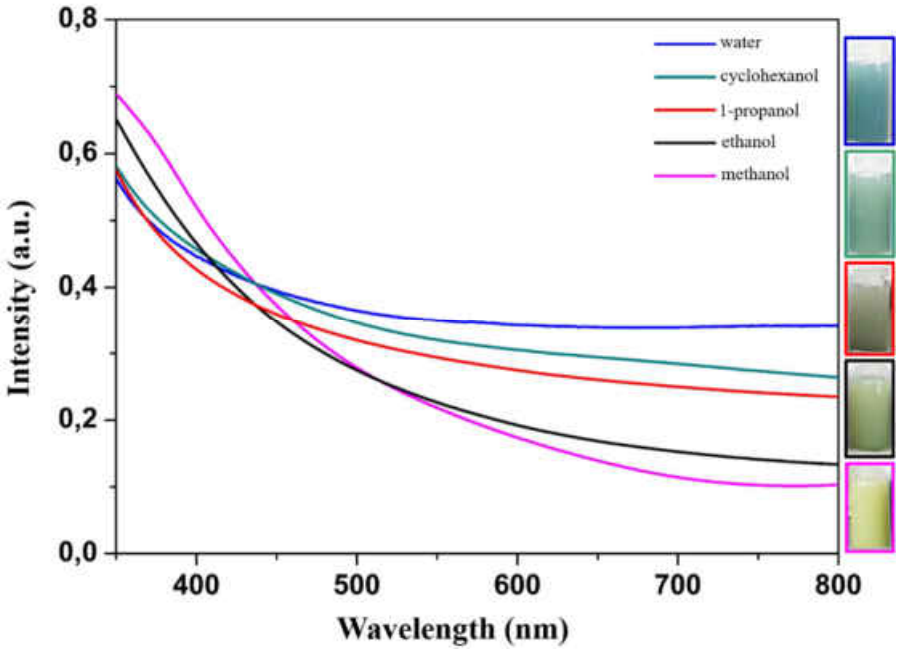

Figure 24. Absorption spectra of the WO_{3-x} nanoflakes prepared in different solvents. All spectra were measured in water, digital photographs of the solutions are shown on the right-hand side of the spectra.

Mixed oxides nanoflakes from 1-propanol. From the experiments conducted in various solvents, it was decided to perform the preparation of the solid solution of tungsten-molybdenum oxides in 1-propanol. Therefore, an appropriate amount of the two precursors was dissolved and directly precipitated by the addition of water, as described for the synthesis in different solvents. Figure 25 shows TEM images of the product containing a 1:1 ratio of tungsten and molybdenum. Single nanoflakes can no longer be observed here, since all particle-like structures seem to have grown into amorphous material. This is in good agreement with the morphology of the material obtained by using only $MoCl_5$ as a precursor (Figure 19). Consequently, the molybdenum seems to be predominant and therefore overcomes the structure-directing properties of the tungsten.

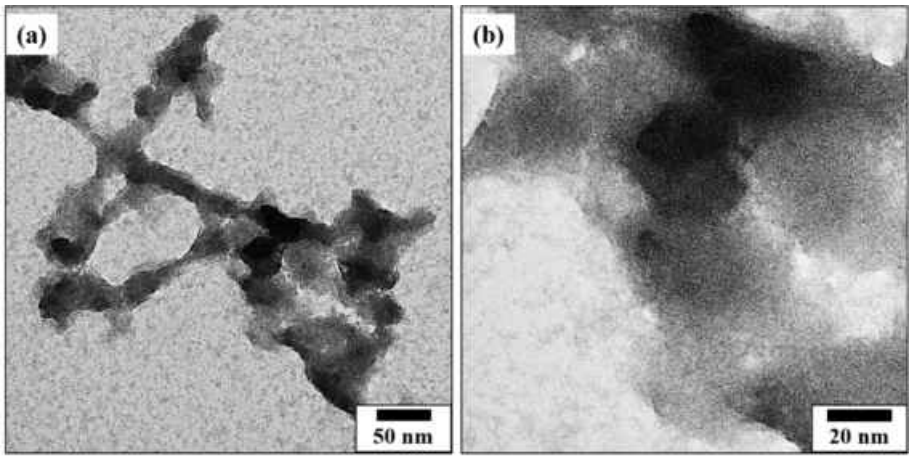

Figure 25. (a) Low- and (b) high-magnification TEM images of $Mo_{0.5}W_{0.5}O_{2.0}$ nanoflakes obtained from simple syntheses in 1-propanol.

Decreasing the amount of molybdenum precursor in the 1.5:1-mixture of W:Mo yields more well-ordered quasi-spherical nanoflakes, which are ~15 nm in diameter (Figure 26). Nonetheless, single nanoflakes cannot be observed as the fusing of the particles dominates.

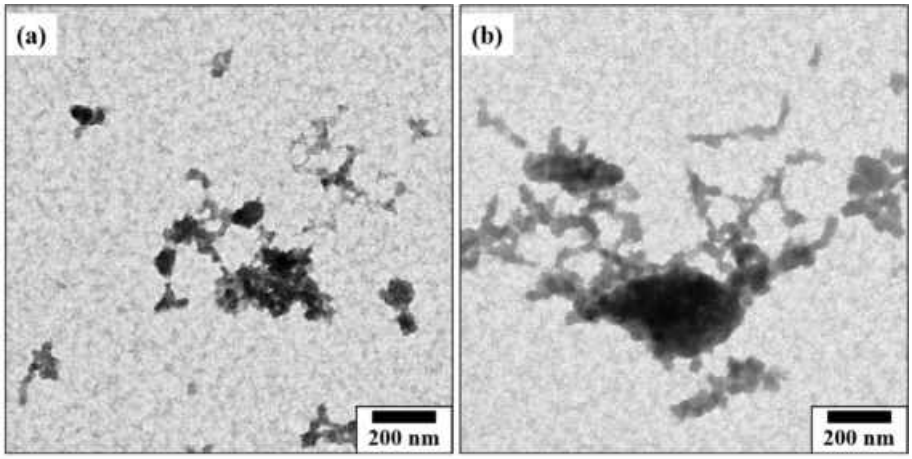

Figure 26. (a, b) Low-magnification TEM images of $Mo_{0.58}W_{0.42}O_{2.2}$ nanoflakes obtained from simple syntheses in 1-propanol.

A further increase in the tungsten-to-molybdenum ratio to 3:1 yields larger nanoflakes (~ 22 nm), but these are coalesced to form smaller agglomerates (Figure 27). In addition, individual distinct nanoflakes can also be observed in this case, but the major composition of the sample is dominated by bulk material.

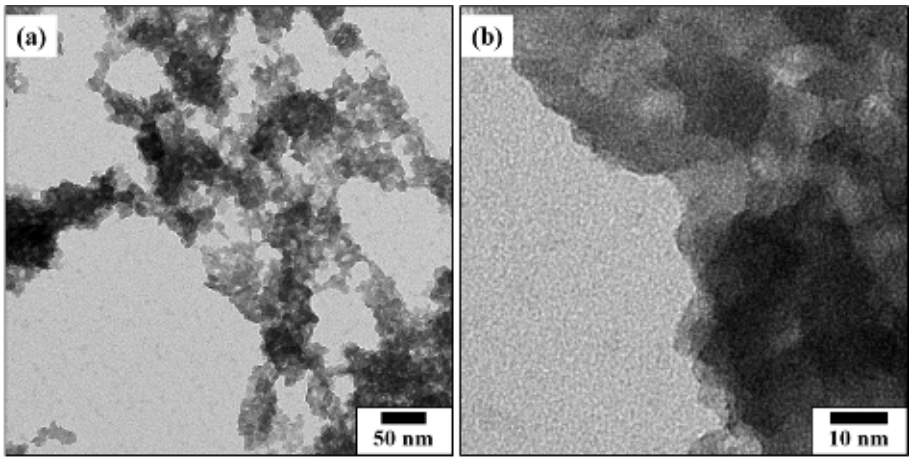

Figure 27. (a) Low- and (b) high-magnification TEM images of $Mo_{0.77}W_{0.23}O_{2.3}$ nanoflakes obtained from simple syntheses in 1-propanol.

Exceeding the three-fold excess of tungsten (6:1 ratio) is accompanied by a transition to flake-like morphology (Figure 28). The obtained particles show strong resemblance with the product known for WCl_6 as precursor only.

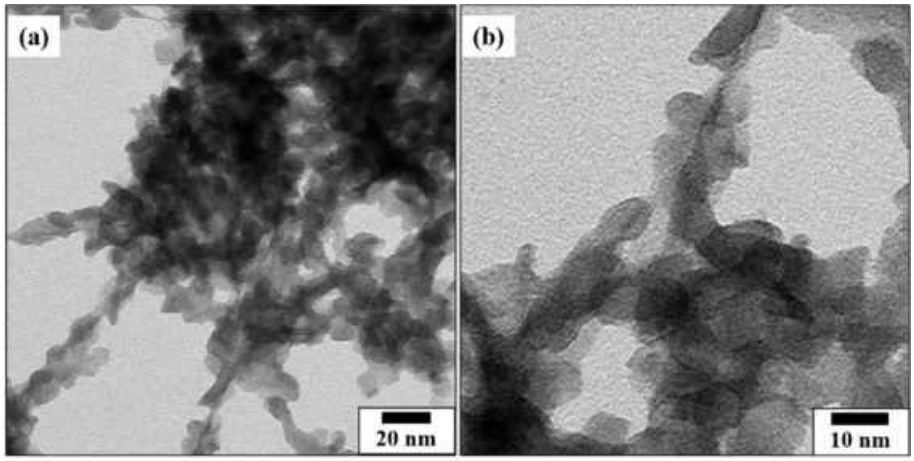

Figure 28. (a, b) Low-magnification TEM images of $Mo_{0.82}W_{0.18}O_{2.1}$ nanoflakes obtained from simple syntheses in 1-propanol.

If the molybdenum content is further reduced, a recurrence of distinct nanoflakes can be observed (Figure 29), which is in good correspondence with the product shown in Figure 16.

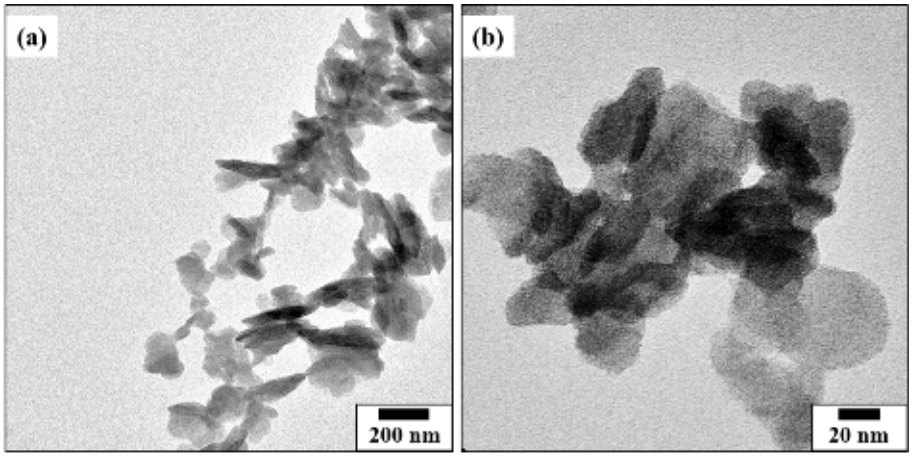

Figure 29. (a, b) High-magnification TEM images of $Mo_{0.88}W_{0.12}O_{2.6}$ nanoflakes obtained from simple syntheses in 1-propanol.

XRD patterns of the solid solutions of tungsten-molybdenum oxides show the strictly amorphous structure of all prepared samples except the pure WO_{3-x} (Figure 30). The reflections in the WO_{3-x} pattern are broadened, which further underlines the sub-stoichiometry and disordering of the as-prepared phase. This suggests that the formation of a crystalline structure is significantly suppressed by the occurrence of molybdenum foreign ions in the reaction solution.

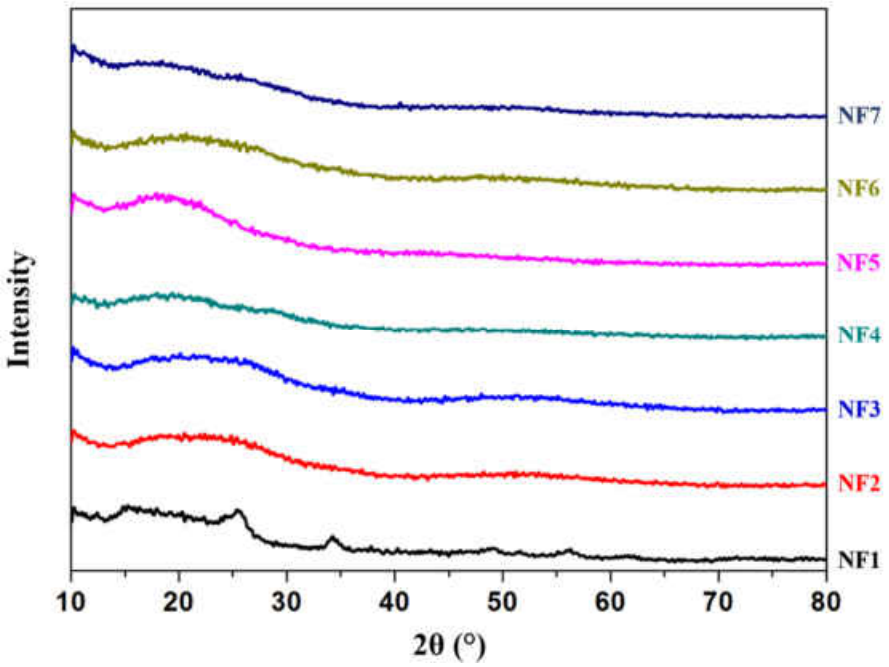

Figure 30. Powder XRD patterns of nanoflakes obtained from the doping series in 1-propanol as solvent: WO_{3-x} (NF1), $W_{0.88}Mo_{0.12}O_{2.6}$ (NF2), $W_{0.82}Mo_{0.18}O_{2.1}$ (NF3), $W_{0.77}Mo_{0.23}O_{2.3}$ (NF4), $W_{0.58}Mo_{0.42}O_{2.2}$ (NF5), $W_{0.5}Mo_{0.5}O_{2.6}$ (NF6) and MoO_{3-x} (NF7).

The Raman spectra of the mixed oxides are depicted in Figure 31. It is apparent that the terminal W=O stretching, originally located at 806 cm^{-1} in the pure WO_{3-x}, is gradually shifted with increasing concentrations of molybdenum in the mixed oxides (sample NF2 → NF6). The amorphous character of the structures is reflected by extensive broadening of the bands. Terminal ν(M=O) bond stretching and stretching vibrations ν(O-M-O) of bridging oxygen atoms undergo continuous convergence to one major band in the process. While the two deformation modes in the low wavenumber region (at 264 and 335 cm^{-1}) are most intense for the $W_{0.82}Mo_{0.18}O_{2.1}$ compound, they diminish to almost miniscule intensity for $W_{0.77}Mo_{0.23}O_{2.3}$ and $W_{0.58}Mo_{0.42}O_{2.2}$ and are ultimately superimposed by newly emerging Mo-O bands in $W_{0.5}Mo_{0.5}O_{2.6}$. For the $W_{0.5}Mo_{0.5}O_{2.6}$, the band between 800–910 cm^{-1} can be split into individual contributions of ν_s Mo=O stretching (820 cm^{-1}, from MoO_3), Mo=O/W=O stretching (845 cm^{-1}, from MoO_3/WO_3) and terminal Mo=O vibrations (861 cm^{-1} and 907 cm^{-1}, from Mo_4O_{11}).[71, 72] The sample prepared with $MoCl_5$ as precursor shows all characteristic bands of MoO_3. Interestingly, the spectrum obtained for $W_{0.82}Mo_{0.18}O_{2.1}$ does not follow any trend. The maximum of the M=O stretching is located at 814 cm^{-1}, therefore suggesting no significant incorporation of molybdenum. In addition, the deformation modes below 400 cm^{-1} show that a certain order prevails in the structure, which, however, contradicts the statement of the XRD pattern. Despite reproductive experiments, it cannot be clarified at this point why this material shows these contradictory characteristics.

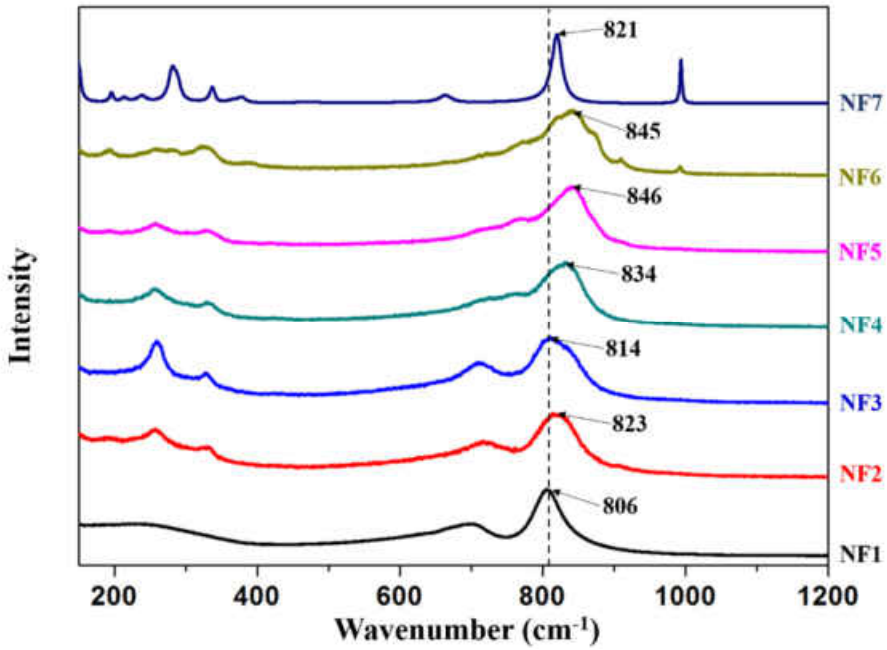

Figure 31. Raman spectra of the nanoflakes obtained from the doping series in 1-propanol as solvent: WO_{3-x} (NF1), $W_{0.88}Mo_{0.12}O_{2.6}$ (NF2), $W_{0.82}Mo_{0.18}O_{2.1}$ (NF3), $W_{0.77}Mo_{0.23}O_{2.3}$ (NF4), $W_{0.58}Mo_{0.42}O_{2.2}$ (NF5), $W_{0.5}Mo_{0.5}O_{2.6}$ (NF6) and MoO_{3-x} (NF7).

The bulk composition of the mixed oxides was determined by EDS analysis, Table 5 presents the results obtained.

Table 5. Elemental compositions of the prepared tungsten molybdenum nanoflakes, as determined by EDS.

Sample	Theoretical Ratio (W:Mo)	Element (*at*%)	Experimental Ratio (W:Mo)	Composition
NF1	1:0	X	X	WO_{3-x}
NF6	1:1	W 16.7 Mo 16.5 O 66.8	1:1	$W_{0.5}Mo_{0.5}O_{2.0}$
NF5	1.5:1	W 18.9 Mo 12.1 O 66.7	1.4:1	$W_{0.58}Mo_{0.42}O_{2.2}$
NF4	3:1	W 22.9 Mo 7.0 O 70.1	3.3:1	$W_{0.77}Mo_{0.23}O_{2.3}$
NF3	6:1	W 26.9 Mo 5.8 O 67.3	4.6:1	$W_{0.82}Mo_{0.18}O_{2.1}$
NF2	12:1	W 24.1 Mo 3.3 O 72.6	7.3:1	$W_{0.88}Mo_{0.12}O_{2.6}$
NF7	0:1	X	X	MoO_{3-x}

From the data in the table, it is apparent that the compounds with higher molybdenum content were successfully produced in the desired composition. For the samples containing a strong excess of tungsten, the precipitation of the tungsten oxide obviously occurs faster than the incorporation of molybdenum ions into the WO_3 lattice. Thus, the produced materials show

deviations from the atomic ratio of -23% (6:1 mixture) and -39% (12:1 mixture) from the one expected.

Figure 32 presents the absorption spectra of all nanoflakes samples prepared in 1-propanol. A clear trend can be identified in the mixing series of the solid solutions. First of all, pure WO_{3-x} shows the known weak absorption behavior, since an increase in intensity can be observed only below 420 nm. The $W_{0.88}Mo_{0.12}O_{2.6}$ mixture also traverses a minimum at 420 nm, after which a weak but steady increase can be observed. From this point onwards the increase of the molybdenum content in the solid solutions of tungsten and molybdenum has a drastic effect on their absorption behavior since a band with a maximum at 692 nm evolves. For the 6:1 mixture it can be seen in the approach, but then undergoes a sudden increase in the transition to the 3:1 oxide (intensity ~ 2.5 times higher) and reaches its maximum intensity for the 1.5:1 mixture. A slightly different picture is obtained for the 1:1 mixture, since the absolute maximum appears to be in the range above 800 nm. For the pure MoO_{3-x} compound, an intense absorption band at ~760 nm can be observed. Therefore, the formation of the absorption maximum at ~690 nm is a synergetic effect caused by the incorporation of both the metal ions into the crystal structure.

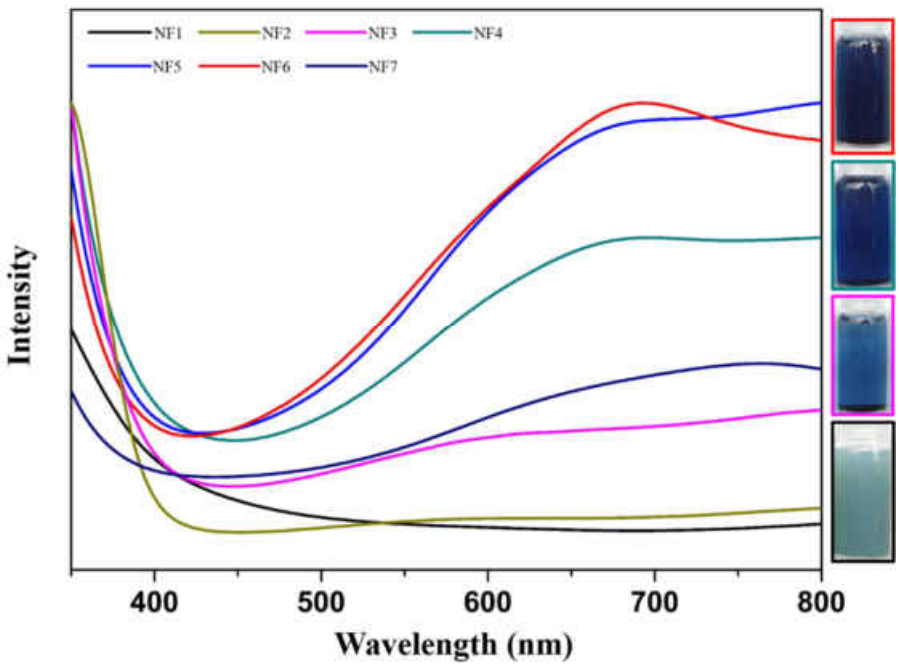

Figure 32. Absorption spectra of the $W_xMo_{1-x}O_{3-y}$ nanoflakes prepared in 1-propanol. All spectra were measured in water, digital photographs of four selected solutions are shown on the right-hand side of the spectra.

Due to their strong absorption in the near IR region (> 680 nm) the tungsten molybdenum oxides theoretically are promising materials regarding photocatalysis. However, in a few experiments, no significant activity in the decomposition of dyes could be observed. After the centrifugation of the dye-nanoparticle-dispersion it was found that the particles separated the dye only by adsorption from the solution and thus led to discoloration of the solution. If the sample was shaken

after centrifugation, a recurring pink color of the solution was observed, suggesting that no degradation of the dye took place.

4.2.2. Sulfidization to WS_2 Nanoflakes

The WO_{3-x} nanoflakes (NF1) were used as precursors for WS_2 nanoflakes syntheses by reductive sulfidization, performed using a homemade vertical fluidized bed reactor (Figure 33).[73] If the required parameters (melting point of the oxide, particle size, particle structure, sulfidization temperature and sulfidization time) are known, nearly every oxide can be sulfidized with this technique due to the creation of a swirling effect in the reactor. Furthermore, highly oxidized starting material can *in-situ* be reduced to a certain extent by optionally introducing H_2-gas to the reaction chamber.

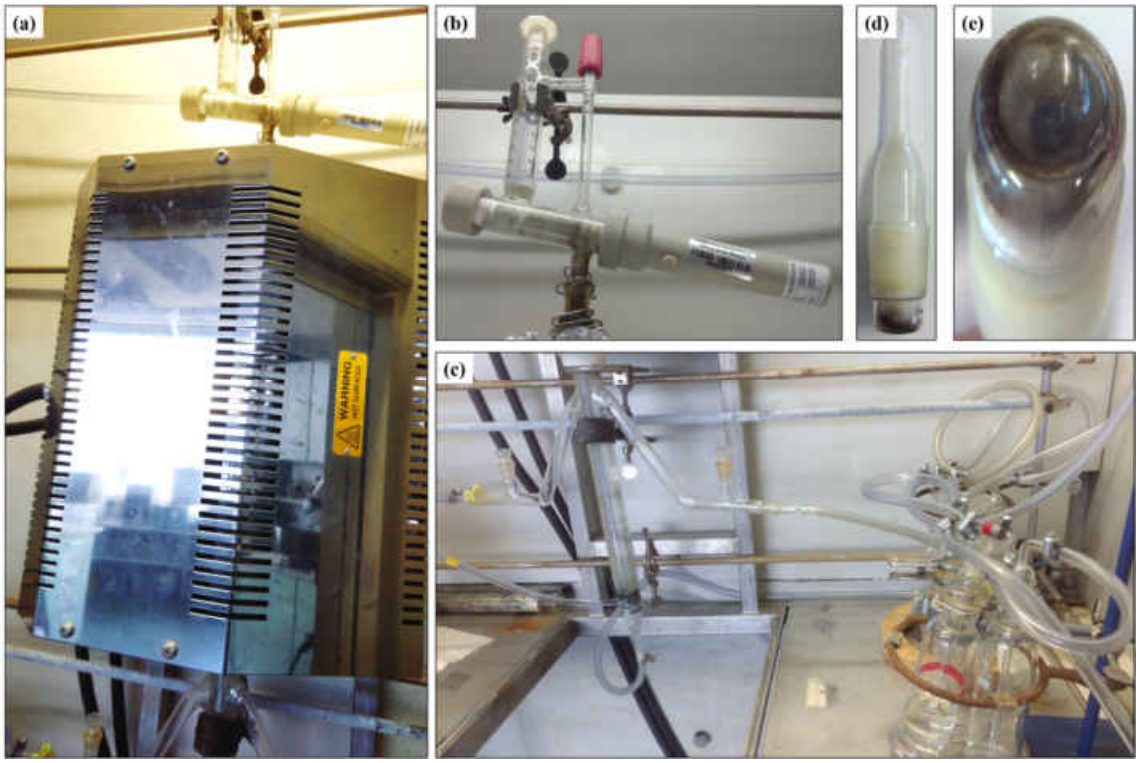

Figure 33. Digital photographs of the home-made vertical fluidized bed reactor for reductive sulfidization processes: (a) overview image of the set-up with the hinged furnace in the front, (b) screw conveyor for continiuous substrate supply, (c) bottom part of the quartz glass tube with connections to gas supply, (d) hollow plug in side view and (e) close-up of the hollow plug.

For the reductive sulfidization, 1 g of WO_{3-x} NF were filled in the metering funnel, equipped with a screw conveyor. Next, the complete apparatus was flushed with argon prior to the reaction to remove oxygen, while the furnace was heated to 800 °C with a rate of 10 °C/min. The gas feed-in was switched to H_2S (controlled with a flow meter) and the screw conveyor was turned on to supply the WO_{3-x} precursor with a rate of 10–15 mg/min. After 150 min in total, the furnace was

cooled to ambient temperature naturally under a constant flow of argon (to remove residual H_2S). The resulting dark-grey powder was extracted with the help of the hollowed plug and used for further characterisation. Furthermore, the as-obtained product was examined for its performance as lubricant's additive in tribological measurements (Chapter 6.2.4.).

The TEM images in Figure 34 show that the WO_{3-x} nanoflakes retain their morphology after sulfidization. Agglomeration of some single layers to bigger, bulk-like arrangements can also be observed (Figure 34 a, b). That can be explained in two ways: firstly, the oxide nanoflakes used as precursor also show a strong tendency to form bigger agglomerates and, secondly, the mechanism of the reductive sulfidization with H_2S itself. As the defects in the WO_{3-x} are considered to be particularly important to achieve a fast conversion of oxides to sulfides, adjacent precursor nanoflakes (with many surface defects) can easily grow together in the process.

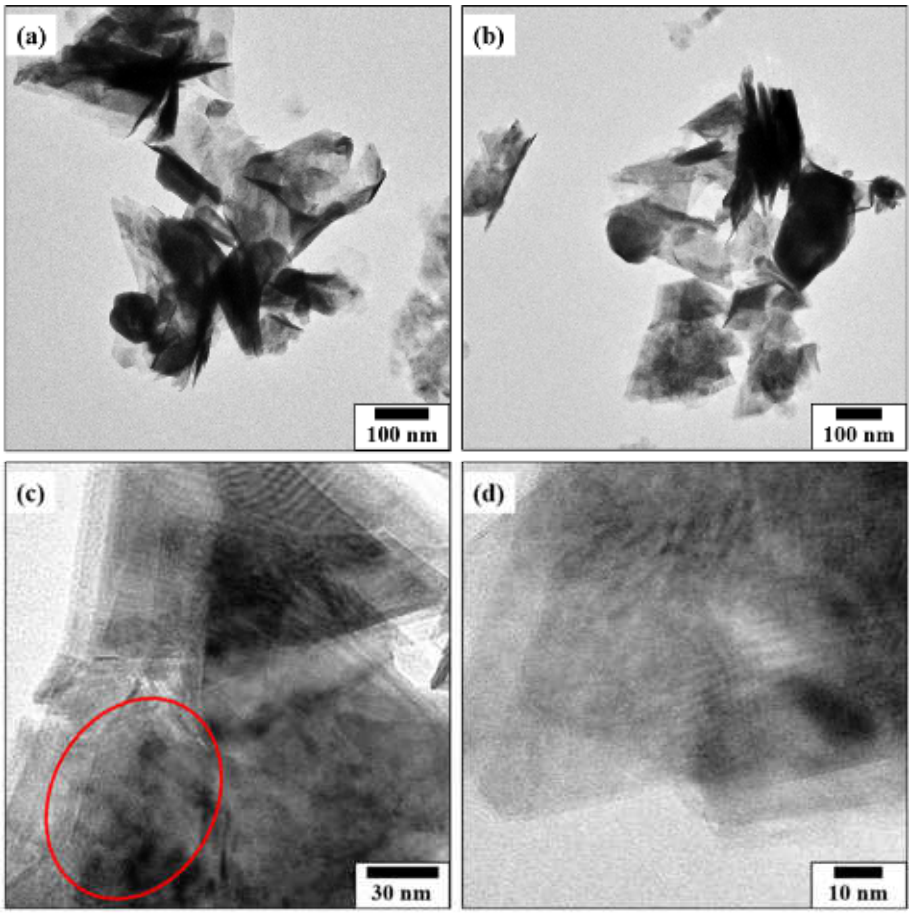

Figure 34. (a-c) Low-magnification and (d) high-magnification TEM images of WS_2 nanoflakes obtained from the reductive sulfidization using the fluidized bed reactor.

Thus, even a good fluidization technique cannot keep the particles from caking together during the sulfidization at 800 °C and single-layer particles or (multi-layer) nanoflakes are obtained with bulky agglomerates in most cases. The multi-layer nanoflakes of WS_2 measure up to 220 nm in length and 10–15 nm in thickness (depending on the number of layers). In contrast to the mainly amorphous character of the WO_{3-x} precursors the sulfides show a more crystalline structure which

can clearly be seen in Figure 34 (c). In that case, the well-known layered structure of WS_2 can be identified on the parts of the particles (red circle).

The formation of bulk material is displayed by SEM. In Figure 35, an assemblage of WS_2 nanoflakes on huge (~25 µm) isles of bulky WS_2 is shown.

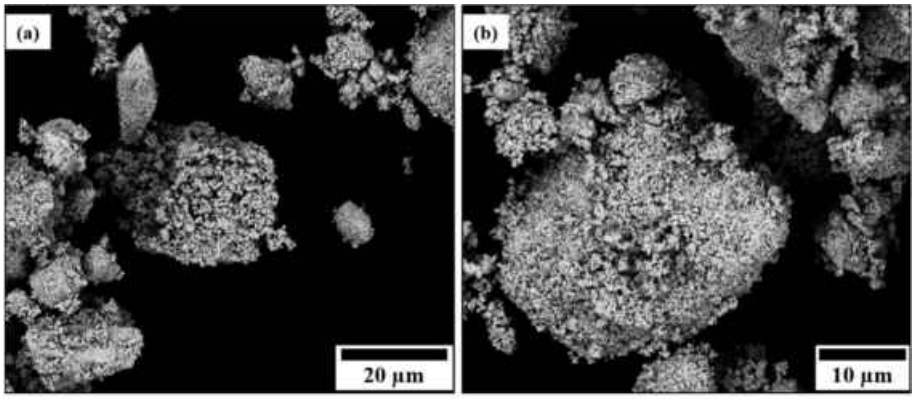

Figure 35. (a, b) SEM images of the agglomerations of WS_2 nanoflakes obtained from the reaction of WO_{3-x} in the fluidized bed reactor.

Furthermore, the XRD pattern of the sulfidized WO_{3-x} nanoflakes shown in Figure 36 exhibits reflections of 2H-WS_2 phase only. However, a slight broadening of the (101) and (013) reflections indicates that a small amount of oxide remained in the product.

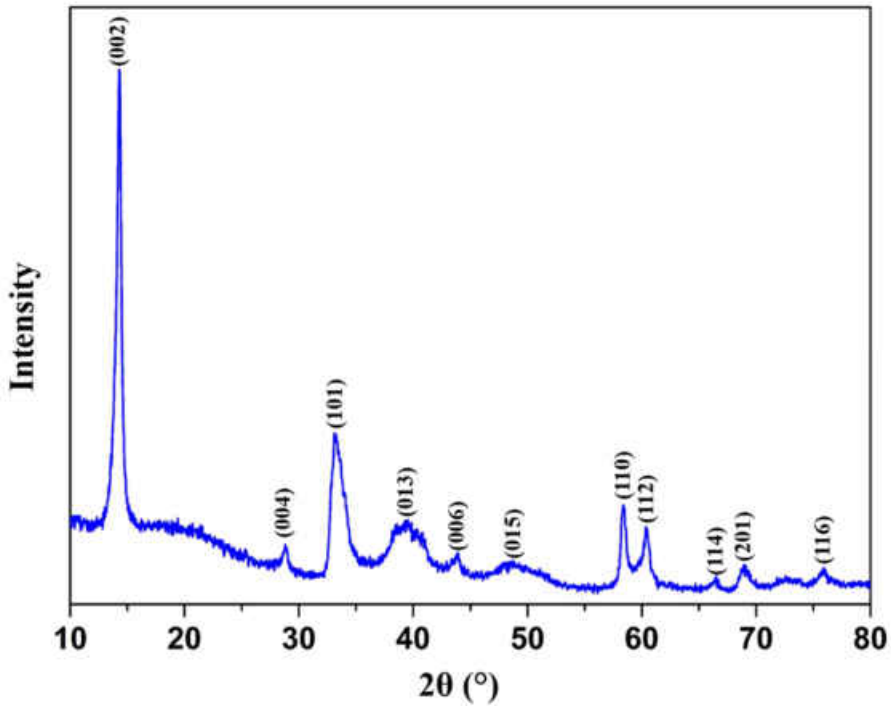

Figure 36. Powder XRD pattern of the sulfidized WO_{3-x} nanoflakes showing pure phase 2H-WS_2.

The content oft he following chapter is partially taken and adapted from a) "Surface Defects as Tools to Solubilize and Funtionalize WS_2 Nanotubes", *Eur. J. Inorg. Chem.* 2017, **15**, 2190-2194 and b) "Solvothermal Synthesis of Molybdenum-Tungsten-Oxides and Their Application as Photoelectrocatalysts in the Hydrogen Evolution Reaction", *J. Mater. Chem. A* (submitted 2017). Taken parts are delimited by single quotation marks ("") in case of a) and doubled quotation marks (""""") in case of b).

Authorship contributions

Category 1

Conception and design of study:

a) D. Spetter, F. Hoshyargar, W. Tremel

b) D. Spetter, M. N. Tahir, W. Tremel

Acquisition of data:

a) D. Spetter, F. Hoshyargar, J. K. Sahoo, R. Brandscheid, B. Barton

b) D. Spetter, I. Khan, H. Lu

Analysis and/or interpretation of data:

a) D. Spetter, F. Hoshyargar, J. K. Sahoo, R. Brandscheid, B. Barton, M. Panthöfer

b) D. Spetter, I. Khan, H. Lu, M. N. Tahir

Category 2

Drafting the manuscript:

a) D. Spetter, F. Hoshyargar, M. N. Tahir

b) D. Spetter, M. N. Tahir, I. Khan

Revising the manuscript critically for important intellectual content:

a) M. N. Tahir, M. Panthöfer, U. Kolb, W. Tremel

b) A. Qurashi, T. Weidner, W. Tremel

Category 3

Approval of the version of the manuscript to be published:

a) D. Spetter, F. Hoshyargar, J. K. Sahoo, M. N. Tahir, R. Brandscheid, B. Barton, M. Panthöfer, U. Kolb, W. Tremel

b) D. Spetter, M. N. Tahir, I. Khan, A. Qurashi, H. Lu, T. Weidner, W. Tremel

Figure 39: Prepared by D. Spetter

Figures 37, 40, 43–46, 50: Prepared by D. Spetter

Figure 48: Prepared by H. Lu and D. Spetter

Figures 49, 51, 52: Prepared by I. Khan and D. Spetter

Table 6: Prepared by D. Spetter

4.3. $W_{18}O_{49}$ Nanowires and MoO_{3-x}–$Mo_xW_{1-x}O_{3-y}$ Microspheres

4.3.1. Synthesis and Characterization

“”For the synthesis of tungsten-molybdenum mixed oxide microspheres 100 mg (0.366 mmol) of molybdenum (V) chloride and *Y* mmol of tungsten (VI) chloride (with $Y = 0.538, 0.355, 0.177, 0.089, 0.044$) was dissolved in ethanol to form a clear solution. The as-prepared solutions were transferred to a 50 mL Teflon®-lined vessel. After sealing the vessel in a stainless steel autoclave the solvothermal reaction was carried out by heating the autoclave at 180 °C for 12 h in an electric oven. After the reaction, black precipitates were collected by centrifugation, rinsed with ethanol two times and dried *in vacuo* for 12 h at 60 °C. The as-prepared samples containing different Mo/W ratios were named as S1 ($Mo_{0.5}W_{0.5}O_{2.1}$), S2 ($Mo_{0.62}W_{0.38}O_{2.3}$), S3 ($Mo_{0.75}$ $W_{0.25}O_{2.4}$), S4 ($Mo_{0.85}W_{0.15}O_{2.6}$), and S5 ($Mo_{0.89}W_{0.11}O_{2.7}$), where the higher number indicates the increasing amount of Mo in the mixed oxide. The solvothermal process is depicted in Figure 37.

Molybdenum oxide microspheres were synthesized in an analogous manner. For that, 100 mg (0.366 mmol) of molybdenum pentachloride ($MoCl_5$) were dissolved in 100 mL ethanol and subsequently transferred to two 100 mL Teflon®-lined vessels. The vessels were sealed in stainless steel autoclaves, which were placed in an electric oven for 12 h at 180 °C. After the reaction, black precipitation was collected by centrifugation, rinsed with ethanol two times and dried *in vacuo* for 12 h at 60 °C. The sample was named S6 (MoO_{3-x}).””

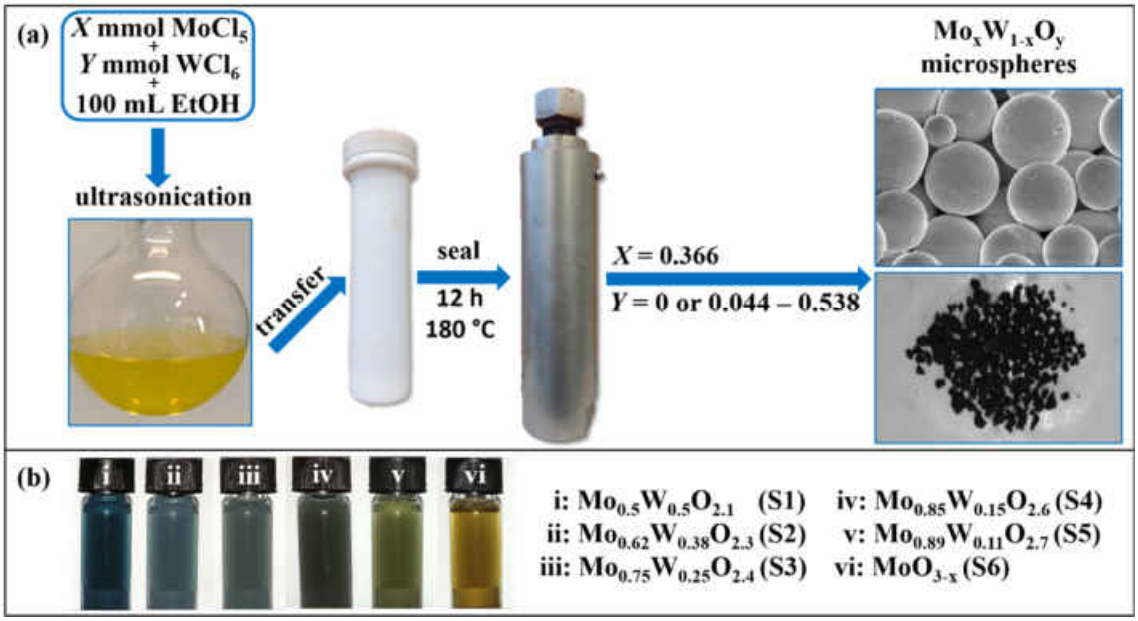

Figure 37. (a) Scheme of the procedure for the solvothermal synthesis of molybdenum oxide and tungsten-molybdenum oxide microspheres, respectively. The SEM image shows the typical morphology of the particles obtained. In the digital photograph, the black powder obtained from the reaction is presented. (b) Photographs of the products dispersed in water.

Guo et al. already showed that the solvothermal reaction of the chlorides in ethanol yields diethyl ether and hydrogen chloride as by-products (Figure 38), which can be washed out with ethanol easily.[74]

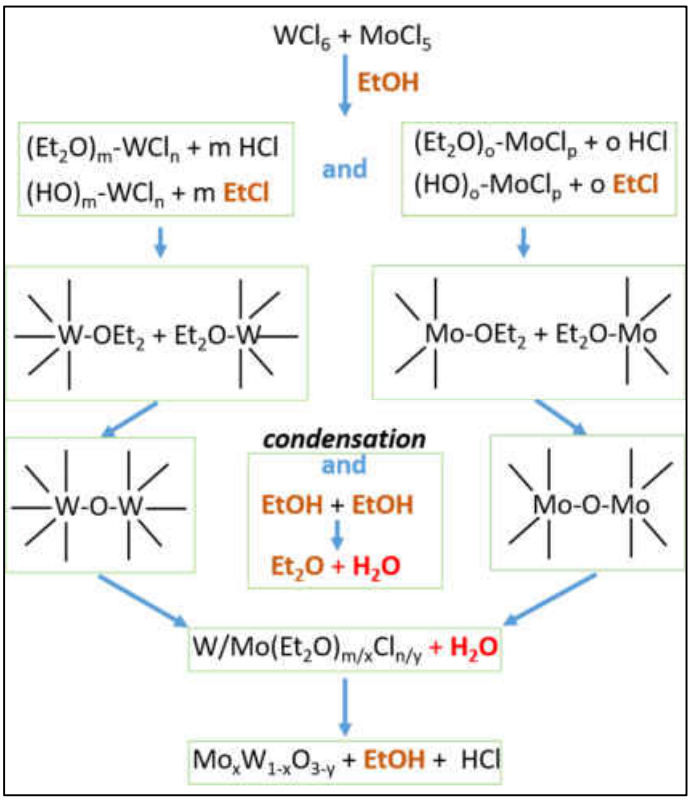

Figure 38. Schematic overview of the reactions taking place during the solvothermal decomposition of molybdenum chloride and tungsten chloride to the mixed oxides.

Morphological consideration. The solvothermal synthesis using ethanol as a solvent yields highly uniform microspheres of Mo/W based mixed metal-oxides. The use of pure $MoCl_5$ as reactant also results in the formation of spherical MoO_{3-x} microparticles. If WCl_6 is used as starting material under the same experimental conditions, the well-known $W_{18}O_{49}$ nanowires are obtained, whose diameter and length can be tuned in different solvents from 10 to 40 nm and 1 to 10 µm, respectively (Figure 39).[75] The as-prepared sample is referred to as S7 in the following.

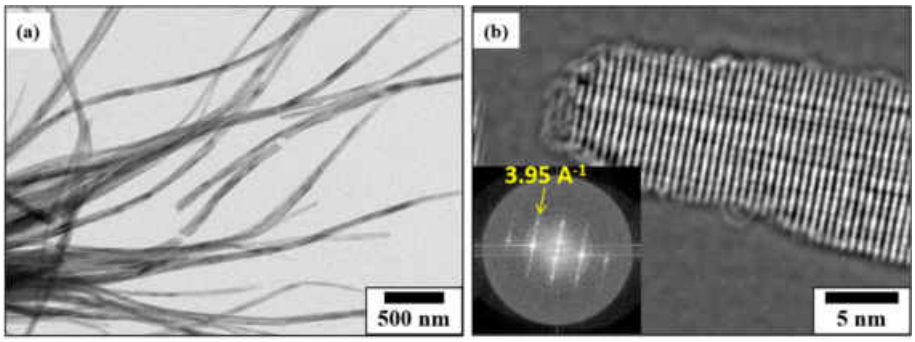

Figure 39. (a) TEM image of a bundle of $W_{18}O_{49}$ nanowires, (b) HR-TEM image of a tip of a single nanowire, the inset shows the appropriate electron diffraction pattern.

“”As shown in Figure 40, the as-obtained mixed oxides particles consistently retain spherical shape throughout the doping series of the non-stoichiometric MoO_{3-x} with various concentrations of tungsten (samples S1 to S5). They are connected by small contact areas, which is illustrated particularly well by the orange marks in Figure 40 (a). These areas can easily be separated by mechanical energy (mortaring) or ultrasonication. As a result, slight indentations are left in the formerly contiguous spheres (green marks in Figure 40 f).

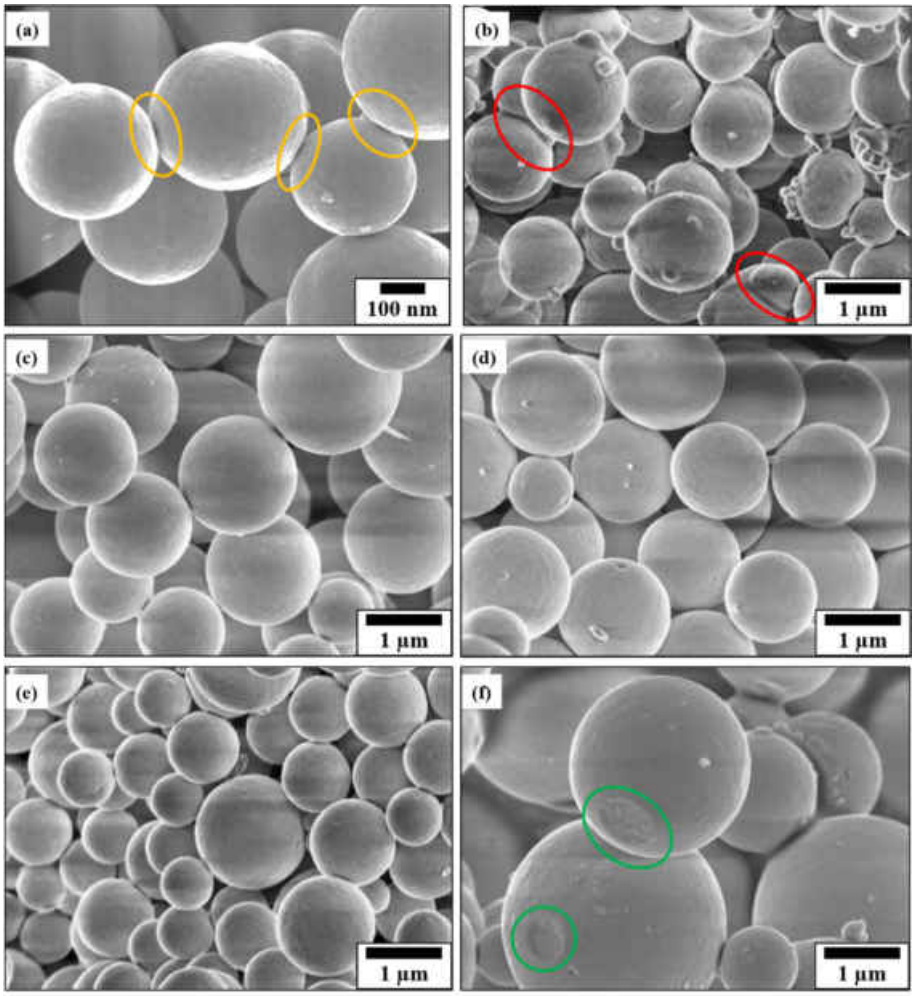

Figure 40. Representative SEM and low magnification TEM images of the as-synthesized microspheres: (a) $Mo_{0.5}W_{0.5}O_{2.1}$, (b) $Mo_{0.62}W_{0.38}O_{2.3}$, (c) $Mo_{0.75}W_{0.25}O_{2.4}$, (d) $Mo_{0.85}W_{0.15}O_{2.6}$, (e) $Mo_{0.89}W_{0.11}O_{2.7}$ and (f) MoO_{3-x}. The coloured marks are explained in the main text.””

A striking feature of $Mo_{0.62}W_{0.38}O_{2.3}$ is that it shows the strongest tendency for phase separation, as many nanometer-sized particles and agglomerates can be found on the surface of the microspheres. In contrast, some of the microspheres (that are well-separated in the case of S1, S3, S4, S5 and S6) are interconnected by great interfaces (red marks in Figure 40 b). This is a hint that the reaction time in the solvothermal process was not sufficient for that particular mixture. Therefore, to examine the influence of the reaction time, another two experiments were carried out for all of the mixtures S1–S5 and the pure MoO_{3-x}, respectively. Figure 41 shows SEM images of the as-obtained products after 24 h and 48 h, which were labelled as S1-24h/S1-48h and

S2-24h/S2-48h. The images of S1-24h/S1-48h are shown as representatives for all samples, because the differences in size and shape of S3–S6 after 24 h/48 h were negligible.

As can be seen in Figure 41, $Mo_{0.5}W_{0.5}O_{2.1}$ shows the same uniformity after a reaction time of 24 h as after the standard 12 h procedure. No bigger agglomerates or merging of particles can be observed. After 48 h, there are still many separated microspheres in the mixture, but the batch mainly consists of bulk-like material. Sample S2-24h shows almost the same inhomogeneity as in Figure 40 (b). This indicates that a doubling of the reaction time has almost no influence on the particles' morphological development. Moreover, preferred formation of bulk material after 48 h can be observed (red marks in Figure 41 b, d).

Solvothermal reactions of acidic molybdenum/tungsten chlorides in aqueous or alcoholic solutions proceed as autocatalytic polycondensations. Thus, it appears that after a certain time the chemical equilibrium shifts from product formation to product dissolution. In the subsequent product formation thus many small agglomerates fuse into larger aggregates or bulk material. Since this is a continuous physico-chemical process, it can be concluded that the poly-condensation of Mo/W to microspheres of $Mo_xW_{1-x}O_{3-y}$ is thermodynamically preferred. The dissolution of the microspheres and their conversion to bulk material at long reaction times is therefore the kinetically preferred counterpart.

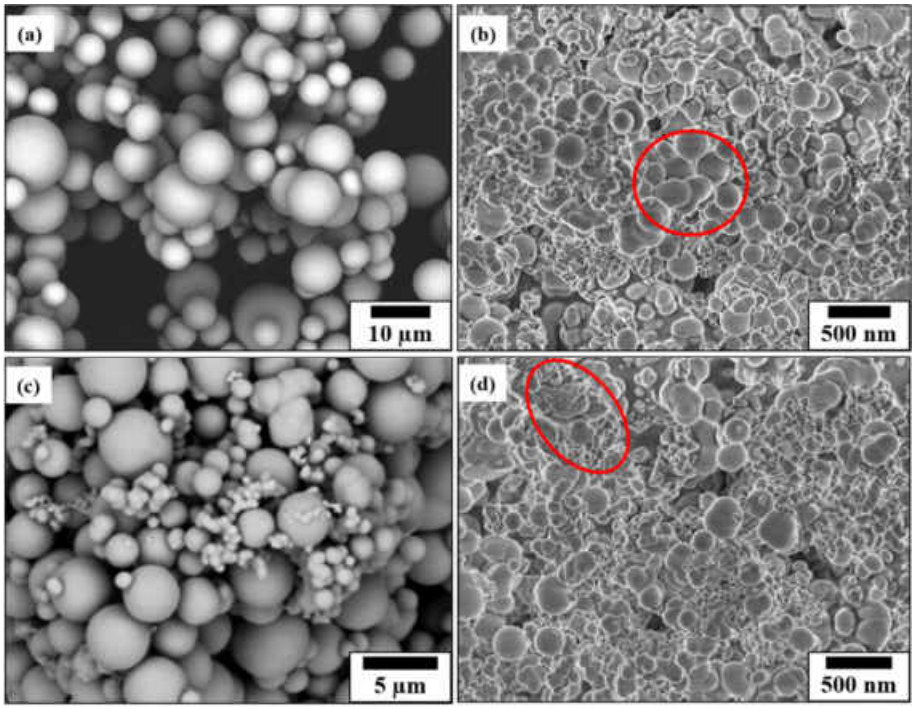

Figure 41. SEM images of the mixed oxides products (a) S1-24h, (b) S1-48h, (c) S2-24h and (d) S2-48h. Red marks in (b) and (d) exemplify the presence of bulk material.

To further investigate the influence of the reaction time on product formation another two experiments were carried out at 4 h reaction time, with two different molar ratios (1:1 or Mo only). The TEM images in Figure 42 clearly show that in both cases small (~80 nm), highly

agglomerated particles are obtained if the reaction time is shortened. The 1:1-mixture yields more elongated structures, while using the $MoCl_5$ precursor results in the formation of particles with pronounced spherical shape. Thus, the growth process of the particles is directly affected by the reaction time.

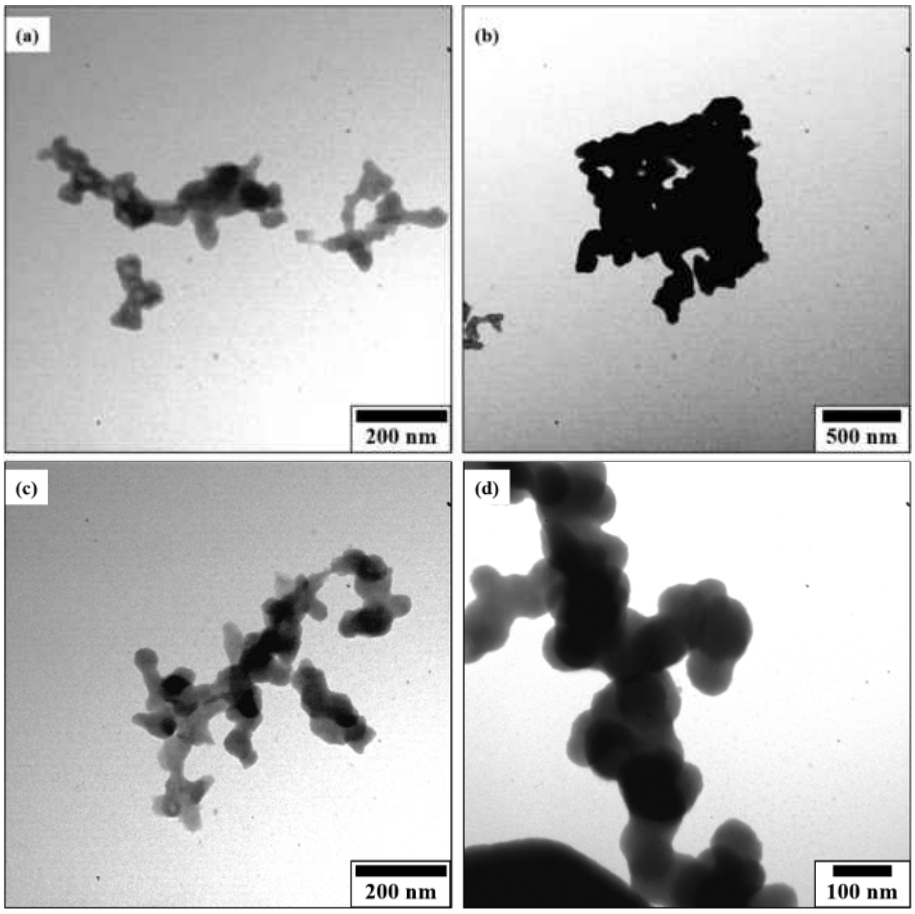

Figure 42. TEM images of the samples obtained after 4 h reaction time: (a, b) molar ratio of precursors 1:1 and (c, d) with Mo-precursor only.

“““To get statistically equitable values for the spherical dimensions of the particles, in two overview images of the appropriate sample a 10·10 grid overlay was utilized. One particle per grid field was measured in diameter, resulting in a total amount of 100 measured particles per overview image. The size of the microspheres varies from 400 nm to 2000 nm in diameter with majority average ~1300 nm. A visualization of the average diameter (200 particles per sample) of all products is depicted in Figure 43.

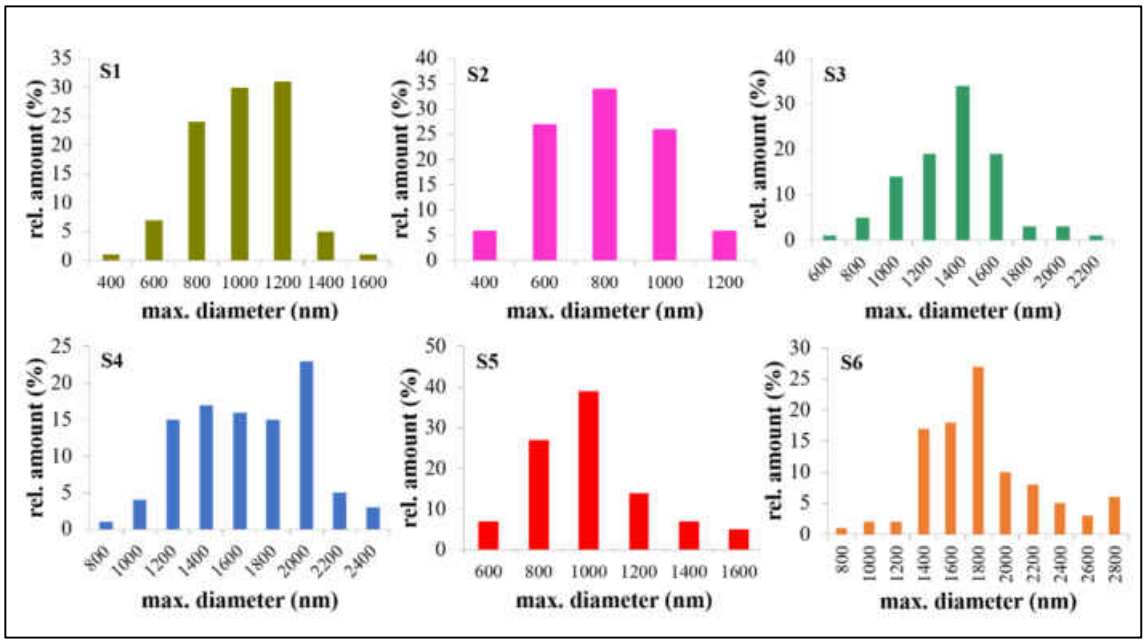

Figure 43. Size-distribution histograms of all synthesized microspheres, showing the relative amount of particles with the appropriate diameter.

The pure MoO_{3-x} exhibits the greatest variation of particles sizes, ranging from 800 nm for the smallest and 2800 nm for the biggest particles. On the other hand, the $Mo_{0.62}W_{0.38}O_{2.3}$ sample shows the narrowest size distribution with 400 nm for the smallest and max. 1200 nm for the biggest spheres.""

"Structural considerations. A first hint at the amorphous structure of the synthesized microparticles is given by the absence of ordered lattice fringes, which usually can be observed in TEM or HR-TEM images, respectively. As can be seen in from Figure 44 (a-c), the surface of the microspheres is not smooth but consistently characterized by irregularities. The HR-TEM image in Figure 44 (d) shows a representative disordered, defect-rich edge of the microparticles. Due to the non-crystalline structure of the product, no lattice fringes, resulting from a superposition of a transmitted wave and diffracted wave from one lattice plane of a crystal, can be identified.

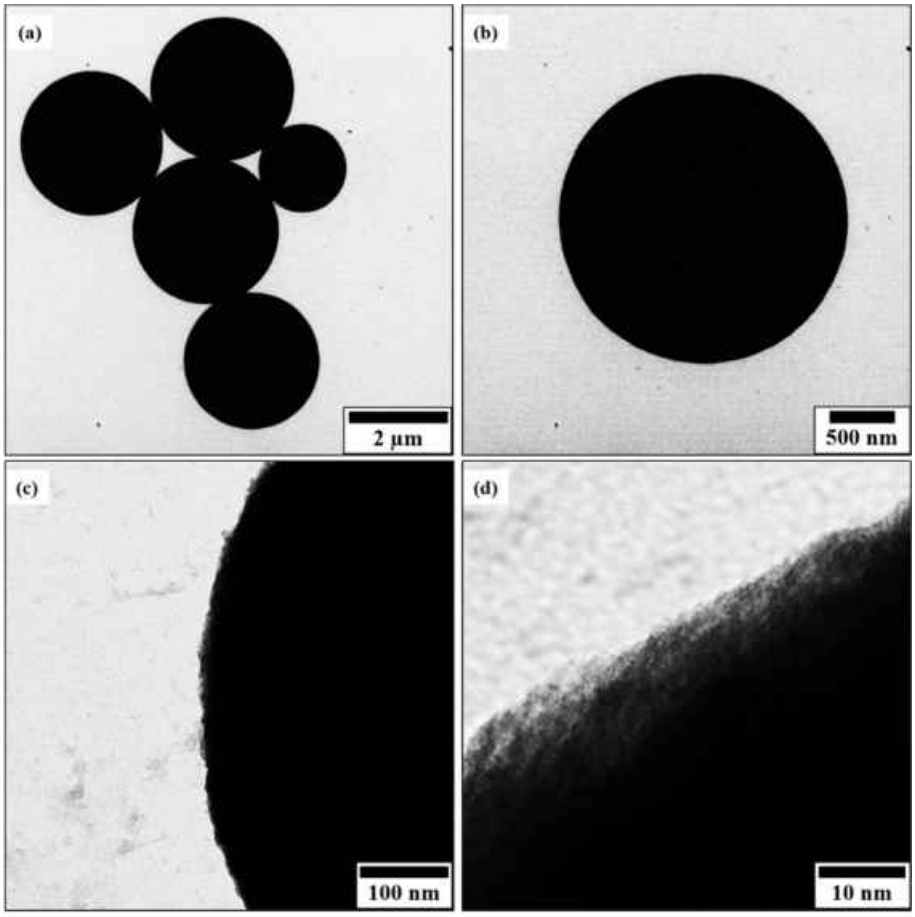

Figure 44. (a-d) Series of TEM images of $Mo_{0.5}W_{0.5}O_{2.1}$ microspheres, captured at different magnifications, showing the defect-rich surface of the microspheres.

All samples were characterized by powder X-ray diffraction to check for their phase identity and crystallinity. The presence of weak and very broad reflections in the X-ray profiles (Figure 45) reveals that the samples are mostly non-crystalline, which precludes a structural identification of the phases or a determination of the composition and oxygen deficiency in the series of $Mo_{1-x}W_xO_{3-y}$. Only a single reflection can be identified at $2\theta \approx 41$ ° for samples S1, S2 and S3, which might be attributed to traces of remnant Mo_4O_{11} (JCPDS No.13-0142). Additionally, in sample S1 a broad feature centered around $2\theta \approx 35$ ° may be compatible with the (114) reflection of $W_{18}O_{49}$.

Broad reflections centered around $2\theta \approx 13$ ° and 26 ° might be assigned to the (020) and (040) reflections of orthorhombic MoO_3 (JCPDS No. 35-0609). The diffractogram of sample S5 shows four weak, but sharp reflections at $2\theta \approx 29$ °, 41 °, 47 °, and 57 °, which indicate the presence of remnants of Mo_4O_{11}. This suggests that a large excess of Mo precursor leads to preferential formation of non-crystalline and non-stoichiometric MoO_{3-x}, domains while the evolution of WO_{3-x} phases is retained. Although the atomic radii of Mo (134 pm) and W (137 pm) are nearly identical,[42] molybdenum and tungsten form a variety of very distinct non-stoichiometric oxides (Magnéli phases).[76-78] In contrast, the molybdenum ions can be substituted by tungsten over a

wide compositional range in these non-crystalline phases, which prevents the phase separation of crystalline (and also metallic) compounds with Magnéli-type structure.

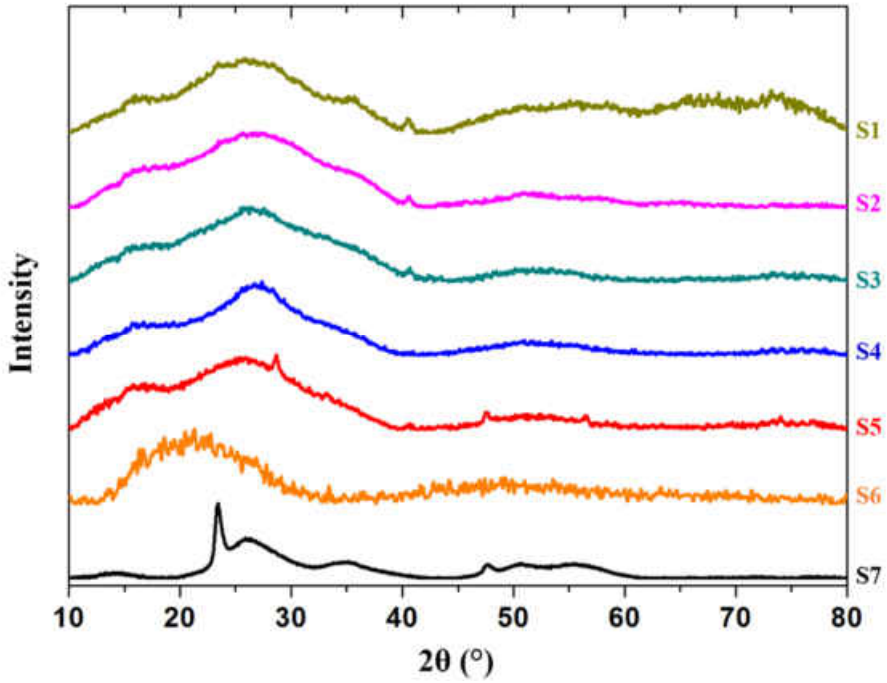

Figure 45. Powder XRD patterns of the as-synthesized molybdenum-tungsten oxides: $Mo_{0.5}W_{0.5}O_{2.1}$ (S1), $Mo_{0.62}W_{0.38}O_{2.3}$ (S2), $Mo_{0.75}W_{0.25}O_{2.4}$ (S3), $Mo_{0.85}W_{0.15}O_{2.6}$ (S4), $Mo_{0.89}W_{0.11}O_{2.7}$ (S5), MoO_{3-x} (S6) and $W_{18}O_{49}$ nanowires (S7).

A clear statement on the incorporation of W into the MoO_{3-x} structure or Mo into the WO_{3-x} structure cannot be made solely on the basis of XRD data. Raman spectroscopy is a valuable tool, because it provides information for non-crystalline phases and allows for an easy discrimination between different localized structural building blocks and different compositions, respectively.

Figure 46 shows Raman spectra of the as-prepared samples. In the sequel, M (= Mo or W) is used to illustrate that in the binary oxides every incorporated W atom can occupy Mo sites and vice versa.

The typical spectra of molybdenum-tungsten mixed oxides (S1–S5) exhibit four main peaks. The two strongest bands, located at 809 and 710 cm^{-1} in S1, can be assigned to the stretching mode of the terminal ν(M=O) bond and stretching vibrations of bridging oxygen atoms ν(O-M-O), respectively. Two additional bands with intermediate intensity in the low wavenumber region (at 260 and 329 cm^{-1}) can be attributed to δ(O-M-O) deformation modes. As the amount of W decreases from 0.538 mmol to 0.044 mmol in samples S1 to S5, the positions of the characteristic bands continuously shift to higher wavenumbers. Interestingly, the terminal W=O stretching mode of $W_{18}O_{49}$ is located at 804 cm^{-1}, while both the stretching vibrations of Mo=O (symmetrical, asymmetrical) in MoO_{3-x} are observed at 819 and 992 cm^{-1}.”””

“It is well known that the $W_{18}O_{49}$ phase has a distorted ReO_3 structure with the largest oxygen deficit with regard to pure WO_3. Due to its nonstoichiometric nature the $W_{18}O_{49}$ structure contains

a wide range of W-O-W bond lengths, thus resulting in the broadening of some Raman bands." ""The Raman spectra of the as-prepared MoO_{3-x} particles is very similar to pure orthorhombic MoO_3. As presented by Lu et al.,[79] laser irradiation on air can induce oxidation and structural transformation of oxygen-deficient compounds to their fully oxidized phase due to the thermal effect.

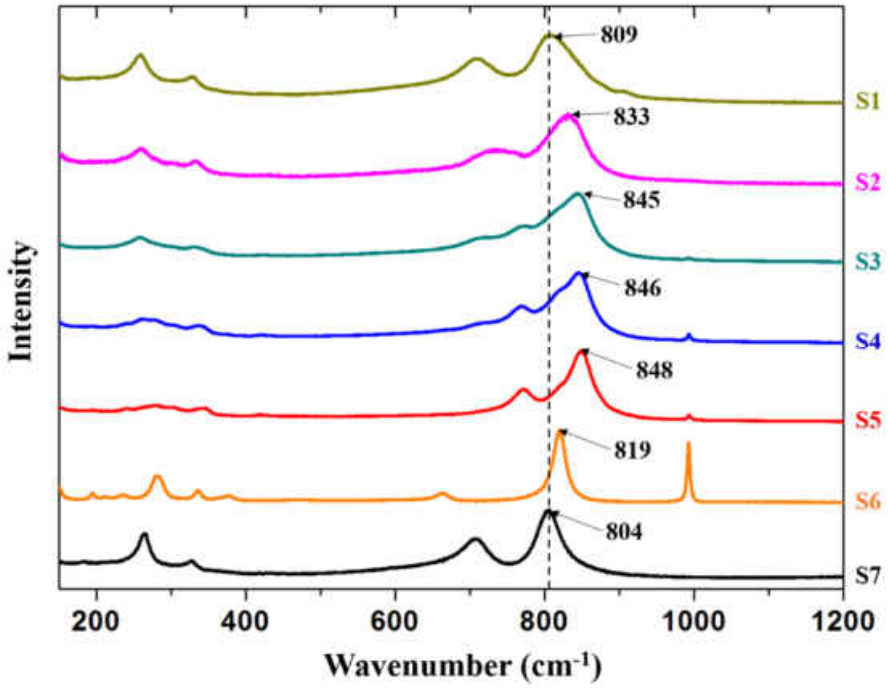

Figure 46. Raman spectra of the as-synthesized molybdenum-tungsten oxides: $Mo_{0.5}W_{0.5}O_{2.1}$ (S1), $Mo_{0.62}W_{0.38}O_{2.3}$ (S2), $Mo_{0.75}W_{0.25}O_{2.4}$ (S3), $Mo_{0.85}W_{0.15}O_{2.6}$ (S4), $Mo_{0.89}W_{0.11}O_{2.7}$ (S5), MoO_{3-x} (S6) and $W_{18}O_{49}$ nanowires (S7).

Thus, it can be concluded that the Raman bands represent a mean value of all possible M=O contributions, and they are gradually blue-shifted upon W substitution. In addition, the profile of the M=O band becomes gradually sharper, and the significant ν_{as}(Mo=O) stretch gains intensity as the molybdenum content in $Mo_xW_{1-x}O_y$ increases. This is in harmony with the results from XRD. All results of the structural characterization obtained by XRD and Raman spectroscopy are summarized in Table A 10 (Appendix).""

To further characterize the structure of the Mo/W oxides pair distribution functions (PDFs) of all as-prepared samples were calculated from the data obtained from synchrotron total scattering measurements. This method allows for the combined analysis of both the Bragg and diffuse components of the scattering. The obtained PDF corresponds to a histogram of the interatomic distances of the substance. Each atom of the sample represents a center, from which all interatomic distances to all other atoms are measured. Summarizing all interatomic distances and projecting them over the radius *r* yields the graphs depicted in Figure 47. Thus, each peak in the histogram corresponds to a distance where neighbouring atoms can be found in the sample.[80-84]

The experimental PDF can be divided into three regions: the short-range (interatomic distances below ~6 Å), the medium-range (6–30 Å) and the long-range (> 30 Å). The short-range region gives information on the first few coordination spheres and therefore mainly contains the information about intramolecular oxide structure and the nearest neighbours in the crystal. The information from the medium and long ranges permits a statement on the periodicity of the particles.

A first interpretation can already be made about the fact that for the mixed oxides and the pure molybdenum oxide no well-defined features above 10 Å can be observed. This reflects the amorphous character of these compounds (which has already been reported with the XRD patterns) and indicates that the range of structural coherence is limited to ~1 nm. As the finite crystallite size diminishes the number of atom pairs separated by distances larger than the crystallite diameter, this consequently leads to abrupt damping of the PDF features.

The first peak observed in the PDFs around $r \sim 1.91$ Å is due to contributions from the nearest neighbours, namely the metal cation (Mo^{6+} or W^{6+}) and the oxygen anion (O^{2-}). However, it is not possible to differentiate between pure Mo-O or W-O bonds since the distances are approximately the same for both oxides and the transition from one atom to the other is quasi-fluid.

The second strong and intense peaks are of metal-metal bonding with distances between 3.76–3.82 Å.[85-90] This signal represents an average of the shortest M-M distances (~3.16 Å) arising from edge sharing of the MO_6 octahedra and the M-M distances at ~3.70 Å resulting from corner sharing of MO_6 octahedra. Smaller peaks can also be observed between 6–8 Å, which are attributed to a second coordination sphere of M-M distances.

All PDFs of the doping series look similar in the short-range region, while a peak at 2.5 Å is becoming more prominent with increasing amount of molybdenum in the product. This indicates that a second Mo-O distance is established as a result of the displacement of corner shared oxygen atoms in the MoO6 octahedra.[91, 92] This is plausible because, with an increasing proportion of molybdenum in the ReO_3-type matrix, this becomes more similar to the MoO_3 structure in the process.

The PDF of $W_{18}O_{49}$ nanowires exhibits well-ordered interatomic correlations in both the short-range and long-range regions. Nonetheless, the peak centered around 3.82 Å (first W-W coordination sphere) is not split into a doublet as it was reported by Saha et al. for pure WO_3 nanoparticles.[89] It can therefore be concluded that the $W_{18}O_{49}$ structure shows significant recurrent dislocations of oxygen atoms resulting in an merging of contributions of edge sharing and corner sharing octahedra, which is in good agreement with the previous findings. The W-O bond distances can be observed at 1.90 Å and 2.14 Å (shoulder),[93] while the peak of the second coordination sphere is found at 5.46 Å.

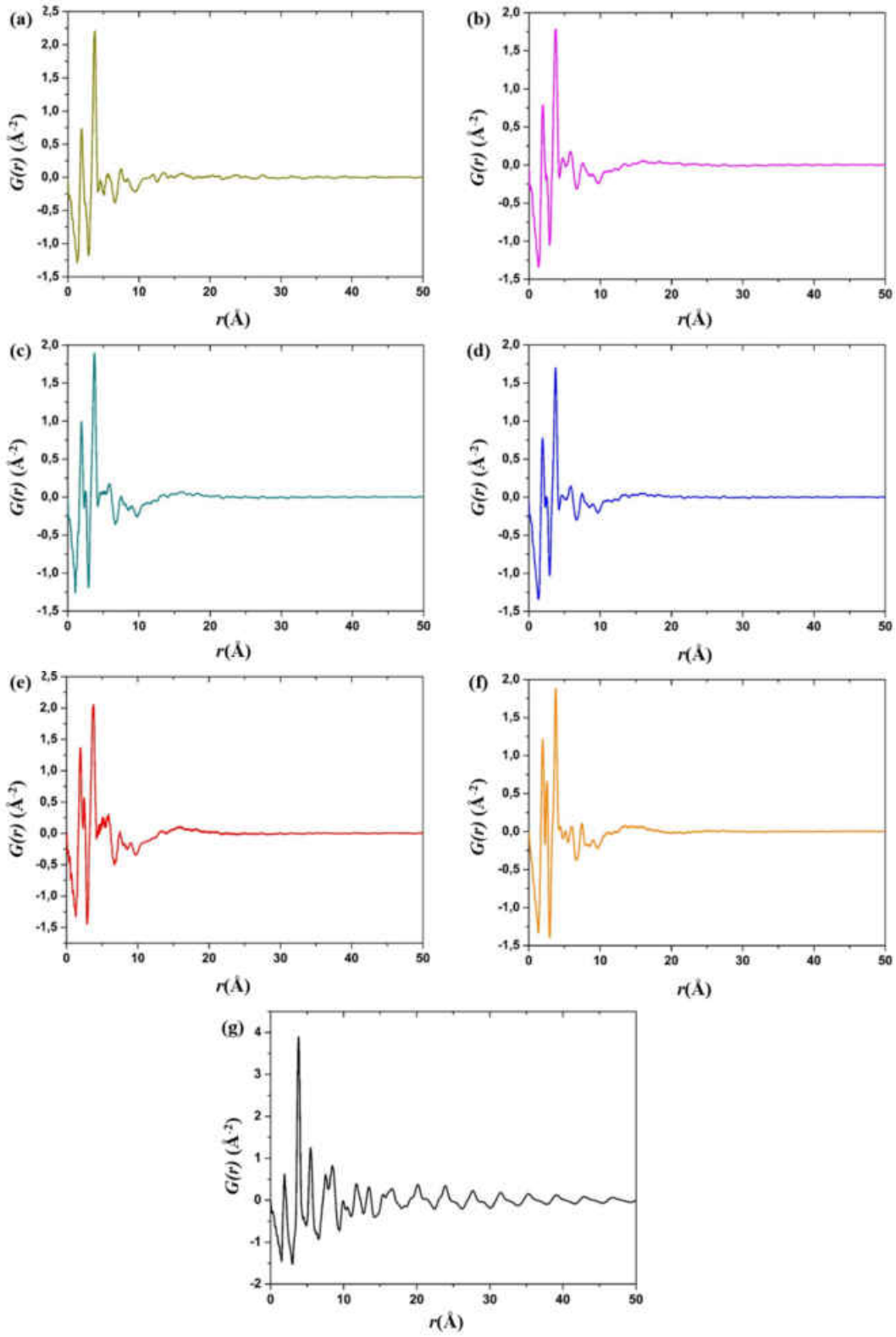

Figure 47. Experimental pair distribution functions of (a) $Mo_{0.5}W_{0.5}O_{2.1}$, (b) $Mo_{0.62}W_{0.38}O_{2.3}$, (c) $Mo_{0.75}W_{0.25}O_{2.4}$, (d) $Mo_{0.85}W_{0.15}O_{2.6}$, (e) $Mo_{0.89}W_{0.11}O_{2.7}$, (f) MoO_{3-x} and (g) $W_{18}O_{49}$ nanowires.

““**Determination of elemental composition.** Furthermore, the effect of W substitution on the oxidation states of MoO_{3-x} in the $Mo_xW_{1-x}O_{3-y}$ molybdenum-tungsten oxide samples was monitored by XPS. The presence of Mo, W, O, and an impurity of C was detected in the XPS

survey spectra (Figure A 152, appendix). C may be attributed to remnants of ethanol adsorbed on the particle surface.

Figure 48 shows the evolution of the W 4f core level region as a function of the Mo content. A spin-orbit doublet with peaks at binding energies of 37.6 ± 0.10 (W $4f_{5/2}$) and 35.5 ± 0.10 eV (W $4f_{7/2}$) characterizes the W 4f core level spectra of the mixed oxides, which can be deconvoluted into contributions from the W^{6+} and W^{5+} oxidation states.

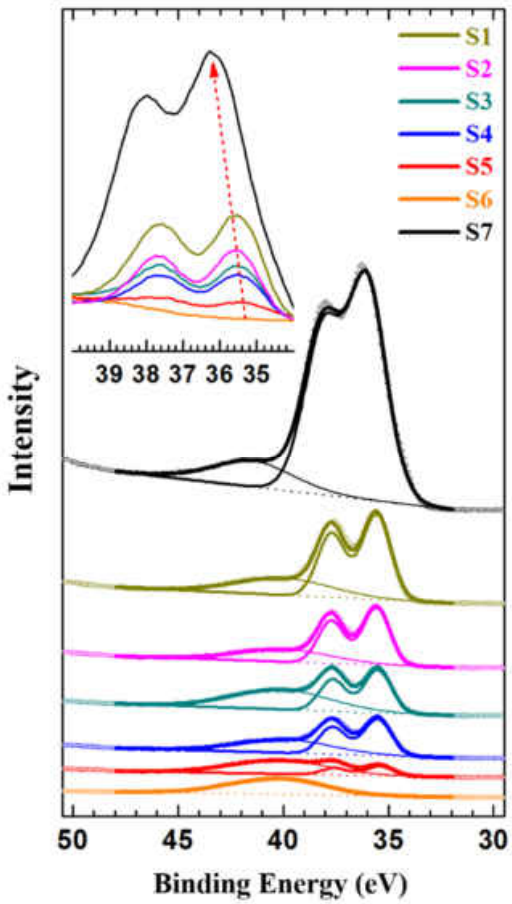

Figure 48. High-resolution XPS spectra of the W 4f core level region of the mixed molybdenum-tungsten oxides $Mo_{0.5}W_{0.5}O_{2.1}$ (S1), $Mo_{0.62}W_{0.38}O_{2.3}$ (S2), $Mo_{0.75}W_{0.25}O_{2.4}$ (S3), $Mo_{0.85}W_{0.15}O_{2.6}$ (S4), $Mo_{0.89}W_{0.11}O_{2.7}$ (S5) and the pure oxides MoO_{3-x} (S6) and $W_{18}O_{49}$ (S7).

As expected, the intensity of the doublet decreases when the Mo content increases, accompanied by a narrowing of the W 4f peaks (from sample S5 to S1). This clearly demonstrates that a substantial amount of the W^{6+} species is consecutively reduced to W^{5+} in the mixed oxides. The broad peak around 41 ± 0.10 eV is attributed to W $5p_{3/2}$, which always can be observed in association with the W 4f peaks.[91]

To determine the relative bulk composition of the particles, EDS coupled with SEM was used. The measurements were conducted over more than 10 positions to obtain reliable information. It appears that molybdenum and tungsten atoms are distributed homogenously in the products.

Moreover, both EDS and XPS confirm the atomic ratio of the Mo host and incorporated W to resemble the proposed composition based on the synthetic setup (Table 6).

*Table 6. Analytically determined elemental compositions and BET surface area of the $Mo_xW_{1-x}O_{3-y}$ microparticles (*at% was determined via EDS; #at% was determined via XPS).*

Sample	*Element$_{EDS}$ (*at%*)	#Element$_{XPS}$ (*at%*)	^Ratio$_{XPS}$ (Mo:W)	Composition$_{EDS}$	BET surface area (m^2/g)
S1	Mo 16.5 W 16.7 O 66.8	Mo 11.2 W 10.9	1:1	$Mo_{0.5}W_{0.5}O_{2.1}$	2.98
S2	Mo 15.5 W 9.6 O 57.7	Mo 12.5 W 10.1	1.3:1	$Mo_{0.62}W_{0.38}O_{2.3}$	1.57
S3	Mo 22.3 W 7.3 O 70.4	Mo 16.5 W 5.8	2.8:1	$Mo_{0.75}W_{0.25}O_{2.4}$	1.49
S4	Mo 23.7 W 4.2 O 72.2	Mo 16.8 W 4.4	3.8	$Mo_{0.85}W_{0.15}O_{2.6}$	0.99
S5	Mo 24.3 W 2.9 O 72.8	Mo 19.3 W 1.3	14.8	$Mo_{0.89}W_{0.11}O_{2.7}$	0.92

Based on the XPS and EDS data a defined composition of the as-synthesized amorphous Mo/W oxides can be calculated. The amount of oxygen in the different samples was determined and, moreover, indicates that the solvothermal synthesis of the microparticles yields oxygen-deficient compounds. As a result, S1 exhibits the structure with the biggest oxygen deficiency, whereas S5 shows considerable higher O saturation. Since the introduction of oxygen vacancies in structures of MoO_3 and WO_3 gives rise to electrical conductivity, it can be concluded that the sub-stoichiometric compounds S1–S5 behave as so-called heavily doped semiconductors.[92]""

Thermal stability of Mo/W oxides. Investigations on the thermal stability of the as-synthesized particles were conducted at three different temperatures. More precisely, all samples were tempered for 1 h in an argon atmosphere at 400 °C, 500 °C or 600 °C, respectively. Furthermore, the temper process is supposed to cause phase separation of the mixed oxides to their appropriate pure phases. Hence, the structures of the tempered samples identified by XRD would supply a statement on the crystal structure of the parent compound.

As can be seen from the TEM images in Figure A 154–Figure A 156 (Appendix), the molybdenum-tungsten and pure MoO_{3-x} microspheres retain their spherical shape, even after tempering at 600 °C. However, an increasing amount of smaller particles can be identified in the samples with a higher amount of tungsten. This indicates clearly, that a phase separation of molybdenum oxide and tungsten oxide takes place at elevated temperatures. Furthermore, the tempered $Mo_{0.5}W_{0.5}O_{2.1}$ and $Mo_{0.75}W_{0.25}O_{2.4}$ show a surface decoration with plate-like particles. On the other hand, the $W_{18}O_{49}$ nanowires are more agglomerated after tempering at 500 °C and

completely lose their morphology after heat treatment at 600 °C (Figure A 156, appendix). The EDS measurements of the $Mo_{0.5}W_{0.5}O_{2.1}$ further confirm the decrease of tungsten concentration in the spherical mixed oxides particles (Figure A 153 and Table A 11, appendix) and the accumulation of tungsten in the smaller particles.

The XRD patterns in Figure A 157–Figure A 159 also show phase separation and crystallisation of the mixed oxides samples with higher temperature. The $W_{18}O_{49}$ continuously transforms to pure monoclinic WO_3, whereas the as-synthesized MoO_{3-x} disaggregates into three different phases (tetragonal MoO_2, orthorhombic Mo_4O_{11} and orthorhombic MoO_3). The Raman spectra of the tempered samples first show a narrowing of the stretching vibrations of Mo=O compared to the untreated compounds (Figure 160). With increasing temperature the spectra show more pronounced shoulders and additional bands in the terminal stretching vibrations region (> 700 cm^{-1}).

4.3.2. Application as Photoelectrocatalyst

“‘‘Photoanodes and the working electrode were fabricated by dip coating. FTO electrodes (1·2 cm^2) were used as conducting substrates. For the preparation of each photoelectrode 20 mg of catalyst were dissolved in 2 mL of ethanol under vigorous sonication to obtain a homogenous mixture. Next, 0.5*v*% of Nafion® was added to the mixture to achieve a stable deposition of the catalysts on the substrate. The photoelectrodes were immersed in the electrolyte and kept there for 5 min to build the charge equilibrium before starting the photoelectrochemical measurements. For reasons of clarity, in the following only the results of the mixed oxides microspheres will be discussed in detail. The results obtained from the measurements of the pure oxides are referred to in the discussion, for the plotted data can be found in the appendix (Figure A 164–Figure A 166). The PEC water splitting function of $Mo_xW_{1-x}O_{3-y}$ photoanodes was evaluated photoelectrochemically using voltammetry and chronoamperometry. Current−voltage (*I-V*) curves were achieved by linear sweeping voltammetry (LSV). The range of sweep voltage ranges from 0.00 V to 1.50 V (SCE) in the dark and light (Figure 49).

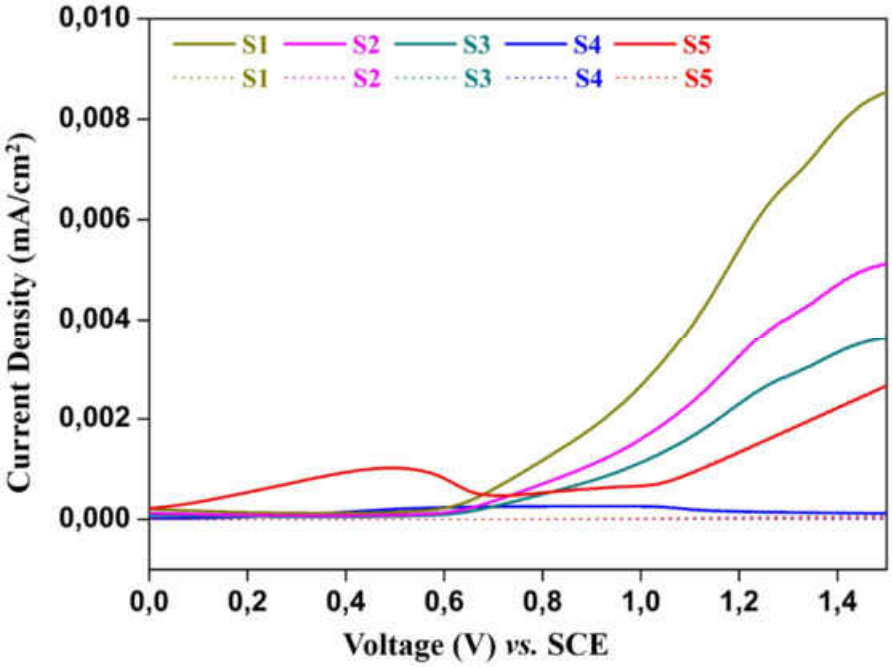

Figure 49. Photocurrent-voltage responses measurements vs. SCE for the $Mo_xW_{1-x}O_{3-y}$ molybdenum-tungsten oxide microsphere electrode, under a potential of 1.23 V.

The dotted lines correspond to the dark current of the photoanodes, which is negligible even at higher voltage as no significant dark current was observed. On the other hand, a significant photocurrent was generated under light irradiation. This shows that $Mo_xW_{1-x}O_{3-y}$ photoanodes are active under light and therefore efficiently split water in the given voltage range. For all photoanodes the onset potential was observed beyond 0.6 V. Subsequently, the current shows a significant elevation with voltage.

The best photocurrent character was observed for the photoanode with composition $Mo_{0.5}W_{0.5}O_{2.1}$ (S1), the most oxygen-deficient mixed metal oxide. The optimum composition maximizes the charge carrier density that compensates for recombination, which is likely to occur radiatively by an electron-hole pair at a defect in the non-crystalline material. Alternative pathways could be non-radiative by self-trapping of a free exciton or by tunneling between defects. Moreover, $Mo_{0.5}W_{0.5}O_{2.1}$ microspheres showed the best optical performance by strongly absorbing in the UV and NIR (Figure 50). The optical behavior, i.e. the band gap relative position of the valence and conductance band, can be tuned by substitution in the $Mo_xW_{1-x}O_{3-y}$ solid solution series.[93, 94]

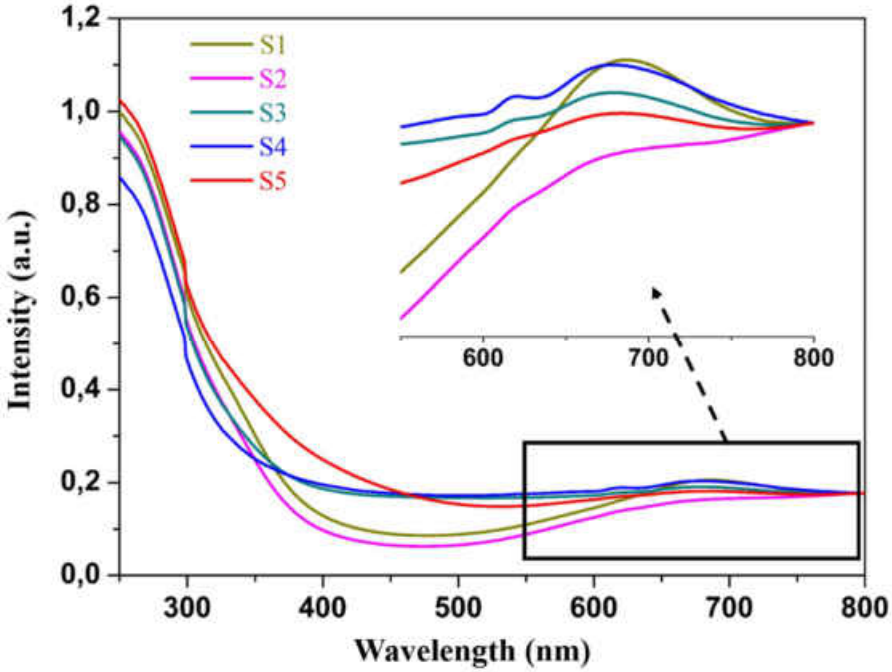

Figure 50. UV-VIS absorbance spectra of $Mo_xW_{1-x}O_{3-y}$ molybdenum-tungsten oxide microparticles dispersed in water.

The photocurrents for S1, S2, S3, S4, and S5 were 5.25, 3.6, 3.1, 0.9, and 1.75 mA/cm^2, at the thermodynamic water oxidation voltage of 1.23 V. The periodic ON-OFF current-time (*I-t*) graph in Figure 51 was derived from chronoamperometric measurements of the photoanodes at the water oxidation potential (i.e., 1.23 V), while the light ON/OFF periodicity was maintained at ~20 s. The graphs clearly indicate that in the absence of light the photocurrent drops off to the base line as no current is generated photocatalytically or electrocatalytically, even at high potential. The photocurrent strongly increased under illumination for all photoanodes, which indicates photocurrent generation for the $Mo_xW_{1-x}O_{3-y}$ molybdenum-tungsten oxides under solar light. The photocurrent was maintained during periodic light chopping as observed in the LSV.

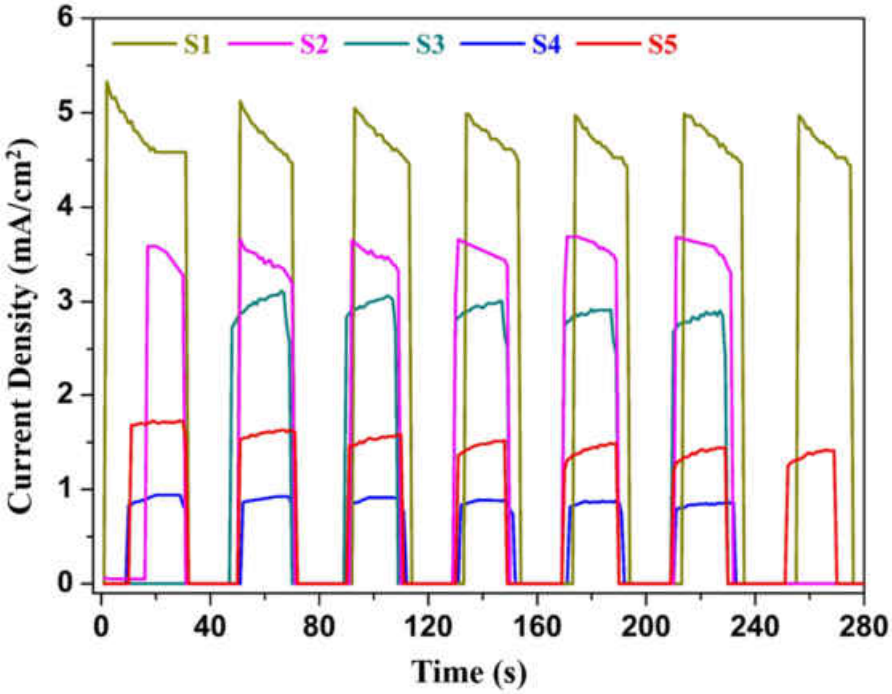

Figure 51. Photocurrent-time responses of the mixed oxides under chopped 1 SUN illumination in 0.5 M Na_2SO_4 electrolyte solution.

Many cycles were measured to analyze the performance of the photoelectrodes. Thus, even after multiple cycles the photocurrent values are stable. To further confirm the stability of the photoanodes, a long-term stability test was performed for 2000 s (Figure 52).

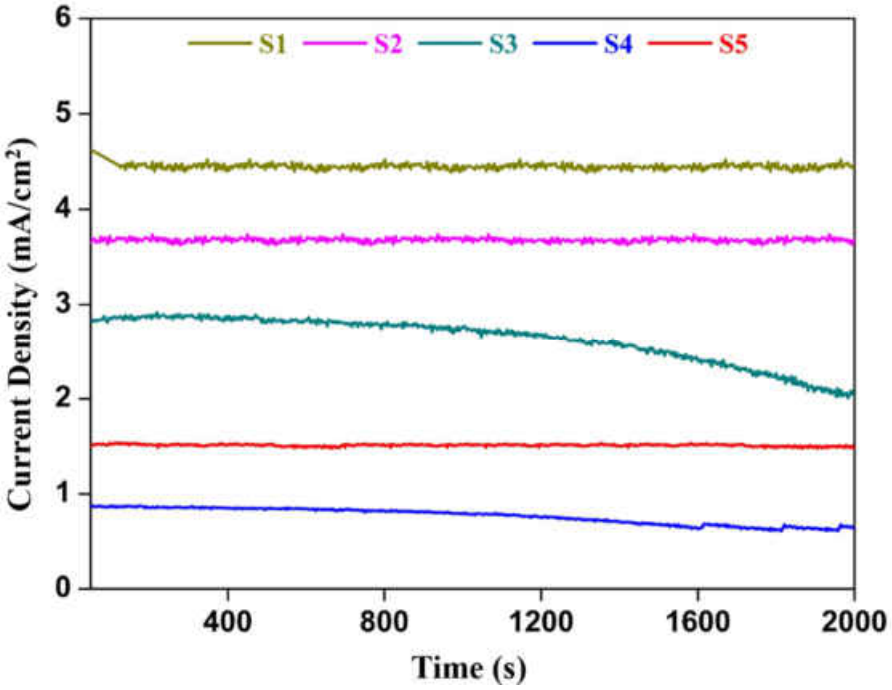

Figure 52. Chronoamperometry analysis of the as-prepared photoanodes, performed for 2000 s.

As expected, the higher current density was maintained by the $Mo_{0.5}W_{0.5}O_{2.1}$ (S1) photoanode. A negligible photocurrent drop was observed, which shows the efficiency and resilience of $Mo_{0.5}W_{0.5}O_{2.1}$ against chemical processes at the interface in the electrolyte.

The PEC water splitting results clearly indicate that the $Mo_{0.5}W_{0.5}O_{2.1}$ photoanode shows the highest photocurrent, the best long-term stability and overall performance. This can be attributed to the number of charge carriers, as $Mo_{0.5}W_{0.5}O_{2.1}$ shows the highest degree of reduction. The optimum amount of component minimizes the charge recombination, and enhances the valence and conductance band separation to suitable levels. [95] The additional charge carriers lead to an enhanced absorption in the visible and particularly the NIR range through the plasmon excitation.[96, 97]”””

4.3.3. Application as Sulfoxidation Catalyst

Experimental procedure. The as-synthesized molybdenum-tungsten mixed oxides and their pure oxide counterparts were investigated as to their catalytical performance in the sulfoxidation reaction. Conversion measurements to the appropriate sulfoxide or sulfone were conducted for a variety of organic sulfides, whereby methyl phenyl sulphide (thioanisole) was chosen to be the model compound for detailed kinetic measurements due to its well-balanced physico-chemical properties: low melting-point and low volatility (to maintain a constant concentration of substrate in the reaction vessel over a long time), an anisotropic shielding of the sulfur atom (to provide for a medium reaction time, which allows easy recording of kinetics) and a sufficiently good solubility of the substrates in water.

The kinetic studies were performed over 1 h reaction time after adding H_2O_2 as the oxidizing agent. For that, NMR spectra were recorded with an interval of one minute. All reactions were carried out in NMR tubes containing the sulfide, 3-(trimethylsilyl) propionic acid (TMSP), 1 and 3 eq H_2O_2, respectively, and the appropriate microparticles or nanoparticles. The reaction solution was filled up to 700 µL with deuterated water (D_2O). The TMSP resonance was manually set to a chemical shift of 0 ppm to standardize the NMR spectra.

In order to retain a good overview, in the following only the results of the $Mo_{0.5}W_{0.5}O_{2.1}$ will be discussed in detail. The data of all other sulfoxidations can be found in the appendix.

Reference measurements of thioanisole. Due to the binding of additional electron-withdrawing oxygen to the sulfur atom, the protons of the methyl group of the appropriate sulfide are deshielded to a greater extent. While the methyl signal of thioanisole (TA) appears at 1.87 ppm, the methyl resonance of the sulfoxide (MPSO) is shifted to lower fields occurring at 2.91 ppm and the signal of the methyl group of the sulfone (MPS) can be found at 3.28 ppm (Figure 53).

Therefore, the oxidation of thioanisole with hydrogen peroxide catalysed by MPs can be monitored directly by means of NMR spectroscopy.

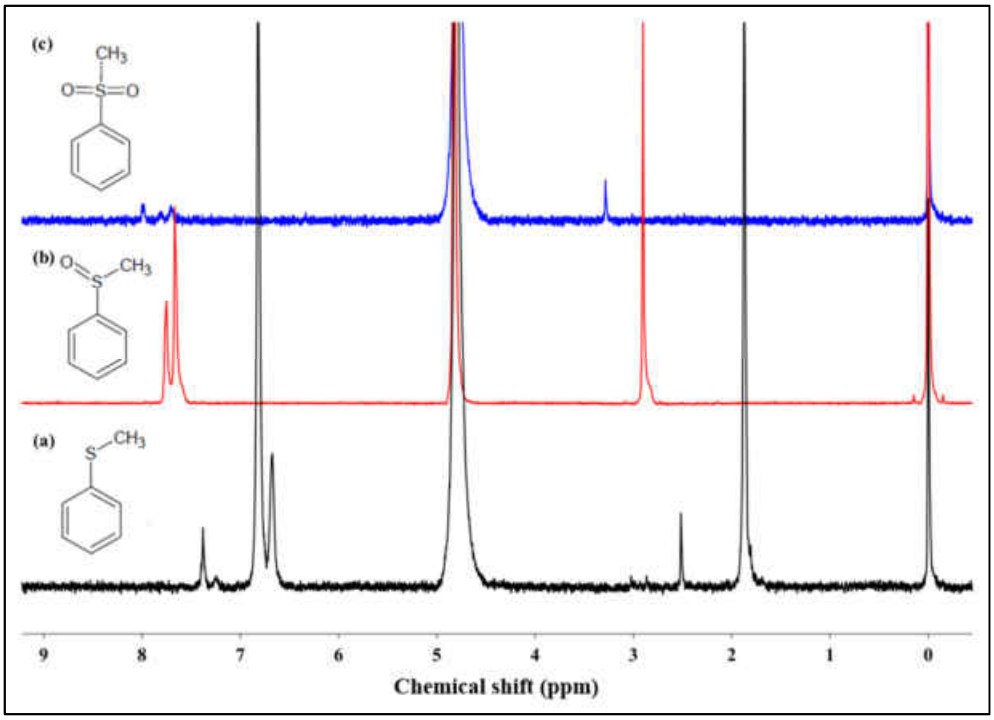

Figure 53. NMR-spectra of the reference compounds measured in D_2O as solvent: (a) thioanisole, (b) methyl phenyl sulfoxide and (c) methyl phenyl sulfone. The insets show the chemical structure of the appropriate compounds.

The signal at 4.75 ppm can be attributed to residual water. It is noteworthy that an emulsion of thioanisole in water always shows pairs of signals with the same multiplicity, but shifted to lower fields. This can be explained by the low miscibility of thioanisole and water, whereby the TA experiences two different chemical environments in the organic or aqueous phase, respectively. All identified signals are summarized in Table 7.

Table 7. ^{1}H-NMR signals of thioanisole, sulfoxide and sulfone obtained from the spectra shown in Figure 53.

Compound	Chemical shift (ppm)	Annotation
Methyl phenyl sulfide	1.87	organic phase (o. p.)
	2.51	aqueous phase (a. p.)
	6.67	o. p.
	6.82	a. p.
	7.25	o. p.
	7.38	a. p.
Methyl phenyl sulfoxide	2.91	a.p.
	7.65	a.p.
	7.75	a.p.
	7.77	a.p.
Methyl phenyl sulfone	3.28	a.p.
	7.68	a.p.
	7.98	a.p.
	8.00	a.p.

Oxidation of thioanisole. It is well known that the oxidation of thioanisole can be controlled by the molar amount of H_2O_2 added to the reaction mixture, while no elevated temperature is needed. Although TA is oxidized by H_2O_2 already, the conversion to the sulfoxide is significantly accelerated by catalytical amounts of transition metal oxides, e.g. MoO_3 (Figure 54). An excess of the oxidizing agent enables full oxidation to the appropriate sulfone, but an addition of catalyst is mandatory. Otherwise, the conversion stops at the sulfoxide product.

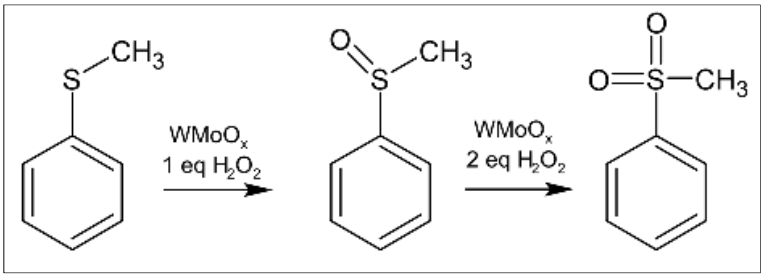

Figure 54. Scheme of the sulfoxidation reaction of thioanisole to methyl phenyl sulfoxide and methyl phenyl sulfone using H_2O_2 and the Mo/W mixed oxides as catalyst, respectively.

The general mechanism of a sulfoxidation reaction is sketched in Figure 55. The reaction starts by the sulfur atom of the sulfide (A) being attacked by the terminal oxygen of the peroxide group (B). As a result, a break in the peroxide bond is induced, forming a sulfoxide protonated on the sulfur atom (C) and an alkoxy anion (D). The sulfoxide (E) and the alcohol (F) corresponding to the peroxide are finally formed under proton exchange. Oxidation of sulfoxide to sulfone follows the same mechanism, if performed in acidic or neutral solution. In basic medium, however, a nucleophilic attack of peroxy anions (G) at the sulfur atom yields a peroxo sulfone (H). The cleavage of the leaving group then provides the sulfone and the alkoxy ion.[98]

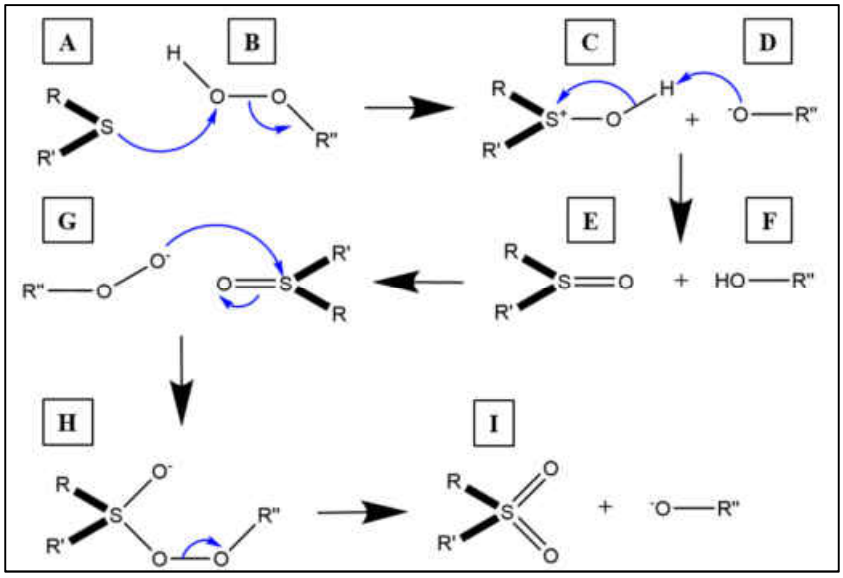

Figure 55. Reaction mechanism of the oxidation of sulfides (A) to sulfoxides (E) and sulfones (I) using peroxides (B) as oxidizing agent.

The reactions sketched in Figure 54 were verified by performing three measurements (directly after addition, after 24 h and after 48 h) per each molar ratio of sulfide to H_2O_2. The ^{1}H-NMR spectra of the oxidation of thioanisole with 1 eq H_2O_2 are shown in Figure 56.

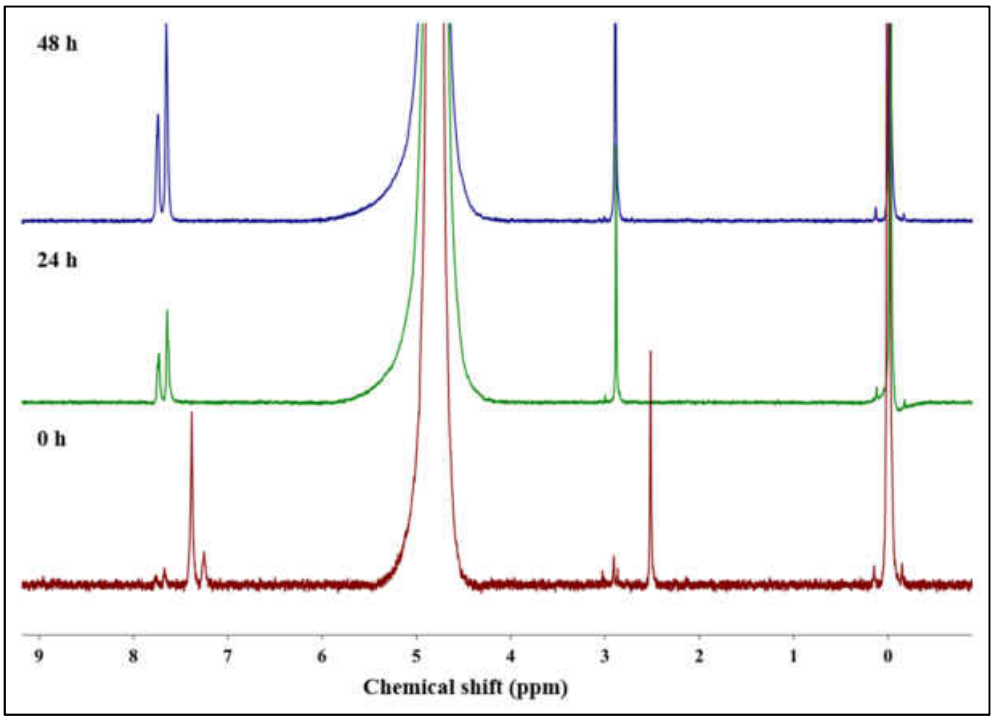

Figure 56. ^{1}H-NMR spectra of the oxidation of thioanisole by 1 eq H_2O_2, shown after different periods of time.

Without the addition of any catalyst, after 48 h reaction time the conversion of MPSO to MPS does not proceed. However, after 24 h full conversion to MPSO and no remnant of thioanisole is detected in the reaction mixture. The same results are obtained with 3 eq H_2O_2 (Figure 57), thus suggesting that even an excess of H_2O_2 cannot accomplish oxidation of TA to MPS within 48 h.

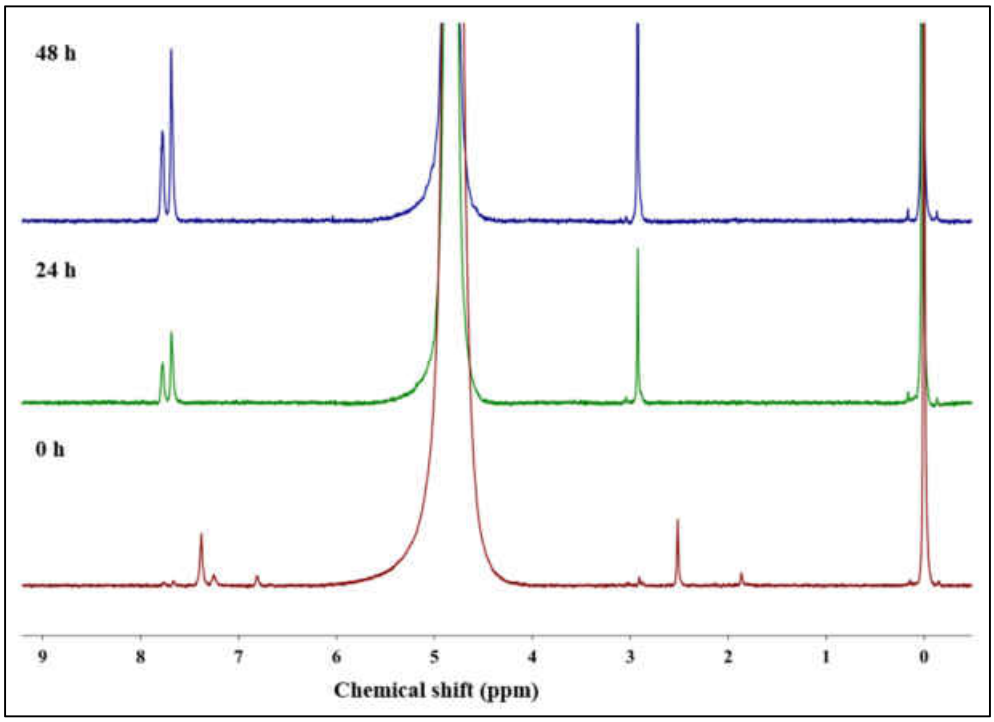

Figure 57. ^{1}H-NMR spectra of the oxidation of thioanisole by 3 eq H_2O_2, shown after different periods of time.

To investigate how big the impact of a catalyst on the conversion time is, kinetic measurements with $Mo_{0.5}W_{0.5}O_{2.1}$ microparticles as catalyst were conducted for 1 h. These particles had been found to be the most effective of all the compounds tested in the previous experiments and were thus selected for further oxidation experiments. The kinetic studies of all other mixed oxides are presented in Figure A 164–Figure A 172 in the appendix.

Figure 58 illustrates the evolution of the ^{1}H-NMR spectra of MPSO after the addition of 1 eq H_2O_2 to a suspension of TA and $Mo_{0.5}W_{0.5}O_{2.1}$ in D_2O. Here, TA is consumed completely within 30 min while only MPSO and no MPS is formed. The same effect can be observed if 0.5 eq H_2O_2 are used for oxidation, while the reaction rate is slightly decreased (Figure A 167, appendix). A full conversion of TA to MPSO is achieved within 50 min in that case.

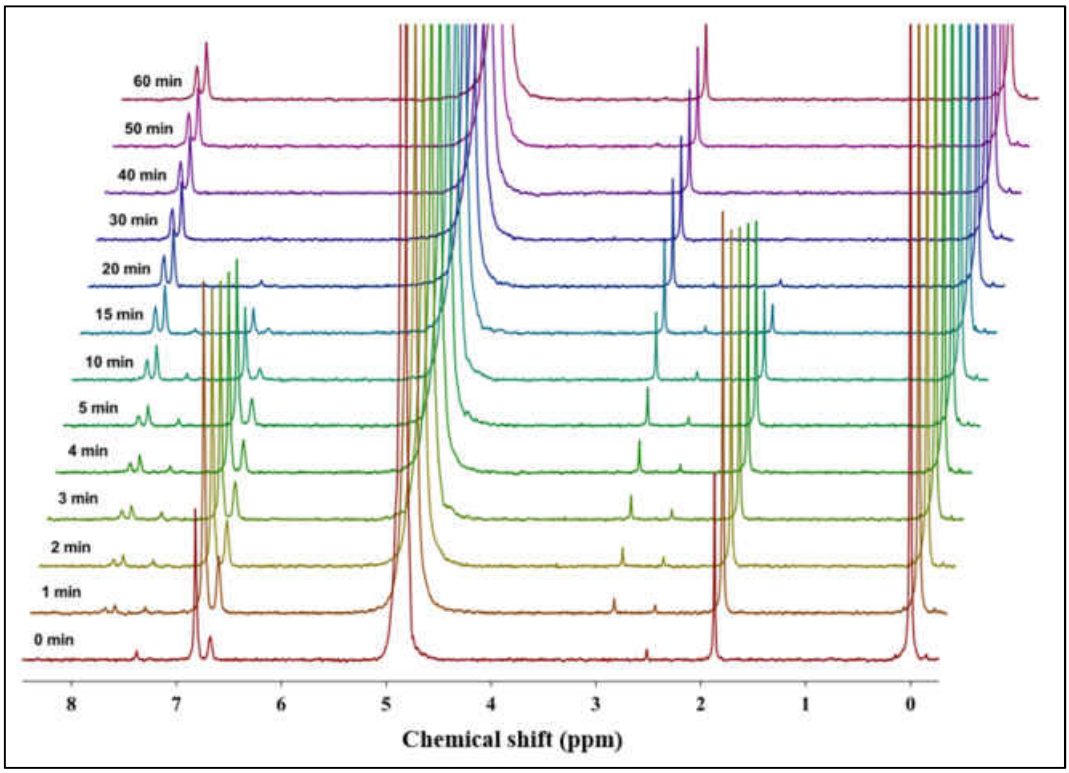

Figure 58. ^{1}H-NMR spectra of the oxidation of thioanisole by 1 eq H_2O_2 and $Mo_{0.5}W_{0.5}O_{2.1}$ microparticles as catalyst, shown after different periods of time.

Interestingly, with 3 eq H_2O_2 and $Mo_{0.5}W_{0.5}O_{2.1}$ catalyst the reaction also stops at the MPSO step. The formation of MPS thus seems to be inhibited (Figure 59). Although TA is consumed completely within 4 min, no further oxidation to MPS can be observed over time.

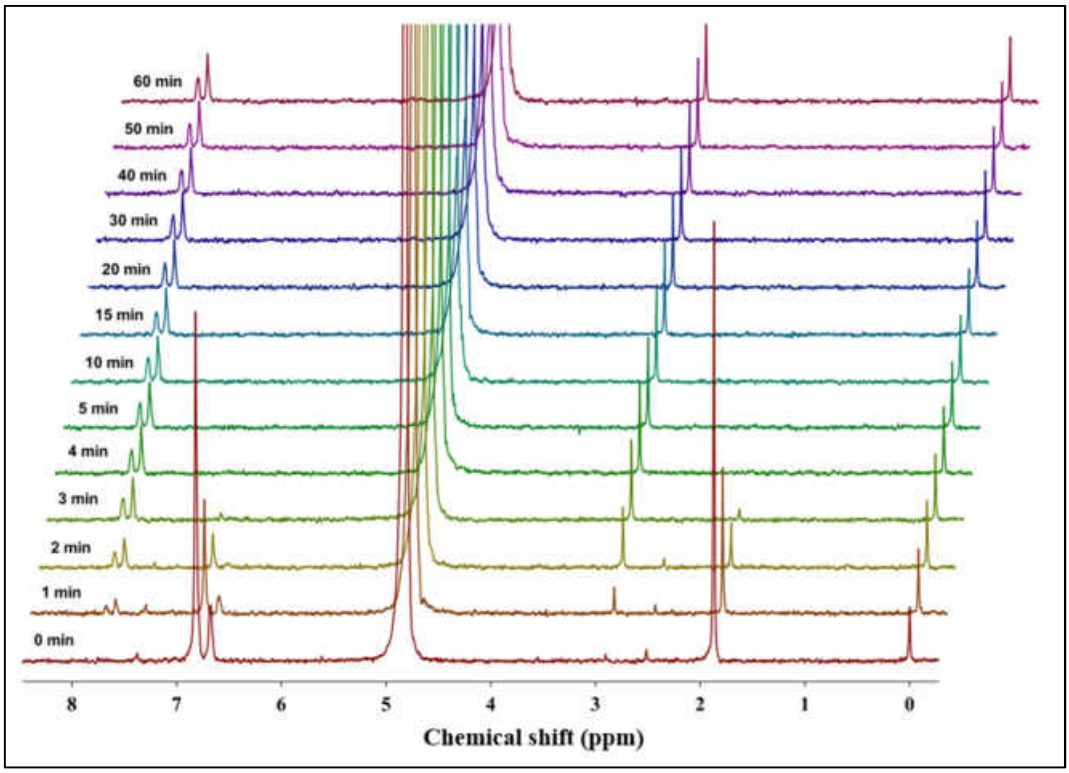

Figure 59. ^{1}H-NMR spectra of the oxidation of thioanisole by 3 eq H_2O_2 and $Mo_{0.5}W_{0.5}O_{2.1}$ microparticles as catalyst, shown after different periods of time.

To investigate whether the oxidation to MPS with the molybdenum-tungsten oxide is possible in the first place, the ^{1}H-NMR spectra of the reaction mixture were measured after 24 h and 48 h (Figure 60). Hence, after 24 h no TA signal can be found and the sulfoxide-to-sulfone ratio is at 40:60. After 48 h the conversion of the MPSO to MPS is almost completed, the sulfoxide-to-sulfone ratio being 6:94. Moreover, directly after the addition of H_2O_2 to the reaction mixture the TA:MPSO ratio is already at 49:51. This fact indicates that the oxidation of TA initially is of a higher speed and is retarded due to a deactivation of the particles activity.

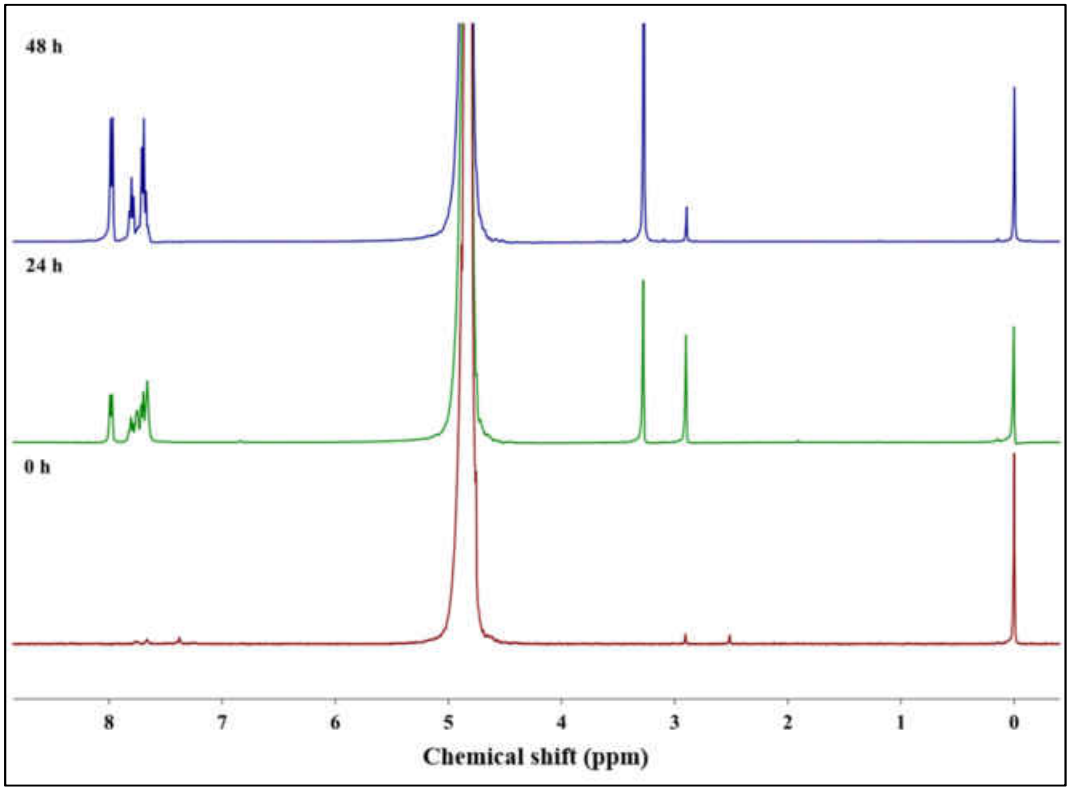

Figure 60. ^{1}H-NMR spectra of the reaction mixture of TA with 3 eq H_2O_2 and $Mo_{0.5}W_{0.5}O_{2.1}$ microparticles as catalyst, after 24 h and 48 h reaction time.

This phenomenon might be explained by the oxidation of the particles' surface, as many reports already have described the sensitivity of sub-stoichiometric molybdenum and tungsten oxides to oxidation by air or by oxygen dissolved in water.[99-104] Therefore, the process sketched in Figure 61 is proposed for the reaction mechanism of sulfoxidation using $Mo_xW_{1-x}O_{3-y}$ compounds, which may explain the inhibition of the oxidation to MPS. Therefore, the oxygen-deficient particles feature many surface defects (Figure 44 d), where the reactive peroxide species can attack. The additional oxygen in the aqueous solution incorporates into the defect sites and thus provides for a healing of the defects. Since now less adhesion surface for catalysis and the coupling of sulfide reagent and oxidic substrate is obtainable, the further oxidation is significantly delayed.

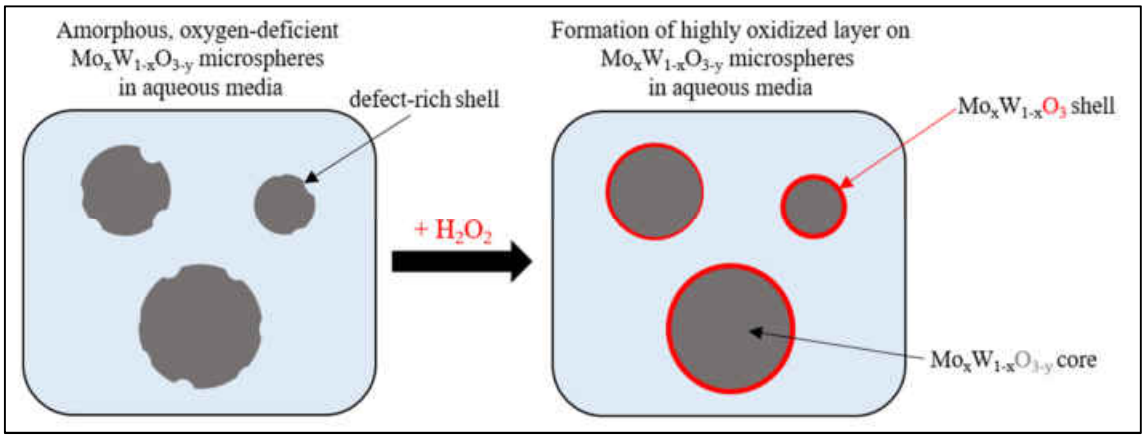

Figure 61. Sketch of the proposed deactivation-oxidation process on the $Mo_xW_{1-x}O_{3-y}$ microparticles surface.

Nonetheless, the mixed oxides particles' reactivity significantly exceeds the one of the pure oxides. In Figure 62, the conversion of TA over time for 1 eq H_2O_2 and MoO_{3-x} particles as catalyst is shown. Obviously, after 60 min reaction time, still over 43% TA was not oxidized. Even after 48 h, a mixture of all three possible compounds (1.8% TA, 47% MPSO and 51.2% MPS) is present and, thus, no full conversion is achieved (Table A 12–Table A 14, appendix).

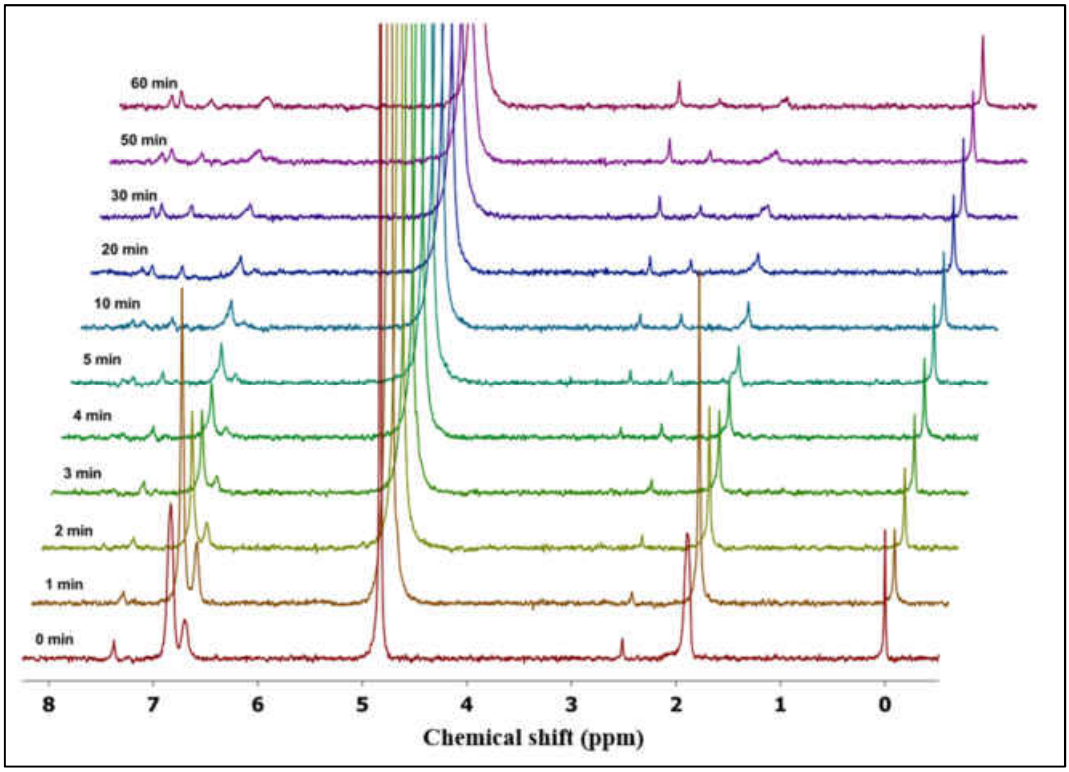

Figure 62. ^{1}H-NMR spectra of the oxidation of thioanisole by 1 eq H_2O_2 and MoO_{3-x} microparticles as catalyst, shown after different periods of time.

The catalytical effect of $W_{18}O_{49}$ nanowires is even worse, exhibiting 48% of unreacted TA and almost evenly distributed portions of 27.1% MPSO and 24.9% MPS, respectively (Figure 63). This suggests that the tungsten suboxide is more sensitive to oxygen than its molybdenum

counterpart. This sensitivity of tungsten oxide (due to its defect-rich structure) to various gas compositions has already been demonstrated in many reports.[105-109]

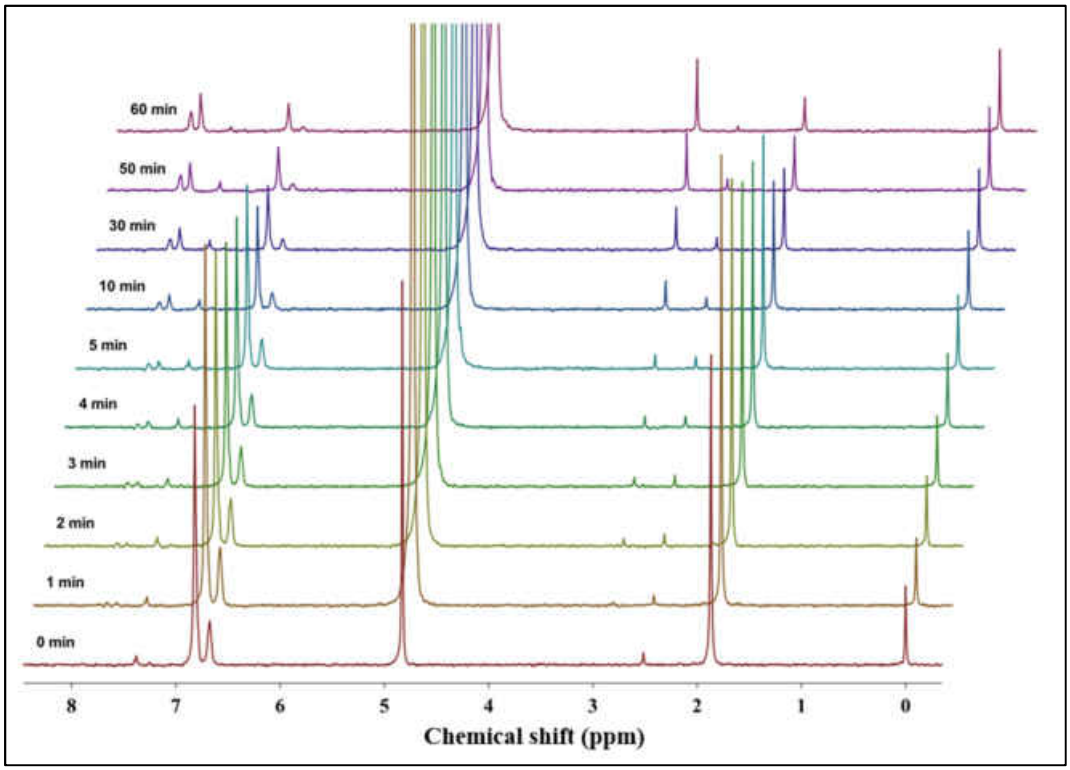

Figure 63. ^{1}H-NMR spectra of the oxidation of thioanisole by 1 eq H_2O_2 and $W_{18}O_{49}$ nanowires microparticles as catalyst, shown after different periods of time.

Figure 64 provides an overview of the sulfoxidation results of the three different catalysts discussed above. It thus underlines the improved catalytical activity of the $Mo_{0.5}W_{0.5}O_{2.1}$ microparticles compared to the pure tungsten oxide nanowires ($W_{18}O_{49}$) and the molybdenum oxide microspheres (MoO_{3-x}). If only the mixed oxides are considered, it is obvious to explain the higher activity of the $Mo_{0.5}W_{0.5}O_{2.1}$ with its BET surface area (compared to that of the other mixed oxides). However, since the measured values are all close to one another and are almost identical in terms of possible error in adsorbent mass, the higher activity cannot be explained by the BET surface solely (Table 6). Rather, several effects have to be considered here.

Thus, the markedly reduced activity of the $W_{18}O_{49}$ can be attributed to the high lability of this compound towards oxidation. Since these are the only nanoparticles in the test, and in these cases the surface-to-volume ratio is known to be higher than for microparticles, more (relative) surface is subjected to the attack by the oxidative reagent. The oxidation of the particles thus progresses faster, which can also be observed at the macroscopic level by a distinct fading of the blue color. Nonetheless, the catalytic activity of the $W_{18}O_{49}$ is significantly higher than that of the pure molybdenum oxide, since here a reaction of 50% is achieved only after 50 min. In this case, the larger surface of the nanowires, despite the oxidation sensitivity of the tungsten oxide, favors the faster conversion of the TA to MPSO.

In the case of the $Mo_{0.5}W_{0.5}O_{2.1}$ both factors (oxidation sensitivity and surface area) seem to have minor effects, since the conversion rate here is significantly higher than for both pure oxides. From this it can be concluded that the chemical stability of the mixed oxides greatly benefits from the incorporation of W-ions into the MoO_3 lattice. The structure-stabilizing effect of doping on the MoO_{3-x}-based catalysts was already reported, while the foreign cation not necessarily has to be tungsten.[110-118] According to this, the substitution of the host ion prevents the formation of crystalline phases and favors a disordering of the structure. This trend can also be deduced from the series of mixed oxides produced, since a decreasing conversion rate is obtained upon reduction of the tungsten content in the solid solutions of $Mo_{1-x}W_xO_y$ (Figure 163–Figure A 172). The only exception is $Mo_{0.89}W_{0.11}O_{2.7}$, which has to be assessed between the $Mo_{0.62}W_{0.38}O_{2.3}$ and $Mo_{0.75}W_{0.25}O_{2.4}$.

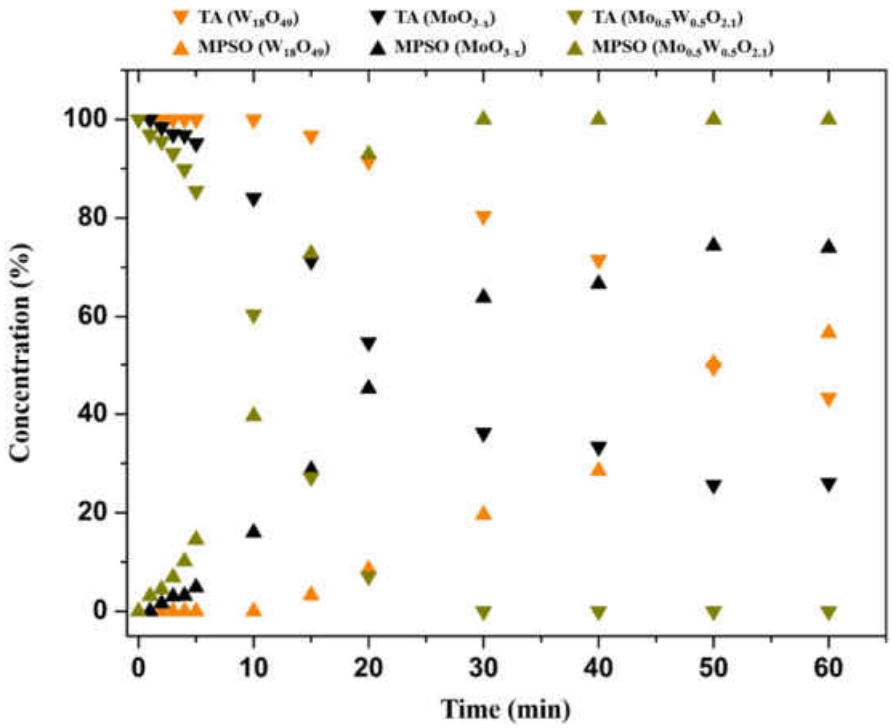

Figure 64. Evolution of the concentrations of reactant and product species during the oxidation of TA with 1 eq and the appropriate Mo/W oxide catalyst.

In contrast to $W_{18}O_{49}$, for the mixed oxides and the MoO_{3-x} microparticles no colour change can be observed. Furthermore, TEM measurements of the particles extracted from the reaction mixture after 48 h show that the tungsten oxide nanowires exhibit a well-ordered structure (Figure 65 a), while both the MoO_{3-x} and $Mo_{0.5}W_{0.5}O_{2.1}$ microparticles do not exhibit any structural changes (Figure 65 b and c).

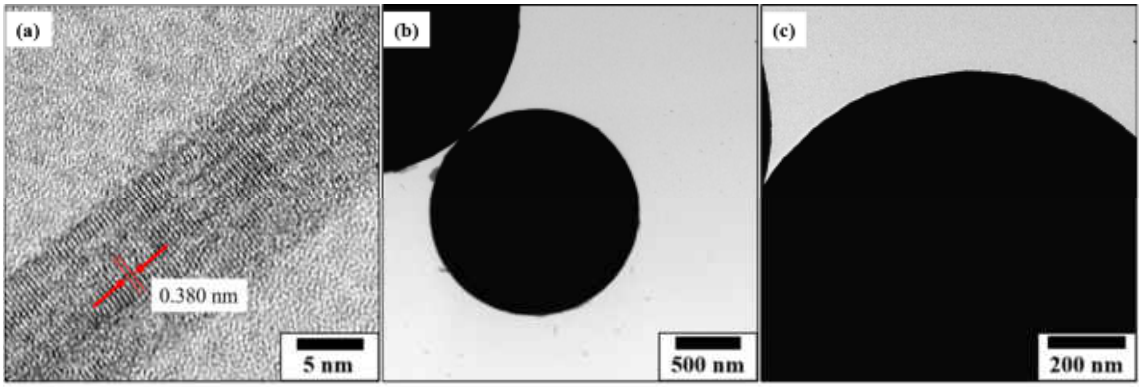

Figure 65. (a) HR-TEM image of the $W_{18}O_{49}$ nanowires, (b) low-magnification TEM image of the MoO_{3-x} microparticles and (c) TEM image of a single $Mo_{0.5}W_{0.5}O_{2.1}$ microparticle after 48 h reaction time.

The XRD patterns of the catalyst particles, which were extracted from the reaction solution after 48 h, are shown in Figure 66. The comparison with the diffractograms from Figure 45 clearly shows that both the mixed oxide and the pure molybdenum compound did not change structurally after use in the oxidative environment. This is different for the tungsten oxide nanowires. Here, additional sharp reflections can be observed at 2θ-values of 14.1, 18.3, 28.2, 36.7 and 50.1°, which can all be assigned to contributions of (100), (111), (200), (201), (202) and (221) plane of the WO_3 phase.[119]

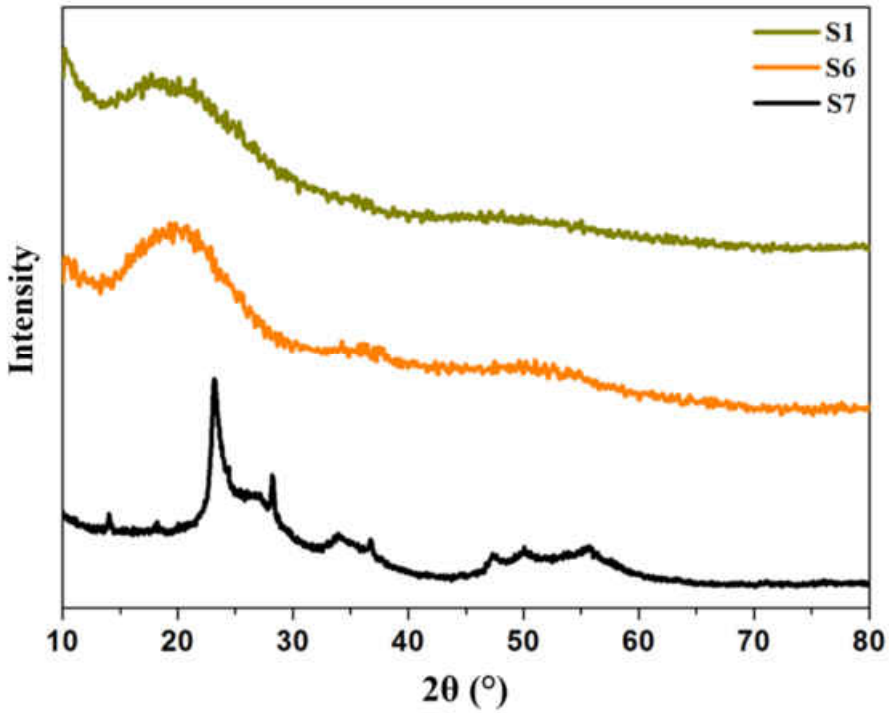

Figure 66. XRD patterns of the particles after 48 h reaction time: (S1) $Mo_{0.5}W_{0.5}O_{2.1}$ microparticles, (S6) MoO_{3-x} microparticles and (S7) $W_{18}O_{49}$ nanowires.

Oxidations of other sulfides with $Mo_{0.5}W_{0.5}O_{2.1}$ particles. The $Mo_{0.5}W_{0.5}O_{2.1}$ microparticles were further tested on their catalytical behaviour in the oxidation of dimethyl sulfide, (methylthio)acetic acid and 2-(methylthio) ethanol. Figure 67 shows the evolution of the ^{1}H-NMR spectra of the oxidation of dimethyl sulfide (CH_3-singlet at 2.1 ppm). The main product dimethyl sulfoxide (CH_3-singlet at 2.7 ppm) is obtained within 1 min, and no remaining signal of the dimethyl sulfide can be observed. Furthermore, the signal of both the methyl groups of dimethyl sulfone at 3.1 ppm, which is detected after 5 min reaction time, continuously gains intensity. After 60 min, almost 13% dimethyl sulfone are found in the mixture. The considerably shorter conversion time needed to form the sulfoxide compared to that of the thioanisole can be attributed to the markedly less pronounced steric shielding of the sulfur atom. Thus, the attack of the oxidative species is facilitated. Owing to the already bound oxygen, the oxidation of the sulfoxide-product to the sulfone-product proceeds by orders of magnitude more slowly. Thus, the electronic and steric influences of the various substrates can be traced more detailed on the given time scale.

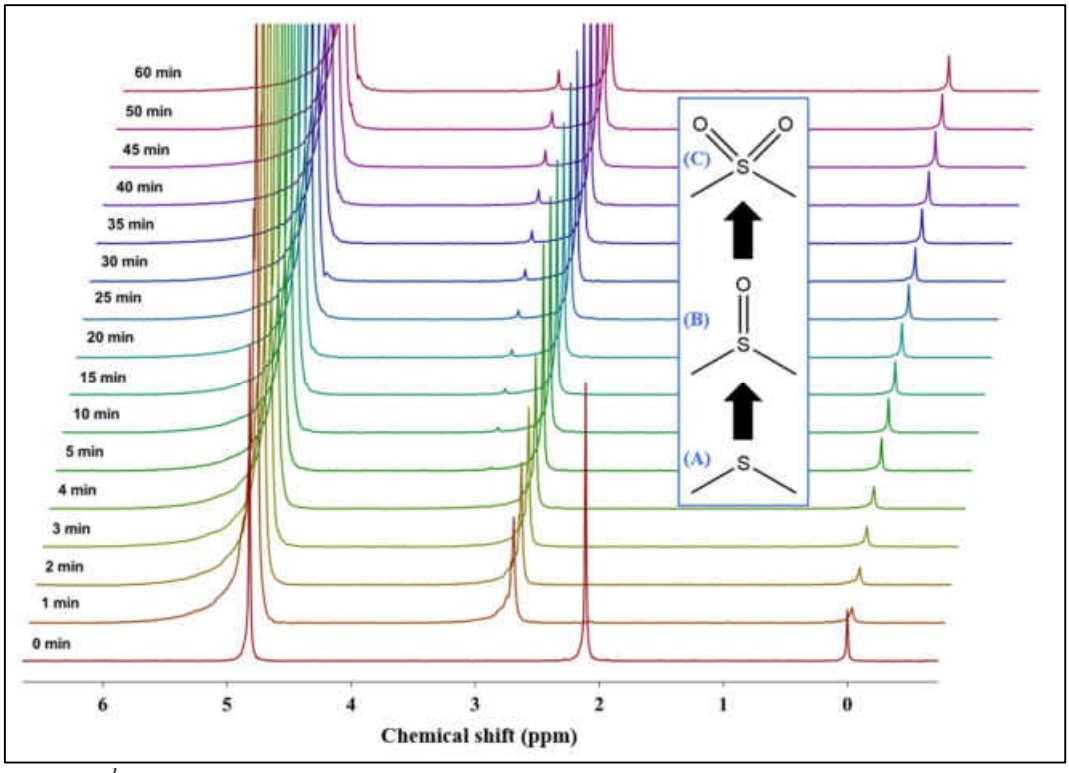

Figure 67. ^{1}H-NMR spectra of the oxidation of dimethyl sulfide by 1 eq H_2O_2 and $Mo_{0.5}W_{0.5}O_{2.1}$ microparticles as catalyst, shown after different periods of time. The inset shows the chemical structure of the reactant dimethyl sulphide (A) and the products dimethyl sulfoxide (B) and dimethyl sulfone (C).

The oxidation of (methylthio)acetic acid (MTA) was performed under the same conditions. It can be seen from Figure 68 that the conversion to the appropriate (methylsulfinyl)acetic acid (MSI) is almost instantaneous. The signal of the CH_3-group and the CH_2-group of the MTA, originally located at 2.06 ppm and 3.28 ppm, are no longer detectable after 3 min reaction time. MSI signals can be observed at 2.81 ppm (CH_3, singlet, 3H) and at 3.95 ppm (CH_2, split-singlet, 2H),[120] while

the signals of the (methylsufonyl)acetic acid (MSO) evolve at 3.25 ppm (CH_3, singlet, 3H) and 4.34 ppm (CH_2, singlet, 2H). After 60 min of reaction, the solution contains 6% MSO and 94% MSI. Therefore, a higher conversion rate, compared to TA, is achieved for this reagent, which can be attributed to the electron-withdrawing effect of the carboxyl group. Due to the de-shielding of the sulfur atom, it thus becomes more accessible for the attack of the oxidant. The absence of additional unexpected signals in the spectra suggests that the carboxylic group remains intact during the oxidation.

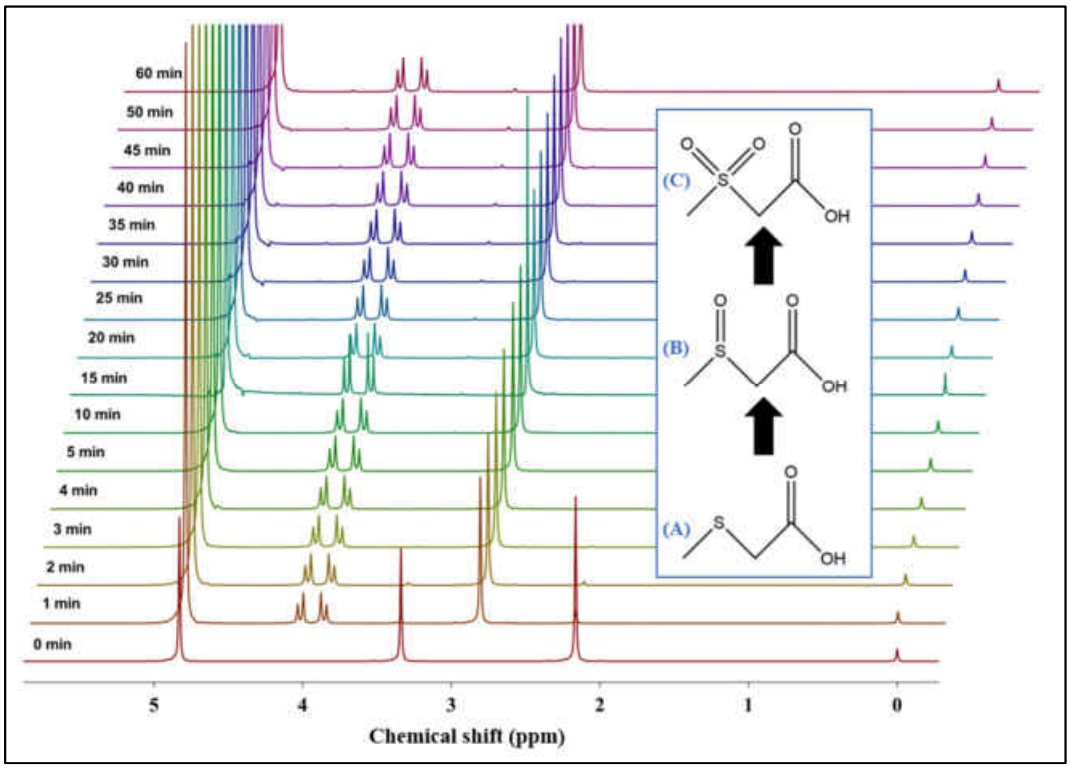

Figure 68. ^{1}H-NMR spectra of the oxidation of (methylthio)acetic acid by 1 eq H_2O_2 and $Mo_{0.5}W_{0.5}O_{2.1}$ microparticles as catalyst, shown after different periods of time. The inset shows the chemical structure of the reactant (methylthio)acetic acid (A) and the products (methylsulfinyl)acetic acid (B) and (methylsulfonyl)acetic acid (C).

The ^{1}H-NMR spectra of the catalytic oxidation of 2-(methylthio) ethanol (MTE) to 2-(methylsufinyl) ethanol (MSE) is depicted in Figure 69. The CH_3-signal at 2.12 ppm (singlet, 3H) is shifted to lower fields (2.76 ppm, singlet, 3H) upon oxidation to MSE. The oxidation is completed within 5 min. Both CH_2 groups produce triplet signals (due to the two adjacent protons) at 2.70 ppm and 3.77 ppm (J = 6.1 Hz), respectively, which are found at 3.07 and 4.01 ppm (J = 4.0 Hz) in the spectra of MSE. After 15 min, the formation of the CH_3-signal of the 2-(methylsufonyl) ethanol (MSOE) can also be observed, the proportion of the reaction product after 60 min being 7%. The triplet signals of both the CH_2-groups of MSOE are detected at 3.46 (J = 4.6 Hz) and 4.05 ppm (J = 5.4 Hz). In this case too, no additional signals can be observed in the spectrum, which is why it can be assumed that the alcohol group is tolerated during the catalytic oxidation.

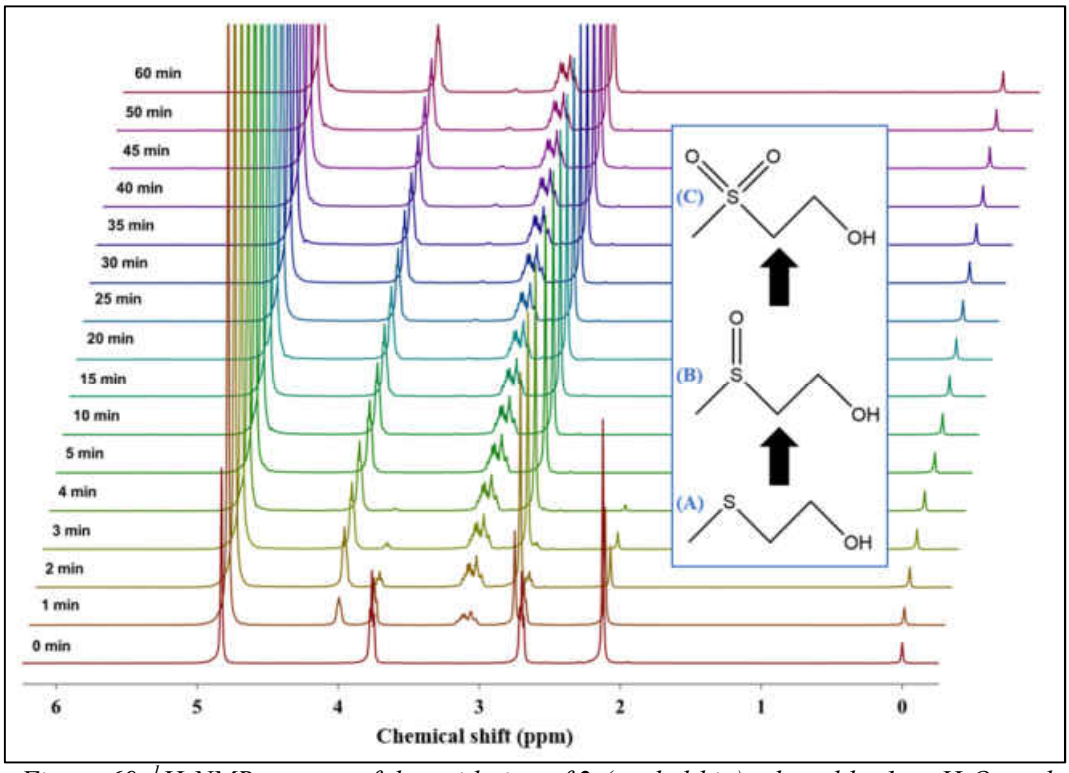

Figure 69. ^{1}H-NMR spectra of the oxidation of 2-(methylthio) ethanol by 1 eq H_2O_2 and $Mo_{0.5}W_{0.5}O_{2.1}$ microparticles as catalyst, shown after different periods of time. The inset shows the chemical structure of the reactant 2-(methylthio) ethanol (A) and the products 2-(methylsulfinyl) ethanol (B) and 2-(methylsulfonyl) ethanol (C).

Thus, in this investigation it was shown that the oxidation occurs selectively only at the sulfur site. This is particularly relevant since organic reactions (for example in the multi-stage synthesis of an active substance) have to be oxidized in a targeted manner without decomposing functional groups. If this is not possible, protective groups must usually be introduced, which subsequently have to be removed from the molecule in further steps. This is accompanied by an increased expenditure and ultimately with additional production costs of the compounds.

4.4. Other TMO Particles

4.4.1. $Mo_{1-(x+y)}W_xV_yO_{3-z}$ Nanobelts

The mixed oxides nanobelts containing molybdenum, tungsten and vanadium were synthesized using a solvothermal approach. For that, a mixture of ammonium metatungstate ($[(NH_4)_6H_2W_{12}O_{40}]$), vanadyl sulfate ($VOSO_4$), ammonium heptamolybdate $[(NH_4)_6Mo_7O_{24}{\cdot}4H_2O]$ and oxalic acid ($C_2O_4H_2{\cdot}2H_2O$) as oxidizing agent were weighted in an appropriate molar ratio. The solids were then dissolved in 60 mL of water under stirring. After transferring the resulting precursor solution into an autoclave, the reaction was performed in an electric oven at 200 °C for 18 h followed by natural cooling. Precipitated product was then

separated by centrifugation (9000 rpm/10 min), washed with water and ethanol and dried *in vacuo*.

The morphology of as-synthesized products was examined by TEM. As Figure 70 shows, all prepared materials resemble nanobelts of different dimensions. The 1:1:2 mixture of tungsten, molybdenum and vanadium yield particles of 5–20 nm thickness and up to 1.2 µm length. Many broken fragments can also be observed, which may be attributed to the preparation of the TEM specimen by means of ultrasonic treatment (Figure 70 a). Increasing the molar amount in the 1:1:3 (W:V:Mo) mixture results in the formation of thicker (15–35 nm) but shorter (500–800 nm) nanobelts (Figure 70 b). The 1:2:3 (W:V:Mo) mixed oxide shows no particles longer than 250 nm, while the majority is ~20 nm thick (Figure 70 c). The product with the biggest amount of vanadium (1:3:2, W:V:Mo) exhibits massive disorder in particles dimension. Belts of 650 nm length and 40 nm thickness, which are spliced at the end, are accompanied by ultra-short (~15 nm) and very thin (~5 nm) lamellae (Figure 70 d).

Targeted control of the morphology or the dimension of the particles obtained could not be established, but the described trend in the particle sizes as a function of the molar composition could be reproduced several times.

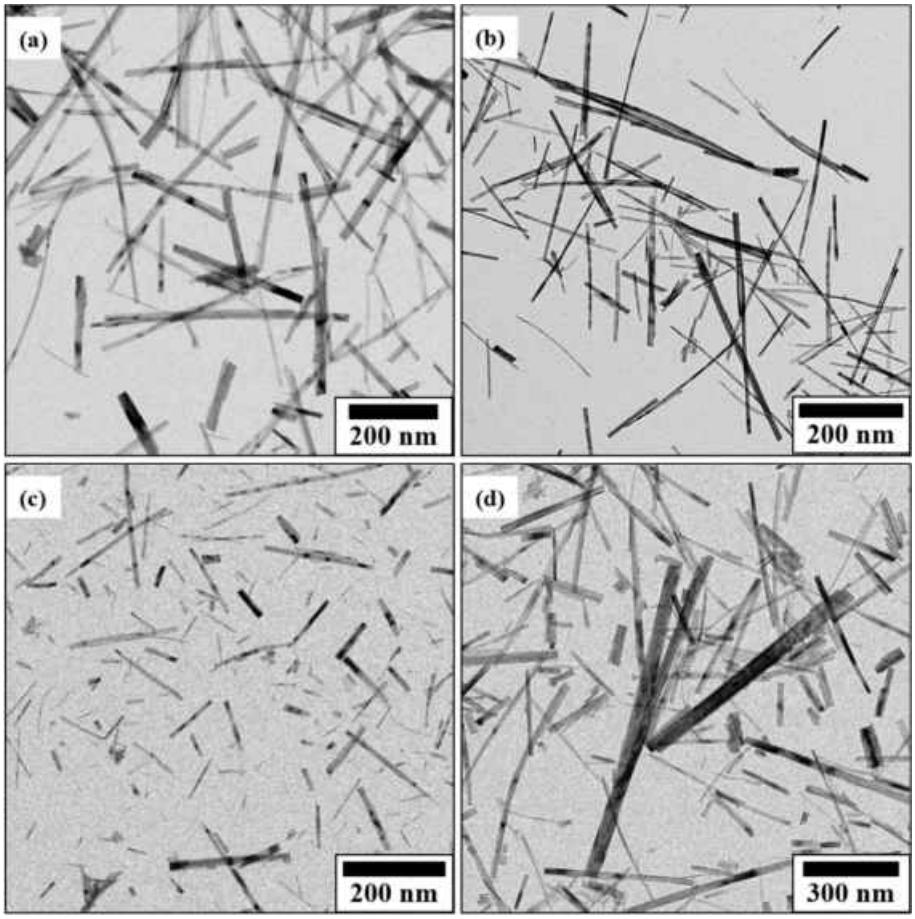

Figure 70. Representative low-magnification TEM images of the mixed oxides of molybdenum, tungsten and vanadium with different molar ratios: (a) W:V:Mo-1:1:2, (b) W:V:Mo-1:1:3, (c) W:V:Mo-1:2:3, (d) W:V:Mo-1:3:2.

In order to determine the structural characteristics, XRD measurements were conducted on the W-V-Mo oxides. Accordingly, all the compounds prepared show a predominantly crystalline structure, as illustrated in Figure 71. The observed reflections can be assigned to known phases of WO_3 (JCPDS-card: 100-4048), V_2O_5 (JCPDS-card: 152-1063) and Mo_4O_{11} (JCPDS-card: 901-1016).

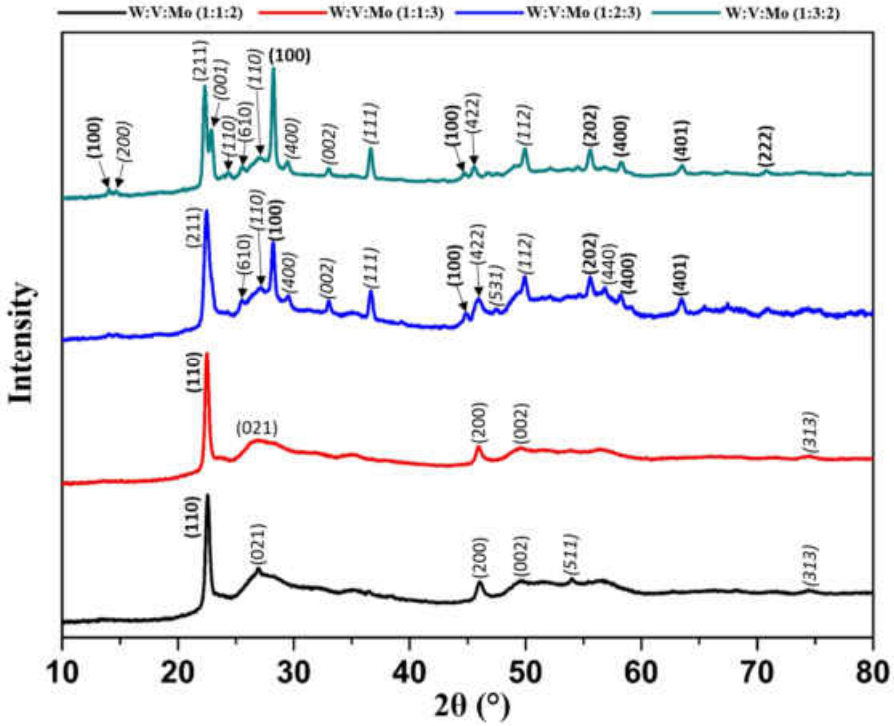

Figure 71. Powder XRD patterns of the mixed oxides of molybdenum, tungsten and vanadium with different molar ratios. The Miller indices were assigned to WO_3 phase (bold typing), Mo_4O_{11} phase (italic typing) and V_2O_5 phase (standard typing).

Raman spectra cannot provide for further information on the definite composition of the W-V-Mo oxides, as the contribution by tungsten oxide seems to dominate over the other phases (Figure 72). Apparently, neither terminal Mo=O vibrations nor V=O stretching modes around 1000 cm^{-1} can be observed. Regarding the spectra, it is also striking that the bands of the stretching vibration are greatly broadened, which in turn is not consistent with the observation from the XRD diffractogram since predominantly ordered structures were observed there.

Since no EDS measurements could be carried out on the samples and the measurements using AAS provided non-reproducible values, it remains to be clarified whether the materials produced are actually those with the desired composition.

These four compounds were, however, tested as catalysts in sulfoxidation. The measurements were carried out under the same conditions as described in Chapter 4.3.3. First results obtained showed a markedly increased conversion rate of the compounds compared with those of the molybdenum-tungsten microspheres, since here the oxidation to the methyl phenyl sulfoxide was already completed within 20 min.

Accordingly, these materials appear particularly suitable for oxidation reactions of sulfides. Further experiments also showed that rapid oxidation rates of sterically uncomplicated amines can be achieved. These results, however, require further verification by reproduction.

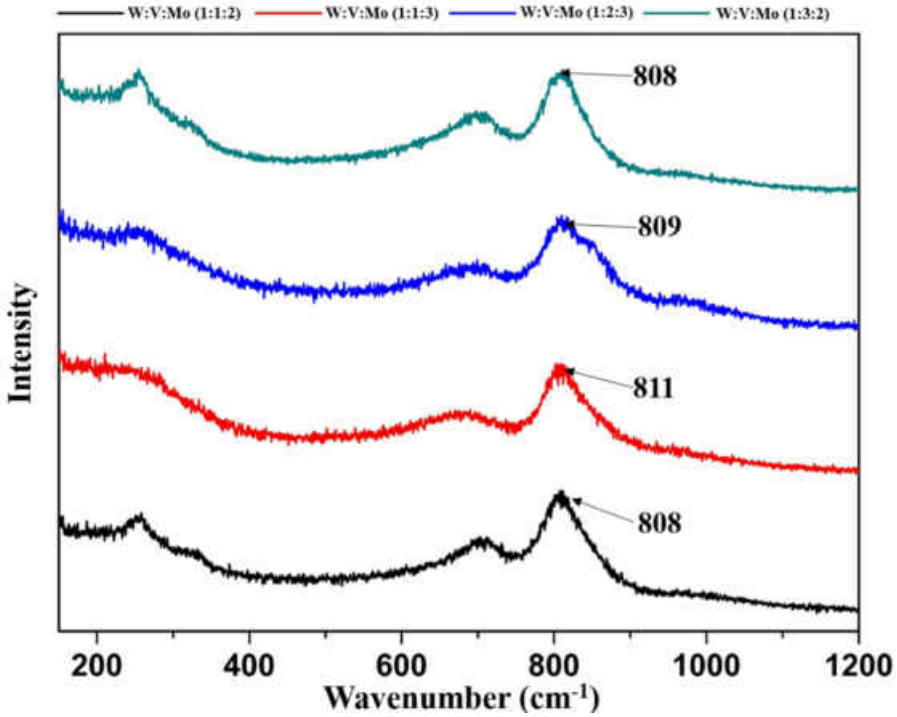

Figure 72. Raman spectra of the mixed oxides of molybdenum, tungsten and vanadium with different molar ratios.

4.4.2. WO_3 Nanoplatelets

The nanoplatelets of WO_3 were synthesized by a solvothermal approach with benzyl alcohol as solvent. For this, 0.1 mmol of WCl_6 were dissolved in 50 mL of benzyl alcohol in a round bottom flask. After the dissolution was completed by means of ultrasonic treatment, the precursor solution was transferred into two Teflon® inlays, which were then sealed inside stainless steel autoclaves. The autoclaves were subjected to thermal treatment at 180 °C for 12 h. After cooling down naturally, the precipitated yellow product was centrifuged (9000 rpm/10 min), washed with ethanol once and then dried *in vacuo*.

The morphology of as-obtained material was examined by TEM and SEM. Figure 73 (a, b) shows that nanoplatelets (with ~70 nm lateral size) were synthesized. Furthermore, a layered structure within the distinct nanoplatelets can be observed, while bigger agglomerates are shown in Figure 73 (c, d).

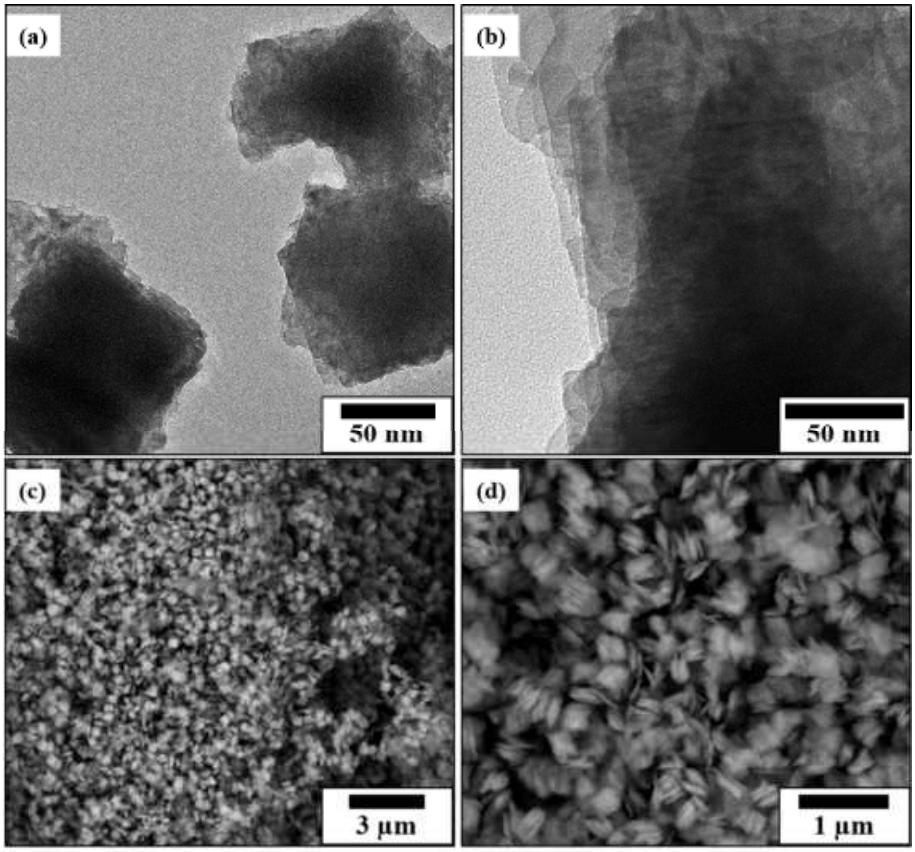

Figure 73. (a, b) TEM images and (c, d) SEM images of the nanoplatelets synthesized in benzyl alcohol.

The XRD pattern of as-synthesized nanoplatelets conforms to that of single phase WO_3.

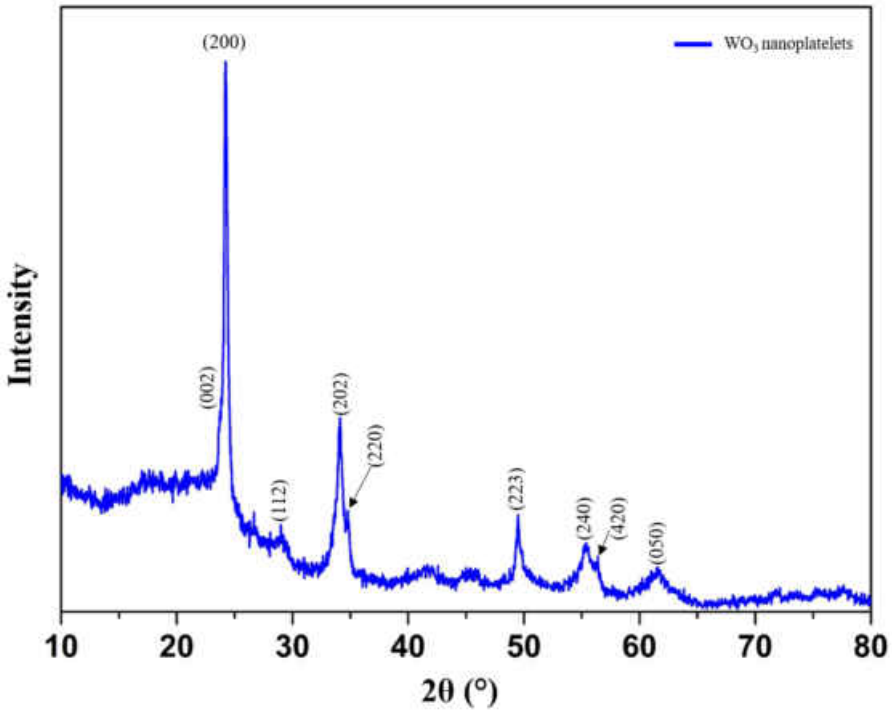

Figure 74. Powder XRD pattern of the WO_3 nanoplatelets synthesized in benzyl alcohol.

4.5. Conclusion

In this chapter the solvothermal synthesis of novel mixed molybdenum-tungsten oxides was presented. Using two different approaches, Mo-doped nanoflakes and W-doped microparticles, respectively, were prepared. Both the mixed series products exhibit unambiguous amorphous character and were tested for different applications.

The tungsten-molybdenum nanoflakes show significant increase of absorbance in the visible light range, which can be utilized for photocatalysis applications. However, the experiments of the photocatalytic decomposition of Rhodamine B carried out in several batches in this work were not successful. The particles showed a strong adsorption behavior towards RhB, wherefore it was not possible to determine exactly how effective they are as photocatalysts. An alternative use of the nanoflakes was as precursors for the reductive sulfidization to WS_2 nanoflakes, which were investigated in tribological experiments (see Chapter 6.2.4.).

Microparticles of amorphous $Mo_xW_{1-x}O_{3-y}$ were prepared using a solvothermal synthesis and exhibited enhanced performance as photoanode materials in the PEC water splitting reaction, combined with superior chemical long-term stability and higher photocurrent values than other semiconducting compounds. This can be attributed to the higher charge carrier density compared to WO_3 and MoO_3 resulting from the partial reduction and the concomitant presence of W^{5+} (and Mo^{5+}) as demonstrated by XPS spectroscopy. This compensates for charge recombination which is likely to occur in these strongly disordered materials. Raman spectra showed that W substitutes homogeneously for Mo, while the elemental composition was determined by XPS and EDS analysis. Mo/W substitution prevents the formation of metallic and crystalline Magnéli-type phases resulting in non-crystalline behavior, as was demonstrated by powder XRD. The additional charge carriers arising from W^{5+} and Mo^{5+} sites lead to an enhanced absorption in the visible and the NIR range through the plasmon excitation. Thus, the improved PEC performance can be attributed to the synergistic effects of (i) increasing the charge carrier concentration by metal reduction, (ii) suppressing the formation of metallic oxides and associated metal-semiconductor transitions through non-crystallinity and (iii) tuning the absorption in the visible and NIR range due to the presence of W^{5+} and Mo^{5+} sites.

In other experiments it was demonstrated that these mixed oxides show a robust activity as sulfoxidation catalyst. The kinetics of the oxidation reaction was examined using thioanisole as model compound. Here, too, it was shown that the mixed oxides are superior to the pure molybdenum or tungsten oxides in terms of catalytic activity, which is also attributed to the structural stabilization by W-substitution. It has also been shown that functional groups are tolerated in the sulfoxidation process, which is advantageous for organic reactions.

Furthermore, in first experiments it was found that ternary oxides based on molybdenum, tungsten and vanadium show even higher catalytic activity for sulfoxidations.

4.6. References of Chapter 4

[1] S. Andersson, A. Magnéli, *Naturwissenschaften* 1956, **43**, 495.

[2] S. Andersson, B. Collen, U. Kuylenstierna, A. Magnéli, *Acta. Chem. Scand.* 1957, **11**, 1641.

[3] U. Schwingenschlögl, V. Eyert, *Ann. Phys.* 2004, **13**(9), 475-510.

[4] F. C. Walsh, R. G. A. Wills, *Electrochimica Acta* 2010, **55**(22), 6342-6351.

[5] A. Hjelm, C. G. Granquist, J. M. Wills, *Phys. Rev. B* 1996, **54**, 2436.

[6] R. Chatten, A. V. Chadwick, A. Rougier, P. J. D. Lindan, *J. Phys. Chem. B* 2005, **109**, 3146.

[7] G. A. de Wijs, R. A. de Groot, *Phys. Rev. B* 1999, **60**, 16463.

[8] D. Lötsch, V. Eberhardt, C. Rabe, *Chromogenic Materials. Ullmann's Encyclopedia of Industrial Chemistry*, 1-26, Wiley-VCH, Weinheim, 2016.

[9] C. G. Granquist, *Thin Solid Films* 2014, **564**, 1-38.

[10] T. He, J. Yao, *J. Photochem. Photobiol. B* 2003, **4**(2), 125-143.

[11] M. A. White, M. LeBlanc, *J. Chem. Educ.* 1999, **76**(9), 1201-1205.

[12] E. Salje, R. Gehlig, K. Viswanathan, *J. Solid State Chem.* 1978, **25**, 239-250.

[13] Y. Bando, S. Muranaka, Y. Shimada, M. Kyoto, T. Takada, *J. Cryst. Growth* 1981, **53**, 443-450.

[14] R. Bartholomew, W. B. White, *J. Cryt. Growth* 1970, **6**, 249-252.

[15] E. Frederiksson, J.-O. Carlsson, *Thin Solid Films* 1985, **124**, 109-116.

[16] R. Nadimicherla, R. Zha, L. Wei, X. Guo, *J. Alloys Compd.* 2016, **687**, 79-86.

[17] W. Mu, X. Xie, X. Li, R. Zhang, Q. Yu, H. Wie, Y. Jian, *RSC Adv.* 2014, **4**, 36064-36070.

[18] Z.-G. Zhao, M. Miyauchi, *Angew. Chem. Int. Ed.* 2008, **37**, 7159-7163.

[19] M. G. Walter, E. L. Warren, J. R. McKone, S. W. Boettcher, Q. Mi, E. A. Santori, N. S. Lewis, *Chem. Rev.* 2010, **110**, 6446-6473.

[20] F. E. Osterloh, *Chem. Soc. Rev.* 2013, **42**, 2294-2320.

[21] P. Dubey, G. A. Lopez, G. Martinez, C. V. Ramana, *J. Appl. Phys.* 2016, **120**, 245103.

[22] P .R. Patil, P. S. Patil, *Thin Solid Films* 2001, **382** (1-2), 13-22.

[23] A. Michailovski, F. Krumeich, G. R. Patzke, *Chem. Mater.* 2004, **16**(8), 1433-1440.

[24] S. Morandi, G. Ghiotti, A. Chiorino, B. Bonelli, E. Comini, G. Sberveglieri, *Sens. Actuators B* 2005, **111-112**, 28-35.

[25] R. R. Kharade, S. S. Mali, S. S. Mohite, V.V. Kondalkar, P. S. Patil, P. N. Bhosale, *Electroanalysis* 2014, **26**(11), 2388-2397.

[26] L. Kondrachova, B. P. Hahn, G. Vijayaraghavan, R. D. Williams, K. J. Stevenson, *Langmuir* 2006, **22**(25), 10490-10498.

[27] M. Farmahini-Farahani, A. V. Saveliev, W. Merchan-Merchan, *Proc. Combust. Inst.* 2017, **36**, 1055-1063.

[28] R. Kiebach, N. Pienack, W. Bensch, J.-D. Grunwaldt, A. Michailovski, A. Baiker, T. Fox, Y. Zhou, G. R. Patzke, *Chem. Mater.* 2008, **20** (9), 3022-3033.

[29] Y. Zhou, N. Pienack, W. Bensch, G. R. Patzke, *Small* 2009, **5**(17), 1978-1983.

[30] Y. Zhou, K. Zheng, J.-D. Grunwaldt, T. Fox, L. Gu, X. Mo, G. Chen, G. R. Patzke, *J. Phys. Chem. C* 2011, **115**, 1134-1142.

[31] B. Xue, J. Peng, Z. Xin, Y. Kong, L. Li, B. Li, *J. Mater. Chem.* 2005, **15**, 4793-4798.

[32] H. Nair, M. J. Liszka, J. E. Gatt, C. D. Baertsch, *J. Phys. Chem. C* 2008, **112** (5), 1612-1620.

[33] S.-H. Baeck, T. F. Jaramillo, D. H. Jeong, E. W. McFarland, *Chem. Commun.* 2004, **4**, 390-391.

[34] S. Morandi, M. C. Paganini, E. Giamello, M. Bini, D. Capsoni, V. Massarotti, G. Ghiotti, *J. Solid State Chem*. 2009, **182**, 3342-3352.

[35] H. Zhou, X. Zou, K. Zhang, P. Sun, Md. S. Islam, J. Gong, Y.Zhang, J. Yang, *ACS Appl. Mater. Interfaces* 2017, **9**, 18699-18709.

[36] R. Rödel, O. Timple, A. Trunschke, G. A. Zenkovets, G. N. Kryukova, R. Schlögl, T. Ressler, *Catal. Today* 2007, **126**(1-2), 112-118.

[37] A. Arzola-Rubio, J. Camarillo-Cisneros, L. Fuentes-Cobas, V. Collins-Martinez, L. De la Torre-Saenz, F. Paraguay-Delgado, *Superlattices Microstruct.* 2015, **81**, 175-184.

[38] T. Jafari, E. Moharreri, A. Shirazi Amin, R. Miao, W. Song, S. L. Suib, *Molecules* 2016, **21**, 900-929.

[39] S. L. Liew, G. S. Subramanian, C. S. Chua, H.-K. Luo, *RSC Adv.* 2016, **6**, 19452-19458.

[40] J. M. O-Rueda de Leon, D. R. Acosta, U. Pal, L. Castaneda, *Electrochim. Acta* 2011, **56**(5), 2599-2605.

[41] V. Madhavi, P. Jeevan Kumar, P. Kondaiah, O. M. Hussain, S. Uthanna, *Ionics* 2014, **20**, 1737-1745.

[42] R. D. Shannon, *Acta Cryst.* 1976, **32**, 751-767.

[43] L. Zhou, J. Zhu, M. Yu, X. Huang, Z. Li, Y. Wang, C. Yu, *J. Phys. Chem. C* 2010, **114**(49), 20947-20954.

[44] N. Li, H. Teng, L. Zhang, J. Zhou, M. Liu, *RSC Adv.* 2015, **5**, 95394.

[45] L. Jin, X. Zheng, W. Liu, L. Cao, Y. Cao, T. Yao, S. Wei, *J. Mater. Chem. A* 2017, **5**, 12022-12026.

[46] X. Zhong, Y. Sun, X. Chen, G. Zhuang, X. Li, J.-G. Wang, *Adv. Funct. Mater.* 2016, **26**(32), 5778-5786.

[50] Y.-J. Tang, M.-R. Gao, C.-H. Liu, S.-L. Li, H.-L. Jiang, Y.-Q. Lan, M. Han, S.-H. Yu, *Angew. Chem. Int. Ed.* 2015, **54**, 12928 –12932.

[51] N. Gaillard, B. Cole, J. Kaneshiro, E. L. Miller, B. Marsen, L. Weinhardt, M. Bär, C. Heske, K.-S. Ahn, Y. Yan, M. M. Al-Jassim, *J. Mater. Res.* 2010, **25**(1), 45-51.

[52] W. Z. Li, J. Li, X. Wang, S. Luo, J. Xiao, Q. Y. Chen, *Electrochim. Acta* 2010, **56**, 620-625.

[53] S. Hilaire, M. J. Süess, N. Kränzlin, K. Bienkowski, R. Solarska, J. Augustinski, M. Niederberger, *J. Mater. Chem. A* 2014, **2**, 20530-20537.

[54] B. Marsen, E. L. Miller, D. D. Paluselli, R. E. Rocheleau, *Int. J. Hydrogen Energ.* 2007, **32**, 3110-3115.

[55] M. Yagi, S. Maruyama, K. Sone, K. Nagai and T. Norimatsu, *J. Solid State Chem.* 2008, **181**, 175–182.

[56] J. K. Kim, K. Shin, S. M. Cho, T. W. Lee and J. H. Park, *Energy Environ. Sci*. 2011, **4**, 1465–1470.

[57] F. Amano, M. Tian, G. S. Wu, B. Ohtani and A. C. Chen, *ACS Appl. Mater. Interfaces* 2011, **3**, 4047–4052.

[58] W. J. Lee, P. S. Shinde, G. H. Go, E. Ramasamy, *Int. J. Hydrogen Energy* 2011, **36**, 5262–5270.

[59] Y. M. Solonin, O. Y. Khyzhun, E. A. Graivoronskaya, *Cryst. Growth. Des.* 2001, **1**(6), 473-477.

[60] S. K. Deb, *Phys. Rev. B: Condens. Matter Mater. Phys.* 1977, **16**, 1020-1024.

[61] G. Wang, Y. Ling, H. Wang, X. Yang, C. Wang, J. Z. Zhang, Y. Li, *Energy Environ. Sci.* 2012, **5**, 6180-6187.

[62] Y. M. Solonin, O. Y. Khyzhun, E. A. Graivoronskaya, *Cryst. Growth. Des.* 2001, **1**(6), 473-477.

[63] Y. Ren, Z. Ma, P. G. Bruce, *Chem. Soc. Rev.* 2012, **41**, 4909-4927.

[64] D. Chen, L. Cao, F. Huang, P. Imperia, Y.-B. Cheng, R. Caruso, *J. Am. Chem. Soc.* 2010, **132**, 4438-4444.

[65] D. Antonelli, J. Ying, *Chem. Mater.* 1996, 874-881.

[66] N. Alexaki, T. Stergiopoulos, A. Kontos, D. Tsoukleris, A. Katsoulidis, P. Pomonis, D. LeClere, P. Skeldon, G. Thompson, P. Falaras, *Microporous Mesoporous Mater.* 2009, **124**, 52-58.

[67] T. Peng, D. Zhao, K. Dai, W. Shi, K. Hirao, *J. Phys. Chem. B* 2005, **109**, 4947-4952.

[68] K. An, N. Musselwhite, G. Kennedy, V. V. Pushkarev, L. Baker, G. Somorjai, *J. Colloid Interface Sci.* 2013, **392**, 122-128.

[69] A. Ismail, D. W. Bahnemann, *J. Mater. Chem.* 2011, **21**, 11686-11707.

[70] L. Guo, S. Ida, T. Daio, H. Hagiwara, T. Ishikara, *New J. Chem.* 2014, **38**, 5846-5855.

[71] M. Dieterle, G. Mestl, *Phys. Chem. Chem. Phys.* 2002, **4**, 822-826.

[72] J. S. Cross, G. L. Schrader, *Thin Solid Films* 1995, **259**, 5.

[73] D. Spetter, W. Tremel, "Process and Device for the Production of Nanoscale Metal Sulfides and after the Process Produced Metal Sulfides", *Ger. Offen.* DE 102015016878.9 (December 31, 2015).

[74] C. Guo, S. Yin, M. Yan, M. Kobayashi, M. Kakihana, T. Sato, *Inorg. Chem.* 2012, **51**, 4763-4771.

[75] D. Spetter, F. Hoshyargar, J. K. Sahoo, M. N. Tahir, R. Branscheid, B. Barton, M. Panthöfer, U. Kolb, W. Tremel, *Eur. J. Inorg. Chem.* 2017, 2190-2194.

[76] A. Magneli, *Acta Cryst.* 1953, **6**, 495-500.

[77] A. Magneli, *Pure Appl. Chem*. 1978, **50**, 1261-1271.

[78] G. Kieslich, G. Ceretti, I. Veremchuk, M. Panthöfer, Yu. Grin, W. Tremel, *Phys. Stat. Sol. A* 2016, **213**, 808-823.

[79] D. Y. Lu, J. Chen, J. Zhou, S. Z. Deng, N. S. Xu, J. B. Xu, *J. Raman Spectrosc.* 2007, **38**, 176-180.

[80] E.-E. Bendeif, A. Gansmuller, K.Y. Hsieh, S. Pillet, Th. Woike, M. Zobel, R. B. Neder, M. Bouazaoui, *RSC Adv.* 2015, **5**, 8895-8902.

[81] S. J. L. Billinge, M. G. Kanatzidis, *Chem. Comm.* 2004, 749-760.

[82] C. A. Young, A. L. Goodwin, *J. Mater. Chem*. 2011, **21**, 6464-6476.

[83] B. Ingham, *Cryst. Rev.* 2015, **21**(4), 229-303.

[84] A. Mancini, L. Malavasi, *Chem. Comm.* 2015, **51**, 16592-16604.

[85] C. A. Triana, C. Moyses Araujo, R. Ahuja, G. A. Niklasson, T. Edvinsson, *Sci. Rep.* 2017, **7**, 2044.

[86] R. Caliandro, T. Sibiliano, B. D. Belviso, R. Scarfiello, J. C. Hanson, E. Dooryhee, M. Manca, P. D. Cozzoli, C. Giannini, *ChemPhysChem* 2016, **17**(5), 699-709.

[87] E. D. Bojesen, K. M. O. Jensen, C. Tyrsted, A. Mamakhel, H. L. Andersen, H. Reardon, J. Chevalier, A.-C. Dippel, B. B. Iversen, *Chem. Sci.* 2016, **7**, 6394-6406.

[88] L.-E. Kalland, A. Magraso, A. Mancini, C. Tealdi, L. Malavasi, *Chem. Mater.* 2013, **25**, 2378-2384.

[89] D. Saha, K. M. O. Jensen, C. Tyrsted, E. D. Bojesen, A. H. Mamakhel, A.-K. Dippel, M. Christensen, B. B. Iversen, *Angew. Chem.* 2014, **53**, 3667-3670.

[90] M. Teck, M. M. Murshe, M. Schowalter, N. Lefeld, H. K. Grossman, T. Grieb, T. Hartmann, L. Robben, A. Rosenauer, L. Mädler, T. M. Gesing, *J. Solid State Chem.* 2017, **254**, 82-89.

[91] G. Andersson, A. Magneli, *Acta Chem. Scand.* 1950, 793-797.

[92] H. Zhou, X. Zou, K. Zhang, P. Sun, Md. S. Islam, J. Gong, Y. Zhang, J. Yang, *ACS. Appl. Mater. Interfaces* 2017, **9**, 18699-18709.

[93] J. Oi, A. Kishimoto, T. Kudo, M. Hiratani, *J. Solid State Chem.* 1992, **96**, 13-19.

[94] F. Y. Xie, L. Gong, X. Liu, Y. T. Tao, W. H. Zhang, S. H. Chen, H. Meng, J. Chen, *J. Electron Spectrosc.* 2012, **185**, 112-118.

[95] H. Gruber, E. Krautz, *Phys. Status Solidi A* 1980, **62**, 615-624.

[96] T. Hisatomi, J. Kubota, K. Domen, *Chem. Soc. Rev.* 2014, **43**, 7520-7535.

[97] L. Yuan, C. Han, M.-Q. Yang, Y.-J. Xu, *Int. Rev. Phys. Chem.* 2016, **35**, 1-36.

[98] T. Hisatomi, K. Maeda, Y. Moriya, K. Domen, *J. Am. Chem. Soc.* 2012, **69**, 8685-8687.

[99] A. Yella, S. Meuer, M. N. Tahir, D. Schollmeyer, M. Panthöfer, R. Zentel, W. Tremel, *J. Am. Chem. Soc.* 2009, **131**, 17566–17575.

[100] K. Manthiram, A. P. Alivisatos, *J. Am. Chem. Soc.* 2012, **134**, 3995-3998.

[101] J. March, *Advanced Organic Chemistry* (7th Edition), Wiley, 2013.

[102] J. Liu, O. Margeat, W. Dachraoui, X. Liu, M. Fahlman, J. Ackermann, *Adv. Funct. Mater.* 2014, **24**(38), 6029-6037.

[103] K. Thummavichai, L. Trimby, N. Wang, C. D. Wright, Y. Xia, Y. Zhu, *J. Phys. Chem. C* 2017, **121**(37), 20498-20506.

[104] Y. Sun, W. Wang, J. Qin, D. Zhao, B. Mao, Y. Xiao, M. Cao, *Electrochimica Acta* 2016, **187**, 329-339.

[105] F. Li, H. Gong, Y. Wang, H. Zhang, Y. Wang, S. Liu, S. Wang, C. Sun, *J. Mater. Chem. A* 2014, **2**, 20154-20163.

[106] B. Moshofsky, T. Mokari, *Chem. Mater.* 2013, **25**(8), 1384-1391.

[107] J. He, P. Wu, Y. Wu, H. Li, W. Jiang, S. Xun, M. Zhang, W. Zhu, H. Li, *ACS Sustainable Chem. Eng.* 2017, **5**(10), 8930-8938.

[108] C. S. Rout, M. Hegde, C. N. R. Rao, *Sens. Actuators B* 2008, **128**(2), 488-493.

[109] J. L. Solis, S. Saukko, L. Kish, C. G. Granqvist, V. Lantlo, *Thin Solid Films* 2001, **391**(2), 255-260.

[110] J. Tamaki, Z. Zhang, K. Fujimori, M. Akiyama, T. Harada, N. Miura, N. Yamazoe, *J. Electrochem. Soc.* 1994, **141**(8), 2207-2210.

[111] S. H. Wang, T. C. Chou, C. C. Liu, *Sens. Actuators B* 2003, **94**(3), 343-351.

[112] E. Llobet, G. Molas, P. Molinas, J. Calderer, X. Vilanova, J. Brezmes, J. E. Sueiras, X. Correig, *J. Electrochem. Soc.* 2000, **147**(2), 776-779.

[113] S. Ishikawa, Y. Goto, Y. Kawahara, S. Inukai, N. Hiyoshi, N. F. Dummer, T. Murayama, A. Yoshida, M. Sadakane, W. Ueda, *Chem. Mater.* 2017, **29**(7), 2939-2950.

[114] O. Merdrignac-Conaneca, P. T. Moseleyb, *Electrochem. Commun.* 1999, **1**(2), 51-54.

[115] W. Chen, L. Mai, Y. Qi, Y. Dai, *J. Phys. Chem. Solids* 2006, **67**, 896-902.

[116] M. Ivanovskaya, P. Bogdanov, G. Faglia, P. Nelli, G. Sberveglieri, A. Taroni, *Sens. Actuators B* 2001, **77**(1-2), 268-274.

[117] R. Muno-Espi, C. Burger, C. V. Krishnan, B. Chu, *Chem. Mater.* 2008, **20**(23), 7301-7311.

[118] W. D. Pyrz, D. A. Blom, M. Sadakane, K. Kpdato, W. Ueda, T. Vogt, D. J. Buttrey, *Chem. Mater.* 2010, **22**(6), 2033-2040.

[119] R. Lopez-Medina, J. L. G. Fierro, M. O. Guerrero-Perez, M. A. Banares, *Appl. Catal. A* 2010, **375**(1), 55-62.

[120] A. L. Pacquette, D. S. Oh, A. A. Gewirth, *J. Phys. Chem. C* 2016, **120**(29), 15553-15562.

[121] H. Peelars, M. L. Chabinyc, C. G. Van der Walle, *Chem. Mater.* 2017, **29**(6), 2563-2567.

[122] S. Rajagopal, D. Nataraj, D. Mangalaraj, Y. Djaoued, J. Robichaud, O. Y. Khyzhun, *Nanoscale Res. Lett.* 2009, **4**, 1335-1342.

[123] A. Pasini, G. D'Alfonso, C. Manzotti, M. Moret, S. Spinelli, M. Valsecchi, *Inorg. Chem.* 1994, **33**, 4140-4148.

5. Porous Hematite

5.1. Introduction Iron Oxides

Iron is the fourth most common element by mass in the earth's crust and forms compounds in several oxidation states. Besides the ubiquitous iron hydroxides, at least four different modifications of iron oxides can be distinct.

Hematite (α-Fe_2O_3) is a n-type semiconductor (E_g = 2.1 eV) and the thermodynamically most stable phase of iron oxide (Figure 75). Due to its corundum structure of Al_2O_3 it possesses the space group $R\bar{3}c$.

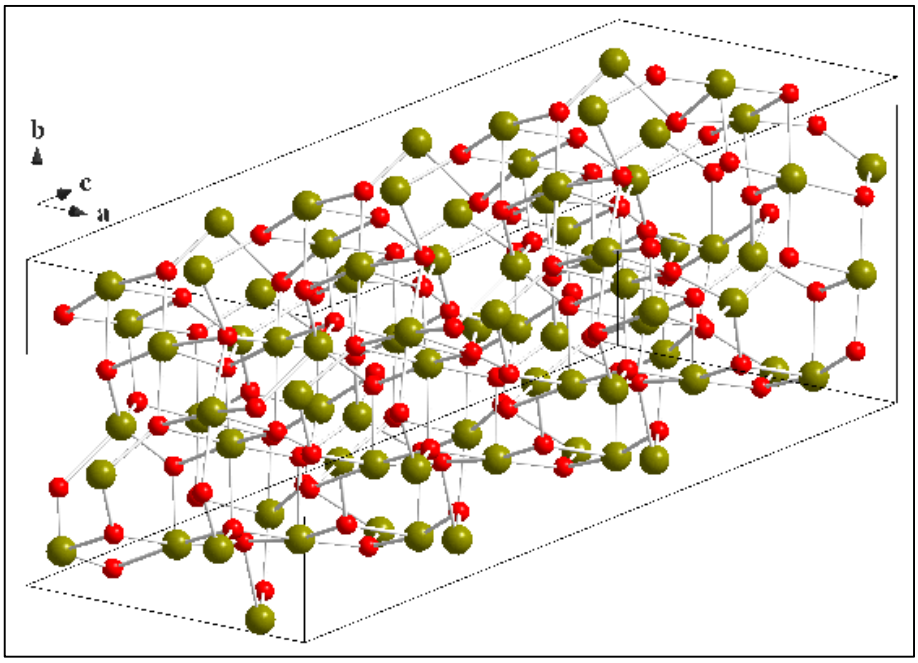

Figure 75. Crystal structure of hematite (α-Fe_2O_3), shown as ball-and-stick model. Green balls represent iron atoms, red balls oxygen.

In this type of structure, the oxygen ions form a hexagonal-dense packing. In the iron layer, which is between two layers of oxygen, the iron ions form six-membered rings with a void in the middle. The Fe^{3+} ions are coordinated by a distorted octahedron of oxygen ions. Hematite is an anti-ferromagnetic compound below the so-called Morin temperature of ~260 K and exhibits weak ferromagnetism between 260 K and 950 K.[1] Above its Néel temperature of 955 K, the antiferromagnetic material becomes paramagnetic, because the thermal energy becomes large enough to destroy the microscopic ordering within the material.[2]

Due to its nontoxicity, dielectrical properties and low processing cost, hematite has been intensively investigated for applications in various fields such as catalysts,[3-6] pigments,[7-9] gas sensors,[10-14] water purification,[15-17] optical devices,[18-20] energy conversion[21-30] and storage technologies.[31-33] Multiple approaches to synthesize nanoscaled hematite by solution chemistry routes or vapor-phase processes and have enhanced its performance in currently existing

applications. Thus, among others, hematite has been synthesized with morphologies including nanocubes,[34, 35] nanorods,[36, 37] nanowires,[38, 39] nanotubes[40, 41] and nanorings.[42, 43]

The second material with Fe_2O_3 composition is **maghemite** (actually denoted as γ-Fe_2O_3), which crystallizes as a defect variant of the **magnetite** (Fe_3O_4) type (Figure 76). Only trivalent iron is present and the octahedral cation positions are statistically subordinate. Slight structural distortions lead to a symmetry reduction of $Fd\bar{3}m$ to space group $P4_132$.

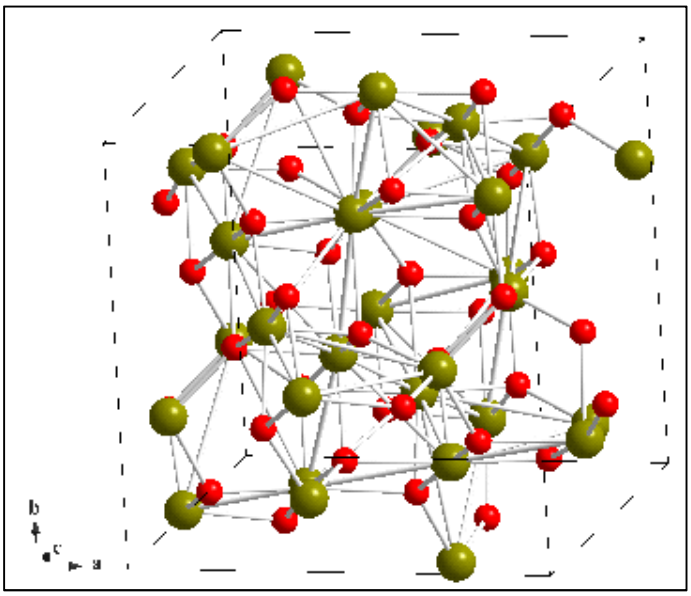

Figure 76. Crystal structure of maghemite (γ-Fe_2O_3), shown as ball-and-stick model. Green balls represent iron atoms, red balls oxygen.

Due to their close structural relationship, Fe_3O_4 and γ-Fe_2O_3 crystallographically differ only in a few weak reflections. More precisely, maghemite can show strong additional reflections in the range of $2\theta = 11\text{-}14$ °. If, as is the case with nanostructured materials, there are additional reflections, no considerable disparity between these two iron oxides can be detected with conventional laboratory powder X-ray diffractometers. Both in magnetite and in maghemite exist two partial lattices (octahedron and tetrahedron gaps) due to the underlying crystal structure of the inverse spinel. Within a partial lattice, the magnetic moments of the atoms are arranged in parallel. Between the crystallographic sublattices, the orientation of the spins is antiparallel, causing them to almost entirely offset each other and ultimately lead to ferrimagnetic behavior of these iron oxides. The anti-ferromagnetic coupling of the sublattices is called super-exchange. The Curie temperature, which is the analogue of Néel temperature for ferromagnetic compounds, is 950 K for maghemite and 850 K for magnetite, respectively.[44, 45]

Magnetite crystallizes as inverse spinel, which exhibits the $Fd\bar{3}m$ space group. It contains iron ions in both the bivalent and trivalent state. The O^{2-} ions form a cubic dense package in which the Fe^{2+} ions are octahedrally coordinated by oxygen. Half of the Fe^{3+} ions are located in the tetrahedron gaps and half of them in the octahedron gaps.

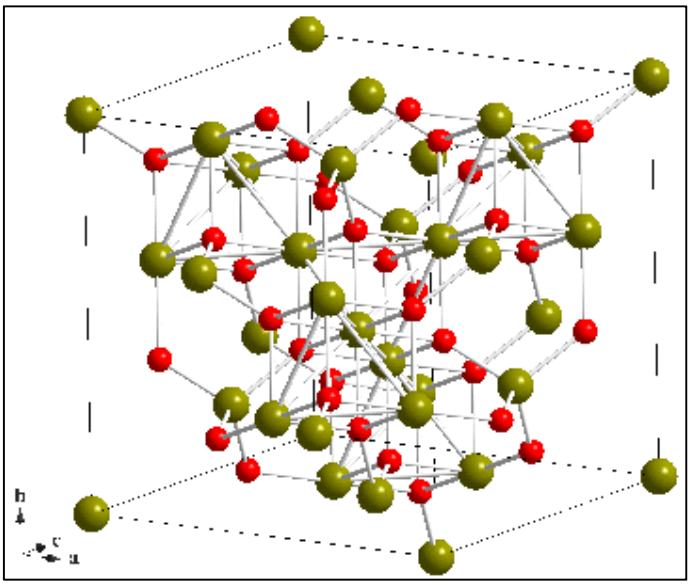

Figure 77. Crystal structure of magnetite (Fe_3O_4), shown as ball-and-stick model. Green balls represent iron atoms, red balls oxygen.

Wüstite has a NaCl-type crystal structure with the space group $Fm\bar{3}m$. Under normal conditions, however, only a defect variant with Fe^{2+} vacancies is known. The resulting anion excess is balanced by partial oxidation of Fe^{3+} species, though the non-stoichiometric oxide is correctly noted as $Fe_{1-x}O$. The antiferromagnetic wustite has a Néel temperature of 198 K.

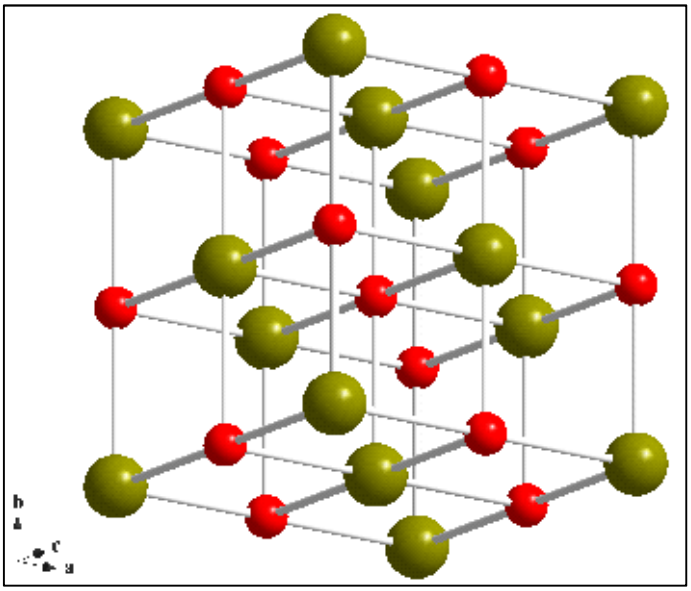

Figure 78. Crystal structure of wüstite (FeO), shown as ball-and-stick model. Green balls represent iron atoms, red balls oxygen.

The abundant availability of a natural Fe source from rocks and soils at minimal cost makes the potential use of these substances as heterogeneous catalysts attractive.

5.2. Fenton and Fenton-like reactions

Wastewater pollution is as serious environmental problem as the increasing level of CO_2 or renewable energy because it also impacts the humanity on mass scale.[46] While bigger particles and molecules can be separated by filtration or captured by scavenger compounds, this method is not easily applicable for synthetic dyes. The increasing environmental burden on water by dyes from the textile industry or printed products requires measures beyond conventional approaches. Biologically based methods (bacteria) can be supplemented by flocculation, activated carbon adsorption, ion-exchange or air sparging, but they are not capable of decoloring the water or destroying the pollutants.[47] Due to the small molecular weight and the immense water solubility of the dyes, a chemical approach is necessary. The most effective ones are based on oxidation processes, which can also be carried out in combination with sunlight.All relevant chemical oxidation reactions can be gropeded under the common term of "advanced oxidation processes (AOPs)".[48] These represent a promising alternative to the methods mentioned above, in particular for not-biodegradable and persistent compounds. The most prominent AOPs are based on the so-called Fenton reaction, named after H. J. H. Fenton (1894).[49] The Fenton oxidation, which is catalyzed by iron salts, proceeds in an acidic medium with hydrogen peroxide as an oxidant and permits the conversion of compounds which are difficult to decompose. More specifically, the Fenton-like systems are highly efficient in generating reactive species such as hydroxyl radicals, even at room temperature and atmospheric pressure.[50]

However, in the homogeneous Fenton reaction, the advantages such as low cost, high degradation efficiency, and wide applicability, are opposed with disadvantages, which are not negligible. For example, a relatively high concentration of iron ions (50–80 ppm) is necessary to achieve a relevant efficiency. Furthermore, the reaction proceeds optimally only in a narrow pH range (2–3), which leads, together with the elaborate processing of the slag, to poor handling and detrimental cost-efficiency of the process.The heterogeneous variant uses catalysts that can be applied to cheap carrier materials of various types.[51-56] Alternatively, the iron-containing catalyst can also be suspended directly in the dye solution. The actual AOP then proceeds via highly reactive radical species, which drive the decomposition of the organic compounds down to water and carbon dioxide. The individual reaction steps for the oxidation process based on the ˙OH radical mechanism (as proposed by Haber and Weiss 1934) can be described as follows:[57]

$Fe^{2+} + H_2O_2$	→	$Fe^{3+} + {}^{\cdot}OH + OH^-$	$K_1 = 76\ M^{-1}S^{-1}$	(1)
${}^{\cdot}OH$ + org.	→	˙org. → … → $H_2O + CO_2$	$K_2 \sim 10^7–10^{10}\ M^{-1}S^{-1}$	(2)
${}^{\cdot}OH + H_2O_2$	→	${}^{\cdot}OH_2 + H_2O$	$K_3 = (1.2\text{-}4.5) \cdot 10^7\ M^{-1}S^{-1}$	(3)
$Fe^{2+} + {}^{\cdot}OH$	→	$Fe^{3+} + OH^-$	$K_4 = 4.3 \cdot 10^8\ M^{-1}S^{-1}$	(4)
${}^{\cdot}OH + {}^{\cdot}OH$	→	H_2O_2	$K_5 = 5.3 \cdot 10^9\ M^{-1}S^{-1}$	(5)
$Fe^{3+} + H_2O_2$	→	$Fe^{2+} + H^+ + {}^{\cdot}O2H$	$K_6 = 0.01–0.02\ M^{-1}S^{-1}$	(6)
$Fe^{3+} + {}^{\cdot}O_2H$	→	$Fe^{2+} + H^+ + O_2$	$K_7 = 3.1 \cdot 10^5\ M^{-1}S^{-1}$	(7)

The reaction of Fe^{2+} ions with H_2O_2 produces the highly reactive hydroxyl radical (equation 1), which has a high redox potential of 2.8 V. The ˙OH then reacts with the organic compound to degrade it via multiple radical intermediates (equation 2) to water and carbon dioxide. The reaction rate for Fe^{2+} ions regenerated from Fe^{3+} is very slow (equation 6) compared to the rate of the oxidation reaction (equation 1). Since Fe^{2+} is the main catalyst species for Fenton reactions, it can be concluded that a greater concentration of ferrous ions can improve the decomposition rate because of the larger amount of hydroxyl radicals produced according to equation (1).
The utilization of Fe-containing compounds in Fenton-like environmental remediation processes have already been widely studied, e.g. zeolites, pillared clays or iron hydroxides and iron oxides were tested for their catalytical performance.[58-61] Furthermore, the specific factors (Fe oxidation state, surface area, crystallinity, pH, temperature and substitution of Fe by other cations), which can affect the Fenton-like reaction, were also discussed in detail.[62-69]

5.3. Porous Silica-Hematite Nanoparticles

5.3.1. Template-Assisted Synthesis

A new route to prepare porous hematite nanoparticles was developed, which uses mesoporous silica nanoparticles (MSN) as templates for the propagation of α-Fe_2O_3 on the surface and in the pores.

Synthesis of the silica template. The preparation of the template followed a report by Zhang et al., with some modifications.[70] In a typical experiment, 24 mL CTAC (25*wt*% in water) and 0.159 mL triethanol amine (TEA) were mixed in 36 mL water and then preheated at 70 °C for 1 h under stirring (150 rpm). Next, a mixture of 4 mL TEOS in 16 mL cyclohexane was added carefully without stirring, so that no mixing of organic phase and aqueous phase occurred. The resulting biphasic mixture was then stirred at 70 °C for another 18 h. After that time, the aqueous phase turned completely white due to precipitation of MSN. The organic phase was removed carefully using a syringe and the aqueous phase was centrifuged after adding ⅓ of *vol*% ethanol. The centrifugation process was repeated three times.

For the removal of templating agents off the MSN surface a detemplation method according to Fenton was applied. For that, 10 mL of the MSN dispersion in water were suspended in 100 mL H_2O_2 (30*wt*%) at room temperature, followed by the addition of 200 µL $Fe(NO_3)_3 \cdot 9\ H_2O$ from a stock solution (2.5 g in 50 mL H_2O). That mixture was heated at 80 °C for 2 h in a preheated oil bath. After the reaction, the remaining solution was centrifuged at 9000 rpm for 10 min. The supernatant was disposed, whereas the precipitated MSN particles were treated with the same Fenton reaction a second time. Finally, the as-obtained particles were dried at 80 °C for 12 h.

Synthesis of hematite nanoparticles. The synthesis of α-Fe_2O_3 was performed solvothermally using an one-pot procedure. A suspension of 75 mg $FeCl_3 \cdot 6\ H_2O$ in 10 mL water and 50 mg MSN in 10 mL water was stirred at room temperature for 1 h to provide sufficient impregnation of the iron precursor compound on the MSN particles. After adding an appropriate amount of NaF (15 mg, 30 mg or 40 mg) as etching agent to dissolve the MSN *in-situ*, the suspension was stirred for another 20 min. Afterwards, the mixture was transferred to a Teflon®-lined vessel, which was sealed in a stainless steel autoclave prior to be subjected to heating in an electric oven at 200 °C for a certain amount of time (2–48 h). The as-obtained orange to dark-red particles were washed with water and ethanol twice and dried *in vacuo*.

5.3.2. Characterization

The morphology of the MSN, hematite nanoparticles (HP) and silica-hematite particles (SHP) synthesized at different times and with varying concentrations of sodium fluoride was analyzed by TEM. In the following, four of the SHP synthesized with 30 mg NaF as etching agent will be discussed in detail, all other analytical data can be found in the appendix.

Mesoporous silica particles and pure hematite. Figure 79 shows TEM images of the as-synthesized silica particles, which were used as templates for the preparation of mesoporous hematite nanoparticles. The spherical particles exhibit a dense core and well-defined conical pores with 10 nm widths on the outer part and a decrease in pore size to 2 nm on the inner part. Total particle diameters vary from 160–180 nm for single particles and up to 270 nm for agglomerates of twin particles.

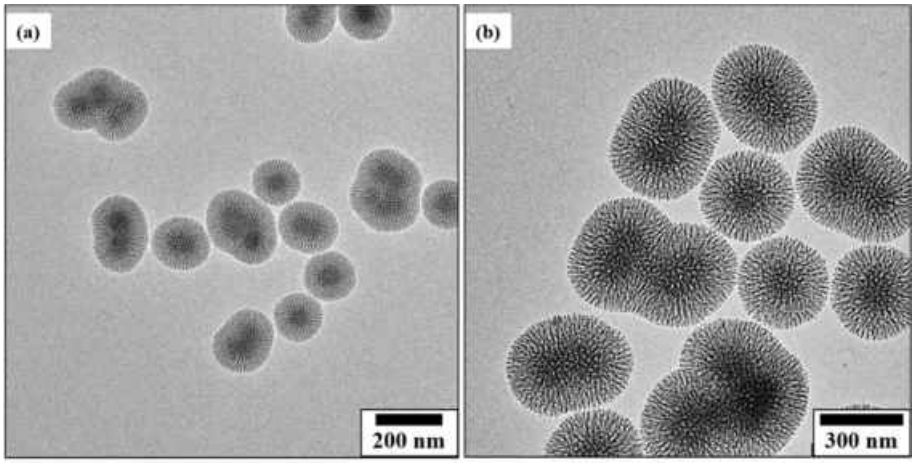

Figure 79. Low-magnification TEM images of the MSN particles obtained from the CTAC method.

Structural examinations with XRD demonstrate the well-known amorphous character of the MSN particles (Figure 80).

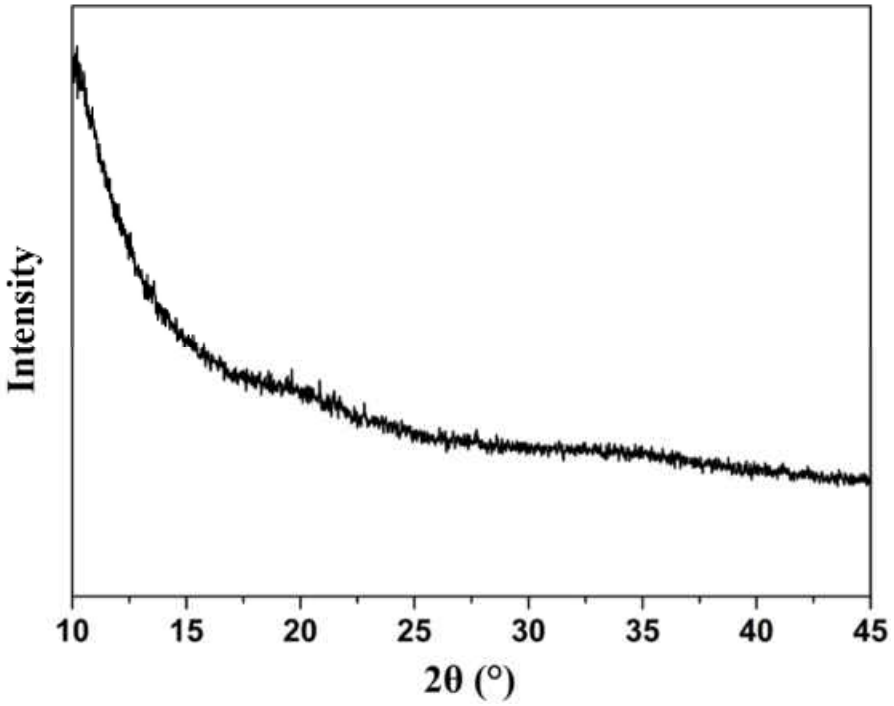

Figure 80. XRD pattern of as-synthesized MSN.

The reference experiments without utilization of MSN templates exhibit huge hexagonal hematite platelets, about 500–800 nm in diameter (Figure 81). As it is shown in Figure A 196 in the appendix, a decrease of the NaF concentration in the solution yields smaller, quasi-spherical particles. Increasing the amount of NaF to 40 mg results in less uniformity of the particles, while many agglomerates are obtained (Figure A 197, appendix).

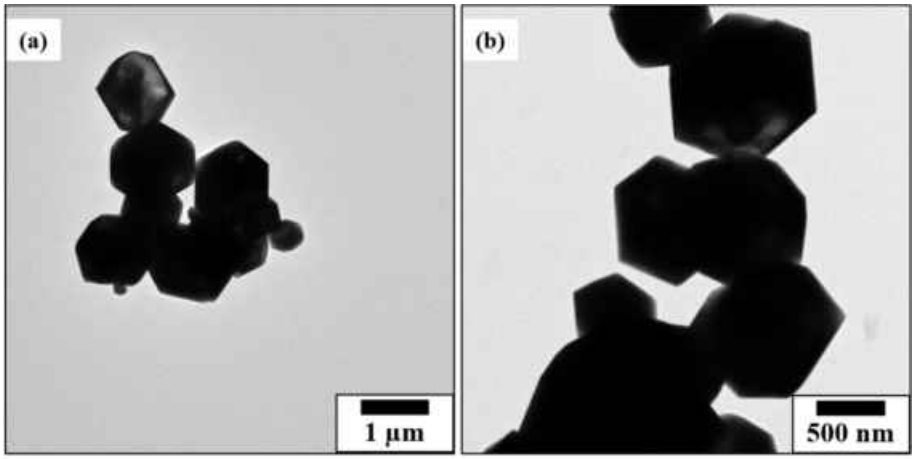

Figure 81. Low-magnification TEM images of hematite particles prepared with 30 mg NaF.

The XRD pattern in Figure 82 confirms that the as-obtained HPs consist of single-crystalline α-Fe_2O_3.

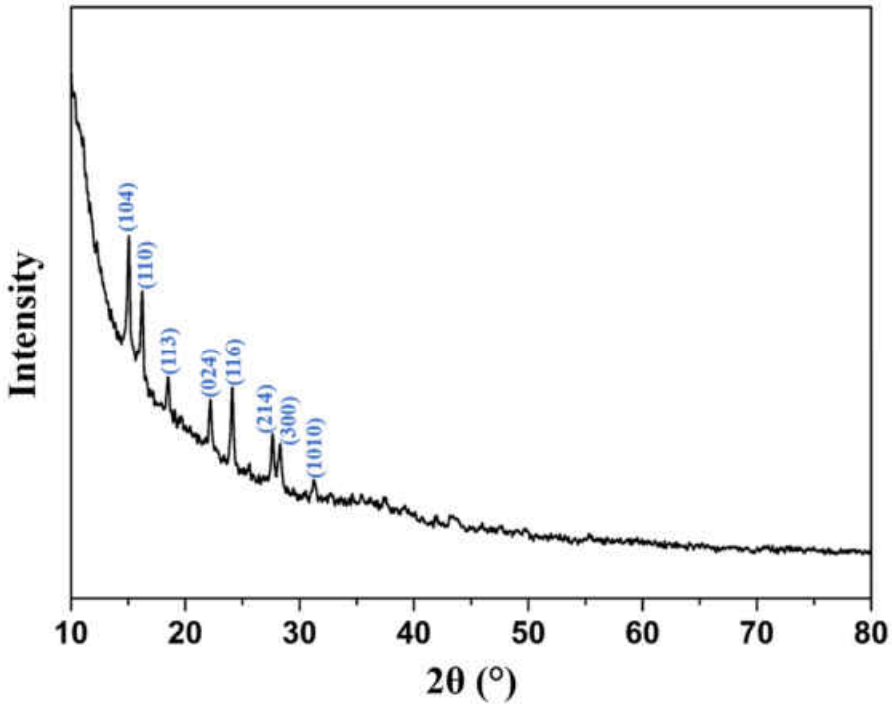

Figure 82. Powder XRD pattern of hematite platelets synthesized as reference material. The strong background below 2θ = 30 ° is caused by the Magic Scotch tape used for sample preparation. All Miller indices can be assigned to the hematite phase.

Silica-hematite-particles. The silica-hematite particles prepared with 30 mg NaF as *in-situ* etching agent were synthesized at different reaction times. In the following, the focus will be on four different samples with different reaction times (6 h, 12 h, 24 h and 48 h), all other experiments and their data are presented in the appendix.

Figure 83 shows TEM images from different areas of the grid of the sample prepared at 6 h reaction time. At first, it can be seen that the product is very inhomogeneous since many large structures have been formed in addition to unused mesoporous silica material. Furthermore, platelet-like shapes of different dimensions can be observed (Figure 83 a, b). Images of individual smaller particles (Figure 83 c, d) show their similarity to the silica template, while the porous structure appears to be strongly damaged. The clean pores, which characterize the mesoporous silica, are collapsed to a large extent.

In Figure A 179–Figure A 187 the evolution of the particles morphology over reaction time and amount of NaF, is presented. In general, the shorter the reaction time and the less NaF is added to the solution, the less homogeneous products are obtained. Neither the product after 2 h nor the one after 4 h reaction time exhibits the pseudo-mesoporous morphology, as most of the silica template is left unreacted in both cases. With an excess of 40 mg NaF all structures collapse into flake-like particles.

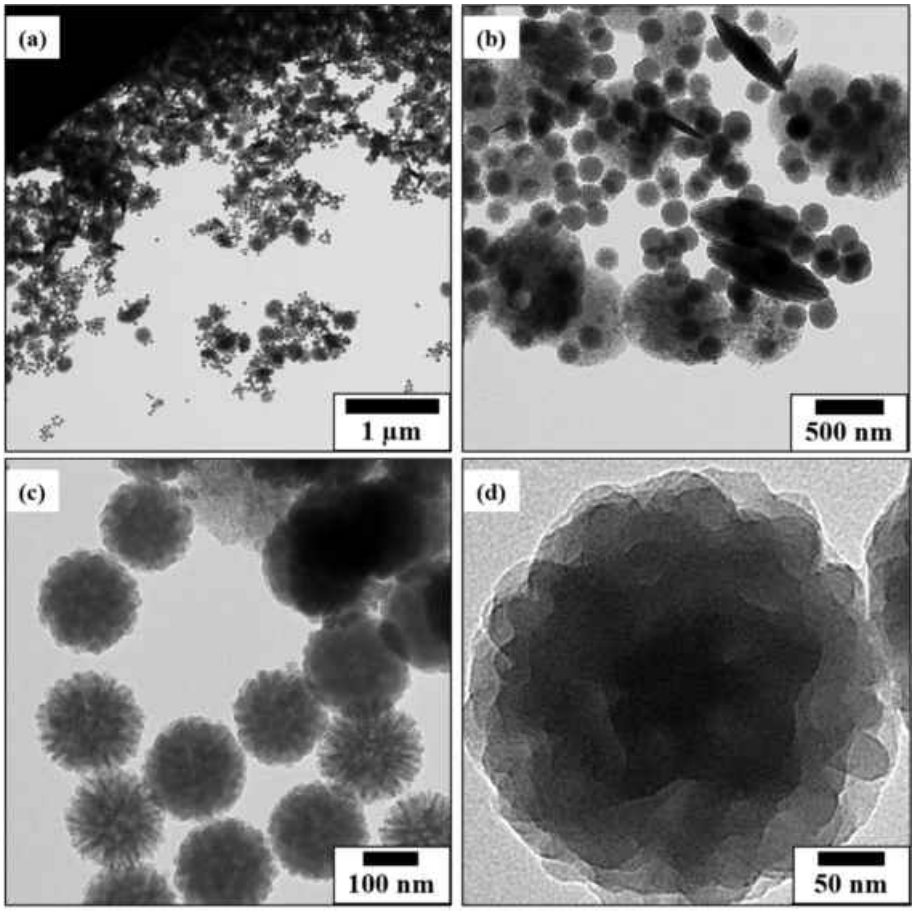

Figure 83. (a-d) TEM images of the particles obtained after 6 h reaction time, captured in different areas of the TEM grid.

TEM images of a single mesoporos particle, which were taken with tilting of the specimen holder to the incident electron beam at two different angles, show that the particle apparently appears to be intrinsically non-homogeneous (Figure 84). For example, no porosity of the surface can be observed under a tilting angle -40 ° (Figure 84 a, d). The particles look rather polished, with a smooth surface. When tilting at +40 ° to the plane, a softening of the porosity is shown again, but not as drastic as in the case of reversal (Figure 84 c, f).

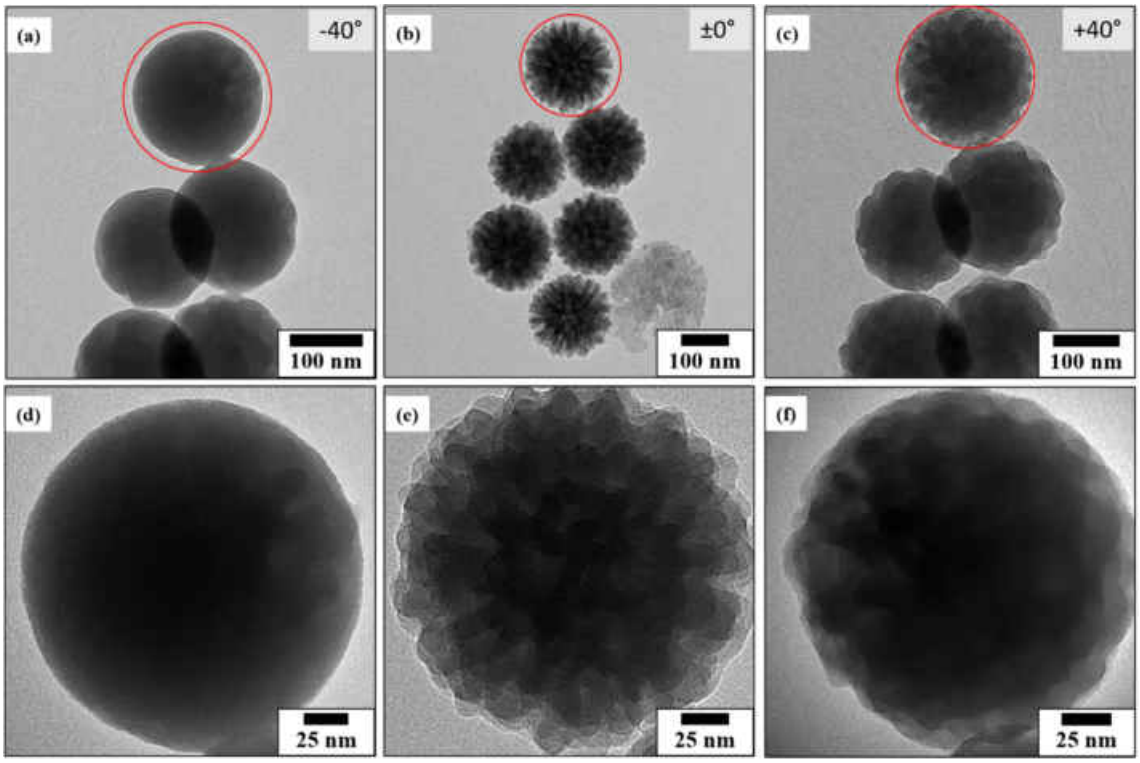

Figure 84. TEM images of a tilting series of a single particle obtained after 6 h reaction time: (a, d) -40 ° tilting, (b, e) no tilting and (c, f) +40 ° tilting imaging of the SHP.

HR-SEM analysis of the 6 h sample reveals that the product consists of two distinct particle types (Figure 85): round platelets with up to 700 nm diameter and nanospheres (250 nm diameter) with a porous surface.

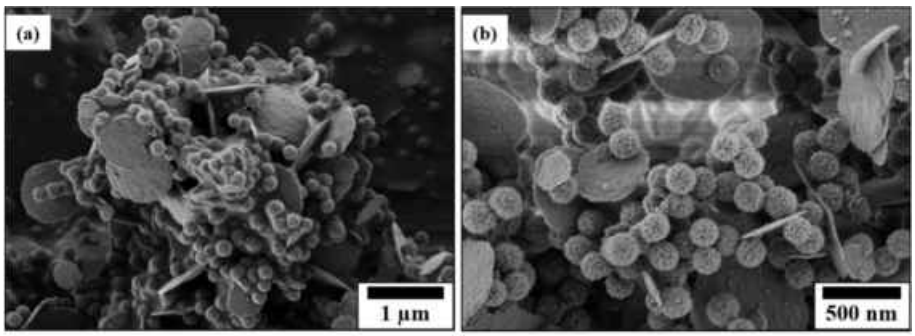

Figure 85. HR-SEM images of the particles obtained after 6 h reaction time.

The XRD pattern of this products shows a strong background at values of $2\theta < 40°$, caused by the amorphous silica phase (Figure 86). All distinct reflections can thus be attributed to the hematite phase.

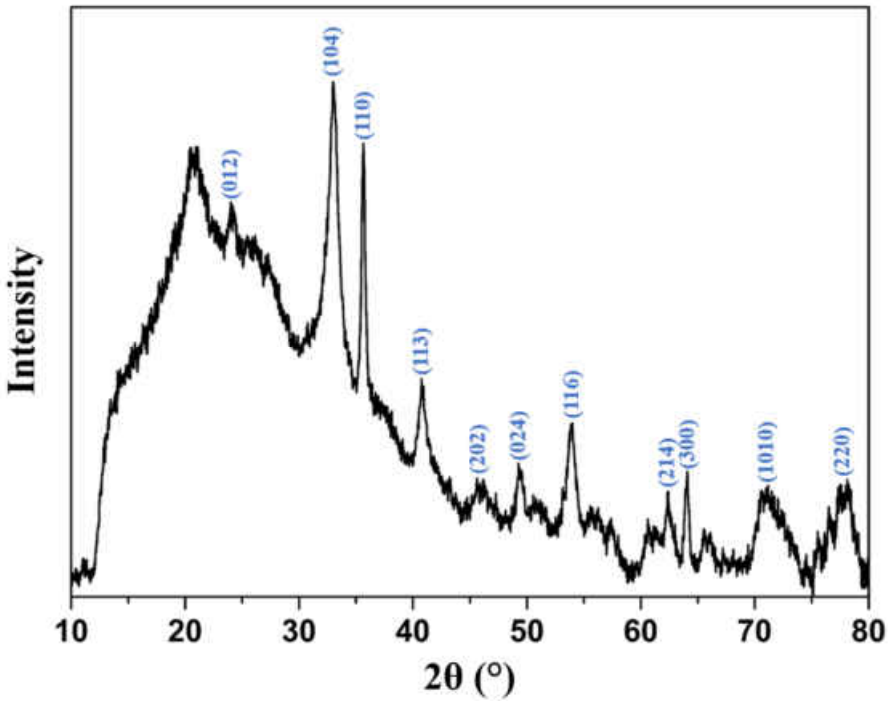

Figure 86. XRD pattern of the product obtained after 6 h reaction time. All noted Miller indices are attributed to the hematite phase.

The product with 12 h reaction time provides a similar morpholgy. The TEM images show collapsed mesoporous silica particles (Figure 87), while no platelets could be observed on the TEM grid. In addition, the pseudo-porous particles have a smaller diameter (~150 nm) than those from the 6 h reaction. This could be due to the fact that more time was available to the etchant, which is why the dissolution process of the silica template has advanced further. A focus-defocus series of TEM images shown in Figure A 188 suggests that the particles obtained are built up more homogeneously than the ones obtained after 6 h.

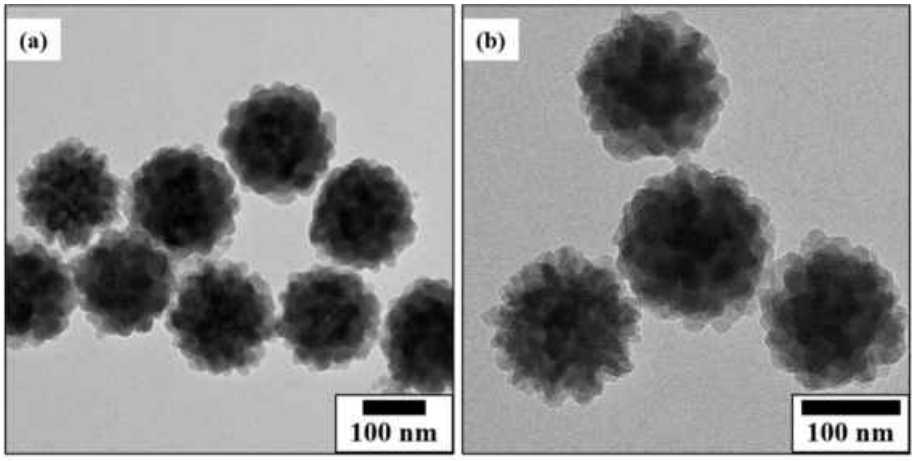

Figure 87. (a, b) TEM images of the particles obtained after 12 h reaction time.

However, the HR-SEM images in Figure 88 reveal that platelets with different diameters can also be found in this sample. The associated EDS data provides a composition of iron oxides for the platelets and silicon oxide for the spherical nanoparticles (Figure A 173 and Figure A 174).

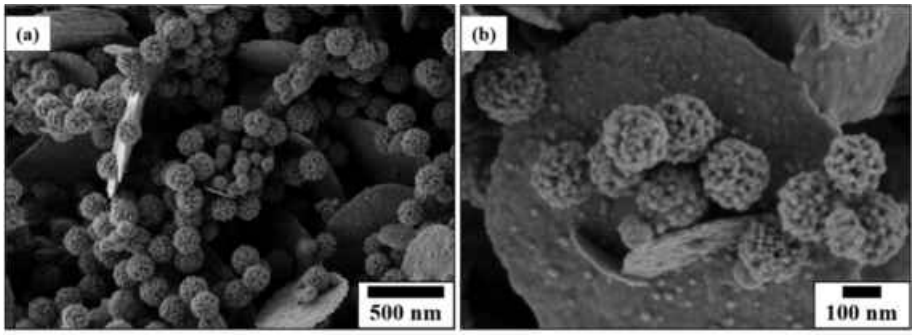

Figure 88. (a, b) HR-SEM images of the particles obtained after 12 h reaction time.

The XRD pattern of the product after 12 h shows a similar structure as after 6 h. Here again an amorphous background dominates at smaller diffraction angles, whereby all sharp reflections can be assigned to the hematite phase (Figure 89).

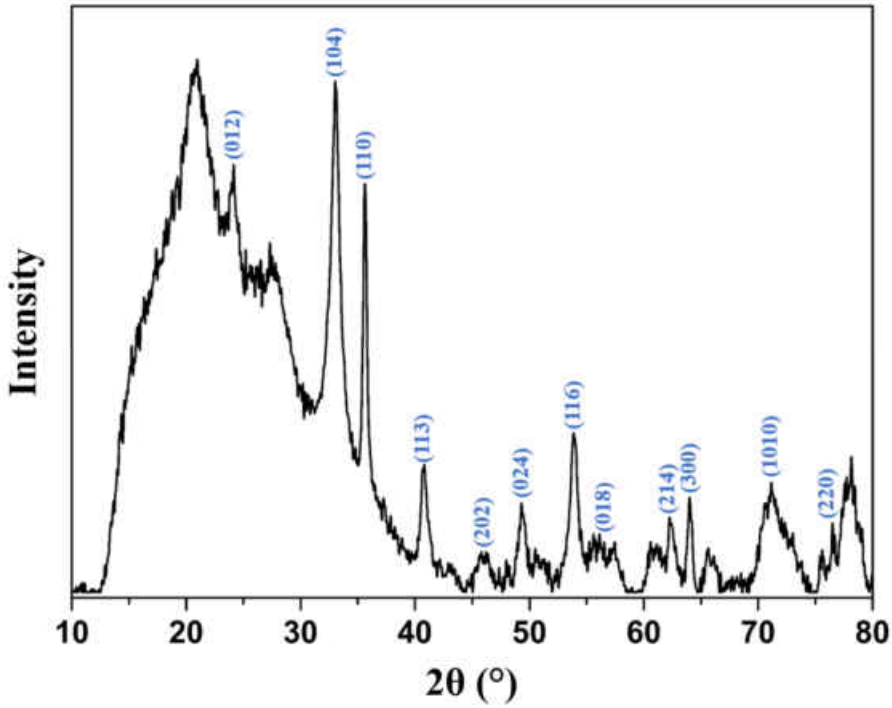

Figure 89. XRD pattern of the product obtained after 12 h reaction time. All noted Miller indices are attributed to hematite phase.

All characteristic Raman bands can be observed in the spectra of this product, which is shown in Figure 90. The typical vibration modes of A_{1g} (220 and 491 cm^{-1}) are accompanied by the E_g modes (286, 403 and 601 cm^{-1}) with a slight shift compared to spectra presented elsewhere.[71] Furthermore, a broadening of the magnon scattering band at 1303 cm^{-1} is detected, which can be ascribed to the presence of silica species in the product.[72, 73] Notably, no significant substitution

of Fe by Si is evident, because the specific band at ~659 cm^{-1} cannot be observed.[74] This band could be correlated with Si-doping of α-Fe_2O_3 and a formation of Si-O, as reported earlier.[75, 76]

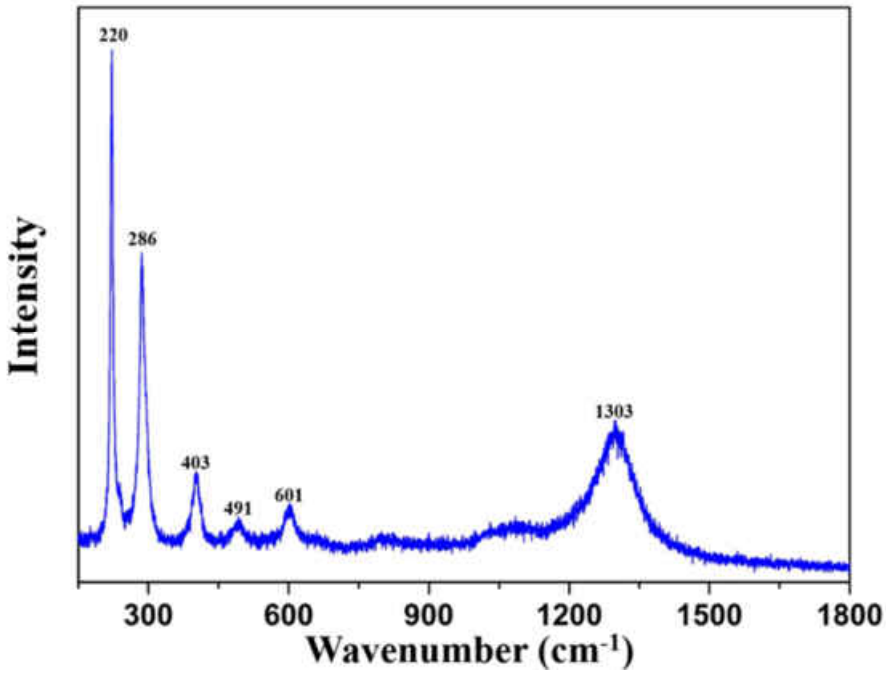

Figure 90. Raman spectra of the SHP obtained after 12 h reaction time, showing all characteristic bands of hematite

After 24 h reaction time, no porous particles can be observed in the TEM images, but rather smaller, spherical particles have predominantly been formed (Figure 91). These have diameters of 30–40 nm, but a closer look reveals that they are strongly interconnected. Even the larger agglomerates are based on a cyclic pattern, which can be seen particularly clear in Figure 91 (d). These round structures, which are up to 300 nm in diameter, have an almost completely dense shell, the surface also being rich in defects. Within the shell, porous structures can be seen, these holes having different shapes and revealing extensions of up to 20 nm.

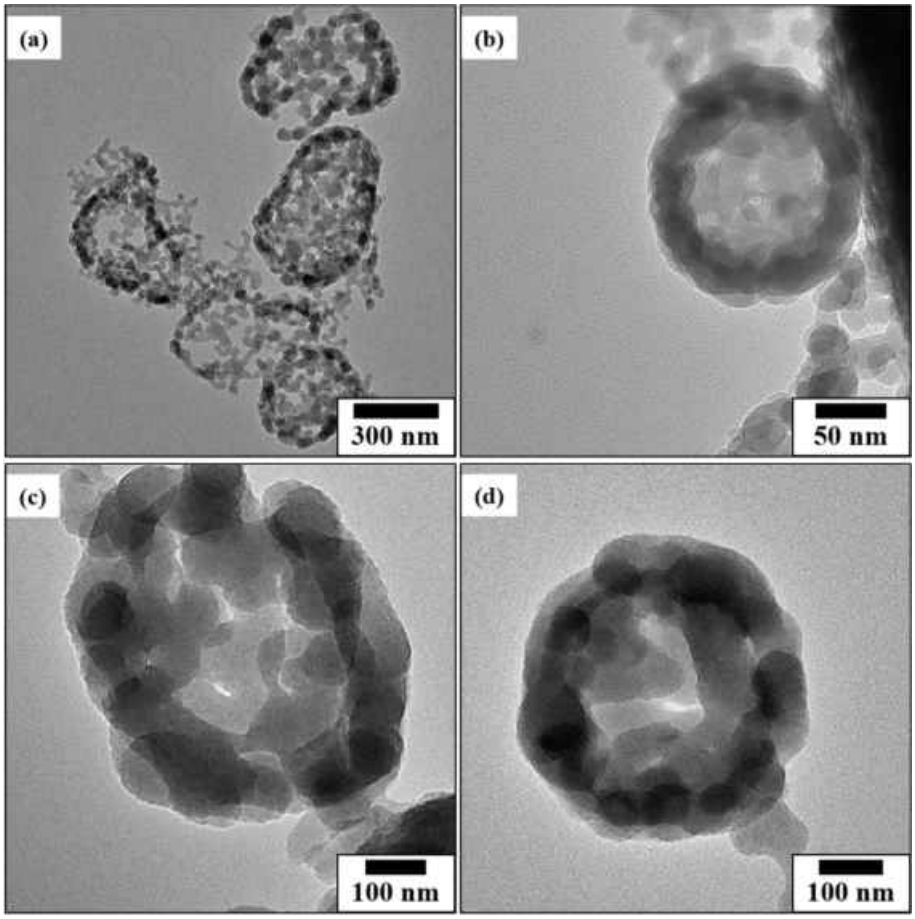

Figure 91. (a-d) TEM images of the particles obtained after 24 h reaction time.

However, the HR-SEM images in Figure 92 reveal that the product consists not only of the particles shown in the TEM images, but unused silica spheres and iron oxide platelets are also present in an inhomogeneous mixture. Furthermore, it can be seen in Figure 92 (b) that some of the spherical particles are hollow. In addition to the two particle types mentioned, however, relatively small particles (< 100 nm) are also observed, which are most likely those from Figure 91. Overall, this sample appears to be very inhomogeneous, since e.g. the silica spheres are also more damaged than in the two products shown after 6 h or 12 h.

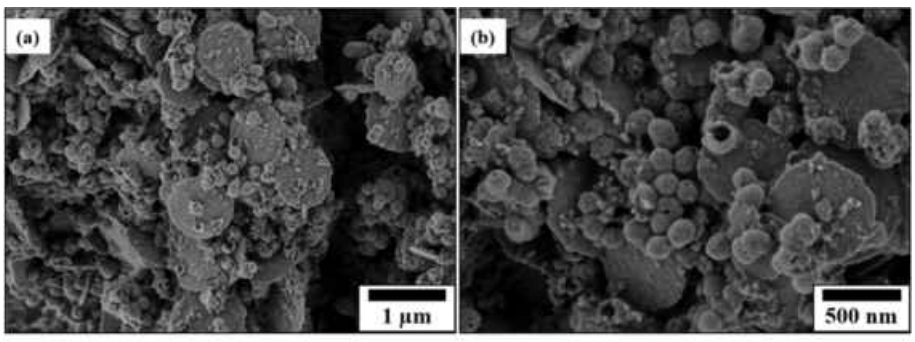

Figure 92. (a, b) HR-SEM images of the particles obtained after 24 h reaction time.

In order to provide more precise statements concerning the qualitative and quantitative composition of the particles shown in Figure 91, EDS measurements were carried out on the

corresponding samples. As shown in the data in Figure A 175 and Figure A 176, both silicon and iron are detected in the particles. The percentage composition of the atomic ratio (13: 1 of Fe: Si) suggests that the growth of iron particles occurrs on the silicate templates. Since the NaF only attacks the silica in the reaction solution, this means that during the growth of the iron particles an intergrowth is favored due to shrinking of the silica core. This probably leads to the observed porous structures of the larger agglomerates. A residual content of silica, however, obviously remains in the particles and cannot be removed by washing with water.

However, the fact that the concentration of silica in the product is not at all distant nor still relatively high and the destroyed silica obviously cannot be removed by washing steps is reflected in the XRD pattern in Figure 93. The well-known intense and wide background dominates below diffraction angles less than $2\theta = 40$ °. All other reflexes can be assigned to the hematite phase. Obviously, the sodium fluoride can indeed destroy the mesoporous silica spheres during this reaction time, but it cannot completely convert the silica into the soluble sodium silicate form.

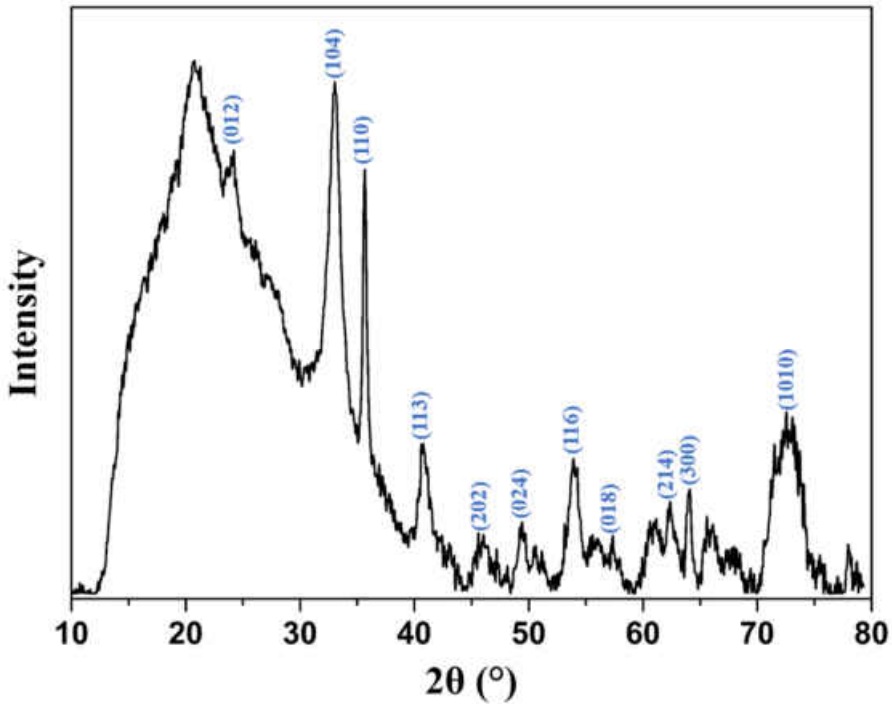

Figure 93. XRD pattern of the product obtained after 24 h reaction time. All noted Miller indices are attributed to hematite phase.

The Raman spectra of this product in Figure 94 reveals the same characteristic bands of hematite, which were discussed earlier.

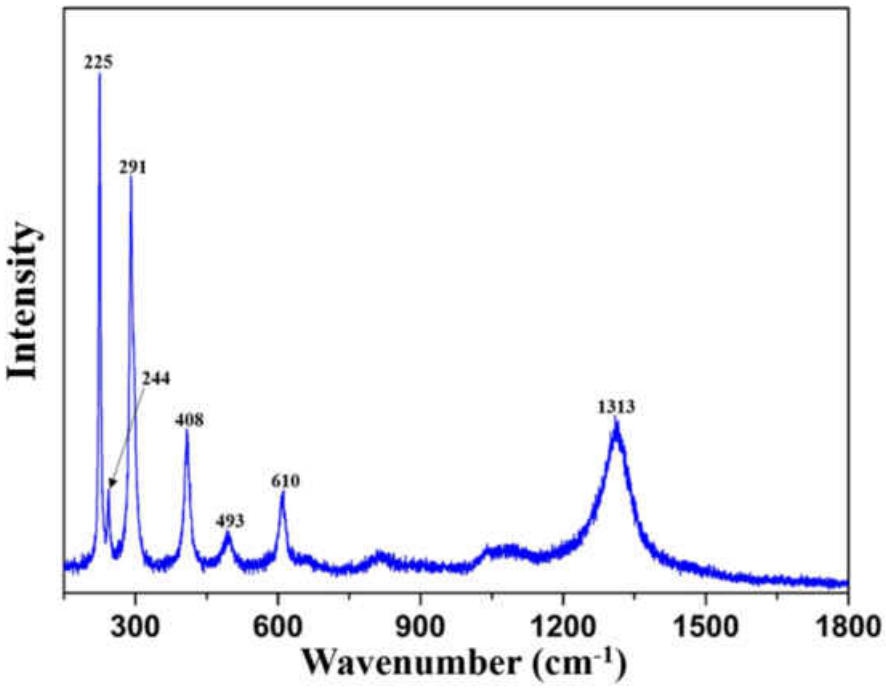

Figure 94. Raman spectra of the SHP obtained after 24 h reaction time, showing all characteristic bands of hematite.

The product after 48 h has some similarity to that after 24 h, since also small (~ 20 nm) quasi-spherical particles are fused into larger structures (Figure 95). In this case, however, the larger agglomerates are no longer based on a round structure but rather exhibit random morphologies. Within the larger interconnections, bigger porous cavities of up to 20 nm can be seen, which is a strong indication of a porous structure.

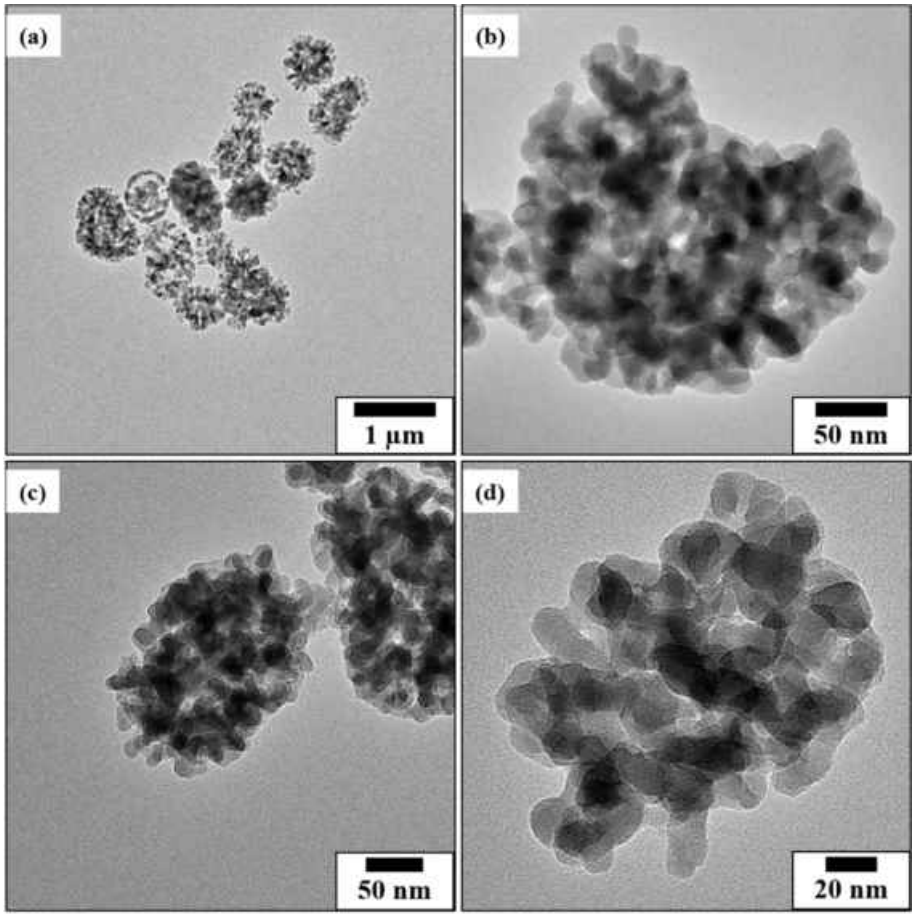

Figure 95. TEM images of the particles obtained after 48 h reaction time.

An EDS analysis of the particles obtained was carried out (Figure A 177 and Figure A 178, appendix). It is found that the residual silicon content in the particles is significantly lower compared to the 24 h reaction since a 13:1 ratio of iron to silicon was detected.

A mixture of different spherical and platelet-like particles can be observed in the HR-SEM images in Figure 96. It is also noticeable that all particle types seem to be fused together into an amorphous structure. This indicates that the interaction between the etchant and the silica was more pronounced than in the previous syntheses at shorter reaction times. The silica is thus dissolved to a greater extent.

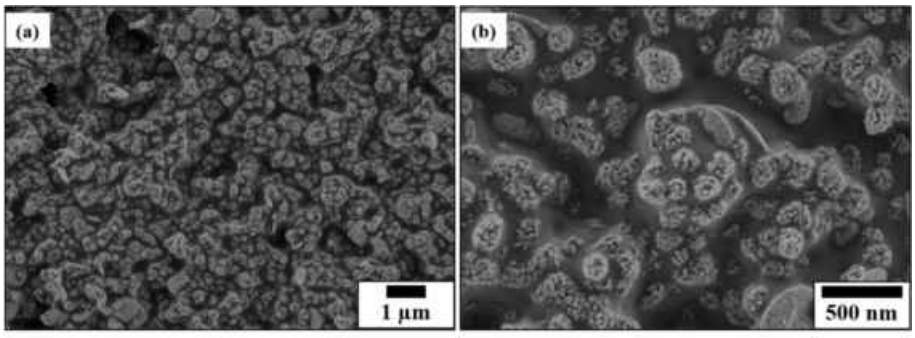

Figure 96. (a, b) HR-SEM of the particles obtained after 48 h reaction time.

The appropriate diffraction pattern shows all relevant reflexes of the hematite phase, whereby a significantly lower amorphous background is observed at smaller diffraction angles. This again indicates that the silica dissolution benefits from longer reaction times.

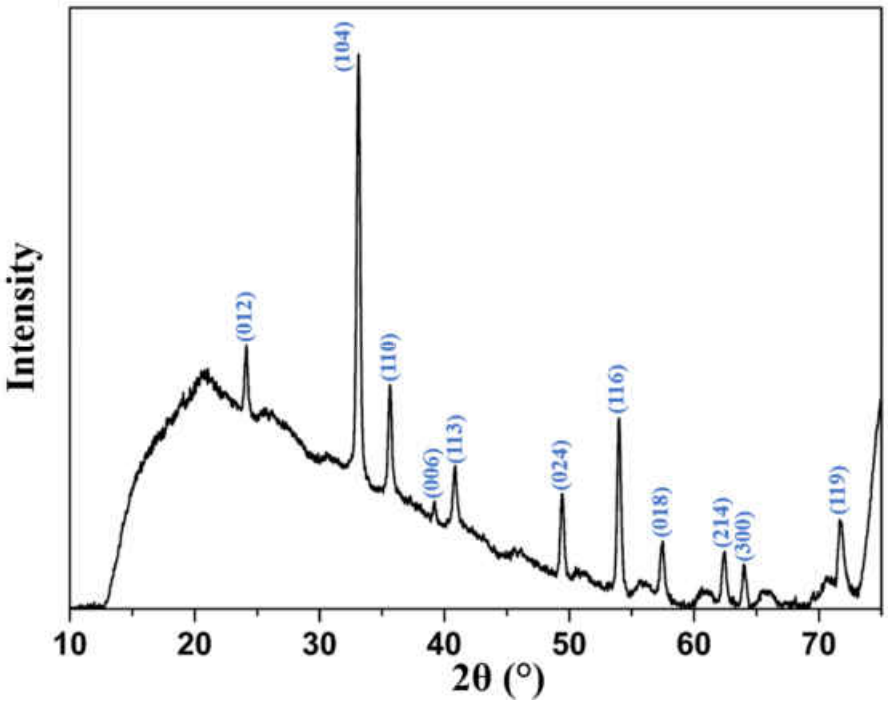

Figure 97. XRD pattern of the product obtained after 48 h reaction time. All noted Miller indices are attributed to hematite phase.

The Raman spectrum of the sample shows all the characteristic bands of the hematite, but less pronounced widening compared to the 24 h sample.

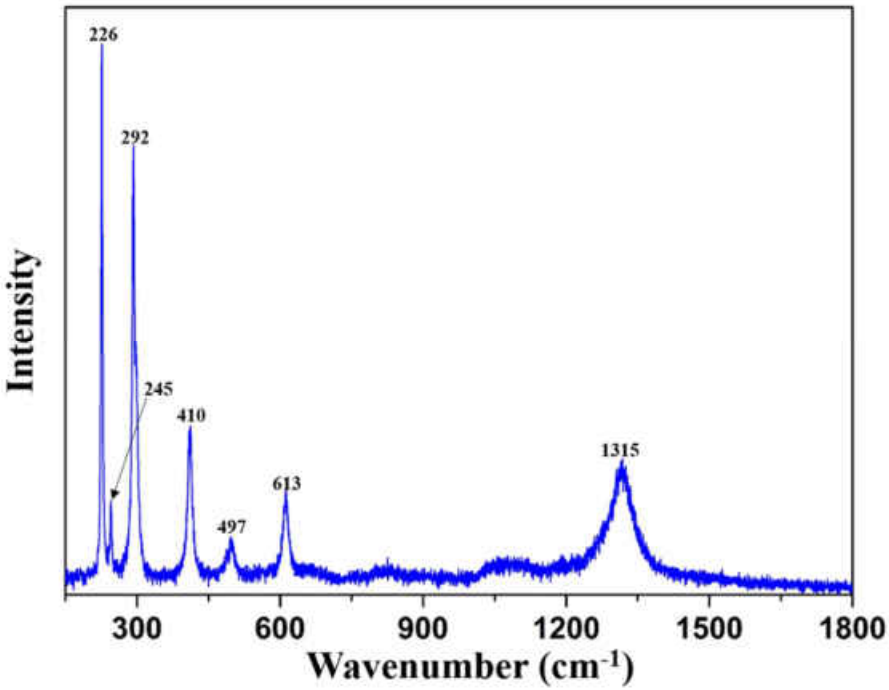

Figure 98. Raman spectrum of the SHP obtained 48 h reaction time.

The absorption spectrum of all presented compounds except the 48 h samples shows the absorption maxima being at 450 nm. At this, the absorption of the pure hematite reference substance shows the highest intensity, followed by the 24 h sample and the two samples with less reaction time. Interestingly, a significant redshift of the absorption maximum to 580 nm can be observed in the 48 h sample. As described in other reports, the absorption spectrum can be subdivided into three regions.[77] The absorption bands between 250–400 nm are attributed to ligand-to-metal charge transfer (LMCT) transitions with combined contributions of the Fe^{3+} ligand field transitions ($^6A^1(^6S)$ to $^4T_1(^4P)$) at 290–310 nm, ($^6A_1(^6S)$ to $^4E(^4D)$) and ($^6A_1(^6S)$ to $^4T_1(^4D)$) at 360–380 nm.[78] In the second region (400–600 nm) pair excitation processes dominate, such as $^6A_1(^6S) + {}^6A_1(^6S)$ to $^4T_1(^4G) + {}^4T_1(^4G)$ at 410–460 nm, which are overlapped by contributions of $^6A_1(^6S)$ to ^4E, $^4A_1(^4G)$ ligand field transitions at 430 nm and the LMCT transition band tail.[79, 80] The region of 600–780 nm corresponds to the $^6A_1(^6S)$ to $^4T_2(^4G)$ ligand field transition at ~630 nm. Among these interband transitions, the double exciton process $^6A_1(^6S) + {}^6A_1(^6S)$ to $^4T_1(^4G) + {}^4T_1(^4G)$ yields the strongest absorption band. It is therefore primarily responsible for the red color of hematite.

It was also reported that the color of hematite nanoparticles and the position of the absorption maxima is affected by size, shape, structure and phase of the nanostructures.[81-87] This might explain why the absorption maximum of the SHP-48h (with the smallest particles observed) is shifted compared to the other products.

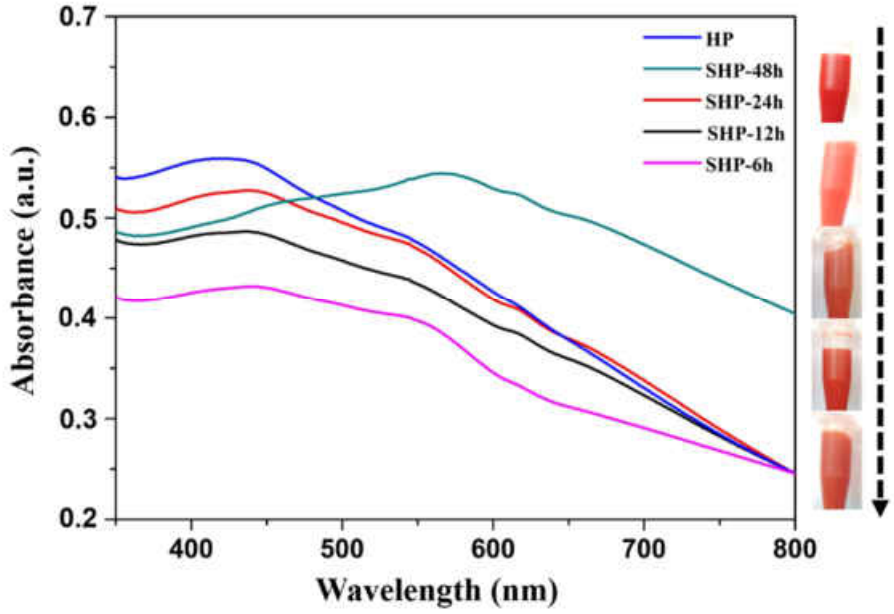

Figure 99. Absorption spectra of silica-hematite particles prepared at different reaction times (SHP-6h – SHP-48h) and pure hematite particles (HP).

5.3.3. Degradation of Rhodamine B

The porous hematite particles were investigated on their catalytic ability in the degradation of Rhodamine B (RB). As one of the most important xanthene dyes, RB (Figure 100) is known for its good stability in effluents. Thus, it is a well-suited model compound in order to monitor the efficiency of wastewater discoloration by means of UV-vis absorption.

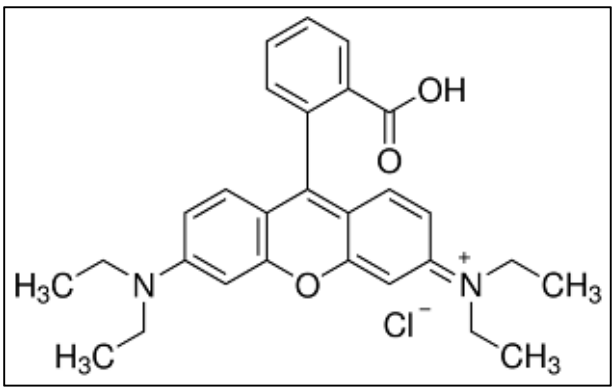

Figure 100. Structure of Rhodamine B in its cationic form, shown as valence bond model.

For the catalytical measurements of the RB degradation a $1 \cdot 10^{-5}$ mol/L aqueous stock solution was prepared. Then, 150 mL of this solution were transferred to a 400 mL beaker and the pH value of the solution was adjusted to 3 using diluted NaOH and HCl. As has been demonstrated by Feng et al.,[88] the pH value has a significant influence on the degradation rate in Fenton-like oxidation reactions due to the possible *in-situ* formation of a $H_3O_2^+$ species, which occurs below pH 3 and stabilizes the H_2O_2. At a pH value higher than 3, the hydrolysis of Fe^{2+} becomes more

dominant and a precipitation of FeOOH from the solution occurs. Thus, the formation of ˙OH radicals is retarded. Prior to the addition of 5.82 mol/L H_2O_2, 25 mg of the appropriate catalyst was dispersed in the solution under stirring in the dark for 1 h to ensure an adsorption-desorption equilibrium of RB on the catalyst surface. All experiments were carried out at 25 °C. During the experiments, aliquots (3 mL) were withdrawn from the mixture at regular time intervals, immediately centrifuged at 9000 rpm for 15 min and the separated supernatant's UV-vis spectra was measured to monitor the catalytic decomposition of RB aqueous solution. A calibration curve was calculated based on the values obtained from the absorption maxima of different aliquots (prepared from the stock solution) at λ_{max} = 554 nm, both illustrated in Figure 101. The calibration curve was derived as the linear fit of the values in the [(Absorbance at 554 nm) *vs*. (Concentration of RB)] plotting and is therefore determined to be $y = (1.1287 \pm 0.0083) \cdot x - (0.0040 \pm 0.0025)$.

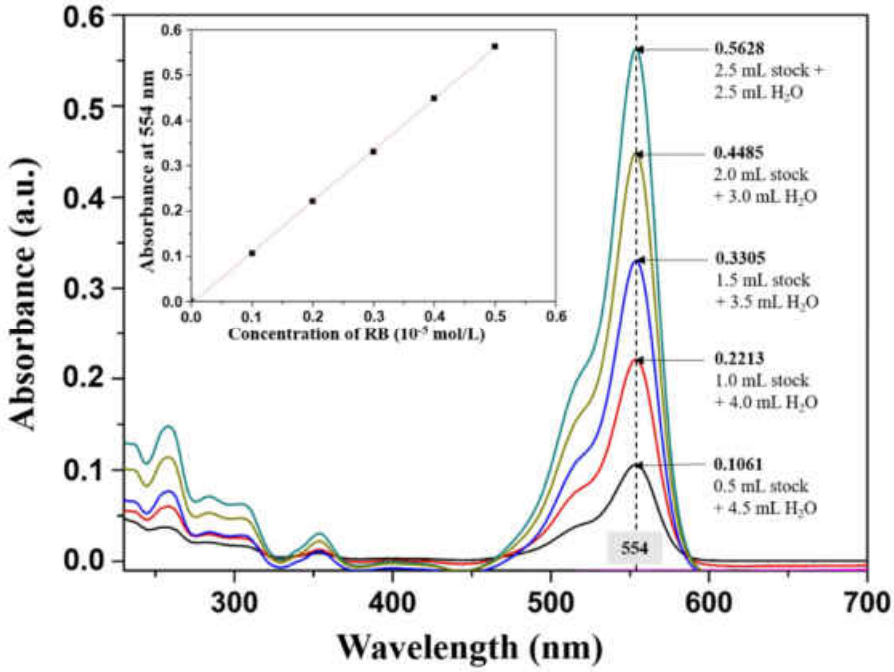

Figure 101. Absorption spectra of Rhodamine B aqueous solutions with different concentrations. The inset shows the linear fit of the plotting of the absorption Values at 554 nm versus the concentration of RB solution.

To examine, whether a synergistic effect between silica and iron oxide enhances a higher degradation rate, four different experiments were conducted: with H_2O_2 only, silica particles and H_2O_2, hematite particles and H_2O_2, 48 h silica-hematite particles and H_2O_2.

Measurements without catalyst. Figure 102 shows the UV-visible absorption spectral changes of RB aqueous solution without the addition of any catalyst, but with H_2O_2 in the solution. The

graph shows that H_2O_2 is able to provide for a discoloration of RB, but not completely. Even after a reaction time of 8000 min, the aqueous solution still contains 27% of unreacted RB.

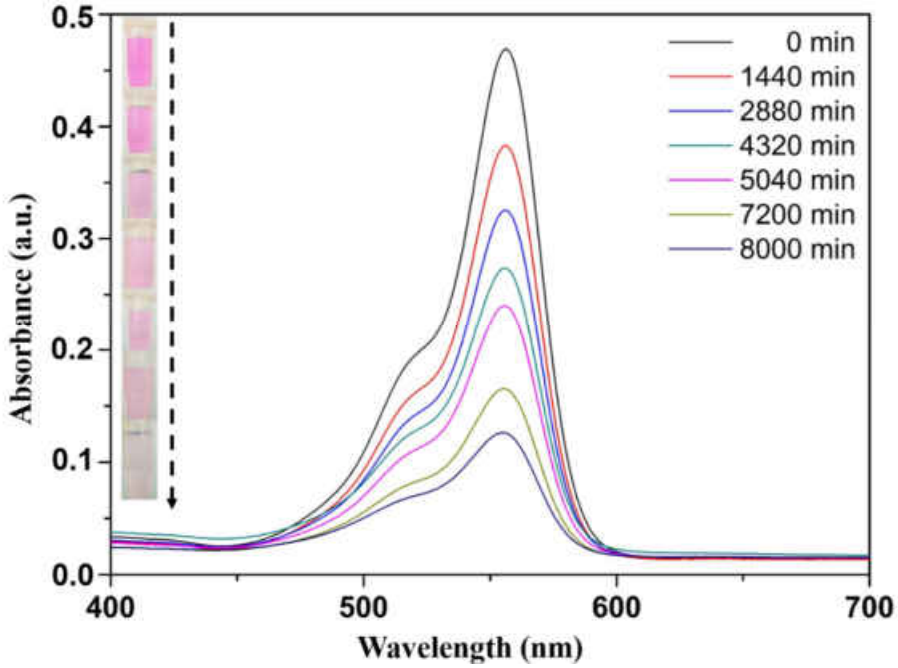

Figure 102. Absorption spectra of Rhodamine B aqueous solution at different degradation times, with $0.5 \cdot 10^{-5}$ mol/L RB and 5.82 mol/L H_2O_2. The inset shows photographs of the measured solutions of RB at the appropriate time periods.

The decomposition of Rhodamine B is based on the catalytically accelerated decomposition of only one component, and thus only depends on the concentration of the RB. Therefore, a pseudo-first order kinetics can be assumed for this reaction. Hence, the rate equation for the degradation of RB in presence of H_2O_2 can be written as:

$$d[RB]/dt = -k[H_2O_2]^m[RB] = -k'[RB],$$

with $-k[H_2O_2]^m$ as the apparent rate constant. The unreacted fraction of RB can be determined by comparing the concentration of RB determined at the appropriate time with the concentrations specified by the calibration curve. The curve obtained by plotting

$$\ln([RB]/[RB]_0) = \ln(r) = -k't$$

over the reaction time t then yields the apparent rate constant as the slope of the curve. The relationship between ln(r) and the degradation time is depicted in Figure A 198 in the appendix. The apparent rate constant for the degradation of RB in the presence of H_2O_2 is therefore $k'(H_2O_2) = (2.53 \pm 0.14) \cdot 10^{-4}$ min^{-1}.

Measurements with silica-hematite particles and H_2O_2. The evolution of the absorption spectra of RB aqueous solution in the presence of 25 mg SHP-48h and 5.815 mol/L H_2O_2 is illustrated in Figure 103. The absorption intensity of the solution before the addition of H_2O_2 (0 min) is slightly lower compared to the measurements without any porous particles. Due to the molecular size of RB of ~1 nm^3 it can easily be incorporated by the pores of the mesoporous adsorbent.[89, 90] Thus, the mesoporous silica particles act as molecular scavengers.[91] Since the catalyst-RB-suspension is stirred before the start of the oxidative decomposition, the pores can be saturated with RB in the process and therefore the concentration of free RB in the solution is significantly reduced. As the degradation process continues over time, the incorporation also impedes a faster decomposition since an equilibrium of free and incorporated RB is established. After 1440 min reaction time the discoloration of RB is at 95%.

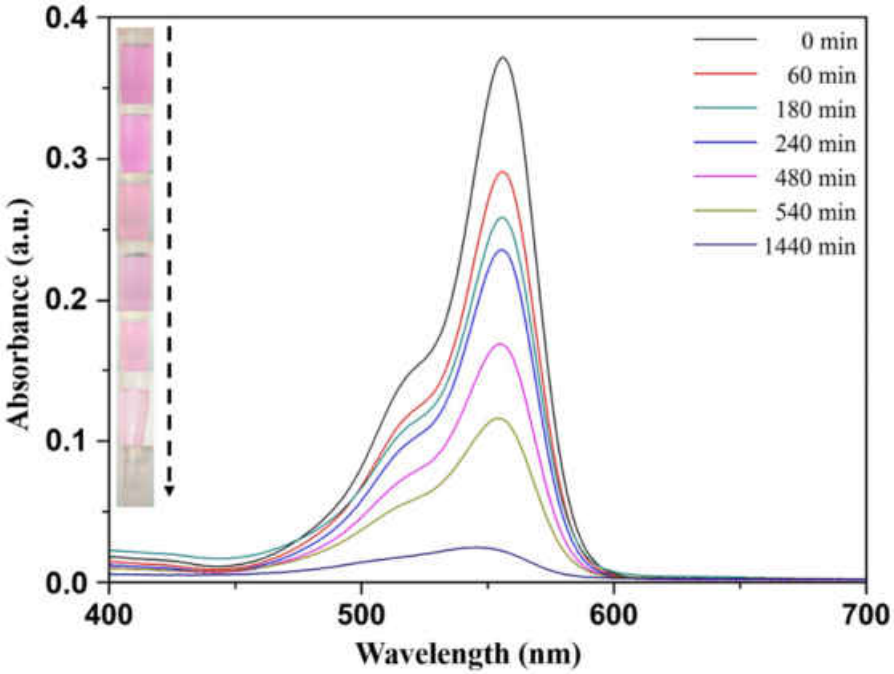

Figure 103. Absorption spectra of Rhodamine B aqueous solution at different degradation times, with $0.5 \cdot 10^{-5}$ mol/L RB, 25 mg SHP-48h and 5.82 mol/L H_2O_2. The inset shows photographs of the measured solutions of RB at the appropriate time periods.

The apparent rate constant for the degradation of RB with SHP-48h and H_2O_2 was calculated as the slope of the ln(r)/t-curve shown in Figure A 199 in the appendix. It is therefore k'(SHP-48h) = $(2.20 \pm 0.07) \cdot 10^{-3}$ min^{-1}. Despite the preceding incorporation of RB into the pores, the rate constant is significantly increased by one order of magnitude compared to the reaction without catalyst. This can be explained by the fact that pure iron oxide particles, silica-hematite-particles and remnants of silica particles are present in the product. Since the Fenton-like degradation of RB is promoted by iron oxide surfaces, it is thus not surprising that a bigger amount of iron oxide in the suspension significantly accelerates the reaction. Nonetheless, the retarding effect of the mesopores is not negligible.

Measurements with hematite particles and H_2O_2. The absorption spectra of RB aqueous solution in the presence of 25 mg HP and 5.82 mol/L H_2O_2 are illustrated in Figure 104. The concentration of RB drastically drops to 80% within 10 min reaction time. In general, the reaction proceeds significantly faster and is almost completed after 70 min, where only 4% of unreacted RB is left in the solution.

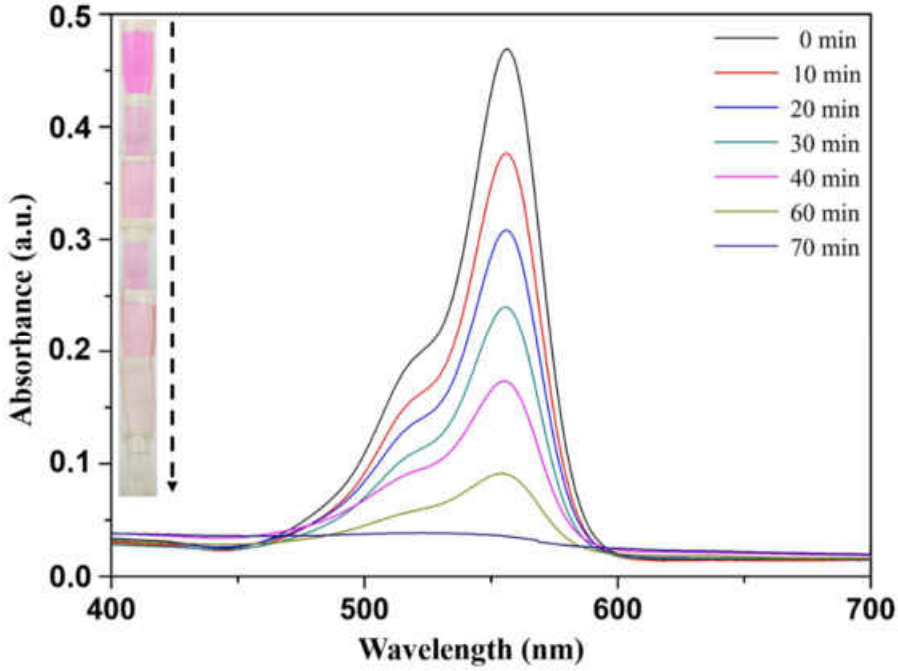

Figure 104. Absorption spectra of Rhodamine B aqueous solution at different degradation times, with $0.5 \cdot 10^{-5}$ mol/L RB, 25 mg HP and 5.82 mol/L H_2O_2. The inset shows photographs of the measured solutions of RB at the appropriate time periods.

The apparent rate constant for the decomposition using HP as catalyst was calculated from the fitting curve in Figure A 200 and is k'(HP) = $(3.65 \pm 0.41) \cdot 10^{-2}$ min^{-1}. As a result, the reaction occurs even faster than the one observed for the SHP-48h and H_2O_2 mixture. That is evident from a mechanistic point of view, as the concentration of iron oxide is increased in this mixture and no retarding effect due to incorporation of RB into pores is expected.

Measurements with mesoporous silica particles and H_2O_2. The evolution of the absorption spectra of RB aqueous solution in the presence of 25 mg MSN and 5.815 mol/L H_2O_2 is illustrated in Figure 105. Herein, a decrease of the absorption maximum at the beginning of the reaction can be observed, which is comparable to the SHP-48h. The MSN provide a bigger contact area, where the dye molecules can react with the reactive peroxide species. Therefore, the decomposition rate of RB is slightly higher compared to the oxidation in the absence of a catalyst. After a reaction time of 7200 min the solution still contains 12% of undegraded RB.

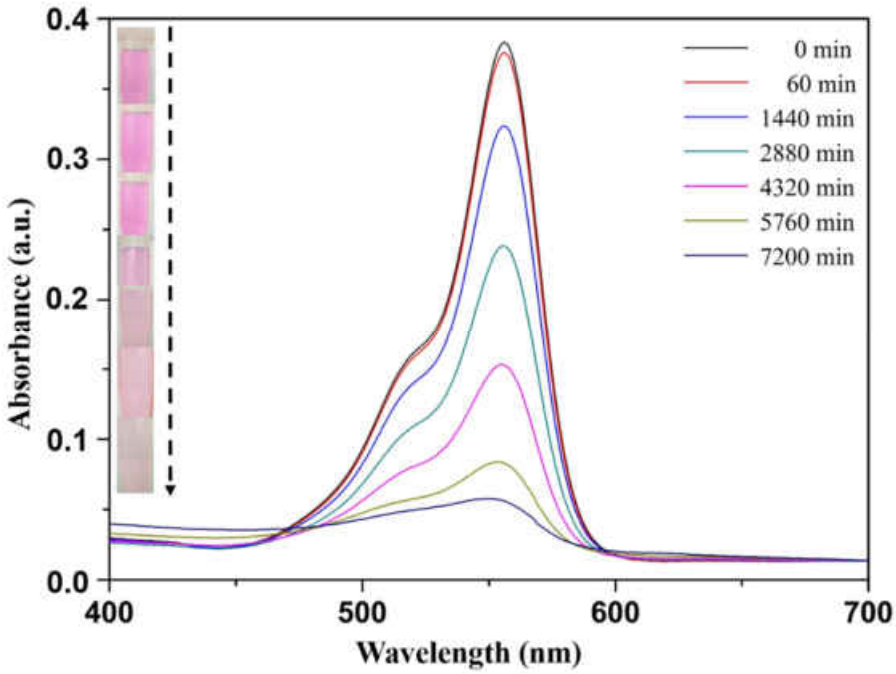

Figure 105. Absorption spectra of Rhodamine B aqueous solution at different degradation times, with $0.5 \cdot 10^{-5}$ mol/L RB, 25 mg MSN and 5.815 mol/L H_2O_2. The inset shows photographs of the measured solutions of RB at the appropriate time periods.

The fitting curve of the decomposition with MSN particles and H_2O_2 shown in Figure A 201 yields an apparent constant of k'(MSN) = $(3.12 \pm 0.07) \cdot 10^{-4}$ min^{-1}. Figure 106 comprises an overview of all four measured kinetics by comparing the discoloration efficiencies of the different catalyst systems over time.

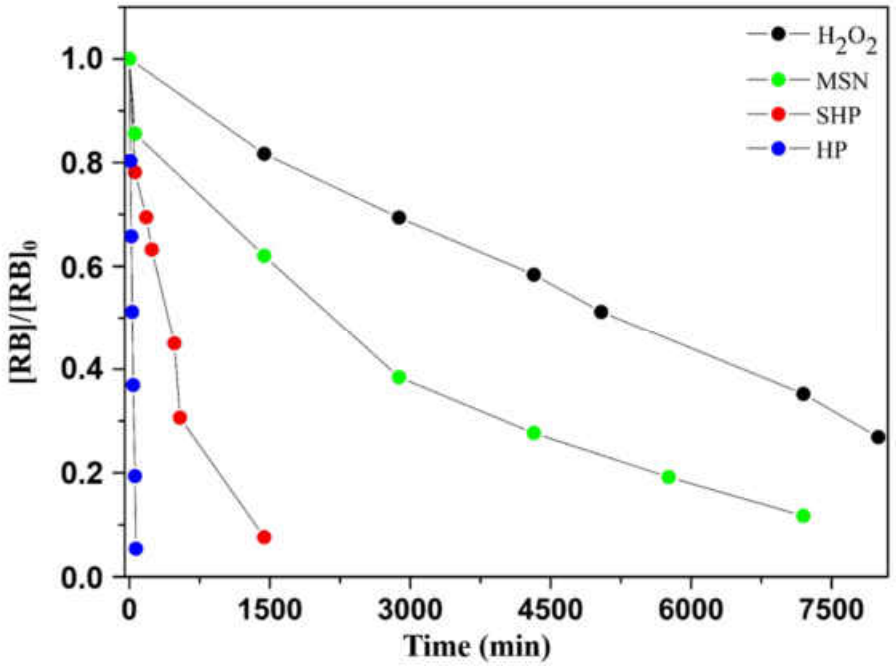

Figure 106. Relationship of unreacted fraction of Rhodamine B and the degradation time in terms of the catalyst used in the reaction.

It can clearly be seen that the pure hematite particles provide a rapid decomposition of RB within 70 min. The SHP-48h display a high activity which, however, is significantly lower compared to HP, due to reasons described above. Using MSN as catalyst does not confer any significant advantage regarding the degradation rate compared to pure H_2O_2.

5.4. Conclusion

In this chapter, a new synthesis of pseudo-porous iron oxide particles was presented. Mesoporous silica act as templates and provide nucleation sites for the growth of iron oxide particles, while long reaction times are required to obtain porous silica-hematite structures However, it was not possible to synthesize pure mesoporous hematite particles since a residual amount of silicon always remained in the product due to the growth of the iron oxide on its surface.

The silicate-hematite particles (SHPs) were, however, tested as catalysts for the decomposition of Rhodamine B. In these Fenton-like reactions it was shown that the SHPs react retarded compared to pure hematite particles due to the remnants of mesoporous silica. This was reflected in much lower reaction rates. However, the product itself showed significantly higher conversion rates than in the absence of a catalyst. Thus, if the silica can be completely removed from the product, these particles may prove to be promising catalysts for dye decomposition.

5.5. References of Chapter 5

[1] L. Suber, P. Imperatori, A. Mari, G. Marchegiani, M. Vasquez Mansilla, D. Fiorani, W. R. Plunkett, D. Rinaldi, C. Cannas, G. Ennas, D. Peddis, *Phys. Chem. Chem. Phys.* 2010, **12**, 6984-6989.

[2] H. M. Lu, X. K. Meng, *J. Phys. Chem. C* 2010, **114**(49), 21291-21295.

[3] S. Jung, S. Bae, W. Lee, *Environ. Sci. Technol.* 2014, **48**(16), 9651-9658.

[4] Z. S. Fishman, Y. He, K. R. Yang, A. W. Lounsbury, J. Zhu, T. M. Tran, J. B. Zimmerman, V. S. Batista, L. D. Pfefferle, *Nanoscale* 2017, **9**, 12984-12995.

[5] J. Pal, T. Pal, *Nanoscale* 2015, **7**, 14159-14190.

[6] P. V. Nidheesh, *RSC Adv.* 2015, **5**, 40552-40577.

[7] D. Walter, *Thermochimica Acta* 2006, **445**(2), 195-199.

[8] J. Wang, W. B. White, J. H. Adair, *J. Am. Ceram. Soc.* 2005, **88**(12), 3449-3454.

[9] M. A. Legodi, D. de Waal, *Dyes Pigm.* 2007, **74**(1), 161-168.

[10] J. Ma, J. Teo, L. Mei, Z. Zhong, Q. Li, T. Wang, X. Duan, J. Lian, W. Zheng, *J. Mater. Chem.* 2012, **22**, 11694-11700.

[11] P. Wang, Z. Zheng, X. Cheng, L. Sui, S. Gao, X. Zhang, Y. Xu, H. Zhao, L. Huo, *J. Mater. Chem. A* 2017, **5**, 19846-19856.

[12] Y. Wang, S. Wang, H. Zhang, X. Gao, J. Yang, L. Wang, *J. Mater. Chem. A* 2014, **2**, 7935-7943.

[13] S. Yan, Q. Wu, *J. Mater. Chem. A* 2015, **3**, 5982-5990.

[14] S. Yan, G. Zan, Q. Wu, *Nano Res.* 2015, **8**(11), 3673-3686.

[15] F. Herrera, A. Lopez, G. Mascolo, P. Albers, J. Kiwi, *Appl. Catal. B* 2001, **29**(2), 147-162.

[16] H. Sharghi, M. Jokar, M. M. Doroodmand, R. Khalifeh, *Adv. Synth. Catal.* 2010, **352**(17), 3031-3044.

[17] X. Zhou, J. Lan, G. Liu, K. Deng, Y. Yang, G. Nie, J. Yu, L. Zhi, *Angew. Chem.* 2012, **124**(1), 182-186.

[18] T. Fujii, M. Kayano, Y. Takada, M. Nakanishi, J. Takada, *Solid State Ionics* 2004, **172**(1-4), 289-292.

[19] H. Yang, W. Mi, H. Bai, Y. Cheng, *RSC Adv.* 2012, **2**, 10708-10716.

[20] J. Lian, X. Duan, J. Ma, P. Peng, T. Kim, W. Zheng, *ACS Nano* 2009, **3**(11), 3749-3761.

[21] S. D. Tilley, M. Cornuz, K. Sivula, M. Grätzel, *Angew. Chem.* 2010, **122**(36), 6549-6552.

[22] Y. Qiu, S.-F. Leung, Q. Zhang, B. Huan, Q. Lin, Z. Wie, K.H. Tsui, Y. Zhang, S. Yang, Z. Fan, *Nano Lett.* 2014, **14**(4), 2123-2129.

[23] R. Zhang, Y. Fang, T. Chen, F. Qu, Z. Liu, G. Du, A. M. Asiri, T. Gao, X. Sun, *ACS Sustainable Chem. Eng.* 2017, **5**(9), 7502-7506.

[24] Z. Hu, Z. Shen, J. C. Yu, *Chem. Mater.* 2016, **28**(2), 564-572.

[25] D. Danaei, R. Saeidi, A. Dabirian, *RSC Adv.* 2015, **5**, 11946-11951.

[26] W. Li, S. W. Sheehan, D. He, Y. He, X. Yao, R. L. Grimm, G. W. Brudvig, D. Wang, *Angew. Chem. Int. Ed.* 2015, **54**(39), 11428-11432.

[27] B. Iandolo, H. Zhang, B. Wickman, I. Zoric, G. Conibeer, A. Hellman, *RSC Adv.* 2015, **5**, 61021-61030.

[28] M. Einert, R. Ostermann, T. Weller, S. Zellmer, G. Garnweitner, B. M. Smarsly, R. Marschall, *J. Mater. Chem. A* 2016, **4**, 18444-18456.

[29] X. Zhao, J. Feng, S. Chen, Y. Huang, T. C. Sum, Z. Chen, *Phys. Chem. Chem. Phys.* 2017, **19**, 1074-1082.

[30] J. Y. Kim, G. Magesh, D. H. Youn, J.-W. Jang, J. Kubota, K. Domen, J. S. Lee, *Sci. Rep.* 2013, **3**, 2681.

[31] X. Cai, H. Lin, X. Zheng, X. Chen, P. Xia, X. Luo, X. Zhong, X. Li, W. Li, *Electrochimica Acta* 2016, **191**, 767-775.

[32] Y. Jiang, D. Zhang, Y. Li, T. Yuan, N. Bahlawane, C. Liang, W. Sun, Y. Lu, M. Yan, *Nano Energy* 2014, **4**, 23-30.

[33] S. Zeng, K. Tang, T. Li, Z. Liang, D. Wang, Y. Wang, Y. Qi, W. Zhou, *J. Phys. Chem. C* 2008, **112**(3), 4836-4843.

[34] S.-B. Wang, Y.-L. Min, S.-H. Yu, *J. Phys. Chem. C* 2007, **111**(9), 3551-3554.

[35] H. Cao, G. Wang, *Appl. Phys. Lett.* 2008, **92**, 013110.

[36] X. Lu, Y. Zeng, M. Yu, T. Zhai, C. Liang, S. Xie, M.-S. Balogun, Y. Tong, *Adv. Mater.* 2014, **26**(19), 3148-3155.

[37] J. Li, S. K. Cushing, P. Zheng, F. Meng, D. Chu, N. Wu, *Nat. Commun.* 2013, **4**, 2651.

[38] Y. Ling, G. Wang, J. Reddy, C. Wang, J. Z. Zhang, Y. Li, *Angew. Chem.* 2012, **124**(17), 4150-4155.

[39] D. R. Cummins, H. B. Russell, J. B. Jasinski, M. Menon, M. K. Sunkara, *Nano Lett.* 2013, **13**(6), 2423-2430.

[40] C.-J. Jia, L.-D. Sun, Z.-G. Yan, L.-P. You, F. Luo, X.-D. Han, Y.-C. Pang, Z. Zhang, C.-H. Yan, *Angew. Chem.* 2005, **117**(28), 4402-4407.

[41] C. Eid, D. Luneau, V. Sallest, R. Asmar, Y. Monteil, A. Khoury, A. Brioude, *J. Phys. Chem. C* 2011, **115**(36), 17643-17646.

[42] X. Hu, J. C. Yu, J. Gong, Q. Li, G. Li, *Adv. Mater.* 2007, **19**(17), 2324-2329.

[43] G. Drazic, G. Stefanic, T. Jurkin, M. Gotic, *J. Mol. Struct.* 2017, **1140**, 113-121.

[44] J. A. Cuenca, K. Bugler, S. Taylor, D. Morgan, P. Williams, J. Bauer, A. Porch, *J. Phys. Condens. Mat.* 2016, **28**(10), 106002.

[45] E. Callen, *Phys. Rev.* 1966, **150**(2), 367-376.

[46] The United Nations World Water Assessment Programme, *The United Nations World Water Development Report 2017. Wastewater: The Untapped Resource.* UNESCO, Paris, 2017.

[47] J. K. Edzwald, *Water quality & treatment: a handbook on drinking water.* McGraw-Hill, New York, 2011.

[48] S. Parsons (Ed.), *Advanced Oxidation Processes for Water and Wastewater Treatment.* IWA Publishing, Cornwall, UK, 2004.

[49] H. J. H. Fenton, *J. Chem. Soc. Trans.* 1894, **65**, 899-910.

[50] E. Neyens, J. Baeyens, *J. Hazard. Mater.* 2003, **98**(1-3), 33-50.

[51] R. Andreozzi, M. Canterino, V. Caprio, I. Di Somma, R. Marotta, *J. Hazard. Mater.* 2008, **152**, 870-875.

[52] R. Gonzalez-Olmos, F. Holzer, F. D. Kopinke, A. Georgi, *Appl. Catal. A* 2011, **398**, 44-53.

[53] I. R. Guimaraes, L. C. A. Oliveira, P. F. Queiroz, T. C. Ramalho, M. Pereira, J. D. Fabris, J. D. Ardisson, *Appl. Catal. A* 2008, **347**, 89-93.

[54] M. Luo, D. Bowden, P. Brimblecombe, *Appl. Catal. B* 2009, **85**, 201-206.

[55] N. Amaral-Silva, R. C. Martins, P. Nunes, S. Castro-Silva, R. M. Quinta-Ferreira, *J. Chem. Technol. Biot.* 2017, **96**(6), 1336-1344.

[56] S. Giannakis, S. Liu, A. Carratala, S. Rtimi, M. T. Amiri, M. Bensimon, C. Pulgarin, *J. Hazard. Mater.* 2017, **339**, 223-231.

[57] J. H. Suna, S. H. Shia, Y. F. Leea, S. P. Sun, *Chem. Eng. J.* 2009, **155**, 680-683.

[58] M. Aleksic, H. Kusic, N. Koprivanac, D. Leszczynska, A. L. Bozic, *Desalination* 2010, **257**, 22-29.

[59] S. Guo, G. K. Zhang, Y. D. Guo, J. C. Yu, *Carbon* 2013, **276**, 437-444.

[60] J. Y. Feng, X. J. Hu, P. L. Yue, *Water. Res.* 2006, **40**, 641-646.

[61] J. X. Chen, L. Z. Zhu, *J. Hazard. Mater.* 2011, **185**, 1477-1481.

[62] I. Robles, F. J. Rodriguez-Valadez, E. Castano, L. A. Godinez, *Sustain. Env. Res.* 2017, **27**(1), 24-31.

[63] A. Fischbacher, C. von Sonntag, T. C. Schmidt, *Chemosphere* 2017, **182**, 738-744.

[64] M. Hermanek, R. Zobril, I. Medrik, J. Pechousek, C. Gregor, *J. Am. Chem. Soc.* 2007, **129**, 10929-10936.

[65] R. C. C. Costa, M. F. F. Lelis, L. C. A. Oliveira, J. D. Fabris, J. D. Ardisson, R. R. V. A. Rios, C. N. Silva, R. M. Lago, *J. Hazard. Mater.* 2006, **129**, 171-178.

[66] C. Gregor, M. Hermanek, D. Jancik, J. Pechousek, J. Filip, J. Hrbac, R. Zboril, Eur. *J. Inorg. Chem.* 2010, 2343-2351.

[67] R. Prucek, M. Hermanek, R. Zboril, *Appl. Catal. A* 2009, **366**, 325-332.

[68] Y. S. Jung, W. T. Lim, J. Y. Park, Y. H. Kim, *Environ. Technol.* 2009, **30**, 189-190.

[69] T. R. Gordon, A. L. Marsh, *Catal. Lett.* 2009, **132**, 349-354.

[70] Z. Zhang, A. Myoral, I. Melian-Cabrera, *Micropor. Mesopor. Mat.* 2016, **220**, 110-119.

[71] J. Liu, C. Liang, H. Zhang, S. Zhang, Z. Tian, *Chem. Commun.* 2011, **47**, 8040-8042.

[72] X. M. Zhou, H. C. Yang, C. X. Wang, X. B. Mao, Y. S. Wang, Y. L. Yang, G. Liu, *J. Phys. Chem. C* 2010, **114**, 17051.

[73] D. Parras-Guijarro, M. Montejo-Gamez, N. Ramos-Martos, A. Sanchez, *Spectrochim. Acta A* 2006, **64**, 1133.

[74] I. Cesar, K. Sivula, A. Kay, R. Zboril, M. Grätzel, *J. Phys. Chem. C* 2009, **113**, 772.

[75] R. J. Hemley, H. K. Mao, P. M. Bell, B. O. Mysen, *Phys. Rev. Lett.* 1986, **57**, 747.

[76] M. Ivanda, R. Clasen, M. Hornfeck, W. Kiefer, *J. Non-Cryst. Solids* 2003, **322**, 46.

[77] D. A. Wheeler, G. Wang, Y. Ling, Y. Li, J. Z. Zhang, *Energy Environ. Sci.* 2012, **5**, 6682-6702.

[78] C. Jorand Sartoretti, B. D. Alexander, R. Solarska, I. A. Rutkowska, J. Augustynski, R. Cerny, *J. Phys. Chem. B* 2005, **109**, 13685–13692.

[79] D. M. Sherman, T. D. Waite, *Am. Mineral.* 1985, **70**, 11–12.

[80] Y. P. He, Y. M. Miao, C. R. Li, S. Q. Wang, L. Cao, S. S. Xie, G. Z. Yang, B. S. Zou, C. Burda, *Phys. Rev. B: Condens. Matter Mater. Phys.* 2005, **71**, 125411.

[81] J. Wang, W. B. White, J. H. Adair, *J. Am. Ceram. Soc.* 2005, **88**, 3449–3454.

[82] L. Chen, X. Yang, J. Chen, J. Liu, H. Wu, H. Zhan, C. Liang, M. Wu, *Inorg. Chem.* 2010, **49**, 8411–8420.

[83] F. Hund, *Angew. Chem. Int. Ed.* 1981, **20**, 723–730.

[84] N. P. Ryde, E. Matijevic, *Appl. Opt.* 1994, **33**, 7275–7281.

[85] Y. Yamanoi, S. Nakashima, M. Katsura, *Am. Mineral.* 2009, **94**, 90–97.

[86] J. Torrent, V. Barron, *Clays Clay Miner.* 2003, **51**, 309–317.

[87] N. Galvez, V. Barron, J. Torrent, *Clays Clay Miner.* 1999, **47**, 375–385.

[88] J. Y. Feng, X. J. Hu, P. L. Yue, H. Y. Zhu, G. Q. Lu, *Ind. Eng. Chem. Res.* 2003, **42**, 2058-2066.

[89] J.-H. Huang, K.-L. Huang, S.-Q. Liu, A-T. Wang, C. Yan, *Colloids Surf. A* 2008, **330**, 55-61.

[90] Y. Guo, J. Zhao, H. Zhang, S. Yang, J. Qi, Z. Wang, H. Xu, *Dyes Pigment* 2005, **66**, 123-128.

[91] C. R. Martin, Z. Siwy, *Nat. Mater.* 2004, **3**, 284-285.

6. Transition Metal Chalcogenides (TMCs) of W and Mo

6.1. Introduction to TMCs

6.1.1 Nanostructured and Layered TMCs

Transition metal dichalcogenides (TMCs) are in the focus of interest because of their exotic properties and many possible applications. Many properties of these nanomaterials, such as tribological behavior, mechanical strength, electrical resistivity, and optical and magnetic properties, are related to their crystal structure. It is characterized by MQ_2 layers, in which metal atoms (M = Mo, W) are surrounded by edge-connected trigonal prisms of hexagonally arranged chalcogen (Q = S, Se, Te) atoms (similar to carbon in graphite). The structures of different MS_2 polytypes were already shown in Figure 6.

Due to the manufacturing processes, TMCs contain defects that can significantly affect their mechanical strength, ionic or electronic transport, and other physical properties. The surface curvature in nanotubes and nested fullerenes induces elastic strain, which requires the insertion of new topological elements or defects to alleviate the strain induced by folding.[1] In general, defects moderate the chemical potential and affect the reactivity. Discrepancies between experiment and theory require TMCs (similar to carbon) to be viewed as real materials with defects rather than layered materials with perfect periodicity.[2, 3] Defects in the MQ_2 layers can be classified as 0D (point defects, impurities, nonhexagonal rings), 1D (edges, grain boundaries), or 2D (stacking faults, soldering, etc.), which can arise as a result of thermal equilibrium or the kinetics of processing.

Single MQ_2 sheets exhibit unsaturated metal and chalcogen atoms at the borderlines and edges (Figure 107). A feature of these atoms are energetically unfavourable “dangling bonds”, which can be compensated in bulk by interlayer interactions. As the ratio of surface to volume increases with size reduction from bulk to the nanometer range, the effect of dangling bonds exceeds that of the interlayer interactions. Therefore, the number of dangling bonds can be minimized by folding of the layers, which becomes more favourable (although it requires overcoming the bending energy).

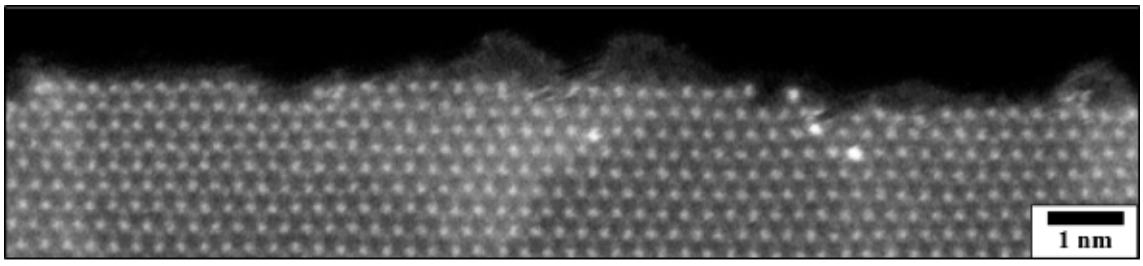

Figure 107. Room temperature ADF-STEM image of the edge of a MoS_2 domain showing atomic corrugations, adapted from [4].

For applications of TMC nanostructures it is essential to control their defect density and interface structure. Although the surfaces of TMC nanomaterials have been tailored in different ways, little is known about their surface and defect structure. It has been demonstrated that point defects on the surfaces of chalcogenide nanotubes (NTs) can be identified as reactive sites with chalcophilic markers such as gold nanoparticles.[5-7] In contrast, silane coating of WS_2 nanotubes passivated point defects, and no binding of gold nanoparticles was observed. These findings suggest that (i) tailoring of layered metal chalcogenide surfaces requires surface defects and (ii) their functionalization density is proportional to the defect concentration. Therefore, there is a need to develop synthetic tools to maximize the number of surface defects while preserving the bulk characteristics.

6.1.2. Syntheses Methods and Applications of TMCs

WS_2 nanomaterials have been prepared by a variety of methods, in general with the goal to obtain defect-free nanoparticles. Reductive sulfidization of WO_x nanoparticles has proven to be the most efficient method for the synthesis of WS_2 nanoparticles, either as inorganic fullerenes (IFs) or as NTs.[8-11] In addition, template assisted self-assembly,[12] electron-beam irradiation,[13] arc discharge,[14-16] and laser ablation[17] have been employed.

Table 8 gives an overview of different preparation methods of TMCs.

MS_2 compounds are used on a large scale in desulfurisation of mineral oils and in hydrorefining processes.[18-22] Nanoparticles of MS_2 have a much larger surface area compared to their bulk counterparts and, thus, the catalyst activity improves significantly.[23-25] Since all the desulfurization reactions necessary to remove sulfur preferably take place along the edges of the planar layers, it is particularly important that the surface offered by the MS_2 particles is as large as possible. Due to their small lateral particle size (5–60 nm), single nanosheets and multilayer nanoflakes have a relatively large number of surface defects. By virtue of this favorable edge-to-surface-ratio, they are particularly suitable for the catalytic degradation of sulfur compounds in fossil fuels.

The generation of hydrogen as a clean fuel can be carried out solar-assisted by catalytic cleavage of water on suitable electrode material,[26, 27] as described in Chapter 2. For this purpose, the good photoelectrocatalytic reactivity of MS_2 compounds[28-30] can be further increased by functionalization with graphene.[31] In other experiments, it has been shown that negative properties of the individual species (e.g. weak charge transport, catalytic activity or unwanted chemical reactivity) can be compensated for with core-shell particles of $MS_{2-x}O_X$. That compensation correlates with quasi-synergistic effects in the H_2-generation.[32] In fuel cells, molybdenum sulfide offers a cheaper alternative to platinum as anode material[33-35] and for hydrogen detection.[36] Futhermore, ultrathin, two-dimensional nanosheets of layered TMCs,

nanotubes, and nested inorganic fullerenes,[37-40] have demonstrated great potential for applications in solid lubrication,[41-45] as cathode materials in rechargeable batteries[46] or as shock-absorbing materials.[47, 48]

Table 8. Synthesis methods of transition metal chalcogenides with different morphologies.

TMC morphology	Preparation Method	Reference No.
single-layer sheets	micromechanical cleavage	[38]
single-layer sheets	mechnical exfoliation	[50]
single-/multi-layer sheets	ion-intercalation, liquid exfoliation	[51]
single-layer sheets	electrochemical lithiation	[52]
large-area few-layer	CVD on SiO_2 substrate	[53]
IF-WS_2	reductive sulfidization	[54]
hollow IF-MoS_2/$MoSe_2$	MOCVD	[55]
large-scale IF-MoS_2/WS_2	APCVD	[56]
core-shell MoS_2	arc-discharge	[14]
nanofibers, nanotubes	thermal decomposition of thiometallates	[57]
IF-MoS_2/WS_2	laser ablation	[58]
irregularly shaped	microwave plasma	[59]
closed nanoboxes	spray pyrolysis	[60]
MoS_2 nanooctahedra	pulsed-laser vaporization	[61]
spheres	solvothermal process	[62]
irregularly shaped	sonochemical process	[63]
nanoflakes	oxidative exfoliation	current work

Modern electronic components should both have a high mobility of the charge carriers and be able to combine them with physical flexibility. In contrast to silicon-based field effect ransistors (FETs) with high mobility, but no flexibility or FETs from organic components (low mobility, high flexibility), MS_2-FETs offer optimal conditions for high flexibility (due to their chemical structure) and electronic conductivity (with only few charge traps on the surface).[49] Depending on the design, these TMC-FETs can be operated with holes or electrons as charge carriers, respectively, which offers further advantages over conventional FETs.

6.2. MoS_2- and WS_2-Nanosheets and Nanoflakes

6.2.1. Synthesis and Characterization of Precursor Compounds

The clustered precursor compounds were prepared using the syntheses published by Müller et al. and McDonald et al., respectively, with slightly modified approaches.[64, 65]

For the synthesis of **$(NH_4)_2[Mo_3S_{13}]$**, 3 mmol of $(NH_4)_6Mo_7O_{24}\cdot 4H_2O$ were dissolved in 20 mL of water. After adding 80 mL of ammonium polysulfide solution, the completely brown mixture was placed in a preheated oil bath (90 °C) and left there to react for 48 h without stirring. The dark-red precipitate was separated by vacuum suction, washed with 20 mL of polysulfide solution, 50 mL of water, 50 mL of ethanol, 20 mL of carbon disulphide and 10 mL diethyl ether and dried on air.

In order to synthesize **$(NH_4)_2WS_4$**, 6 mmol of H_2WO_4 were dissolved in 30 mL of ammonia solution. After heating the solution to 60 °C in an oil bath, a vigorous flow of H_2S was passed through, which caused a colour change from yellow to dark-red immediately. After 80 min of reaction time the precipitation of the red-brownish crystals was completed. The product was separated by vacuum suction, washed with water and ethanol and dried on air.

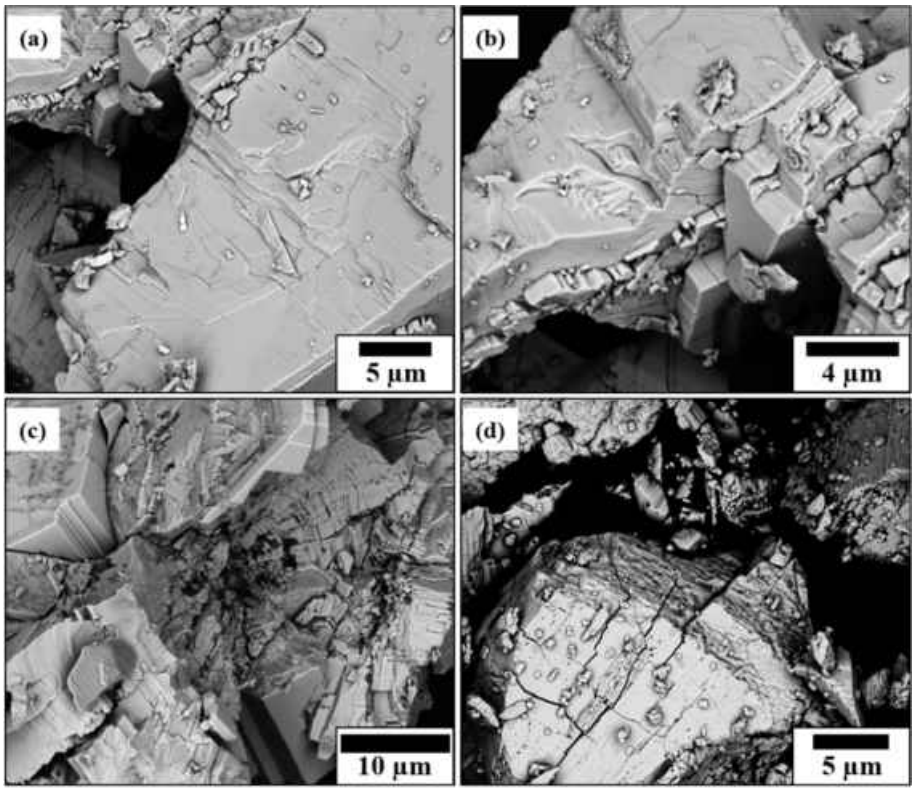

Figure 108. SEM images of the precursor compounds $(NH_4)_2[Mo_3S_{13}]$ (a, b) and NH_4WS_4 (c, d).

The SEM images in Figure 108 show bulk material of the two different thiometallate compounds. Both the materials exhibit distinct layered structures, which are well-known for these types of clusters. As it was reported by Müller et al.,[66] the structure of $(NH_4)_2[Mo_3S_{13}]$ must actually be

denoted as $(NH_4)_2[Mo_3S(S_2)_6]$, because of the presence of S_2^{2-} ligands in the cluster. The S_2^{2-} ligand favours high oxidation numbers and therefore is capable of stabilizing the metal-clusters. The XRD patterns of the thiomtallates underline their phase purity and crystallinity (Figure 109), both of them conform to XRD patterns known for these compounds.[67, 68]

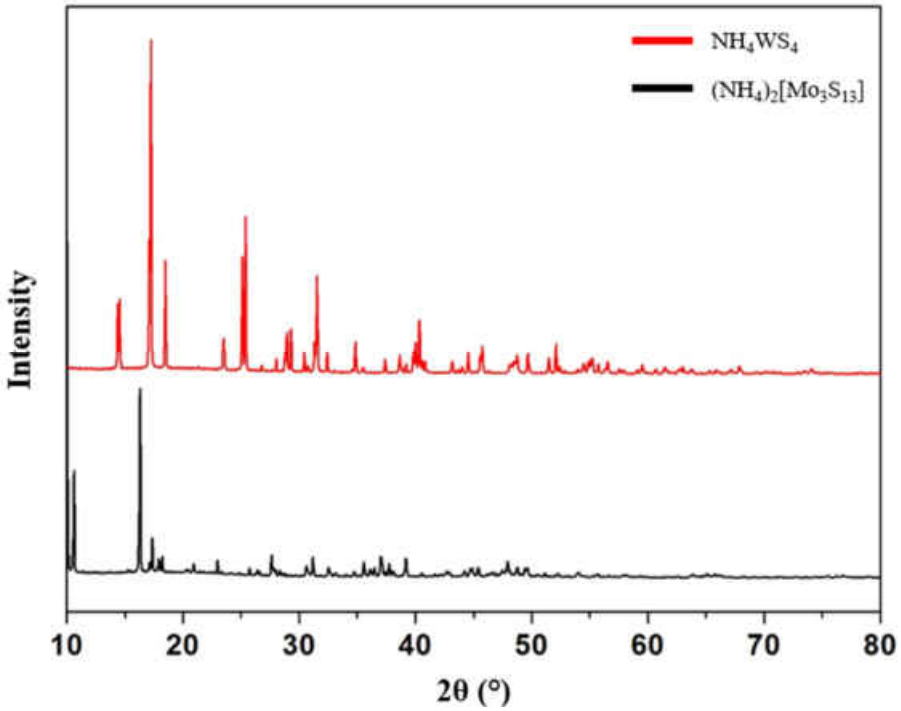

Figure 109. XRD patterns of the $(NH_4)_2[Mo_3S_{13}]$ (black) and NH_4WS_4 (red), which were used as precursor compound for the nanosheets/nanoflakes production.

Since the solubility of the precursor compounds is important (e.g. for purification of the nanoparticle product), 30 mg of each thiometallate were treated with 5 mL of different solvents. As shown in Figure 110, $(NH_4)_2[Mo_3S_{13}]$ exhibits better solubility in a wider range of solvents compared to NH_4WS_4. Nonpolar solvents such as hexane or toluene leave the molybdenum thiometallate completely undissolved. Furthermore, the different colours of the solution demonstrate that acetonitrile seems to dissolve only elemental sulfur, which always accompanies the formation of the thiomolybdate precursor due to the utilization of ammonia polysulfide solution as sulfur source. Polar solvents such as water, ethanol or DMF are able to dissolve the whole $(NH_4)_2[Mo_3S_{13}]$ cluster and, thus, show dark-red coloured solutions.[69]

In the case of NH_4WS_4 only yellow or yellowish colours can be observed, whereby it appears to be completely soluble in acetone. Water and ethanol yield turbid solutions, which is another hint that only elemental sulfur is dissolved.

Figure 110. Solubility experiments of the precursor compounds in different solvents: (a) ethanol, (b) 2-propanol, (c) acetone, (d) ethyl acetate, (e) hexane, (f) benzyl alcohol, (g) water, (h) chloroform, (i) acetonitrile, (k) toluene and (m) DMF.

6.2.2. Solvent-Assisted Exfoliation to Nanosheets and Nanoflakes

A wet chemistry approach was used to decompose single-source precursors containing both the metal and sulfur in a one-pot synthesis. For the synthesis in oleylamine, the method reported by Altavilla et al. was adapted.[71] For the preparation of MS_2 nanosheets (nanoflakes) 0.34 mmol $(NH_4)_2[Mo_3S_{13}]$ or NH_4WS_4 were dispersed in 40 mL of oleylamine (benzyl alcohol). The mixture was heated to 320 °C (oleylamine) or 210 °C (benzyl alcohol) with a heating rate 10 °C/min and left there for 60 min (90 min) under stirring. For the solvothermal route, the same amount of precursor and solvent was used, but with a reaction temperature of 180 °C and 12 h duration. After cooling down the dispersion to room temperature, the nanosheets (nanoflakes) were precipitated with ethanol and then centrifuged (9000 rpm, 15 min), followed by another washing step with a 1:1 mixture of methanol:chloroform. The washed samples were then dried *in vacuo* for 24 h.

The synthetical approaches to obtain nanosheets/nanoflakes of MS_2 are illustrated in Figure 111, whereas the products were identical in both ways. Some digital photographs acquired during the thermal decomposition in the flask indicate that the reaction progress can be traced by the color change of the precursor-olelyamine mixture.

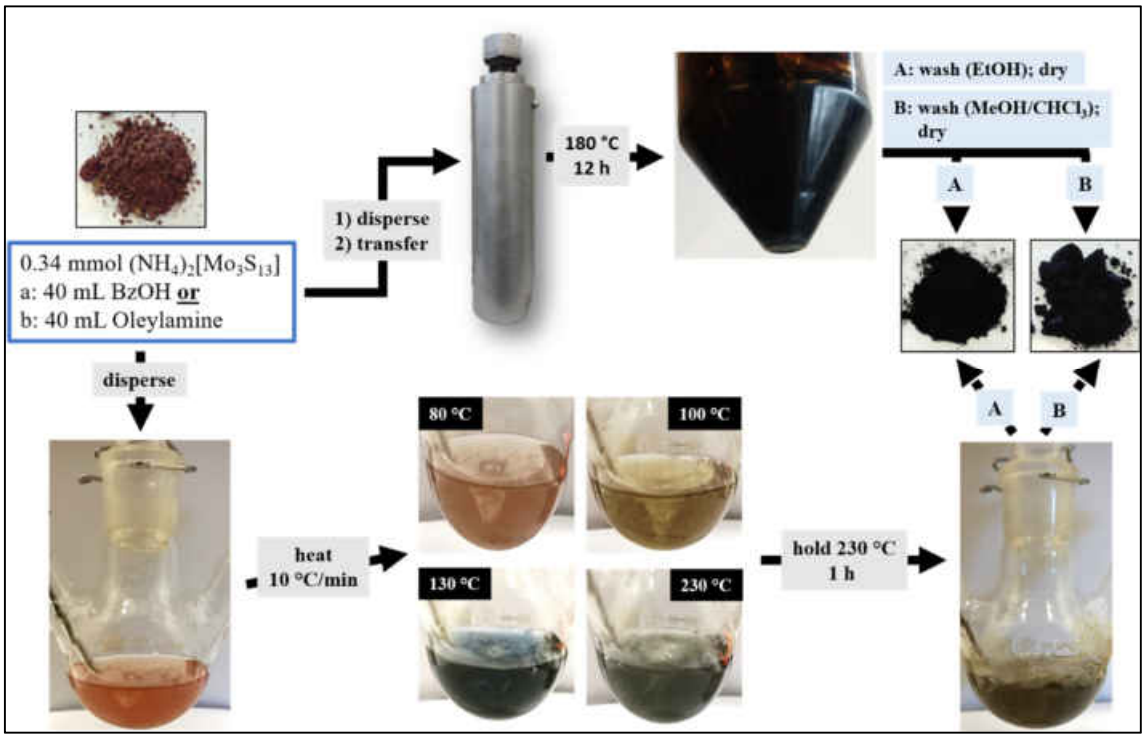

Figure 111. Schematic process for the production of nanosheets and nanoflakes on two different routes, shown for $(NH_4)_2Mo_3S_{13}$ as precursor compound. The upper route shows the solvothermal synthesis, the bottom route the approach in flask.

Nanosheets of MS_2@Oleylamine. The solubility tests of MoS_2@oleylamine (MoS_2@OA) nanosheets propose toluene as a suitable solvent, as it is the only one to yield a complete clear solution without any precipitated product (see Figure 112). It is plausible that due to the *in-situ* functionalization of the MoS_2 sheets by oleylamine, the particles become nonpolar as a whole and therefore are preferably soluble in solvents of the same kind. Then again, it is somewhat surprising that hexane and chloroform can't provide for a complete solubility of MoS_2@OA nanosheets, as most of the product precipitates.

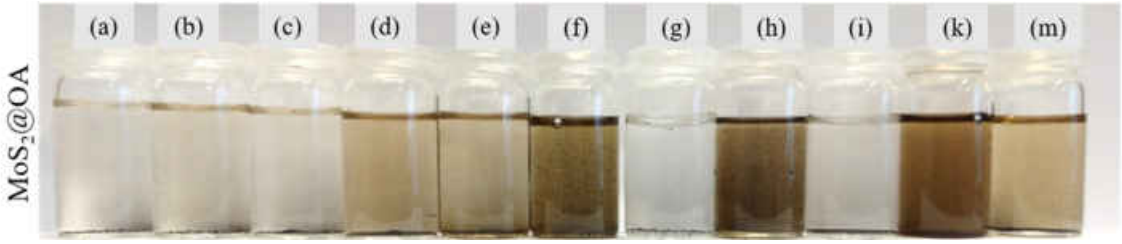

Figure 112. Solubility experiments of the MoS2@OA nanosheets in various solvents: (a) ethanol, (b) 2-propanol, (c) acetone, (d) ethyl acetate, (e) hexane, (f) benzyl alcohol, (g) water, (h) chloroform, (i) acetonitrile, (k) toluene and (m) DMF.

The TEM images of the product in Figure 113 (a, b) show that ultra-thin (< 1 nm thickness) nanosheets were obtained, which form highly-disordered structures. The MoS_2@OA nanosheets are randomly oriented within an oleylamine matrix, exhibiting lateral sizes of 10–30 nm. The strongest phase contrast in the TEM imaging is observed, if the basal planes of the nanosheets are

oriented in parallel to the incident electron beam.[70] If they are not dispersed in an appropriate solvent, an even stronger tendency towards agglomeration into bulk material can be observed, as indicated by the SEM images in Figure 113 (c, d). The oleylamine, which simultaneously serves as a solvent and exfoliating agent, is chemisorbed onto the surface of the individual sheets and therefore leads to their agglomeration. This can also be observed at a macro scale, since all samples were very oily and the pure, dry powder could only be obtained after washing four times with hexane. However, a change in the particle's size as a function of the reaction time, as reported by Altavilla et al. could not be observed.[71]

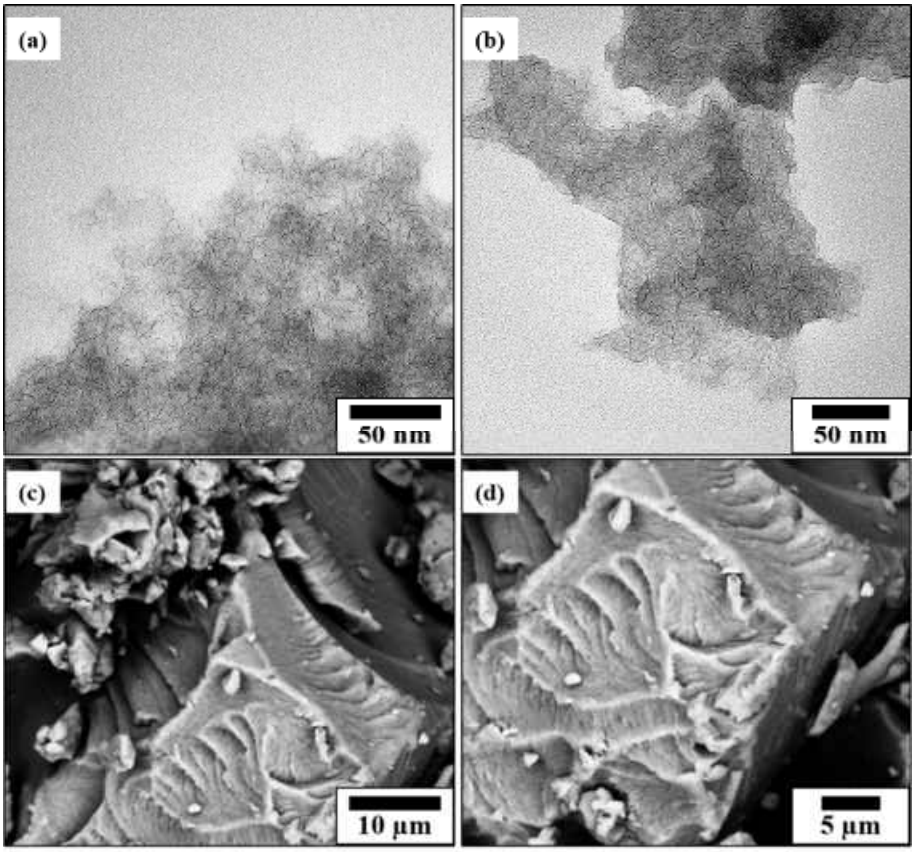

Figure 113. (a, b) TEM images of single layer MoS_2@OA nanosheets and (c, d) SEM images of bigger MoS_2@OA agglomerates. TEM images were recorded in different areas of the grid.

Selected area electron diffraction (SAED) patterns of bigger flocculates of monolayer MoS_2 supports the identification of the product (insets in Figure 114). Therefore, the phase of the molybdenum sulfide can be attributed to 1H-crystallites of MoS_2.[72]

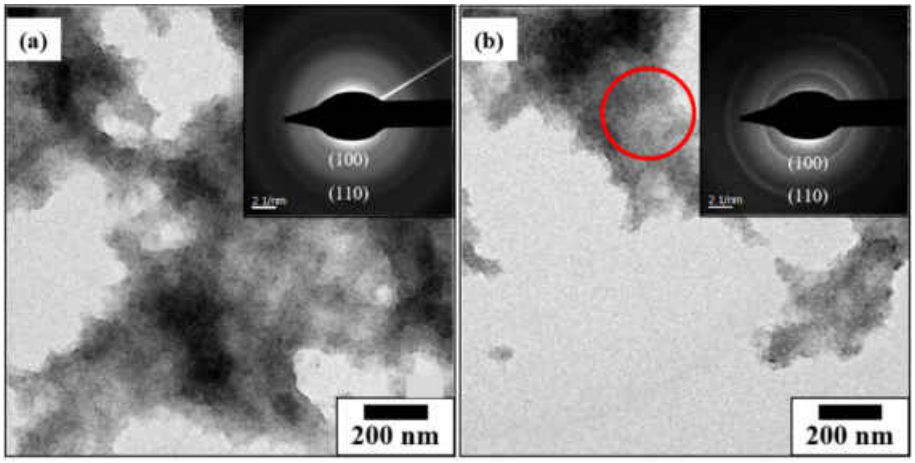

Figure 114. (a, b) TEM images of the MoS_2@OA nanosheets. The insets represent selected area electron diffraction patterns with a scale bar of 2/nm.

In the case of the reaction of the NH_4WS_4 under the same conditions, also ultra-thin nanosheets known from the thiomolybdate analogue are obtained, but with slightly smaller lateral sizes of 5–15 nm (Figure 115 a, b). The agglomerate formation, which can be seen from the SEM images (Figure 115 c, d), can also be explained by the use of oleylamine as the solvent. The surface of the bulk appears to have a finer structure here, which might be explained by the fact that originally the tungsten thiosulfate precursor contains less free sulfur than $(NH_4)_2[Mo_3S_{13}]$. Therefore, the crystal structure of the NH_4WS_4 is more easily accessible for the oleylamine molecules during the decomposition and less sulfidic by-product is formed.

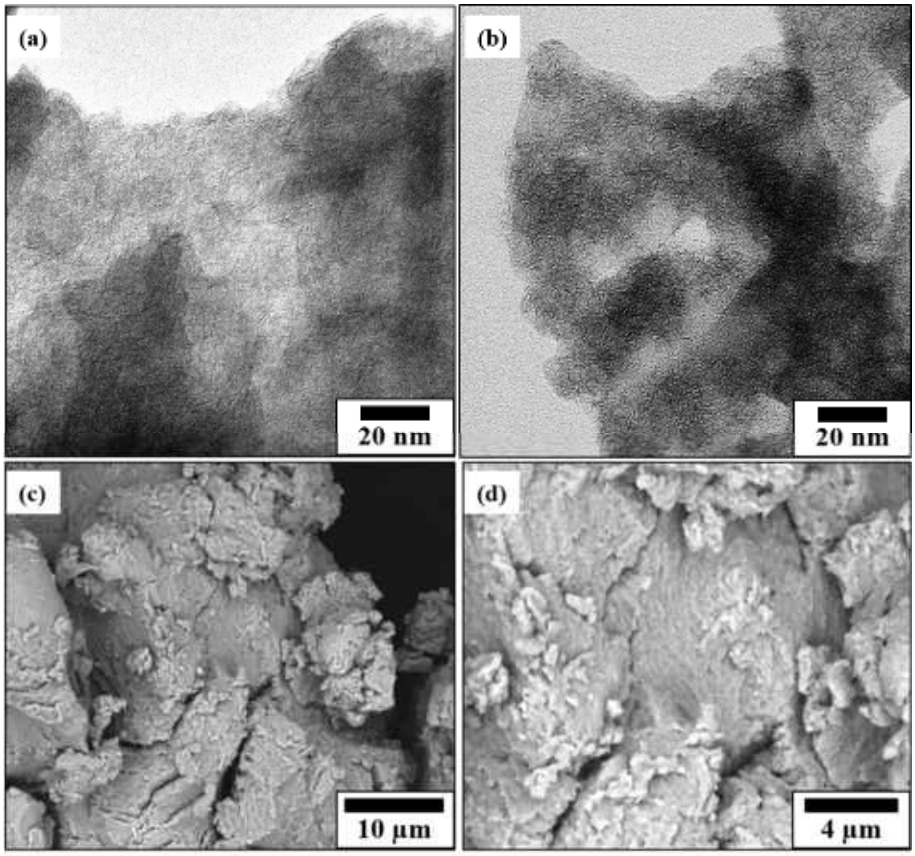

Figure 115. (a, b) TEM images of single layer WS_2@OA nanosheets and (c, d) SEM images of bigger WS_2@OA agglomerates.

The XRD patterns show only a few sharp reflections in the case of tungsten, which can be assigned to the 3R-WS_2 phase without exception (Figure 116). The molybdenum product shows an amorphous pattern where no definite phase can be concluded and no verification of the 1H-MoS_2 phase can be provided. However, it is shown by means of XPS measurements that this is MoS_2, which is why, for the sake of simplicity, there will be a discussion of MoS_2 sheets throughout the following parts. The absence of reflections in the case of the molybdenum, but also the broadening of the known reflections of the WS_2, can be explained by the fact that the oleylamine shields the individual particles strongly and therefor an interaction of the X-ray radiation with the actual MS_2 structure does not take place at all or is significantly reduced in intensity. In addition, XRD reflections of nanoparticles generally undergo widening due to small crystallite sizes. Both the XRD patterns show strong background because of oleylamine presence in the samples on the one hand and the sample preparation on *Scotch tape* (excessive broadening and high intensity reflection below $2\theta < 30°$) on the other hand.

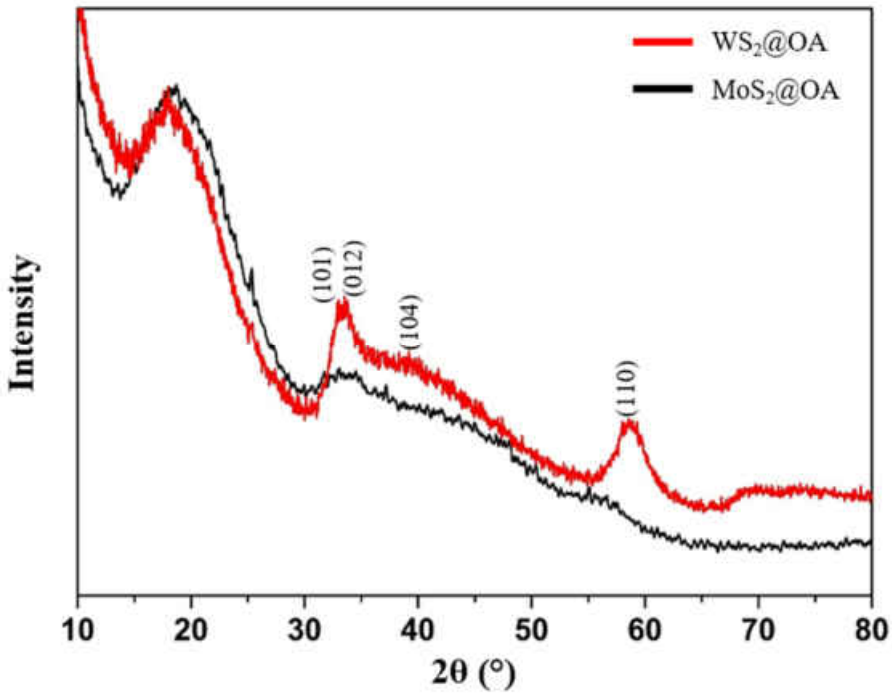

Figure 116. XRD patterns of the MS_2 nanosheets from the solvent exfoliation in oleylamine.

To investigate whether the surface of the nanosheets was functionalized with oleylamine, ATR-IR measurements of the as-prepared greasy samples were conducted (Figure 117). The IR spectra of the MoS_2 and WS_2 products look quite similar, whereas the presence of oleylamine on the surface is confirmed by the two characteristic peaks of the oleic group in the region of 2800–3000 cm^{-1}. Furthermore, the C=C stretching mode at 1672 cm^{-1} (WS_2) and 1664 cm^{-1} (MoS_2) and the peak at 1470/1463 cm^{-1} (WS_2/MoS_2), due to the C-H bending mode are also observed.[73]

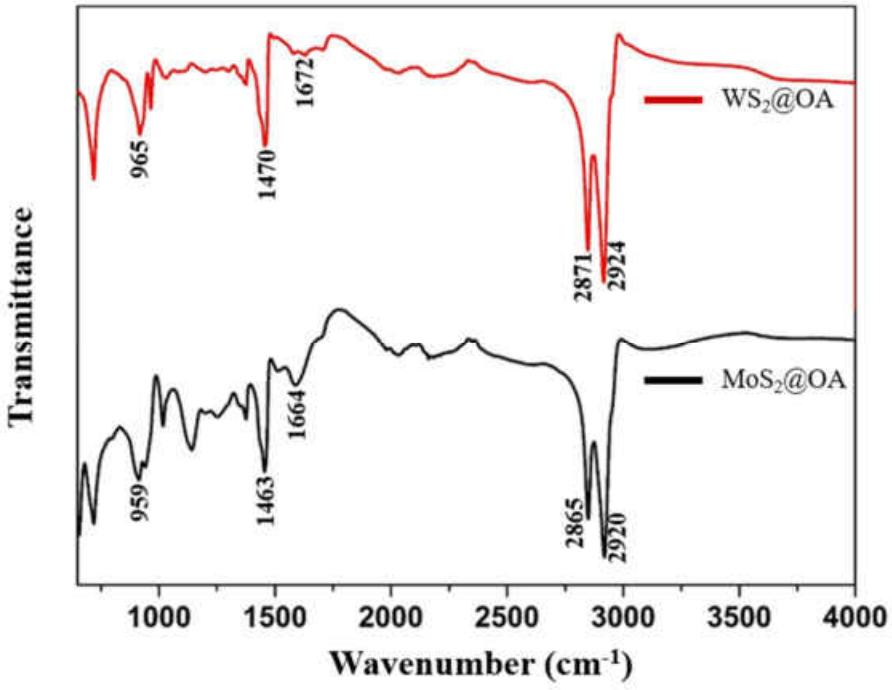

Figure 117. ATR-IR spectra of the nanosheets synthesized in oleylamine.

Signals of free primary amine group, which usually are detected as N-H stretching modes at ~3300 cm^{-1}, cannot be seen although the presence of the amine group is verified by the $–NH_2$ bending mode at 965/956 cm^{-1} (WS_2/MoS_2) in both spectra. Pure oleylamine also exhibits a $–NH_2$ scissoring mode at ~1560 cm^{-1}, which is significantly diminished by the capping of both the chalcogenide nanosheets.[74] The reduction of that specific scissoring mode was reported in successful oleylamine functionalization of nanoparticles earlier.[75]

Nanoflakes of MO_xS_{2-x}. The products of the reaction of the thiometallate compounds in benzyl alcohol yield spherical nanoparticles with sizes of 70–80 nm in diameter (Figure 118 a, b). The particles are spherical but not of closed shell inorganic fullerene type (IF-type), which are presented in Section 6.2.3. On the outer edges fan-like lamellae can be observed, whereas on approaching the particles' core a considerable amount of point defects and grain boundaries is shown, hereby proving their poorly crystalline character. Usage of benzyl alcohol omitted the sticking effect observed for oleylamine. Residual alcohol was removed by repeated washing of the samples, leaving them completely dry and powdery. In general, the particles are agglomerated, possibly a result of dangling bond saturation in the incipient stages of growth. The strong tendency to agglomeration can also be witnessed by means of SEM, as it is presented in Figure 118 (c, d). Nonetheless, many flake-like particles can be observed atop of the bigger agglomerates.

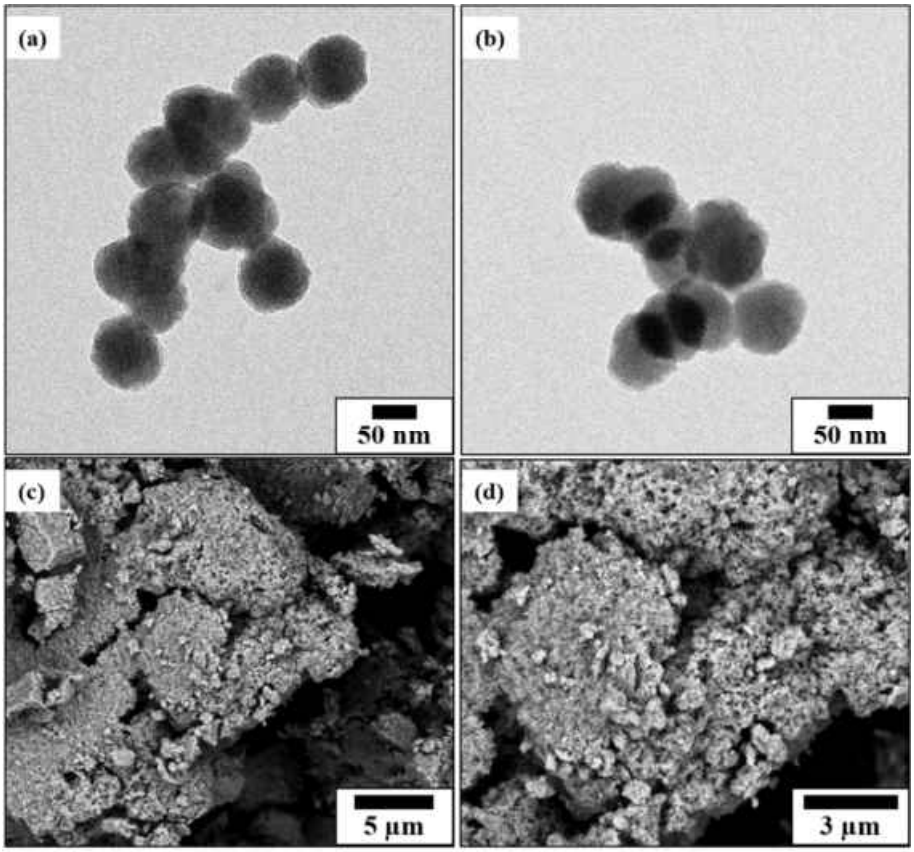

Figure 118. (a, b) TEM images of MoO_xS_{2-x} nanoflakes and (c, d) SEM images of MoO_xS_{2-x} nanoflakes agglomerates.

Figure 119 shows low-magnification TEM images and the corresponding selected area electron diffraction patterns of two different agglomerates of the nanoflakes produced in benzyl alcohol. Particles with both amorphous and crystalline structure can be found in the same batch. As the SAED pattern neither represents pure MoS_2 nor the MoO_{3-x} phase, it is supposed that a molybdenum oxysulfide is obtained as the product of the decomposition of $(NH_4)_2[Mo_3S_{13}]$. The presence of an oxysulfide product can also be confirmed by EDS, as it is shown in Figure A 202 in the appendix.

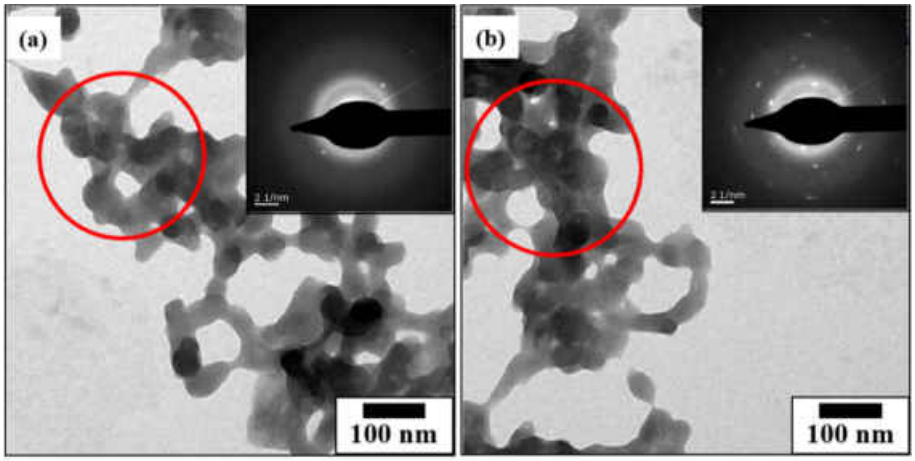

Figure 119. (a, b) TEM images and selected area electron diffraction (insets) of the MoO_xS_{2-x} nanoflakes obtained from the syntheses in benzyl alcohol.

The XRD pattern of the nanoflakes further confirms pronounced amorphicity of the product, with some sharp reflections in the $2\theta < 30°$ region (Figure 120). More interestingly, only two of the Bragg reflections can be assigned to 2H-MoS_2, but all other distinct reflections with strong intensity are contributed by the Mo_4O_{11} phase. This might be surprising in that the molybdenum thiometallate precursor does not exhibit any oxide phases. Accordingly, the oxygen would have to come either from ambient air or from the solvent. As reported by Niederberger et al. in various publications,[76-79] benzyl alcohol reacts not only as a solvent, but also as an oxidizing agent, which is why oxygen is believed to come from benzyl alcohol in this case. To verify this, a synthesis of the same product in isotope-labeled (^{17}O or ^{18}O) benzyl alcohol would be necessary. This is, however, a very time-consuming process, since no isotopically-labeled benzyl alcohol can be obtained commercially and this should be produced in several steps by ourselves, and was not done in this work. However, it should be pointed out that in one of the diploma thesis prepared in our working group it could already be demonstrated by means of NMR measurements that not only oxygen is incorporated into the nanoflakes, but also that the benzyl alcohol used was partly converted into benzyl thiol after the reaction.[80] Since only the suboxide Mo_4O_{11} phase was found, the oxidizing ability of the benzyl alcohol does not seem to be sufficient to convert the thiometallate into the completely oxidized species of molybdenum, namely MoO_3. Furthermore, some decomposition experiments using Soxhlet extraction purified $(NH_4)_2[Mo_3S_{13}]$ as precursor

yielded wire- and tube-like particles with a crystal structure quite similar to the one of the precursor compound (Figure A 203 and Figure A 204 in the appendix).

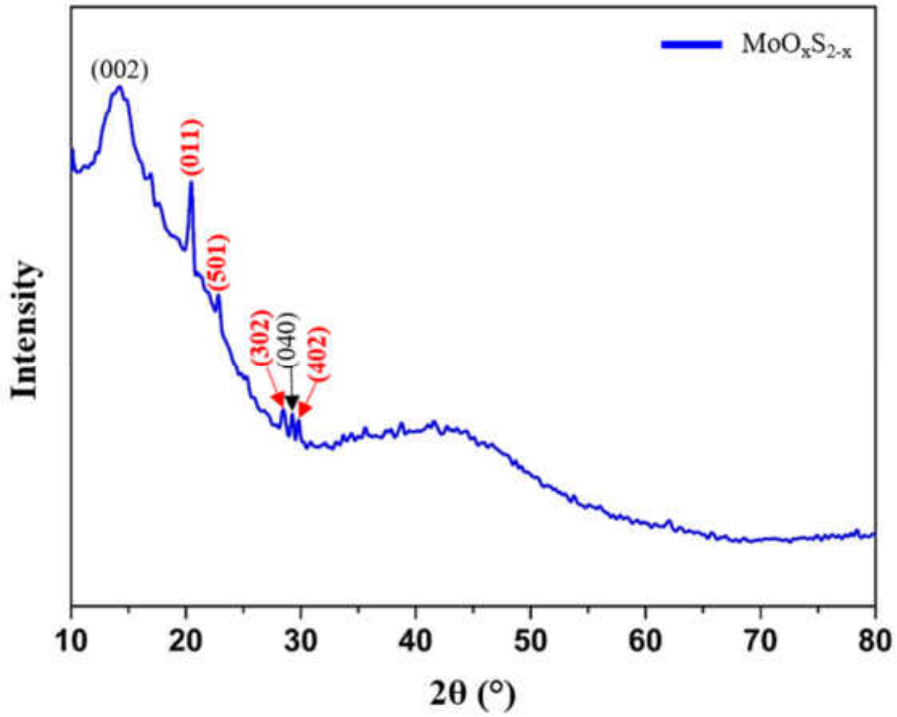

Figure 120. XRD pattern of the MoO_xS_{2-x} nanoflakes obtained from the syntheses in benzyl alcohol. The reflections assigned to Mo_4O_{11} phase are typed red.

The nanoflakes obtained from the decomposition of NH_4WS_4 in benzyl alcohol under the same conditions show different morphologies (Figure 121). Besides single-layer nanosheets with lateral dimensions of 10–30 nm multi-layered, non-spherical nanoflakes (~40 nm) and bigger agglomerates can be observed. SEM images (Figure 121 c, d) acquired after the washing treatment show the presence of bulk material, which is decorated by little aggregates (average size of ~200 nm) of flake-like product.

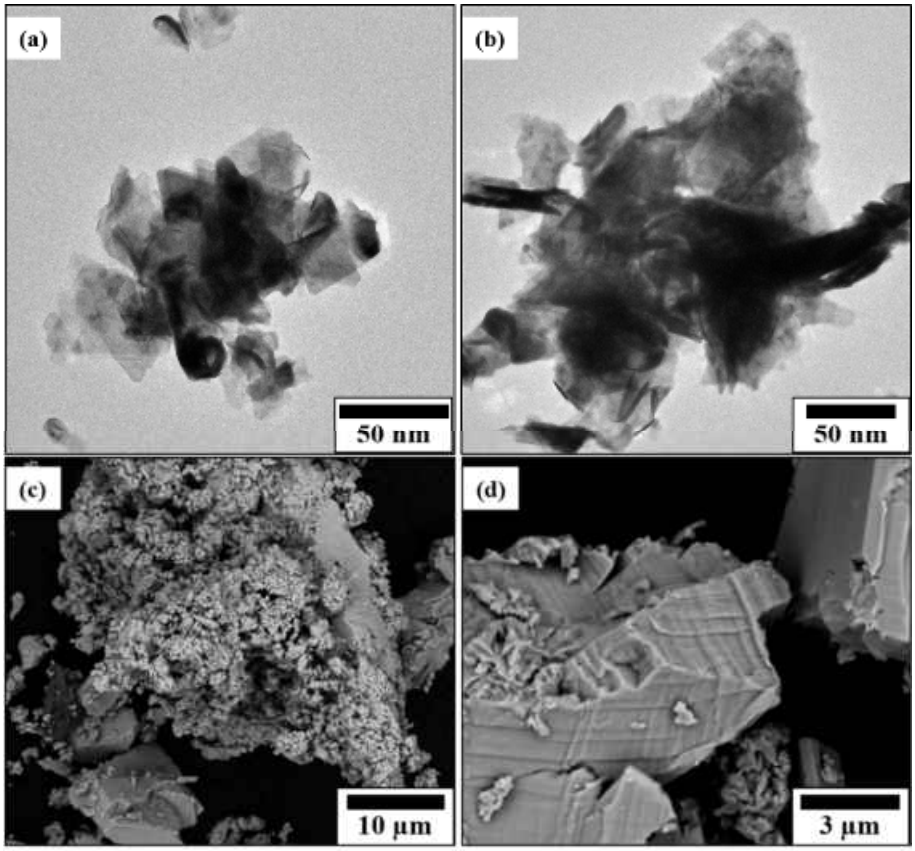

Figure 121. (a, b) TEM images of single layer WO_xS_{2-x} nanoflakes and (c, d) SEM images of WO_xS_{2-x} nanoflakes agglomerates.

As it was mentioned before, reactions performed in benzyl alcohol as solvent usually feature oxidized by-products or an oxidation of the main product itself. Therefore, it was expected to obtain an oxidic or oxysulfidic species of the nanoparticles. The complex XRD pattern of the WO_xS_{2-x} nanoflakes presented in Figure 122 exhibits a crystalline structure. An indexed version of the pattern can be found in the appendix (Figure A 205), thus showing that the product exhibits reflections of two oxidic phases (WO_3 and W_2O_7) besides WS_2. Since the NH_4WS_4 precursor does not provide for an excess of free sulfur (as it is the case for $(NH_4)_2[Mo_3S_{13}]$), it can be concluded that the tungsten thiometallate is more assailable in terms of benzyl alcohol oxidation. Nonetheless, a complete conversion of the sulfidic precursor to tungsten oxide could not be observed, even after increasing the reaction time to 72 h.

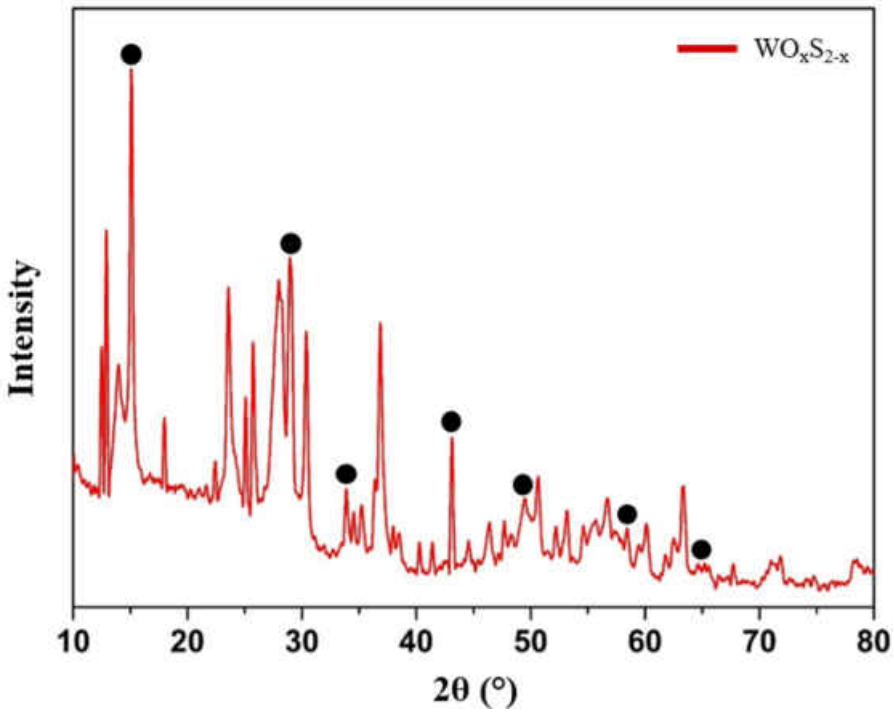

Figure 122. XRD pattern of the WO_xS_{2-x} nanoflakes obtained from the syntheses in benzyl alcohol. The reflections marker with a black dot are attributed to WS_2 phase.

The Raman spectra of both nanoflakes products further confirm the oxysulfidic character of these compounds (Figure 123). For the WO_xS_{2-x} nanoflakes W=O stretching modes (791 cm^{-1}) and a broadening of the stretching of bridging oxygen atoms (O-W-O) at ~680 cm^{-1} is accompanied by the out-of-plane (A_{1g}) and in-plane (E^1_{2g}) Raman modes of WS_2 at 422 cm^{-1} and 381 cm^{-1}, respectively. A massive broadening of the second-order Raman peak (2*LA*(M)) of WS_2 can be observed, which might also overlap with other tungsten oxide bands.[81]

The Raman spectra of MoO_xS_{2-x} nanoflakes exhibits narrow bands of asymmetrical Mo=O stretching (993 cm^{-1}) and symmetrical Mo=O stretching modes at 820 cm^{-1} with an intensity many times higher than the sulfidic species. An additional asymmetrical O-Mo-O stretching mode can be observed at 667 cm^{-1}. Low-intensity MoS_2 bands are ascribed to A_{1g} and E^1_{2g} modes at 385 cm^{-1} and 347 cm^{-1}, respectively. As it was shown by Li et al. and Wu et al.,[82, 83] a strong red-shift of the Raman bands maxima represents a transition from bulk-MoS_2 to multi- or single-layer compounds.

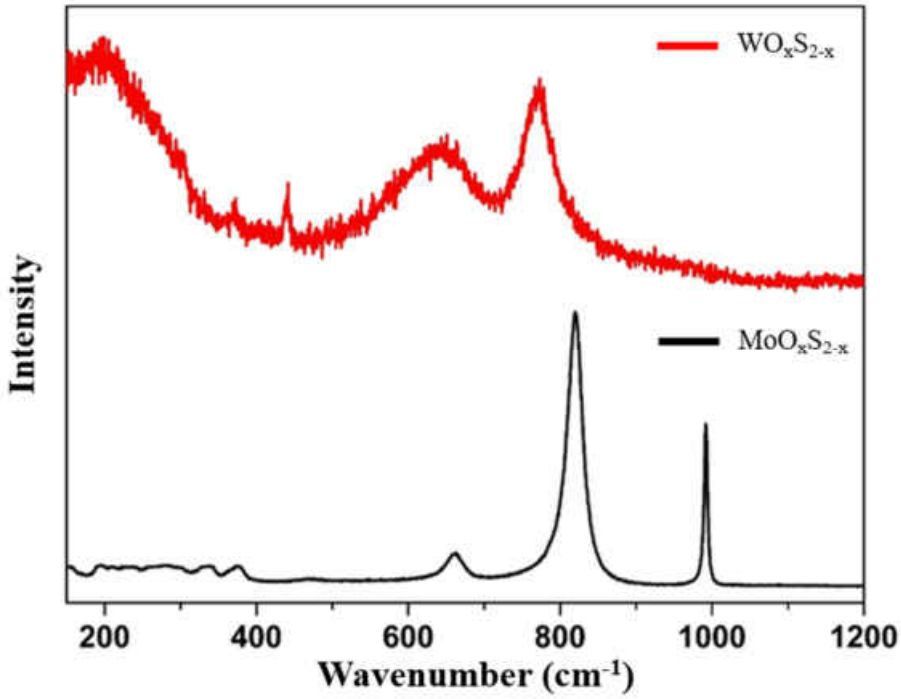

Figure 123. Raman spectra of the oxysulfide nanoflakes from the solvent exfoliation in benzyl alcohol.

On the basis of the results of the tribological measurements (presented in Chapter 6.2.4.), in which the WO_xS_{2-x} nanoflakes emerged as a particularly effective friction reducing agent, it was decided to perfom SEM-EDS and XPS analysis of the pristine product powder. This should allow to draw conclusions about the exact composition of the nanoflakes.

Figure 124 shows the results obtained from EDS mapping of the powdered nanoflakes sample, which was sputtered with silver prior to the measurements. It can be seen that tungsten and sulfur are homogeneously distributed in the sample (Figure 124 b, d). Furthermore, a massive carbon contamination of the powder can be detected (Figure 124 e). This might be explained by the synthesis process using benzyl alcohol as solvent. The washing steps with ethanol further introduce carbonaceous impurities into the product, which remain on the particles' surface. It is noteworthy that a significant amount of oxygen can also be detected on the sample surface. However, this is not homogeneously distributed over the entire sample, but is concentrated in several spots. Thus, it can be concluded that the prepared WO_xS_{2-x} nanoflakes are mainly composed of WS_2, with WO_3 as a major contaminant.

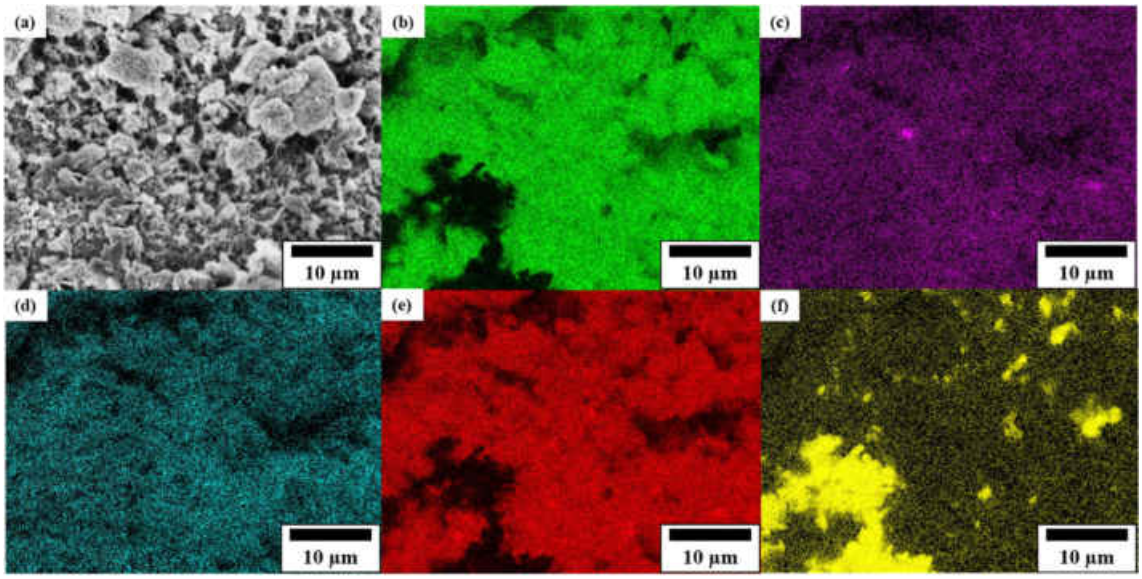

Figure 124. SEM-EDS analysis of WO_xS_{2-x} nanoflakes, sputtered with Ag: (a) SEM image of the powdered product, (b) W-atom mapping, (c) O-atom mapping, (d) S-atom mapping, (e) C-atom mapping and (f) Ag-atom mapping.

The appropriate XPS data presented in Figure 125 prove the atomic composition of the powder to be a mixture of both WS_2 and WO_3, respectively. In addition, a carbon peak at 283.9 eV can be attributed to the presence of amorphous carbon with sp^2 configuration in the sample.[84] In amorphous carbon the atoms are cross-linked without long-range order. The material can be produced with almost any sp^2/sp^3 hybridization ratio, the material properties easily merge from those of the graphite to those of the diamond. This is another indication of carbon impurities in the powder.

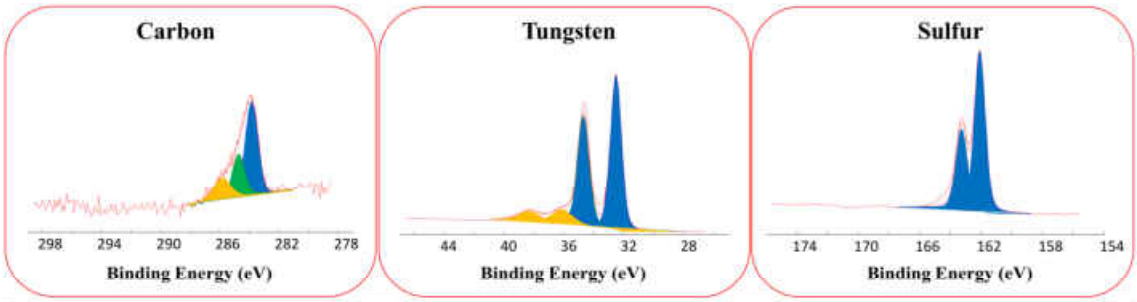

	Carbon		Oxygen	Tungsten		Sulfur
Species	Aliphatic	Amorphous C	Oxide	W (IV)	W (VI)	S (II)
BE (eV)	284.8	283.9	530.8	32.5	36.1	162.1
Concentration (atom%)	6	16	14	22	3.5	43

Figure 125. XPS analysis of WO_xS_{2-x} nanoflakes powder shown in Figure 124.

6.2.3. Preparation of IF-WS_2 and WS_2 nanotubes

The inorganic fullerene-like WS_2 (IF-WS_2) particles and the WS_2 nanotubes (NTs) were prepared by reductive sulfidization. For the IF-WS_2 commercially available quasi-spherical WO_3 nanoparticles (60–80 nm in diameter, Sigma-Aldrich) were treated in the fluidized bed reactor described in Chapter 4.2.3.

TEM images in Figure 126 (a, b) show that several particles of different size agglomerate to bigger entities. Using the software *Image J*, 100 particles from different areas of the TEM grid were measured in size, of which only eleven particles exceed the maximum diameter of 100 nm as specified by the manufacturer. All other particles considered were smaller than 100 nm, the majority being in the range of 60–70 nm.

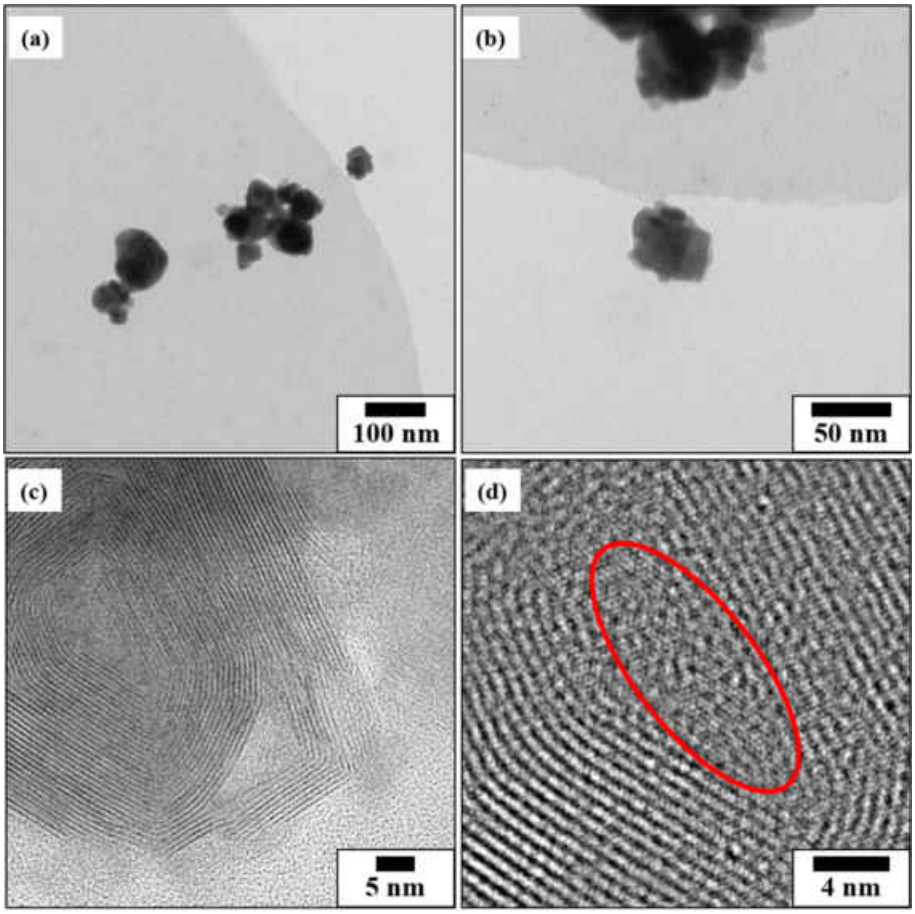

Figure 126. (a, b) Low magnification TEM images of the commercially available WO_3 particles and (c, d) HR-TEM images IF-WS_2 obtained from reductive sulfidization of the WO_3 particles, the red circle indicating the oxide core.

Furthermore, the TEM images show that only a few particles are of perfect spherical shape, most of the WO_3 nanoparticles are flattened at the edges.

The sulfidization mechanism is the same as for the WS_2 nanotubes (progressing from the outside to the inside). Therefore, it is not surprising that the product exhibits the same quasi-spherical and defect-rich morphology, where only the inner spheres are closed shells. In any case, a small oxide

core (~5 nm diameter) is surrounded by at least 35 distinct layers of IF-WS_2, depending on the size of the WO_3 particle that underwent sulfidization.

All Bragg reflections of the oxide nanopowder can be attributed to pure rhombic WO_3, as can be seen from the XRD pattern in Figure 127. The sulfidized product is of pure 2H-WS_2 phase.

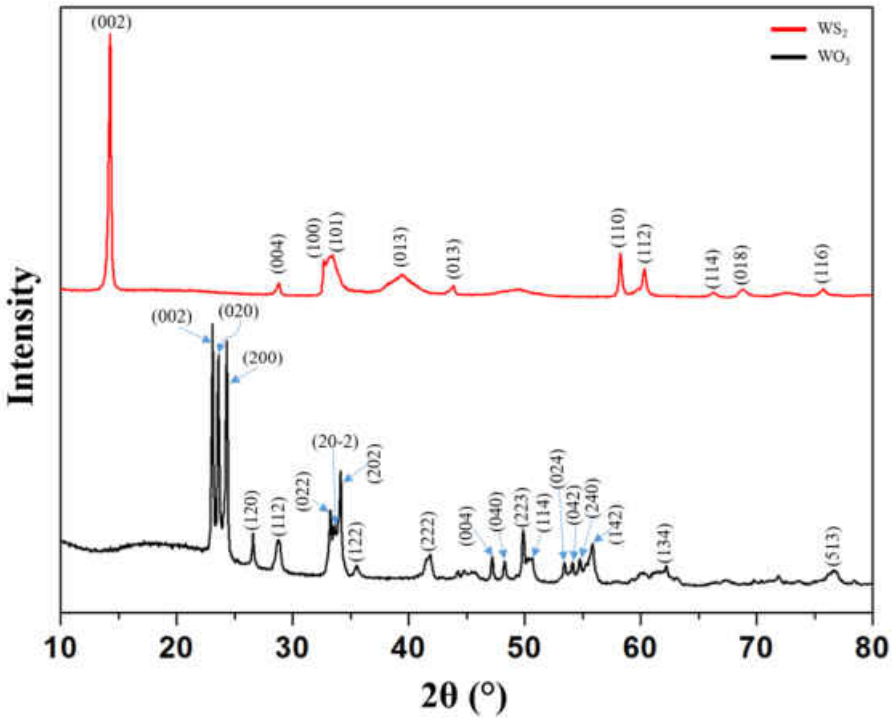

Figure 127. XRD patterns of WO_3 particles (black) and IF-WS_2 (red).

Sulfidization of $W_{18}O_{49}$ was chosen to prepare WS_2 nanotubes. Therefore, 100 mg of the as-synthesized $W_{18}O_{49}$ nanowires (see Chapter 4.3.1) were filled in a corundum boat, which was placed inside the middle of a quartz tube in a furnace. The tube was flushed with argon for 1 h prior to the reaction to remove oxygen. Next, the furnace was heated to 800 °C at a rate of 10 °C/min under a constant flow of argon. Just before reaching 850 °C, the flow was switched to H_2S gas and kept at this temperature for 30 min. The H_2S flow was carefully controlled with a flow meter. After 30 min, the furnace was cooled to ambient temperature naturally under a constant flow of argon. The resulting black powder was collected and used for further characterization.

Figure 128 (a, b) shows TEM and HR-TEM images of the nanowires obtained from solvothermal synthesis in ethanol. The nanowires exhibit little variation in diameter (15–25 nm) and are 2–5 µm long. The corresponding sulfidized products are WS_2 nanotubes, which reveal numerous crystal defects on the outer surface while the inner side is quite regular, as it is indicated by the HR-TEM images in Figure 128 (c, d). Up to 4 µm long, uniform and flexible WS_2 nanotubes with large aspect ratio were obtained after sulfidization of the $W_{18}O_{49}$ nanowires. As mentioned earlier, the sulfidization can be assumed to start at the outer surface and to progress towards the inside.

Therefore, the defects shown manifest themselves as remnants of the $W_{18}O_{49}$ precursor.[85] The nanowires get completely sulfidized within 30 min and no remaining oxide core can be observed.

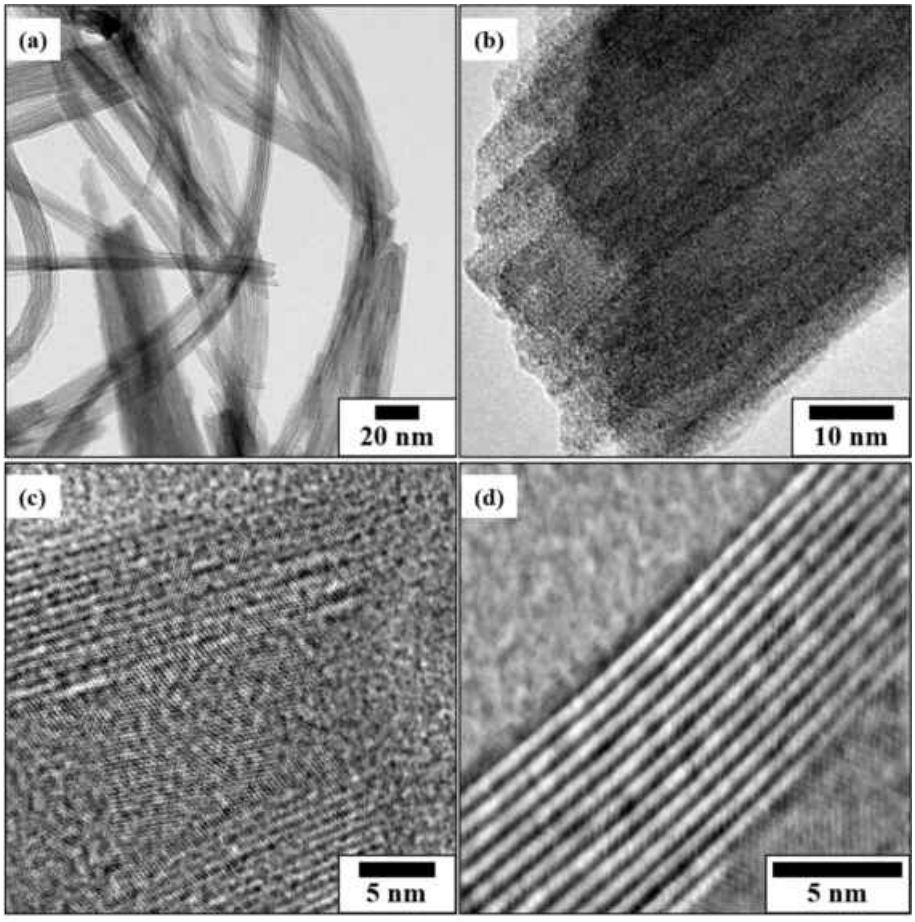

Figure 128. (a) TEM image, (b) HR-TEM image of $W_{18}O_{49}$ nanowires obtained from solvothermal syntheses in ethanol and (c, d) HR-TEM images of a single WS_2 nanotube.

The XRD patterns in Figure 129 further confirm that the nanowires obtained are single phase monoclinic $W_{18}O_{49}$ and the sulfidized nanotubes consist of single phase 2H-WS_2. However, by comparing the XRD pattern with WS_2 nanotubes reported by Houben et al., there might be also some stacking defects in the layers which could be attributed to the 3R phase of WS_2.[86]

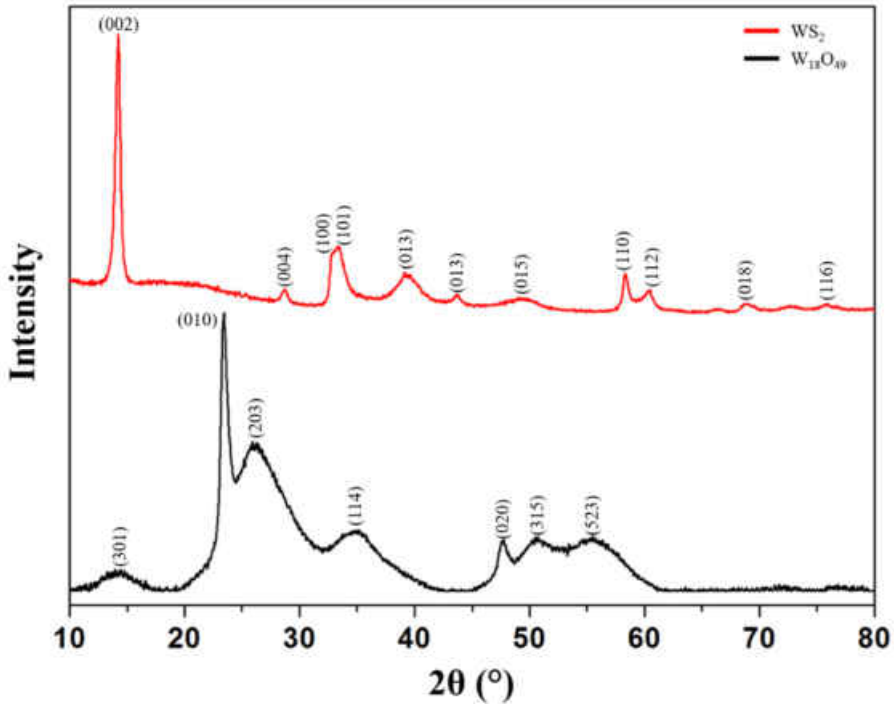

Figure 129. XRD patterns of $W_{18}O_{49}$ nanowires (black) and WS_2-NT (red).

6.2.4. Tribological Application as Lubricant Additives

All prepared samples were examined on their performance as additives in standard reference oil (poly alpha olefine 6, PAO 6) in tribological measurements. The friction tests were performed on a linear tribometer with a ball-on-disc geometry (Figure 130) internally made at LTDS (Laboratoire de Tribologie et Dynamique des Systèmes, Lyon, France). The disc (10 mm diameter) and ball (6 mm diameter) used were made of steel AISI 52100 with similar roughness value of R_a = 20 nm. Both the ball and disc were initially cleaned in an ultrasonic bath with three different solvents (acetone, ethanol and n-heptane) for 15 min each. Same disc and ball were used to perform up to four tests with the same lubricant. After each test, the ball and disc were cleaned by wiping the surface with a tissue soaked with n-heptane.

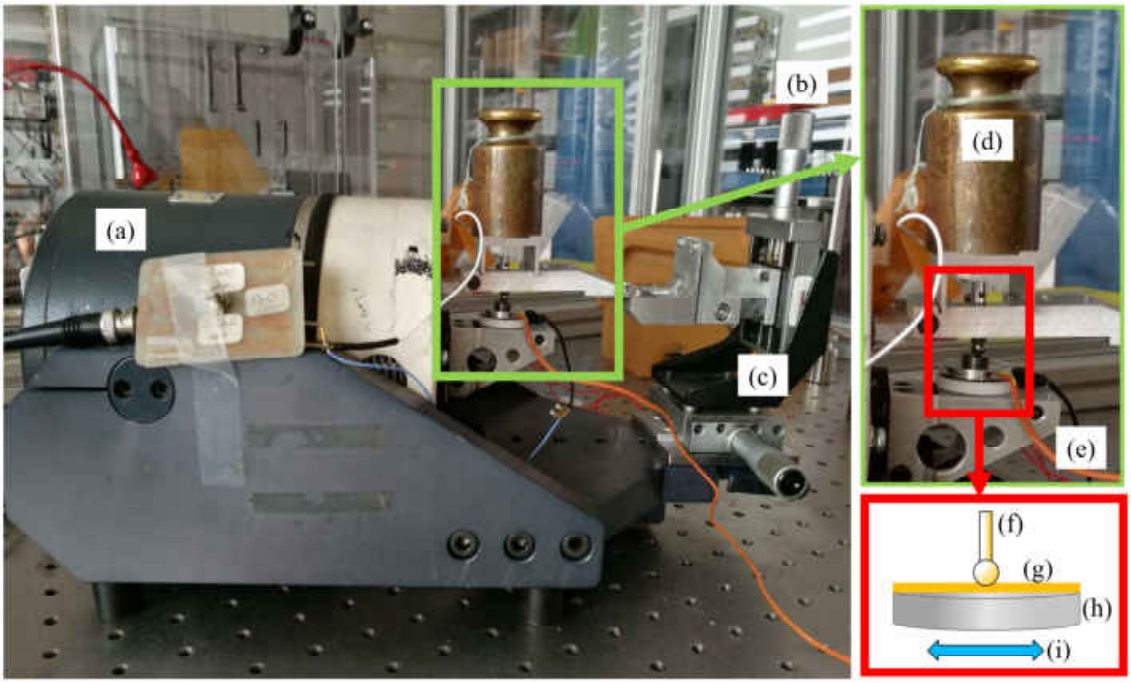

Figure 130. Digital photograph and scheme of the tribometer used for the friction measurements. The components are: (a) linear motor, (b) charge meter, (c) Piezo detector, (d) load, (e) connection to heating system, (f) standing specimen with ball, (g) lubricating layer, (h) disc and (i) double arrow to indicate the reciprocating motion of the disc during the tests.

Before conducting the friction tests a load was set atop of the specimen to adjust the contact pressure on the disc. Then the reciprocating motion of the disc was initiated to measure the friction coefficient of the lubricants. All relevant parameters of the tribo-tests are summarized in Table 9.

Table 9. All nanoparticles samples, which underwent tribological studies as additives to standard poly alpha olefine oil and the materials used for the measurements.

Sample	Materials/Methods
PAO 6CST (Reference base oil)	Load: 5 N
PAO6 + 0.992 *wt%* molybdenum sulfide nanosheets (MoS_2)	Hertzian contact pressure: 1.1 GPa
PAO6 + 1.218 *wt%* tungsten sulfide nanosheets (WS_x)	
PAO6 + 0.992 *wt%* molybdenum tungsten sulfide nanosheets ($MoWS_x$)	Hertzian contact diameter: 93.3 µm
PAO6 + 0.997 *wt%* molybdenum oxysulfide nanoflakes (MoO_xS_{2-x})	
PAO6 + 1.002 *wt%* tungsten sulfide fullerenes (IF-WS_2)	Lubrication regime: 0.8 Λ
PAO6 + 1.001 *wt%* tungsten oxysulfide nanosflakes (WO_xS_{2-x})	Reciprocating speed: 3 mm/s
PAO6 + 0.999 *wt%* tungsten sulfide fullerenes (NT-WS_2)	Steel: AISI 52100

In general, during a generic tribological process two different periods can be observed: the running-in and the steady state period. The running-in period is defined as the period where all the parameters (e.g. surface parameters, wear, friction, etc.) are in continuous modification. Then,

once all the possible chemical reactions and surface adaptation occur, the process enters the steady-state, where all the parameters are considered almost constant.[87] In the case of the friction curves, which will be shown in the following, the friction steady state is calculated for each single test as the average value of all friction coefficients after the end of the running-in period. In this work, it is referred to the values obtained after the first 500 cycles. The number of cycles where the running-in ends is always an assumption based on the observation of different friction curves. The tests were repeated at least three times for each sample to get statistical representation of the real values, the single measurements can be seen from Figure A 206–Figure A 212 in the appendix. The friction steady state values shown in the bar charts (Figure 136–Figure 143) are the average values of the three friction steady state values obtained and the error bars represent the variation of these values between the tests. Thus, the calculated value gives an indication of the behaviour of the additive or lubricant during its working life.

Measurements at ambient temperature. First, the friction coefficients of all nanoparticle samples as additives in PAO and the PAO as reference, respectively, were measured at ambient temperature. Figure 131 shows the evolution of the friction coefficient with the number of cycles for the different samples.

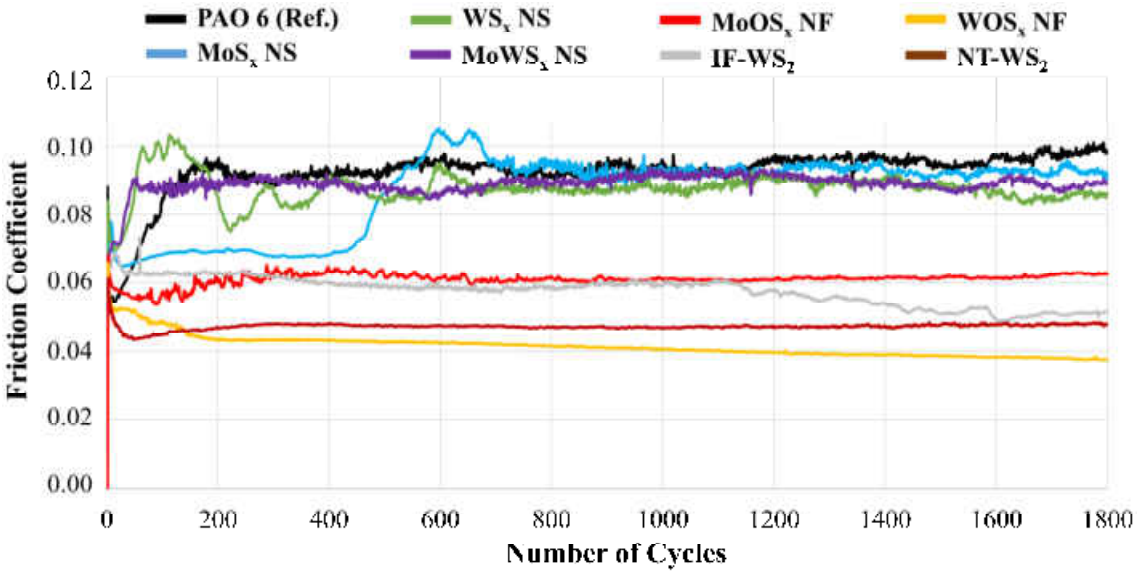

Figure 131. Friction coefficient over the number of measuring cycles for all prepared samples, measured at ambient temperature.

MS_2 sheets with oleylamine. Primarily, it can be observed that all samples with particles prepared in oleylamine do not considerably reduce friction after 600 cycles. Therefore, the friction coefficient of MoS_2@OA nanosheets to 0.064, but then levels off at a value of 0.091. To gain further information on the tribochemical reactions and elemental composition of the tribofilm, XPS analysis of the worn surfaces of the lower disc specimen was conducted (Figure 132).

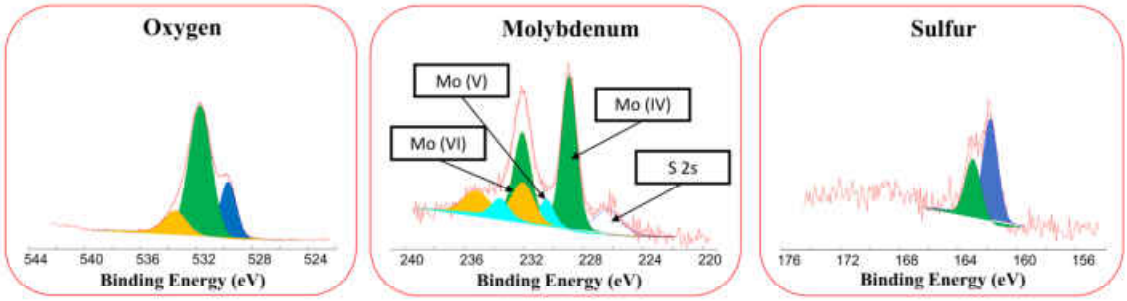

	Carbon		Oxygen			Molybdenum			Sulfur
Species	Aliphatic	Carbide	Oxide	R-O-R	R=O	Mo (IV)	Mo (V)	Mo (VI)	S (II)
BE (eV)	284.8	283.8	529.7	531.7	533.5	229.0	230.5	232.0	161.8
Concentration (atom%)	50.2	1.5	5.3	16.4	2.7	0.3	0.0(4)	0.1	0.6

Figure 132. XPS analysis of the wear track on the steel surface after tribological tests were performed with MoS_2@OA nanosheets in PAO.

Due to the results obtained from XPS the ratio of Mo(IV) species and S(II) species is 1:2. Therefore, it can be concluded that MoS_2 in present in the wear track of the steel surface. As it was shown above, the friction values for this additive are comparable to the pure PAO. As a result, there was no significant influence of the MoS_2 particles on the friction.

WS_x@OA nanosheets in PAO yield a friction coefficient of 0.087, which is very similar to the one of the mixed sulfide nanosheets of $MoWS_x$@OA (0.092). Figure 133 compares the oxygen 2p, tungsten 4f and sulfur 2p XPS spectrum of the tribofilm after lubrication by WS_x@OA nanosheets. The data analysis provides a possible presence of WS_2 in the wear track, although the ratio of the W(IV)/S(II) cannot be confirmed. The different ratio could be obtained due to the presence of WO_2, which would also explain the massive amount (24.4*at*%) of oxygen. The fact that a low-energy signal was found at 31.7 eV, which can be assigned to tungsten carbide, strongly indicates that the sample was subjected to enormous stress during the test.

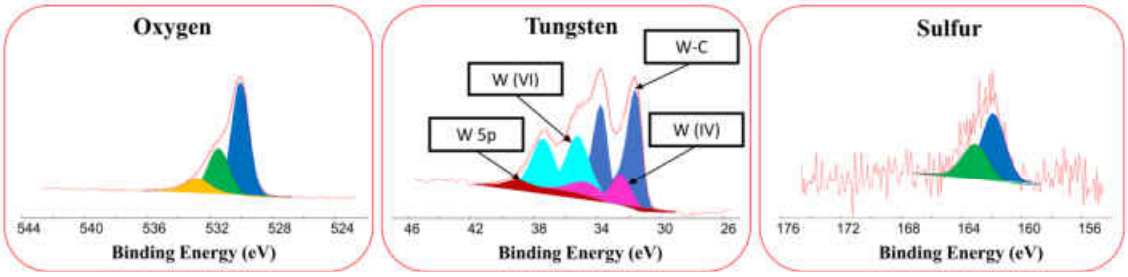

	Carbon		Oxygen			Tungsten			Sulfur
Species	Aliphatic	Carbide	Oxide	R-O-R	R=O	W (I)	W (IV)	W (VI)	S (II)
BE (eV)	284.8	283.2	530.1	531.5	532.9	31.7	32.6	35.3	162.0
Concentration (atom%)	19.3	2.9	24.4	11.2	4.3	0.4	0.6	0.7	0.4

Figure 133. XPS analysis of the wear track on the steel surface after tribological tests were performed with WS_2@OA nanosheets in PAO.

Since all friction coefficients of the samples produced in oleylamine are on the level of the base oil PAO, this combination of particles in PAO6 does not prove itself to be a suitable material for friction reduction. Their poor performance can be explained by the high friction coefficient of pure oleylamine of ~0.09,[88] which is comparable with PAO. While the oleylamine-capped nanosheets show a far better dispersibility and low sedimentation in the PAO than the particle produced in benzyl alcohol, the friction reducing effect of the MS_x particles is practically non-existent due to strong inhibition by oleylamine.

MoO_xS_{2-x} and WO_xS_{2-x} nanoflakes. The MoO_xS_{2-x} nanoflakes prepared via the benzyl alcohol route show quite different behaviour under boundary lubrication. Notwithstanding their fast sedimentation in the oil, a protective layer is formed which gives constant low friction values (0.061). Furthermore, the reproducibility of the wear is very good, with particular shape on the ball (Figure 138). The XPS studies of the ball surface exhibit that no Mo(IV) species can be detected on the wear track (Figure 134). More interestingly, the species observed is Mo(V), which leads to a $MoSO_{1.5}$ compound and a Mo(VI) species rather corresponding to MoO_3. An additional S(VI) species can be detected at 168.3 eV, which corresponds to the sulfur $2p_{3/2}$ with oxidation number (6+). The peak arising at 169 eV is a doublet and contributed by the sulfur $2p_{1/2}$, which is a result of the oxidation of the nanoparticles during the test. The oxidation state of S^{6+} would indicate a formation of sulfate, suggesting a relation of the oxidized sulfur to the iron surface. The signal at lower energy (162.2 eV) can be attributed to the S^{2+} species. An oxidation state of IV is not properly detectable as it has an energy similar to that of the S(VI).

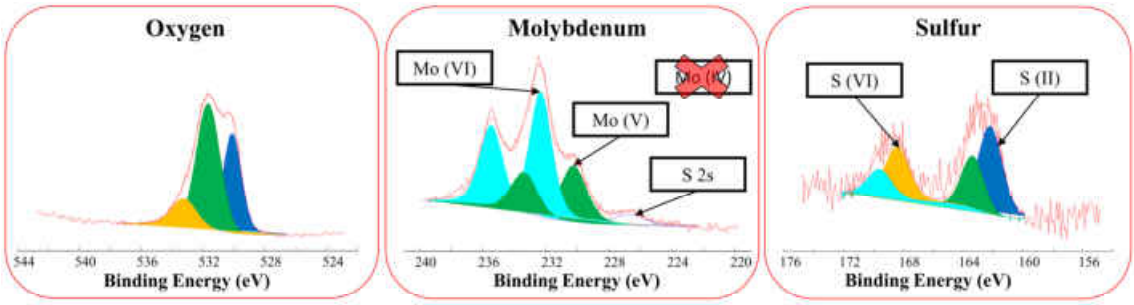

	Carbon		Oxygen			Molybdenum		Sulfur	
Species	Aliphatic	Carbide	Oxide	R-O-R	R=O	Mo (V)	Mo (VI)	S (II)	S (VI)
BE (eV)	284.8	283.8	530.1	531.7	533.2	230.2	232.3	162.2	168.3
Concentration (atom%)	53.4	1.8	7.3	10.8	2.5	0.8	1.1	0.9	0.5

Figure 134. XPS analysis of the wear track on the steel surface after tribological tests were performed with MoO_xS_{2-x} nanoflakes in PAO.

The tungsten-containing counterpart of WO_xS_{2-x} is also easy to disperse in the oil and reduces friction to a value of 0.04 with good reproducibility. In addition, low wear volumes are observed in the contact area. The XPS measurements of the tribofilm show signals of both the S(II) and S(VI) species, which can be attributed to the presence of WS_2 (as the ratio of W(IV)/S(II) is 1:2)

and some oxidized sulfur (Figure 135). Additionally, a high concentration of WO_3 was detected on the surface, suggesting that the nanoflakes might completely be oxidized during the tests. Oxidation of the tribofilm is expected in all measurements in air due to heavy stress, which has been reported.[89] Since the oleylamine-functionalized particles appear to be more strongly shielded from external influences, they cannot be completely oxidized.

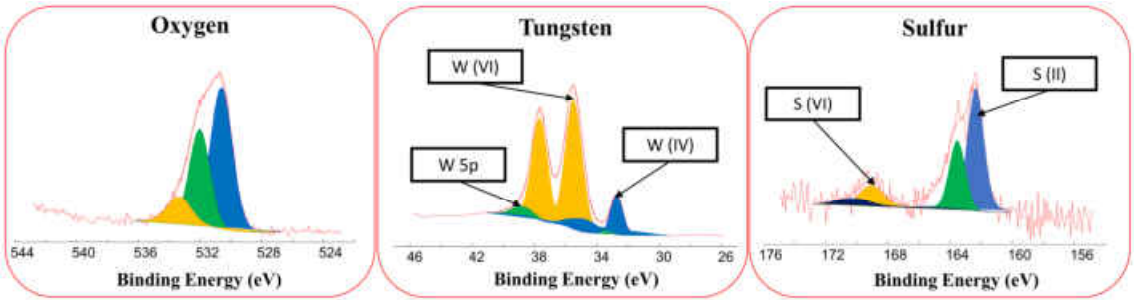

	Carbon		Oxygen			Tungsten		Sulfur	
Species	Aliphatic	Carbide	Oxide	R-O-R	R=O	W (IV)	W (VI)	S (II)	S (VI)
BE (eV)	284.8	283.5	530.6	532.0	533.3	32.7	35.5	162.3	169.0
Concentration (atom%)	56.6	11.7	9.7	6.0	2.0	0.6	3.6	1.2	0.3

Figure 135. XPS analysis of the wear track on the steel surface after tribological tests were performed with WO_xS_{2-x} nanoflakes in PAO.

IF-WS_2 and NT-WS_2. The two reference materials of WS_2 fullerenes (IF-WS_2) and WS_2 nanotubes (NT-WS_2), known for their superior lubricating properties, show the expected behaviour. They are easy to disperse, but without agitation the sedimentation occurs almost immediately. IF-WS_2 forms a protective layer due to delamination under load and the wear is easily reproducible, with a tribolayer formed on the ball. In general, the main advantage of IF-WS_2 in relation to other particles is their spherical shape, which allows them to act as nano- or microscopic ball bearings on contact surfaces, as well as their closed cage structure resulting in excellent chemical inertness due to the absence of dangling bonds. As Schwarz et al. previously showed, the van der Waals interactions cause strong adhesion to the substrate, which might facilitate the release of exfoliated layers onto the substrate.[90]

In general, during sliding contact, a shear force is needed to break the adhesive bonds at the real area of surface contact. A direct relationship of the real contact area A_r and the average shear strength of nanoscale asperity contacts τ is defined as the friction, which is measured during tribological experiments:[91]

$$F = A_r \cdot \tau.$$

Therefore, both reduction in shear strength and in contact area reduces friction as well as wear. On the other hand, particles deformation (e.g. compression or partially delamination) extends A_r and thus causes an increase in friction and wear. A similar behaviour is expected for NT-WS_2,

whereas here the rolling effect of the particles plays a more important role due to their anisotropic morphology. They are easy to disperse in the PAO and show low friction (0.048) directly from the beginning of the measurements while an increase can be observed almost at the end. On the flat sample, almost no wear can be detected (Figure 137 h).

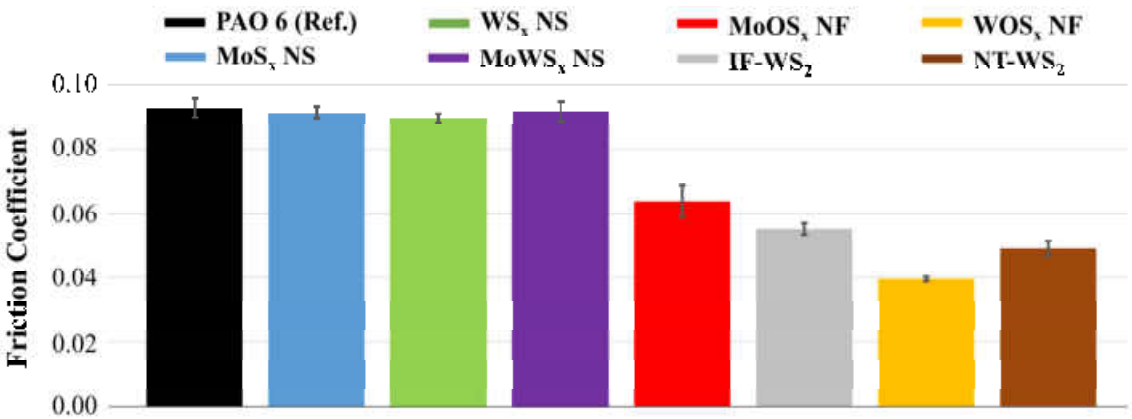

Figure 136. Friction steady state for all measured samples at ambient temperature.

The friction steady state shown in Figure 136 illustrates that all samples show constant friction after the running-in period. As indicated above, the particles functionalized with oleylamine not only show poor performance as friction reducing agents, but also yield high volumes of wear with huge variations (Figure 137). Therefore, oleylamine is completely detrimental in terms of being a good functionalization agent for MS_x particles, which shall be subjected to lubrication experiments.

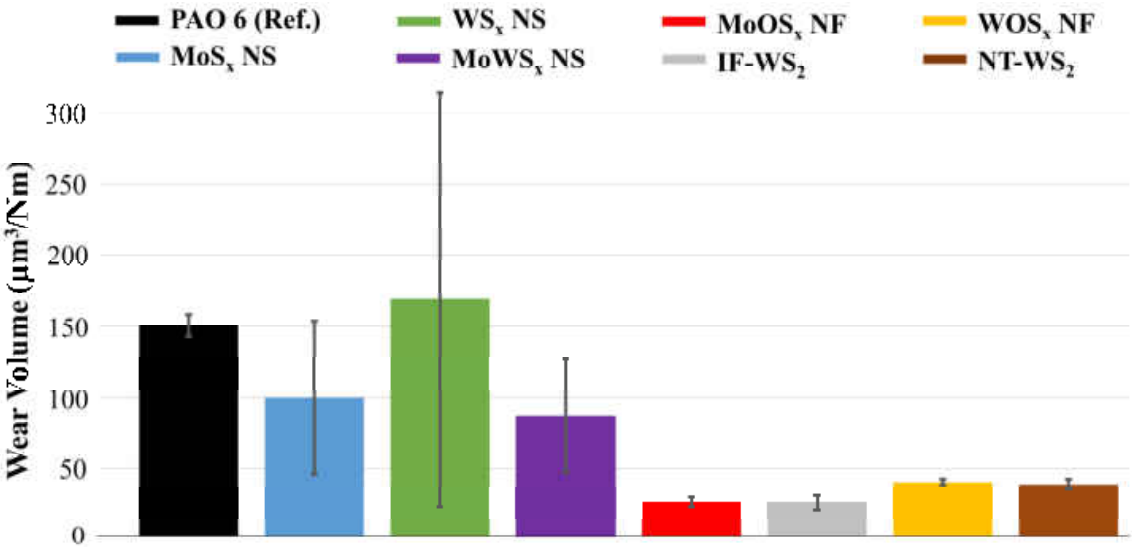

Figure 137. Wear volume of all measured samples at ambient temperature.

All oleylamine functionalized samples show heavy wear on both contact surfaces (the ball and the flat substrate). Hence, the wear volumes are up to 1180% higher than the ones obtained for the additives which were prepared in benzyl alcohol. Furthermore, digital photographs of the pin wear scars after the tribo-tests at 1.1 GPa contact pressure in Figure 138 illustrate that apparently

every additive is able to reduce the abrasion of the steel substrates to a certain extent compared to PAO, whereby both the layered products of NT-WS_2 and IF-WS_2 exhibit the lowest amount of remnants on the worn surfaces. Studies by Tenne et al. show the same behaviour of these two compounds, but the friction coefficient was found to be slightly lower (~0.055 for IF-WS_2) under similar pressure.[92] In any case, the calculated Hertz contact diameter of 93.3 µm is below the measured diameters of the ball wear scars.

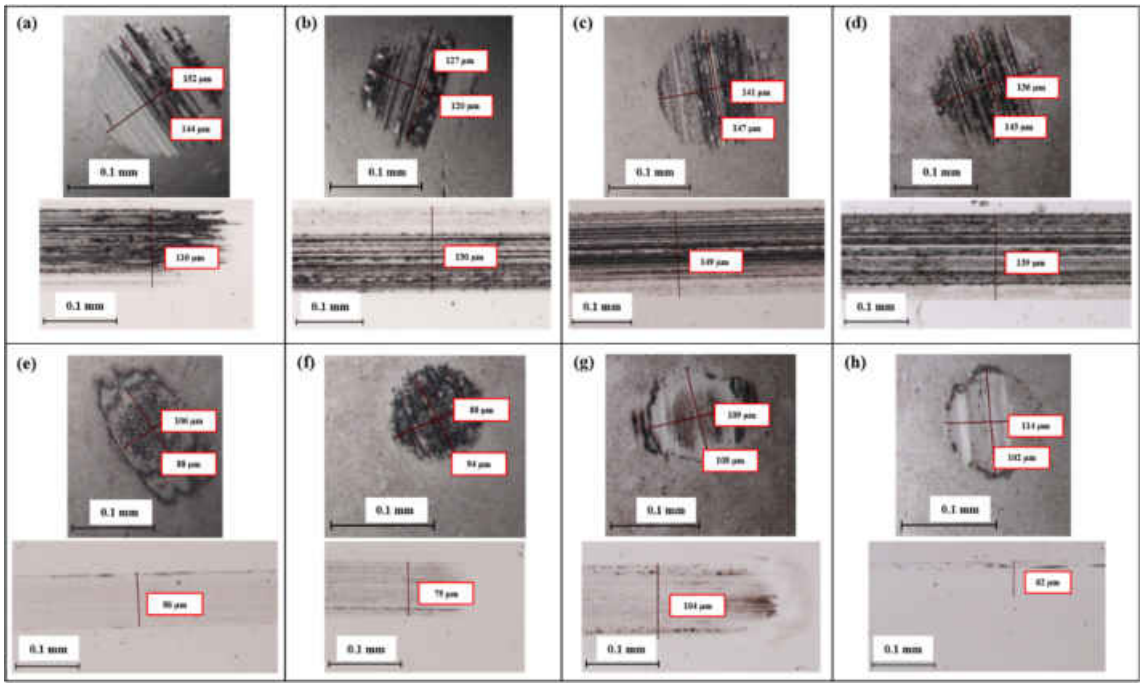

Figure 138. Digital photographs of worn surfaces of (a) PAO only, (b) MoS_2 nanosheets, (c) WS_x nanosheets, (d) $MoWS_x$ nanosheets, (e) MoO_xS_{2-x} nanoflakes, (f) IF-WS_2, (g) WO_xS_{2-x} and (h) NT-WS_2 after 1800 cycles of running at ambient temperature. The upper images show the wear scars on the ball, the bottom images the wear on the flat samples.

EDS analysis of the wear track on the disc was conducted for the WO_xS_{2-x} nanoflakes sample after 1800 cycles running (Figure 139). It thus illustrates that both tungsten and oxygen is present in the wear track (Figure 139 b, c), particularly in the areas of the highest penetration depth. In contrast to that, the sulfur is mainly located at the edges of the track. A possible explanation for these results could be that during the tribo measurements the main stress occurs in the middle of the specimens. A large part of the additive particles is thereby delaminated or driven to the edge of the dispersion (without being damaged). In the course of the measurement, oxidation processes then cause a faster oxidation of the single WS_2 or WO_xS_{2-X} layers, which are subjected to higher stress, than the layers on the edge of the abrasive surface. Carbon also shows a higher concentration in the wear track, which can be attributed to a significantly higher concentration of PAO in that area due to wear-induced volume increase.

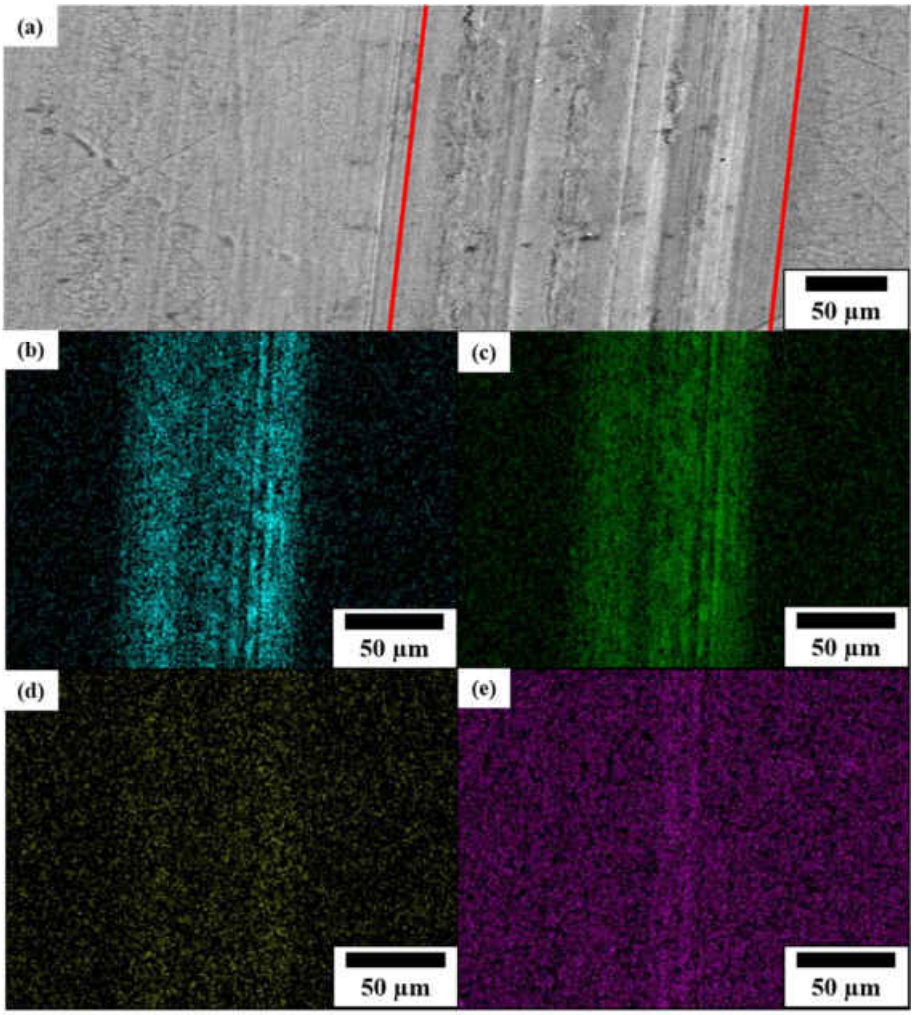

Figure 139. EDS mapping analysis of the surfaces subjected to tribo-tests using WO_xS_{2-x} nanoflakes as additive to PAO: (a) SEM image of the worn surface showing the area of the EDS measurements, (b) W-atom distribution, (c) O-atom distribution, (d) S-atom distribution and (e) C-atom distribution.

XPS analysis of the wear track shows the presence of W(IV) and S(II) species, with a ratio of 1:2. Furthermore, a high concentration of WO_3 can be detected, owing to the oxidation of the tribofilm during the process.

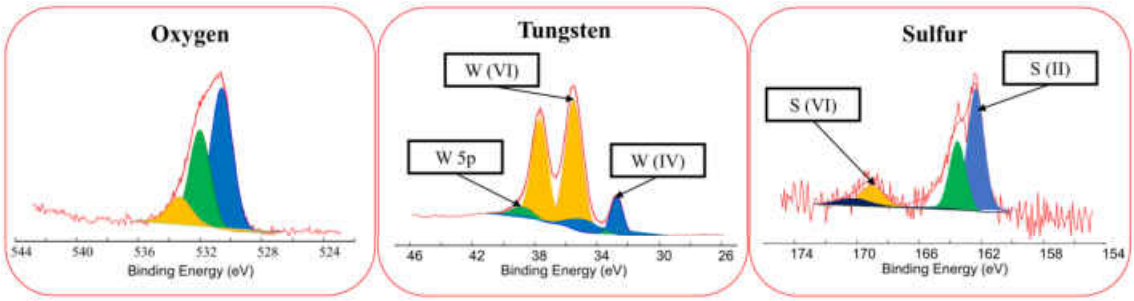

	Carbon		Oxygen			Tungsten		Sulfur	
Species	Aliphatic	Carbide	Oxide	R-O-R	R=O	W (IV)	W (VI)	S (II)	S (VI)
BE (eV)	284.8	283.5	530.6	532.0	533.3	32.7	35.5	162.3	169.0
Concentration (atom%)	56.6	0.7	9.7	6.0	2.0	0.6	2.6	1.2	0.3

Figure 140. XPS analysis of the surface shown in Figure 137.

The composition of the tribofilm was further investigated via XPS analysis coupled with sputtering of the appropriate layer. The time-resolved atomic composition of the specimens' surface is illustrated in Figure 141. Initially, almost 60% content of aliphatic carbon is detected, which is attributed to the PAO. After a sputtering time of 2 min, the proportion of oxide increases rapidly to 30%, passes through a maximum (34%) at 12 min, and then decreases steadily until it completely diminishes after 80 min. The proportions of the different tungsten and sulfur species all remain below 10%, while WO_xS_{2-x} accompanied by pure WS_2 and WO_3 can be detected. The course of all tungsten signals is very similar, the W(VI) species thus disappears earlier (~15 min) than the W(IV) species (after ~20 min). Miniscule amounts of WO_XS_{2-X} can be detected even after 100 min. A continuous increase of the (metallic) iron signal can be observed, which is explained by the progressive exposition of the specimen surface.

As the tribolayer almost completely disappears after 50 min of sputtering time, it can be deduced that the layer thickness is ~20 nm. The removal rate was calculated as the time needed to remove the oxide layer on a steel surface (~5 nm) and therefore corresponds to ~0.4 nm/min.

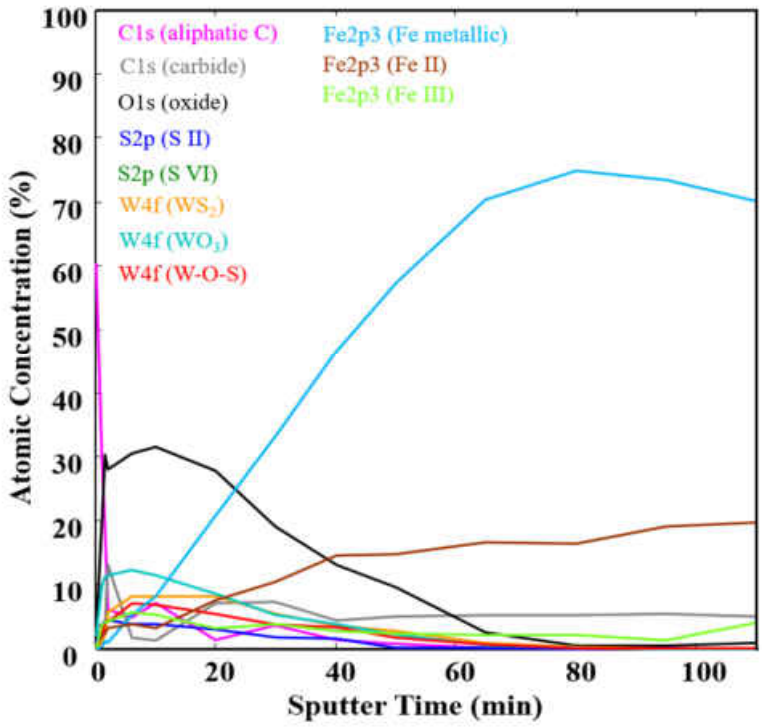

Figure 141. XPS analysis profile, measured on the disc after tribo-test using WO_xS_{2-x} nanoflakes as additive to PAO. The atomic concentration was determined with respect to the sputtering time of the surface.

Measurements at 80 °C. With the results obtained from ambient temperature measurements, the operating temperature was increased to 80 °C to simulate the conditions in conventional combustion engines. As the viscosity of the PAO is decreased at higher temperature, the sedimentation of the particles occurs faster. Thus, more reliable results on the tribological properties of the additives can be obtained. All parameters except the temperature were kept constant and the same materials were used.

Figure 142 shows the change of the friction coefficient for MoO_xS_{2-x} nanoflakes, WOS_x nanoflakes, IF-WS_2 and NT-WS_2 particles as lubricants additives over the number of cycles. The nanosheets samples were not used because of their poor performance at ambient temperature.

The MoO_xS_{2-x} nanoflakes show a different behaviour at 80 °C compared to the one observed at ambient temperature with a friction coefficient constantly decreasing to 0.03 after 1800 cycles. This result shows the lowest level of a friction coefficient of oxysulfide particles achieved so far, to our best knowledge. Generally, transition metal oxides or oxysulfides are regarded as less powerful lubricants due to their less pronounced ability to be exfoliated in boundary lubrication. However, in the case of oxysulfides this conclusion even might be a fallacy. As Zhou et al. reported, oxygen-incorporated MoS_2 nanosheets show expanded van der Waals gaps of 8.3 Å compared to 6.4 Å for the unsubstituted MoS_2 lattice.[93] The expansion of the interlayer spacing might therefore be beneficial for the gradually exfoliation of single molecular nanosheets of the multi-layered nanoflakes and their transfer onto the asperities of the reciprocating surfaces. This would further enhance the lubricating effect of these particles. As it was reported by Tannous et al.,[89] tribochemistry of boundary lubrication in steel substrates is based on the formation of Fe-O-Mo, Fe-O-S-Mo and Fe-S-Mo bonds. Therefore, it is considered that the additional oxygen provides a bigger amount of stable Fe-O-S bonds. As a consequence, the iron surface can be occupied by single-layer MoO_xS_{2-x} more extensively and thus an easier sliding of the opposing interfaces is enabled, resulting in a massive decrease of the friction coefficient.

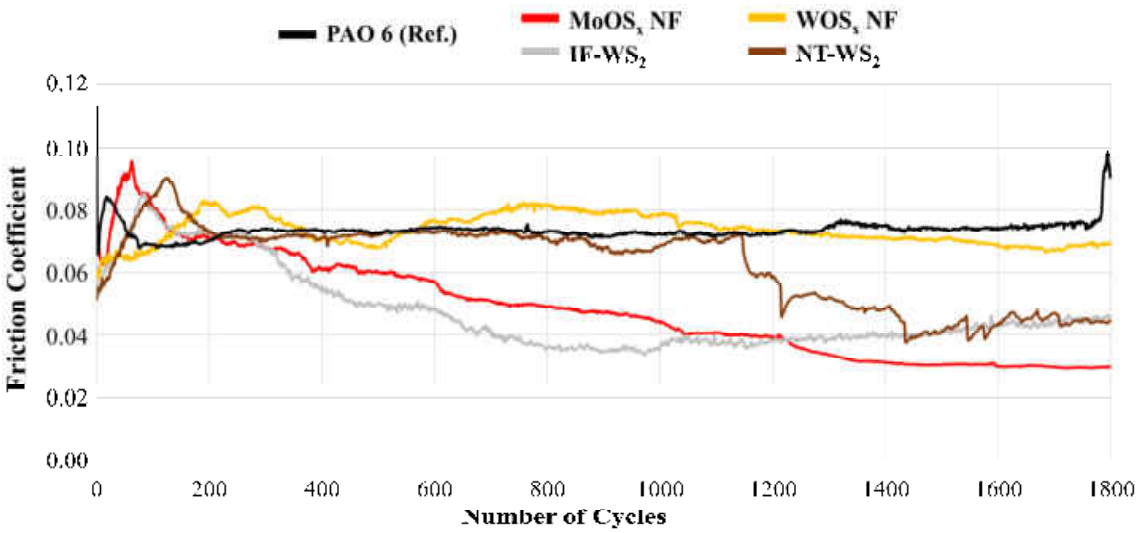

Figure 142. Friction coefficient over the number of measuring cycles for the four best-performing particles at 80 °C.

It was expected that expanding of the interlayer should also apply for the WOS_x nanoflakes and improve the lubricating properties. This is not the case, as these particles show extreme deterioration of their lubricating properties at elevated temperature. The friction coefficient at 80 °C (0.081) is more than 170% higher than the one measured at ambient temperature (0.030). The friction curve is similar to the one observed for the model base oil, which shows a poor dispersibility of the WOS_x nanoflakes in the PAO. Furthermore, during the measurements a tendency for the sedimented particles to move away from the contact was noticed.

The IF-WS_2 gives lower friction at 80 °C (0.036) compared to AT (0.052) and a different course of the data. At ambient temperature the friction coefficient attains a maximum value of 0.061 after ~950 cycles and then slowly decreases to 0.051. However, the trend at 80 °C is precisely the reverse: the friction coefficient decreases from the start, after about 980 cycles a minimum is passed and an increase of the friction coefficient is observed again thereafter. Since the friction coefficient initially (~170 cycles) is above the one measured for the PAO, the behavior might be explained by a retarded formation of the protective film, which also causes a higher wear compared to AT. After the test was completed, a layer on top of the surface was detected, similar to the one observed at ambient temperature.

NT-WS_2 show even higher friction in the running-in period with a continuous decrease until ~1170 cycles. After that point, a major drop can be observed from a friction coefficient of 0.07 to 0.048 within 100 cycles. Then the friction coefficient gradually declines with some ups and downs (up to 0.038), until it reaches a constant value of 0.044 at the end of the experiment. This behavior (characterized by marked decreases or increases in friction coefficient) may indicate a change from solid to liquid lubrication, i. e. if the concentration of NT-WS_2 drastically drops in the contact area. The wear was found to be lower at 80 °C because of the formation of a thicker protective film.

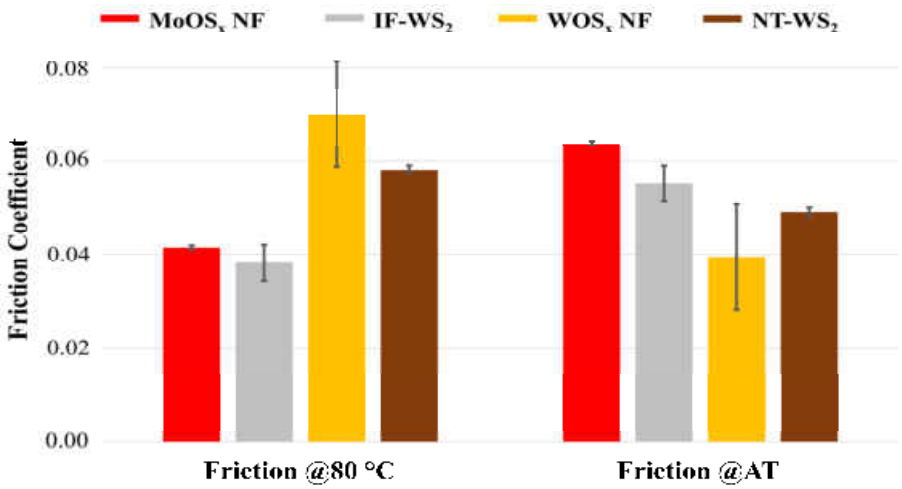

Figure 143. Comparison of the friction steady state of the four best-performing particles at 80 °C and ambient temperature.

The data of friction steady state emphasizes that the MoO_xS_{2-x} nanoflakes show the best and most stable tribological performance (Figure 143), whereas the WOS_x nanoflakes lose their lubricating properties and show a wide variation of the friction coefficient in the steady state.

The wear tests done at ambient temperature generally show a clear difference between the nanoflakes of IF-WS_2 and the samples of MoO_xS_{2-x}, NT-WS_2 and WO_xS_{2-x} (Figure 144). At 80 °C similar values of wear were obtained for all nanoparticles, with the lowest wear volume observed for the WS_2 nanotubes. In the case of MoO_xS_{2-x} a slight reduction (~ 8%) of wear can be detected, while it significantly increases (~ 20%) for IF-WS_2. Compared to the model base oil PAO, wear is lower in all cases.

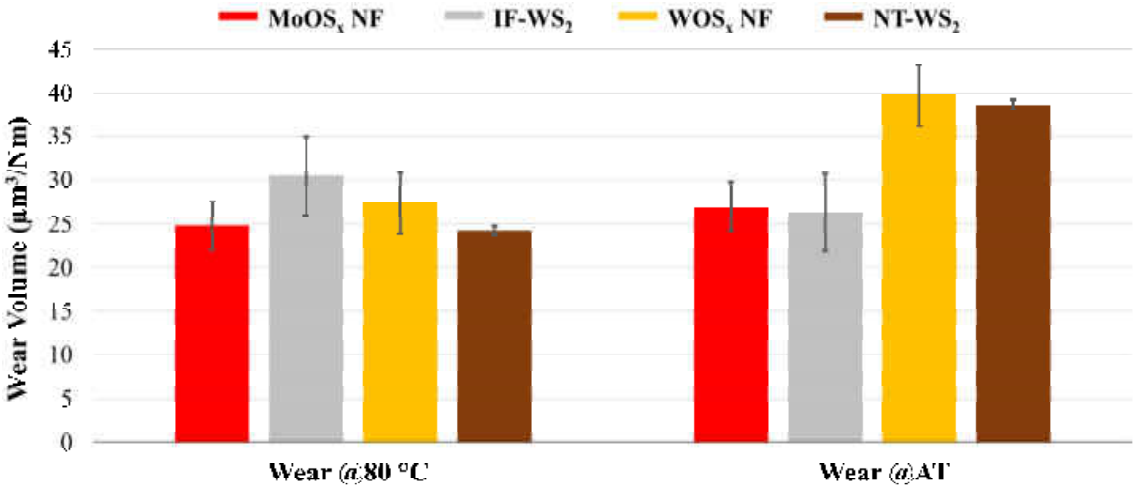

Figure 144. Comparison of the wear volume of the four best-performing particles at 80 °C and ambient temperature.

Digital photographs of all surfaces lubricated by the nanoparticles added to PAO6 oil are shown in Figure 145. Due to the formation of a less protective film for IF-WS_2 and NT-WS_2, the steel surfaces show more scratchings than after the tests at ambient temperature. The Hertzian contact diameter is exceeded for every sample except NT-WS_2, as the dimension of the wear scar diameter of this additive can be regarded as similar to the calculated one in terms of possible errors during the measurements.

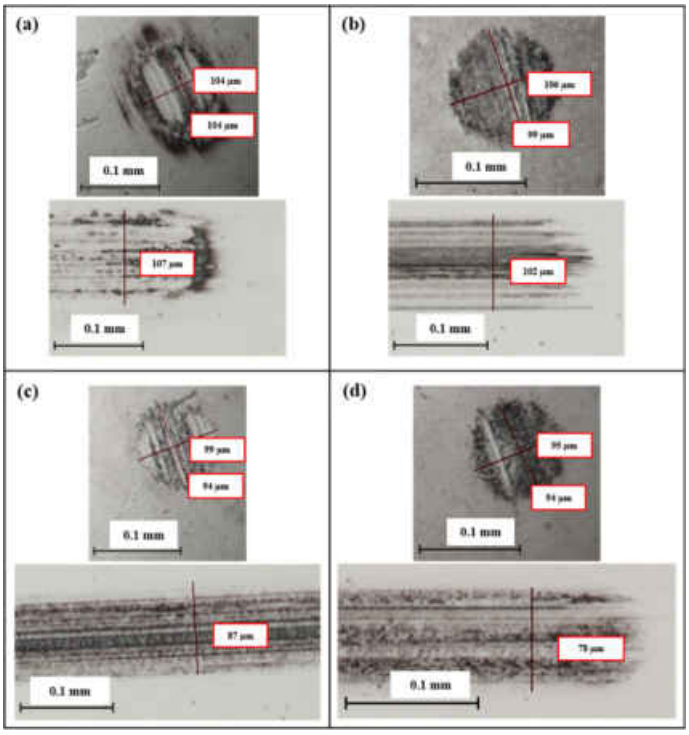

Figure 145. Digital photographs of worn surfaces after 1800 cycles of running at 80 °C for (a) MoO_xS_{2-x} nanoflakes, (b) IF-WS_2, (c) WO_xS_{2-x} and (d) NT-WS_2 particles. The upper images show the wear tracks on the ball, while the lower images represent the the disc surface after the tribo-measurements.

6.3. Other TMC Particles

6.3.1 MoS_x Microsponges

Microsponges of MoS_x were obtained as by-product from the same synthesis used for the production of MoO_xS_{2-x} nanoflakes, but could not be reproduced more than once. Figure 146 presents SEM images of the sponges with a variety of different pore sizes. The porous structure exhibits cavities of 80–300 nm height and up to 2 µm in length. Additionally, some erupted hollow spheres can be observed (Figure 146 b), accompanied by a great amount of bulk material.

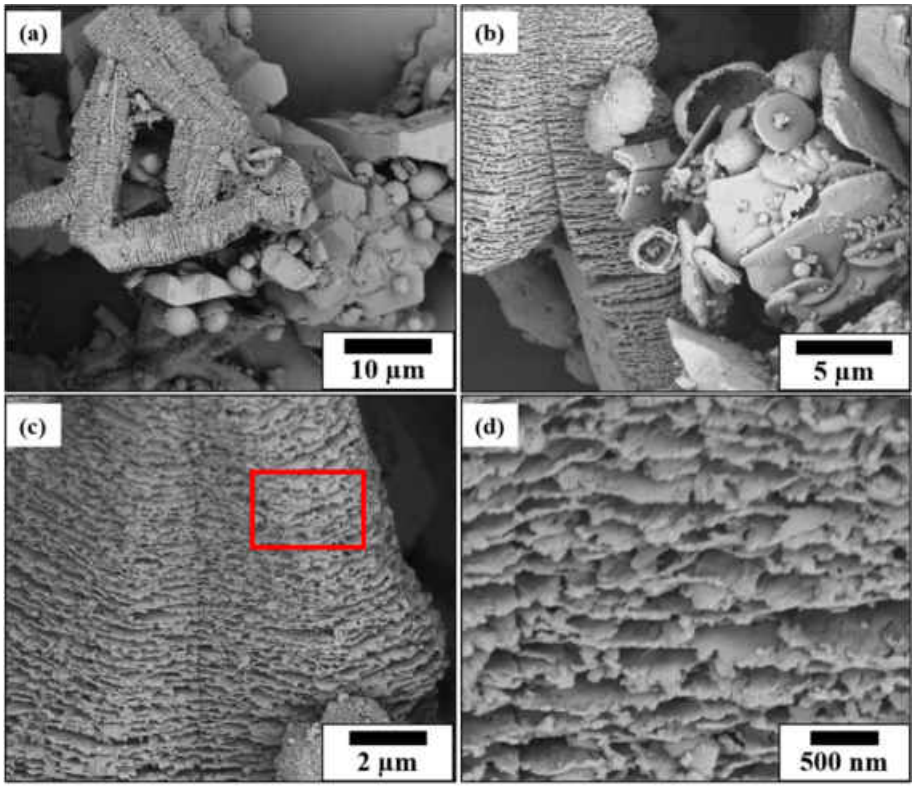

Figure 146. SEM images of the macroporous product obtained as by-product from the benzyl alcohol decomposition of $(NH_4)[Mo_3S_{13}]$.

SEM images of the reproduced sample in Figure 147 show large (~80 µm), elongated structures with pores of comparable dimensions (~70·400 nm). In general, the batch shows vast morphological inhomogeneity (Figure 147 b), as it also contains microspheres (1–3 µm diameter), platelets (up to 8 µm), bulk and the nanoflakes presented in Chapter 6.2.2.

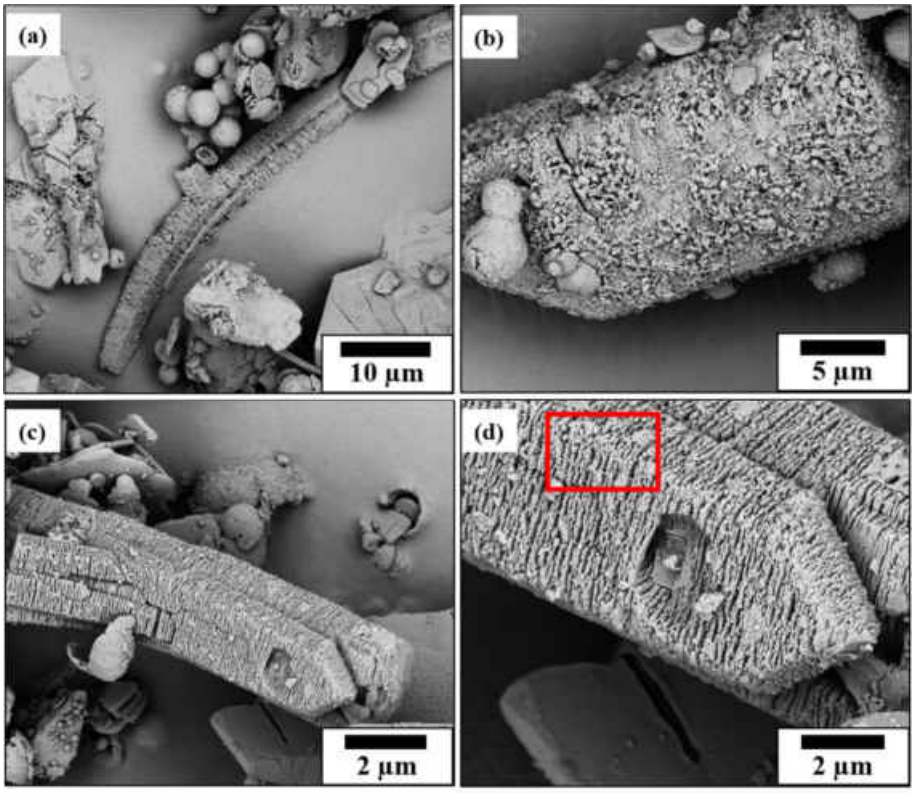

Figure 147. SEM images of the macroporous product from another batch obtained as by-product from the benzyl alcohol decomposition of $(NH_4)[Mo_3S_{13}]$.

EDS data of both red marked areas in Figure 146 (c) and Figure 147 d proposes a composition of MoS_3 for these compounds (*at*% ratio of Mo:S is 25:75), which cannot definitely be confirmed by means of XRD analysis. The pattern exhibits both contributions of Mo_2S_3 phase and Mo_4O_{11} phase, which is not surprising as it was mentioned earlier that benzyl alcohol features a significant oxidation potential.

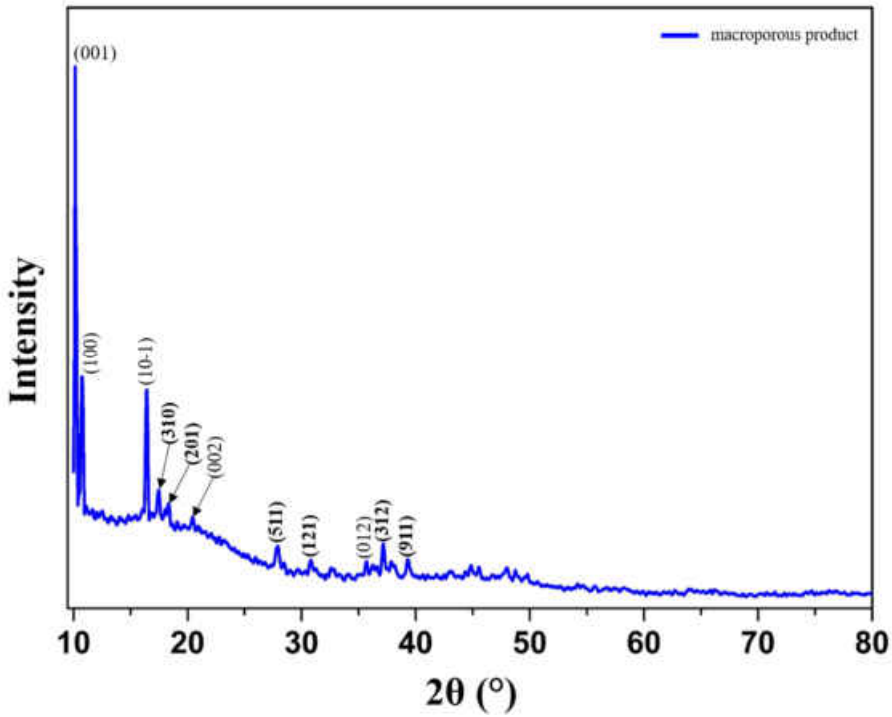

Figure 148. XRD pattern of the sample containing the macroporous product; bold typed Miller indices are attributed to Mo_4O_{11} phase, normal typeface is used for Mo_2S_3 phase.

The Raman spectrum of the sample also shows bands of both sulfide (< 400 cm^{-1}) and oxide products (600–1000 cm^{-1}), as discussed in the previous chapters.

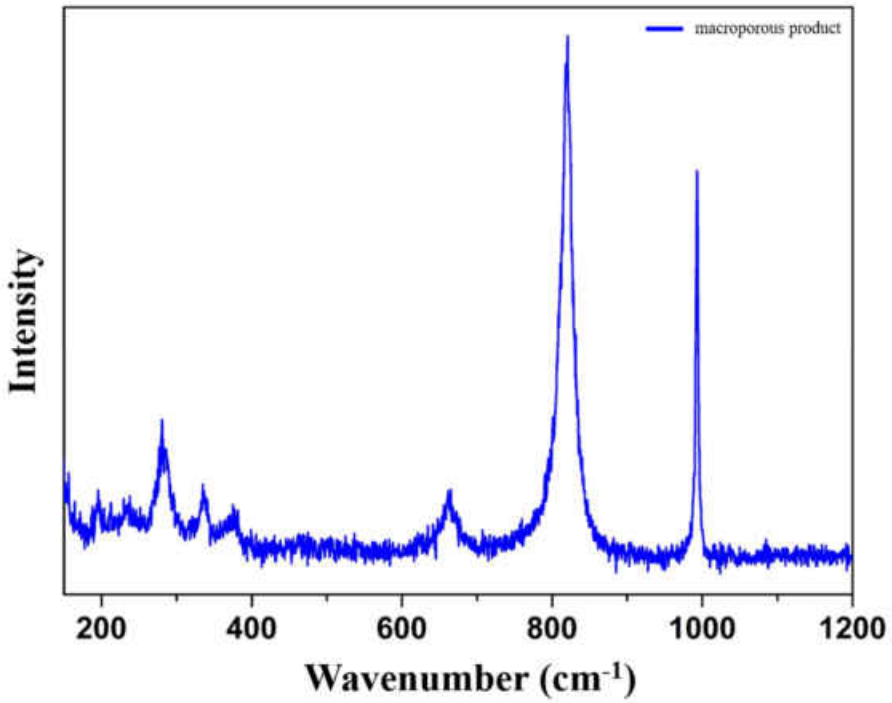

Figure 149. Raman spectrum of the sample containing the macroporous product.

A reproducibility of the macroporous structures, and thus also the verification of MoS_3 as a dominant structure, would open up many interesting fields of application for these

compounds.[94, 95] It was already shown in many reports, these materials are extremely promising for the use as H_2-generation catalysts,[96-100] in lithium batteries,[101-103] for hydrogen storage[104] or in boundary lubrication (due to their layered structure).

6.3.2. WS_2 platelets

Platelets of WS_2 were synthesized via reductive sulfidization (Chapter 6.2.3.) using WO_3 nanoplatelets (Chapter 4.4.1.). The SEM images presented Figure 150 show that the plate-like particles (~300–400 nm lateral length) obtained are strongly agglomerated and many flakes of WS_2 can be observed as by-product. The formation of flakes can be explained by the sulfidization growth mechanism of oxide precursors. As the particles were not fluidized during the conversion, their immediate vicinity favours growth of individual sheets due to healing of edge defects in the process.[105-107]

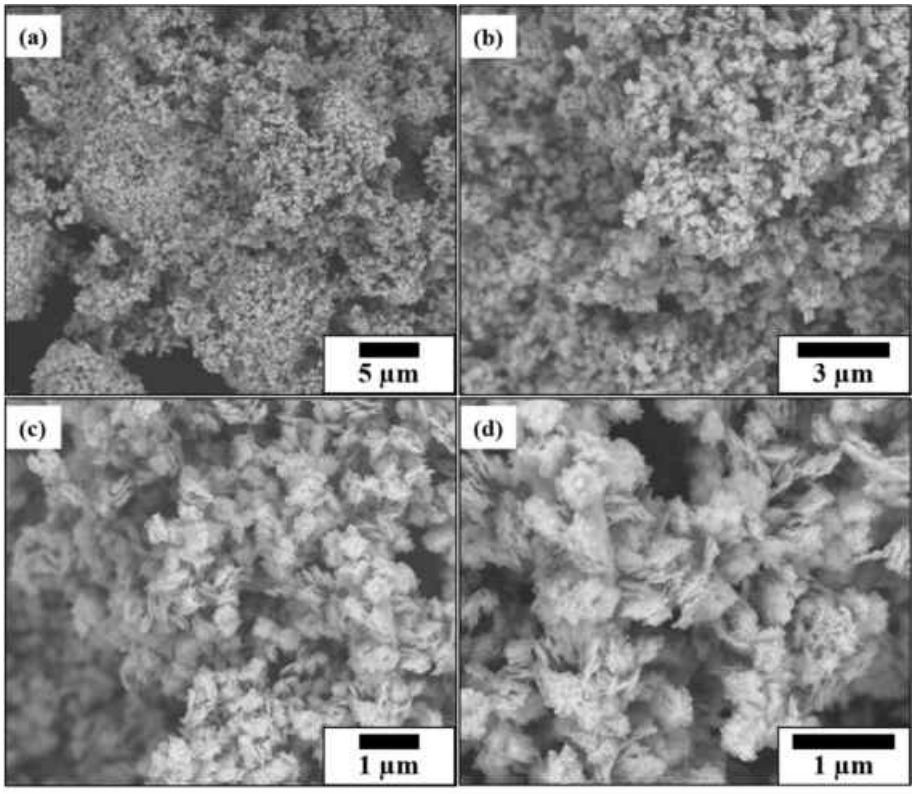

Figure 150. (a-d) SEM images of sulfidized WO_3 nanoplatelets, from different areas of the sample. The images were taken from gold-sputtered substrates to achieve higher magnifications.

The XRD pattern shown in Figure 151 confirms the phase purity of the WS_2 nanoplatelets, as all reflections can be attributed to 2H-WS_2.

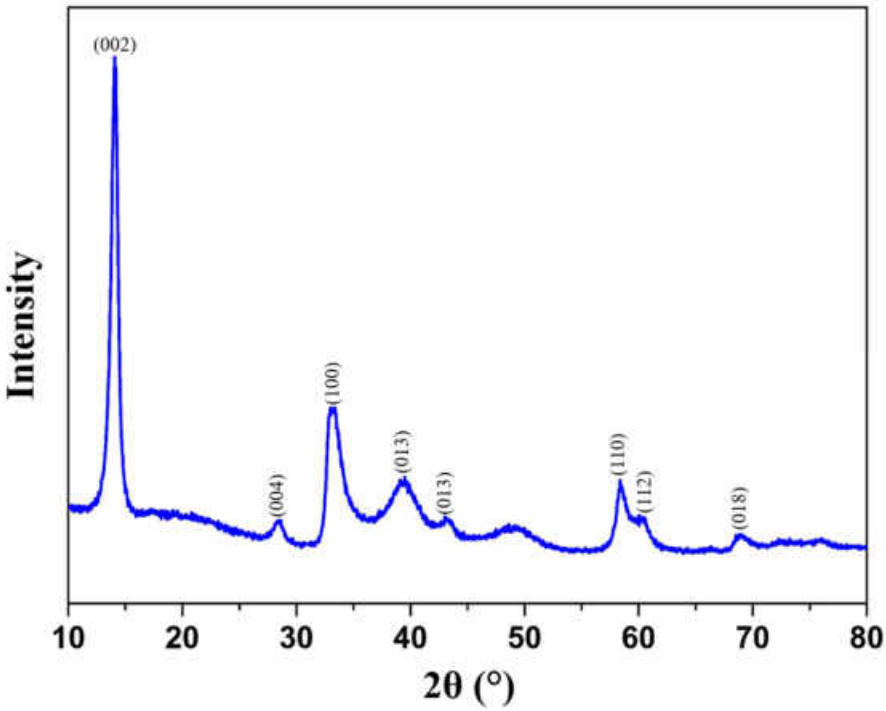

Figure 151. Powder XRD pattern of sulfidized WO_3 nanoplatelets, showing phase pure WS_2.

6.4. Conclusion

In this part of the work, novel nanoparticulate compounds were obtained via a simple one-step synthesis in oleylamine or benzyl alcohol as solvents. In oleylamine, tiny nanosheets can be produced, which are already functionalized with oleylamine as capping agent and therefore show high dispersibility in non-polar solvents. Using benzyl alcohol, new structures of molybdenum or tungsten oxysulfides can be prepared, which have not yet been presented in other publications to my best knowledge. In comparison to other compounds already known, such as fullerene-like compounds or nanotubes of WS_2, blended results are obtained in their examination in tribological applications.

Although the oleylamine-functionalized particles give more homogeneous mixtures with the reference oil, they have almost no effect as a friction-reducing additive due to the high residual content of oleylamine. In the case of the oxysulfides, however, a considerable reduction in the coefficient of friction is observed, which provides completely new results for these compounds. Until now, friction coefficients < 0.04 are exclusively known for sulfide compounds. It is proposed, that due to the incorporation of oxide into the sulfide lattice the van-der-Waals gap between the distinct layers is expanded and, thus, facilitates delamination of the MoO_xS_{2-x} layers. Furthermore, knowing that the tribochemistry of boundary lubrication in steel substrates is based on the formation of Fe-O-Mo, Fe-O-S-Mo and Fe-S-Mo bonds (as revealed by XPS analysis) it is considered that the additional oxygen provides a bigger amount of stable Fe-O-S bonds.

Therefore, the iron surface can be occupied by single-layer MoO_xS_{2-x} more extensively and thus an easier sliding of the opposing interfaces is enabled, resulting in a massive decrease of the friction coefficient.

Since this effect is even more pronounced at elevated temperatures, wear reducing application in gear or engine oils seems to be very promising. However, there is no explanation for this effect not being observed for the similar compound with tungsten instead of molybdenum (WO_xS_{2-x}).

6.5. References of Chapter 6

[1] G. Z. Shen, Y. Bando, D. Golberg, C. Zhou, *J. Phys. Chem. C* 2008, **112**, 5856-5859.

[2] X. Zou, B. I. Yakobson, *Acc. Chem. Res.* 2015, **48**, 73-80.

[3] F. Banhart, J. Kotakoski, A. V. Krasheninnikov, *ACS Nano* 2011, **5**, 26-41.

[4] Q. Chen, H. Li, W. Xu, S. Wang, H. Sawada, C. S. Allen, A. I. Kirkland, J. C. Grossman, J. H. Warner, *Nano Lett.* 2017, **17**, 5502-5507.

[5] A. R. Adini, M. Redlich, R. Tenne, *J. Mater. Chem.* 2011, **21**, 15121-15131.

[6] C. S. Reddy, A. Zak, E. Zussman, *J. Mater. Chem.* 2011, **21**, 16086-16093.

[7] C. Shahar, R. Levi, S. R. Cohen, R. Tenne, *J. Phys. Chem. Lett.* 2010, **1**, 540-543.

[8] C. Shahar, D. Zbaida, L. Rapoport, H. Cohen, T. Bendikov, J. Tannous, F. Dassenoy, R. Tenne, *Langmuir* 2010, **26**, 4409-4414.

[9] A. Rothschild, J. Sloan, R. Tenne, *J. Am. Chem. Soc.* 2000, **122**, 5169-5179.

[10] H. A. Therese, J. Li, U. Kolb, W. Tremel, *Solid State Sci.* 2005, **7**, 67-72.

[11] M. Remskar, M. Virsek, A. Jesih, *Nano Lett.* 2008, **8**, 76-80.

[12] Y. D. Li, X. L. Li, R. R. He, J. Zhu, Z. X. Deng, *J. Am. Chem. Soc.* 2002, **124**, 1411-1416.

[13] M. J. Yacaman, H. Lopes, P. Santiago, D. H. Galvan, I. L. Garzon, A. Reyes, *Appl. Phys. Lett.* 1996, **69**(8), 1065-1067.

[14] I. Alexandrou, N. Sano, A. Burrows, R. R. Meyer, H. Wang, A. I. Kirkland, C. J. Kiely, G. A. J. Amaratunga, *Nanotechnology* 2003, **14**, 913-917.

[15] J. J. Hu, J. E. Bultman, J. S. Zabinski, *Tribol. Lett.* 2004, **17**, 543-546.

[16] V. Brüser, R. Popovitz-Biro, A. Albu-Yaron, T. Lorenz, G. Seifert, R. Tenne, A. Zak, *Inorganics* 2014, **2**(2), 177-190.

[17] R. Sen, A. Govindaraj, K. Suenaga, S. Suzuki, H. Kataura, S. Iijima, Y. Achiba, *Chem. Phys. Lett.* 2001, **340**, 242-248.

[18] S. A. Kareem, R. Miranda, *J. Mol. Catal.* 1989, **53**(2), 275-283.

[19] T. A. Pecorano, R. R. Chianelli, *J. Catal.* 1981, **67**(2), 430-445.

[20] J.H. Gary, G.E. Handwerk, *Petroleum Refining Technology and Economics* (2nd Edition), Marcel Dekker, 1984.

[21] W. L. Leffler, *Petroleum refining for the nontechnical person*, 2nd Edition (1985), PennWell Books.

[22] James G. Speight, *The Chemistry and Technology of Petroleum,* 4th Edition (2006), CRC Press.

[23] J. V. Lauritsen, M. Nyberg, J. K. Norskov, B. S. Clausen, H. Topsoe, E. Laegsgaard, F. Besenbacher, *J. Catal.* 2004, **224** (1), 94-106.

[24] B. G. Rao, H. S. S. R. Matte, P. Chaturbedy, C. N. R. Rao, *ChemPlusChem* 2013, **78** (5), 419-422.

[25] Y. Okamoto, A. Kato, Usman, K. Sato, T. Kubota, *Chem. Lett.* 2005, **34** (9), 1258-1259.

[26] K. S. Joya, Y. F. Joya, K. Ocakoglu, R. van de Krol, *Angew. Chem.* 2013, **125**, 10618-10630.

[27] X. Zhou, B. I. Yakobson, *Acc. Chem. Res*. 2015, **48**, 73-80.

[28] Z. Wu, B. Fang, Z. Wang, C. Wang, Z. Liu, F. Liu, W. Wang, A. Alfantazi, D. Wang, D. P. Wilkinson, *ACS Catal.* 2013, **3**, 2101-2107.

[29] L. Cheng, W. Huang, Q. Gong, C. Liu, Z. Liu, Y. Li, H. Dai, *Angew. Chem. Int. Ed.* 2014, **53**, 7860-7863.

[30] M. Chatti, T. Gengenbach, R. King, L. Spiccia, A. N. Simonov, *Chem. Mater.* 2017, **29**, 3092-3099.

[31] R. K. Biroju, D. Das, R. Sharma, S. Pal, L. P. L. Mawlong, K. Bhorkar, P. K. Giri, A. K. Singh, T. N. Narayanan, *ACS Energy Lett.* 2017, **2**, 1355-1361.

[32] Z. Chen, D. Cumminst, B. N. Reinecke, E. Clark, M. K. Sunkarat, T. F. Jaramillo, *Nano Lett.* 2011, **11** (10), 4168-4175.

[33] N. M. Galea, E. S. Kadantsev, T. Ziegler, *J. Phys. Chem. C* 2009, **113**(1), 193-203.

[34] T. Corrales-Sanchez, J. Ampurdanes, A. Urakawa, *Int. J. Hydrogen Energy* 2014, **39**, 20837-20843.

[35] Y. Hu, D. H. C. Hua, *Sci. Rep.* 2016, **6**, 28088.

[36] C. Kuru, C. Choi, A. Kargar, D. Choi, Y. J. Kim, C. H. Liu, S. Yavuz, S. Jin, *Adv. Sci.* 2015, **2**, 1500004.

[37] A. Nag, K. Raidongia, K. P. S. S. Hembram, R. Datta, U. V. Waghmare, C. N. R. Rao, *ACS Nano* 2010, **4**, 1539-1544.

[38] K. S. Novoselov, D. Jiang, F. Schedin, T. J. Booth, V. V. Khotkevich, S. V. Morozov, and A. K. Geim, *Proc. Natl. Acad. Sci. USA* 2005, **102**, 10451-10453.

[39] F. Hoshyargar, J. K. Sahoo, M. N. Tahir, A. Yella, M. Dietzsch, F. Natalio, R. Branscheid, U. Kolb, M. Panthöfer, W. Tremel, *Dalton Trans.* 2013, **42**, 5292-5297.

[40] M. Chhowalla, H. S. Shin, G. Eda, L.-J. Li, K. P. Loh, H. Zhang, *Nat. Chem.* 2013, **5,** 263-275.

[41] A. Katz, M. Redlich, L. Rapoport, H. D. Wagner, R. Tenne, *Tribol. Lett.* 2006, **21**, 135-139.

[42] C. Lee, Q. Li, W. Kalb, X. Z. Liu, H. Berger, R. W. Carpick, J. Hone, *Science* 2010, **328**, 76-80.

[43] I. Lahouij, E.W. Bucholz, B. Vacher, S.B. Sinnott, J.M. Martin, F. Dassenoy, *Nanotechnology* 2012, **23**, 375701.

[44] J. Kogovšek, M. Kalin, *Tribol. Lett*. 2014, **53**, 585-597.

[45] R. Greenberg, G. Halperin, I. Etsion, R. Tenne, *Tribol. Lett*. 2004, **17(2)**, 179-186.

[46] S. J. Ding, D. Y. Zhang, J. S. Chen, X. W. Lou, *Nanoscale* 2012, **4**, 95-98.

[47] Y. Q. Zhu, T. Sekine, Y. H. Li, W. X. Wang, M. W. Fay, H. Edwards, P. D. Brown, N. Fleischer, R. Tenne, *Adv. Mater*. 2005, **17**, 1500-1503.

[48] C. S. Reddy, A. Zak, and E. Zussman, *J. Mater. Chem.* 2011, **21***,* 16086-16093.

[49] V. Podzorov, M. E. Gershenson, Ch. Kloc, R. Zeis, E. Bucher, *Appl. Phys. Lett.* 2004, **84**, 3301-3303.

[50] H. Li, J. Wu, Z. Yin, H. Zhang, *Acc. Chem. Res.* 2014, **47**, 1067-1075.

[51] J. N. Coleman, M. Lotya, A. O'Neill, S. D. Bergin, P. J. King, U. Khan, K. Young, A. Gaucher, S. De, R. J. Smith, I.V. Shvets, S. K. Arora, G. Stanton, H. Y. Kim, K. Lee, G. T. Kim, G. S. Duesberg, T. Hallam, J. J. Boland, J. J. Wang, J. F. Donegan, J. C. Grunlan, G. Moriarty, A. Shmeliov, R. J. Nicholls, J. M. Perkins, E. M. Grieveson, K. Theuwissen, D.W. McComb, P.D. Nellist, V. Nicolosi, *Science* 2011, **331**, 568−571.

[52] P. Joensen, R. F. Frindt, S. R. Morrison, Mater. *Res. Bull.* 1986, **21**, 457-461.

[53] Y. Zhan, Z. Liu, S. Najmaei, P. M. Ajayan, J. Lou, *Small* 2012, **7**, 966-971.

[54] R. Tenne, L. Margulis, M. Genut, G. Hodes, *Nature* 1992, **360**, 444-445.

[55] J. Ezkorn, H. A. Therese, F. Rocker, N. Zink, U. Kolb, W. Tremel, *Adv. Mater.* 2005, **17**, 2372-2375.

[56] X.-L. Li, J.-P. Ge, Y.-D. Li, *Chem. Eur. J.* 2004, **10**, 6163-6171.

[57] C. M. Zelenski, P. K. Dorhout, *J. Am. Chem. Soc.* 1998, **120**, 734-742.

[58] R. Sen, A. Govindaraj, K. Suenaga, S. Suzuki, H. Kataura, S. Iijima, Y. Achiba, *Chem. Phys. Lett.* 2001, **340**, 242-248.

[59] D. Vollath, D. V. Szabo, *Mater. Lett.* 1998, **35**, 236-244.

[60] S. Bastide, D. Duphil, J. P. Borra, C. Levy-Clement, *Adv. Mater.* 2006, **18**, 106-109.

[61] P. A. Parilla, A. C. Dillon, B. A. Parkinson, K. M. Jones, J. Alleman, G. Riker, D. S. Ginley, M. J. Heben, *J. Phys. Chem. B* 2004, **108**, 6197-6207.

[62] Q. Li, M. Li, Z. Chen, C. Li, *Mater. Res. Bull.* 2004, **39**, 981-986.

[63] M. M. Mdleleni, T, Hyeon, K. S. Suslick, *J. Am. Chem. Soc.* 1998, **120**(24), 6189–6190.

[64] A. Müller, E. Diemann, A. Branding, F. W. Baumann, M. Breysse, M. Vrinat, *Appl. Catal.* 1990, **62**, 13.

[65] J. W. McDonald, G. D. Friesen, L. D. Rosenheim, W.E. Newton, *Inorganica Chimica Acta* 1983, **72**, 205-210.

[66] A. Müller, R. G. Bhattacharyya, B. Pfefferkorn, *Chem. Ber.* 1979, **112**, 778-780.

[67] A. Müller, V. Wittneben, E. Krickemeyer, H. Bogge, M. Lemke, *Z. Anorg. Allg. Chem.* 1991, **605**, 175-188.

[68] B. R. Srinivasan, S. N. Dhuri, M. Poisot, C. Näther, W. Bensch, *Z. Anorg. Allg. Chem.* 2005, **631**, 1087-1094.

[69] A. Müller, E. Diemann, R. Jostes, H. Brögge, *Angew. Chem. Int. Ed.* 1981, **20**, 934-955.

[70] L. Cheng, W. Huang, Q. Gong, C. Liu, Z. Liu, Y. Li, H. Dai, *Angew. Chem. Int. Ed.* 2014, **53**, 7860-7863.

[71] C. Altavilla, M. Sarno, P. Ciambelli, *Chem. Mater.* 2011, **23**, 3879-3885.

[72] N. Savjani, E. A. Lewis, M. A. Bissett, J. R. Brent, R. A. W. Dryfe, S. J. Haigh, P. O'Brien, *Chem. Mater.* 2016, **28**, 657-664.

[73] N. Li, X. Zhang, S. Chen, X. Hou, Y. Liu, X. Zhai, *Mater.Sci. Eng., B* 2011, **176**, 688–691.

[74] M. Salavati-Niasari, F. Davar, N. Mir, *Polyhedron* 2008, **27**, 3514–3518.

[75] N. Bertram, J. Cordes, Y. D. Kim, G. Ganteför, S. Gemming, G. Seifert, *Chem. Phys. Lett.* 2006, **418**, 36 –39.

[76] M. Niederberger, M. A. Bartl, G. D. Stucky, *J. Am. Chem. Soc.* 2002, **124**(46), 13642-13643.

[77] N. Pinna, M. Niederberger, *Angew. Chem. Int. Ed.* 2008, **47**(29), 5292-5304.

[78] M. Niederberger, *Chem. Eur. J.* 2006, **12**, 7282-7302.

[79] I. Bilecka, P. Elser, M. Niederberger, *ACS Nano* 2009, **3**(2), 467-477.

[80] A. Wahl, *Diploma Thesis* 2017, Johannes Gutenberg-Universität Mainz.

[81] A. Bekdemir, H. R. Gutierrez, A. R. Botello-Mendez, N. Pere-Lopez, A. L. Elias, C.-I. Chia, B. Wang, V. H. Crespi, F. Lopez-Urias, J.-C. Charlier, H. Terrones, M. Terrones, *Sci. Rep.* 2013, **3**, 1755.

[82] H. Li, Q. Zhang, C. C. R. Yap, B. K. Tay, T. H. T. Edwin, A. Olivier, D. Baillargeat, *Adv. Funct. Mater.* 2012, **22**, 1385-1390.

[83] J. Wu, M. Liu, K. Chatterjee, K. P. Hackenberg, J. Shen, X. Zou, Y. Yan, J. Gu, Y. Yang, J. Lou, P. M. Ajayan, *Adv. Mater. Interfaces* 2016, **1500669**, 1-6.

[84] J. C. Lascovich, R. Giorgi, S. Scaglione, *Appl. Surf. Sci.* 1991, **47**(1), 17-21.

[85] D. Spetter, F. Hoshyargar, J. K. Sahoo, M. N. Tahir, R. Brandscheid, B. Barton, M. Panthöfer, U. Kolb, W. Tremel, *Eur. J. Inorg. Chem.* 2017, **15**, 2190-2194.

[86] L. Houben, A. N. Enyashin, Y. Feldman, R. Rosentsveig, D. G. Stroppa, M. Bar-Sadan, *J. Phys. Chem. C* 2012, **116**, 24350-24357.

[87] P. J. Blau, *Tribol. Int.* 2005, **38**, 1007-1012.

[88] Z. Jiang, Y. Zhang, G. Yang, J. Ma, S. Zhang, L. Yu, P. Zhang, *Ind. Eng. Chem. Res.* 2017, **56**, 1365-1375.

[89] J. Tannous, F. Dassenoy, I. Lahouij, T. Le Mogne, B. Vacher, A. Bruhacs, W. Tremel, *Tribol. Lett.* 2011, **41**, 55-64.

[90] U. S. Schwarz, S. Komura, S. A. Safran, *Europhys. Lett.* 2000, **50**(6), 762-768.

[91] B. Bhushan, *Introduction to Tribology*, 4th edition (2013), Wiley, New York.

[92] R. Rosentsveig, A. Gorodnev, N. Feuerstein, H. Friedman, A. Zak, N. Fleischer, J. Tannous, F. Dassenoy, R. Tenne, *Trib. Lett.* 2009, **36**(2), 175-182.

[93] J. Zhou, G. Fang, A. Pan, S. Liang, *ACS Appl. Mater. Interfaces* 2016, **8**, 33681-33689.

[94] S. J. Hibblea, R. I. Waltona, D. M. Pickupa, A. C. Hannonb, *J. Non-Cryst. Solids* 1998, **232-234**, 434-439.

[95] C. H. Chang, S. S. Chan, *J. Cat.* 1981, **72**(1), 139-148.

[96] M. L. Tang, D. C. Grauer, B. Lassalle-Kaiser, V. K. Yachandra, L. Amirav, J. R. Long, J. Yano, A. P. Alivisatos, *Angew. Chem.* 2011, **123**(43), 10385-10389.

[97] W. Zhang, T. Zhou, J. Zheng, J. Hong, Y. Pan, R. Xu, *ChemSusChem* 2015, **8**(8), 1464-1471.

[98] J. D. Benck, Z. Chen, L. Y. Kuritzky, A. J. Forman, T. F. Jaramillo, *ACS Catalysis* 2012, **2**(9), 1916-1923.

[99] T. Bourgeteau, D. Tondelier, B. Geffroy, R. Brisse, C. Laberty-Robert, S. Campidelli, R. de Bettignies, V. Artero, S. Palacin, B. Jousselme, *Energy Environ. Sci.* 2013, **6**, 2806-2713.

[100] L. Yu, B. Y. Xia, X. Wang, X. W. Lou, *Adv. Mater.* 2016, **28**(1), 92-97.

[101] T. Matsuyama, M. Deguchi, A. Hayashi, M. Tatsumisago, T. Ozaki, Y. Togawa, S. Mori, *Electrochemistry* 2015, **83**(10), 889-893.

[102] X. Wang, Q. Weng, Y. Yang, Y. Bando, D. Goldberg, *Chem. Soc. Rev.* 2016, **45**(15), 4042-4073.

[103] F. Fusalba, D. Belanger, *Electrochimica Acta* 2000, **45**(22-23), 3877-3883.

[104] P. Afanasiev, H. Jobic, C. Lorentz, P. Leverd, N. Mastubayashi, L. Piccolo, M. Vrinat, *J. Phys. Chem. C* 2009, **113**(10), 4139-4146.

[105] A. Margolin, R. Rosentsveig, A. Albu-Yaron, R. Popovitz-Biro, R. Tenne, *J. Mater. Chem.* 2004, **14**, 617-624.

[106] F. L. Deepak, R. Tenne, *Centr. Eur. J. Chem.* 2008, **6**(3), 373-389.

[107] C. L. Choi, J. Feng, Y. Li, J. Wu, A. Zak, R. Tenne, H. Dai, *Nano Res.* 2013, **6**(12), 921-928.

7. Summary and Outlook

This thesis discusses the synthesis and characterization of various transition metal oxides/-chalcogenides and their utilization in both catalysis and energy conversion applications. All particles are prepared using simple approaches involving solution based methods under benign conditions which are quite promising and practical for scale-up on the industrial scale.

First, two series of solid solutions consisting of molybdenum and tungsten are presented. Mo-doped nanoflakes and W-doped microparticles were prepared using precipitation from the precursor solutions or using a solvothermal method, respectively. Both the mixed series products exhibit unambiguous amorphous character and were tested for several catalytical applications.
Doping the tungsten nanoflakes with molybdenum affects the absorbency of the appropriate oxides in the UV-vis range, which showcases these compounds as promising for photocatalysis applications. The composition of the nanoflakes is determined using EDS analysis, while Raman spectroscopy demonstrates the homogeneous substitution of tungsten by molybdenum. Initial attempts to establish the photocatalytic properties in the decomposition of Rhodamine B (RB) were, however, not successful. Since the particles showed a strong adsorption behavior towards RB, an unimpaired determination of the photocatalytical activity of the $WMoO_x$-particles is not possible. Accordingly, the use of these compounds in photocatalysis requires further investigations. An alternative use of the nanoflakes is as oxidic precursors for the production of WS_2 nanoflakes, which were investigated in tribological experiments in another part of this thesis.
Novel microparticles of amorphous $Mo_xW_{1-x}O_{3-y}$ are prepared via a solvothermal synthesis and are tested as photoanode materials in the PEC water splitting reaction. They exhibit enhanced performance combined with superior chemical long-term stability and higher photocurrent values than other semiconducting compounds. These properties can be explained by the higher charge carrier density compared to WO_3 and MoO_3 resulting from the partial reduction and the concomitant presence of W^{5+} (and Mo^{5+}) as demonstrated by XPS spectroscopy. This compensates for charge recombination which is likely to occur in these strongly disordered materials. As the Mo/W substitution prevents the formation of metallic and crystalline Magnéli-type phases, a non-crystalline behavior is provoked, as is demonstrated by powder XRD and PDF analysis. Furthermore, the additional charge carriers arising from W^{5+} and Mo^{5+} sites lead to an enhanced absorption in the visible and the NIR range through the plasmon excitation. Raman spectroscopy shows that W substitutes homogeneously for Mo, while the elemental composition of the surface and in bulk is determined by XPS and EDS analysis, respectively. The improved PEC performance can thus be attributed to the synergistic effects of (i) increasing the charge carrier concentration by metal reduction, (ii) suppressing the formation of metallic oxides and associated metal-semiconductor transitions through non-crystallinity and (iii) tuning the absorption in the visible and NIR range due to the presence of W^{5+} and Mo^{5+} sites.

Examining the mixed oxides microspheres as sulfoxidation reactions shows their superior activity as oxidation catalyst. The kinetics of the oxidation reaction is studied using thioanisole as model compound, while it is also shown that functional groups (alcohols or acids) are tolerated in the sulfoxidation process. Moreover, it is presented that the mixed oxides are superior to the pure molybdenum or tungsten oxides in terms of catalytic activity, which is also attributed to the structural stabilization by substitution with W. Furthermore, in first experiments it was found that ternary oxides based on molybdenum, tungsten and vanadium show even higher catalytic activity for sulfoxidations.

In the second part of this thesis, a new synthesis of porous iron oxide particles is presented. The method uses mesoporous silica as both template and nucleation sites for the growth of iron oxide particles in the hematite phase, while long reaction times are required to obtain porous silica-hematite structures. However, it was not possible to synthesize pure mesoporous hematite particles since a residual amount of silicon always remained in the product due to the growth of the iron oxide on its surface. The silicate-hematite particles (SHPs) were investigated on their catalytical activity in the decomposition of RB. In these Fenton-like reactions it was shown that the SHPs react retarded compared to pure hematite particles due to the remnants of mesoporous silica. As a result, significantly lower reaction rates are achieved. However, the product itself shows significantly higher conversion rates than in the absence of a catalyst. For future applications as catalysts for dye decomposition it is thus necessary to completely remove the silica from the product.

In the last part of the work, the synthesis of novel sulfidic nanoparticles involving a simple one-step synthesis in oleylamine or benzyl alcohol as solvents is presented. In oleylamine, single-layer nanosheets are produced, which are highly dispersible in non-polar solvents due to their capping by oleylamine. Perfoming the same reaction in benzyl alcohol, new structures of molybdenum or tungsten oxysulfides are obtained. The as-prepared oxysulfide nanoflakes show significantly lower friction coefficients in tribological applications, when compared to other compounds already known, such as fullerene-like particles or nanotubes of WS_2.
The composition of the particles is determined by EDS and XPS analysis, while their oxysulfide structure is revealed by XRD. Although the oleylamine-functionalized particles give more homogeneous mixtures with the reference oil, they have almost no effect as a friction-reducing additive due to the high residual content of oleylamine. In the case of the oxysulfides, however, a considerable reduction in the coefficient of friction is observed, which provides completely new results for these compounds. It is proposed, that due to the incorporation of oxide into the sulfide lattice, the van-der-Waals gap between the distinct layers is expanded and, thus, facilitates delamination of the MoO_xS_{2-x} layers. Knowing that the tribochemistry of boundary lubrication in steel substrates is based on the formation of Fe-O-Mo, Fe-O-S-Mo and Fe-S-Mo bonds (as

revealed by XPS analysis) it is considered that the additional oxygen provides a bigger amount of stable Fe-O-S bonds. Therefore, the iron surface can be occupied by single-layer MoO_xS_{2-x} more extensively and thus an easier sliding of the opposing interfaces is enabled, resulting in a massive decrease of the friction coefficient.

Since this effect is even more pronounced at elevated temperatures, wear reducing application in gear or engine oils seems to be very promising as the normal working temperature is around 80-100 °C. However, there is no explanation for this effect not being observed for the similar compound with tungsten instead of molybdenum (WO_xS_{2-x}).

8. Appendix

8.1 Additional Data for TMOs (Chapter 4)

8.1.1. Particles Characterization

Table A 10. Structural characteristics of all synthesized compounds S1-S7, measured with XRD and Raman spectroscopy (with M = Mo or W).

Sample	2θ / ° (Miller index)	Assigned Phase	Wavenumber / cm^{-1} (characteristic Raman band)
S1	35.6 (114) 40.4	$W_{18}O_{49}$ Mo_4O_{11}	260 (O-M-O bending) 329 (δ O-M-O bending) 710 (ν_s O-M-O stretching) 810 (ν_{as} M=O stretching) 906 (ν_{as} Mo=O stretching)
S2	35.5 (114) 40.3	$W_{18}O_{49}$ Mo_4O_{11}	261 (O-M-O bending) 331 (δ O-M-O bending) 744 (ν_s O-M-O stretching) 833 (ν_{as} M=O stretching)
S3	40.6	Mo_4O_{11}	258 (O-M-O bending) 333 (δ O-M-O bending) 718 (ν_s O-W-O stretching) 771 (ν_s O-M-O stretching) 845 (ν_{as} M=O stretching) 992 (ν_{as} Mo=O stretching)
S4	X	X	261 (O-M-O bending) 338 (δ O-M-O bending) 769 (ν_s O-M-O stretching) 823 (ν_s Mo=O stretching) 846 (ν_{as} M=O stretching) 992 (ν_{as} Mo=O stretching)
S5	28.6 47.4 56.5	Mo_4O_{11} X X	280 (O-M-O bending) 345 (δ O-M-O bending) 772 (ν_s O-M-O stretching) 850 (ν_{as} M=O stretching) 992 (ν_{as} Mo=O stretching)
S6	X	Amorphous MoO_{3-x}	194 (τ O=Mo=O twisting) 280 (ν_{as} O=Mo=O wagging) 336 (δ O-Mo-O bending) 661 (ν_{as} O-Mo-O stretching) 819 (ν_s Mo=O stretching) 992 (ν_{as} Mo=O stretching)
S7	23.4 (010) 25.9 (203) 35.0 (114) 47.7 (020) 50.5 (315) 55.5 (523)	$W_{18}O_{49}$ (JCPDS No. 712450)	182 (O-W-O bending) 248 (δ O-W-O bending) 687 (ν_s O-W-O stretching) 804 (ν_{as} W=O stretching)

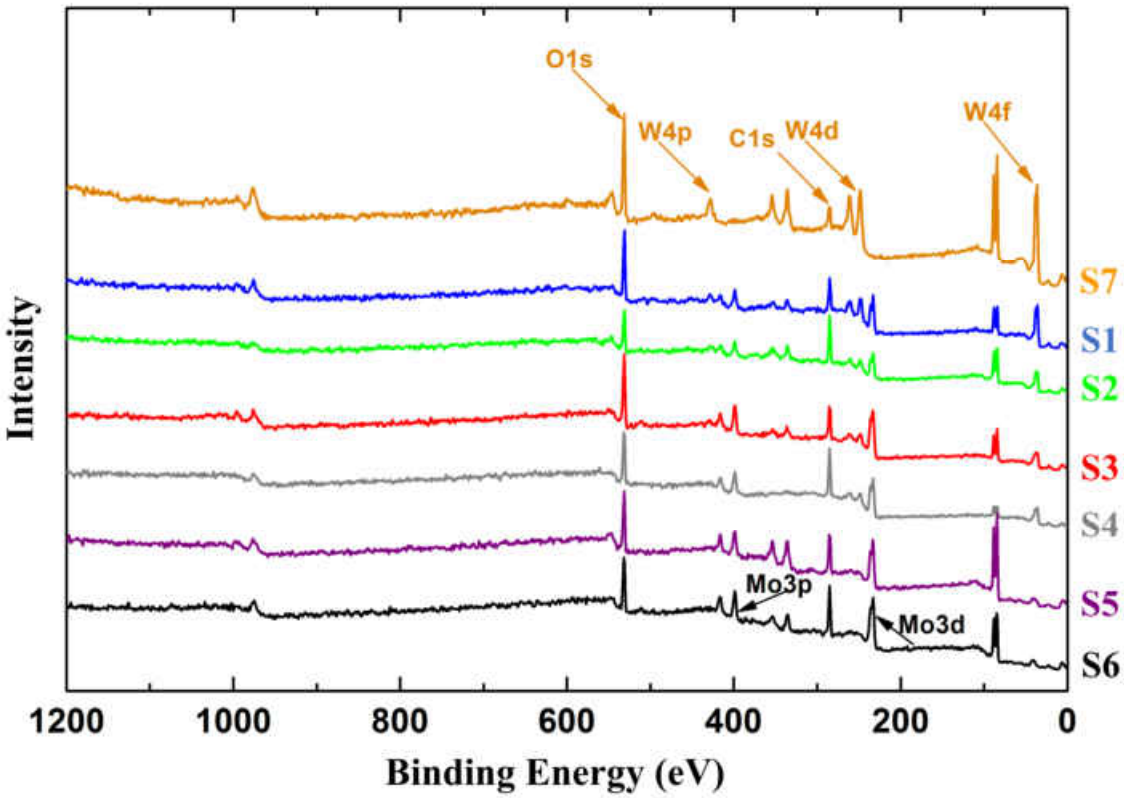

Figure A 152. XPS survey spectra of the as-synthesized molybdenum-tungsten oxides: $Mo_{0.5}W_{0.5}O_{2.1}$ (S1), $Mo_{0.62}W_{0.38}O_{2.3}$ (S2), $Mo_{0.75}W_{0.25}O_{2.4}$ (S3), $Mo_{0.85}W_{0.15}O_{2.6}$ (S4), $Mo_{0.89}W_{0.11}O_{2.7}$ (S5), MoO_{3-x} (S6) and $W_{18}O_{49}$ (S7).

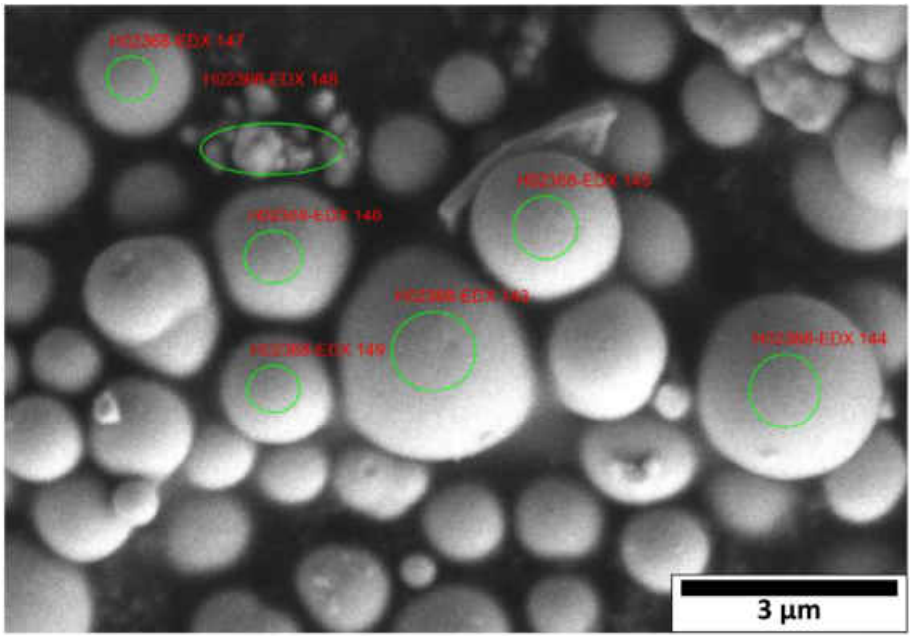

Figure A 153. SEM image of $Mo0_{.5}W_{0.5}O_{2.1}$, tempered at 600 °C for 1h. The green circles mark the areas, in which EDS was measured.

Table A 11. EDS data collected from the green marked areas in Figure A 153.

H02368-EDX 147

Element	Ord. Z.	Netto	Masse [%]	Masse Norm. [%]	Atom [%]	abs. Fehler [%] (1 sigma)	rel. Fehler [%] (1 sigma)
Natrium	11	243	0,27	0,24	0,28	0,05	19,72
Kohlenstoff	6	13698	24,78	22,60	49,34	3,35	13,52
Sauerstoff	8	12222	24,81	22,63	37,08	3,40	13,72
Molybdän	42	10447	46,24	42,17	11,53	2,38	5,16
Wolfram	74	5058	13,55	12,36	1,76	0,71	5,26
Aluminium	13	10	0,01	0,01	0,01	0,00	34,54
		Sum	**109,66**	**100,00**	**100,00**		

Mo:W ratio 6.6:1

H02368-EDX 148

Element	Ord. Z.	Netto	Masse [%]	Masse Norm. [%]	Atom [%]	abs. Fehler [%] (1 sigma)	rel. Fehler [%] (1 sigma)
Natrium	11	244	0,29	0,30	0,30	0,06	18,96
Kohlenstoff	6	16409	29,77	31,15	59,54	3,93	13,21
Sauerstoff	8	10100	20,93	21,91	31,43	2,95	14,10
Molybdän	42	4447	23,79	24,89	5,96	1,30	5,48
Wolfram	74	6685	20,70	21,67	2,71	1,06	5,10
Aluminium	13	51	0,07	0,07	0,06	0,04	52,62
		Sum	**95,55**	**100,00**	**100,00**		

Mo:W ratio 2.2:1

H02368-EDX 146

Element	Ord. Z.	Netto	Masse [%]	Masse Norm. [%]	Atom [%]	abs. Fehler [%] (1 sigma)	rel. Fehler [%] (1 sigma)
Natrium	11	714	0,63	0,62	0,75	0,07	11,87
Kohlenstoff	6	9869	15,13	14,92	34,86	2,15	14,19
Sauerstoff	8	17485	28,69	28,29	49,62	3,76	13,11
Molybdän	42	12261	44,75	44,13	12,91	2,29	5,13
Wolfram	74	5597	12,20	12,03	1,84	0,64	5,24
Aluminium	13	24	0,02	0,02	0,02	0,01	23,41
		Sum	**101,42**	**100,00**	**100,00**		

Mo:W ratio 7:1

H02368-EDX 149

Element	Ord. Z.	Netto	Masse [%]	Masse Norm. [%]	Atom [%]	abs. Fehler [%] (1 sigma)	rel. Fehler [%] (1 sigma)
Kohlenstoff	6	10603	18,00	17,95	42,06	2,52	14,02
Sauerstoff	8	13238	24,32	24,26	42,67	3,30	13,58
Molybdän	42	10405	42,61	42,51	12,47	2,20	5,16
Wolfram	74	6044	14,88	14,84	2,27	0,77	5,18
Natrium	11	433	0,44	0,43	0,53	0,06	14,58
		Sum	**100,25**	**100,00**	**100,00**		

Mo:W ratio 5.5:1

H02368-EDX 145

Element	Ord. Z.	Netto	Masse [%]	Masse Norm. [%]	Atom [%]	abs. Fehler [%] (1 sigma)	rel. Fehler [%] (1 sigma)
Natrium	11	493	0,48	0,49	0,75	0,07	13,73
Kohlenstoff	6	2620	4,60	4,65	13,56	0,84	18,36
Sauerstoff	8	16407	28,96	29,32	64,12	3,83	13,21
Molybdän	42	13416	51,07	51,70	18,86	2,61	5,10
Wolfram	74	5846	13,58	13,75	2,62	0,71	5,21
Aluminium	13	79	0,08	0,09	0,11	0,04	43,91
		Sum	**98,78**	**100,00**	**100,00**		

Mo:W ratio 7.2:1

H02368-EDX 144

Element	Ord. Z.	Netto	Masse [%]	Masse Norm. [%]	Atom [%]	abs. Fehler [%] (1 sigma)	rel. Fehler [%] (1 sigma)
Natrium	11	428	0,41	0,42	0,64	0,06	14,94
Kohlenstoff	6	2169	3,81	3,86	11,43	0,73	19,24
Sauerstoff	8	16623	29,25	29,60	65,79	3,86	13,19
Molybdän	42	13501	51,40	52,02	19,28	2,62	5,10
Wolfram	74	5994	13,82	13,98	2,70	0,72	5,19
Aluminium	13	103	0,11	0,11	0,14	0,04	36,03
		Sum	**98,80**	**100,00**	**100,00**		

Mo:W ratio 7.1:1

H02368-EDX 143

Element	Ord. Z.	Netto	Masse [%]	Masse Norm. [%]	Atom [%]	abs. Fehler [%] (1 sigma)	rel. Fehler [%] (1 sigma)
Natrium	11	639	0,54	0,55	0,82	0,07	12,72
Kohlenstoff	6	2327	3,83	3,91	11,12	0,73	18,94
Sauerstoff	8	18833	30,98	31,65	67,57	4,03	13,00
Molybdän	42	13571	49,56	50,64	18,03	2,53	5,10
Wolfram	74	6086	12,97	13,25	2,46	0,67	5,20
Aluminium	13	0	0,00	0,00	0,00	0,00	2,75
		Sum	**97,87**	**100,00**	**100,00**		

Mo:W ratio 7.3:1

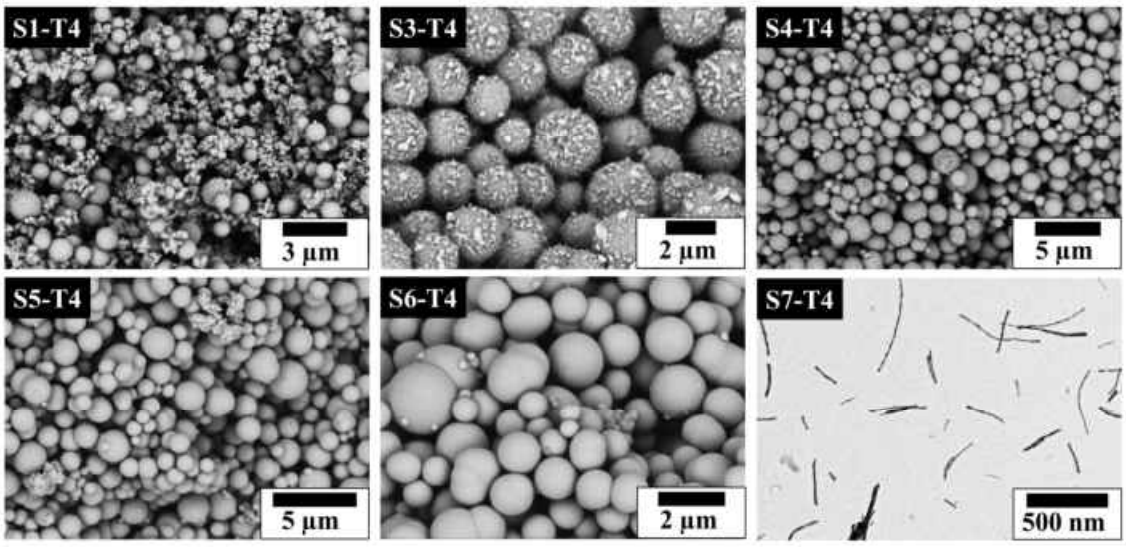

Figure A 154. Representative SEM and low magnification TEM images of the samples after heat treatment at 400 °C for 24 h: (S1-T4) $Mo_{0.5}W_{0.5}O_{2.1}$, (S3-T4) $Mo_{0.75}W_{0.25}O_{2.4}$, (S4-T4) $Mo_{0.85}W_{0.15}O_{2.6}$, (S5-T4) $Mo_{0.89}W_{0.11}O_{2.7}$, (S6-T4) MoO_{3-x} and (S7-T4) $W_{18}O_{49}$.

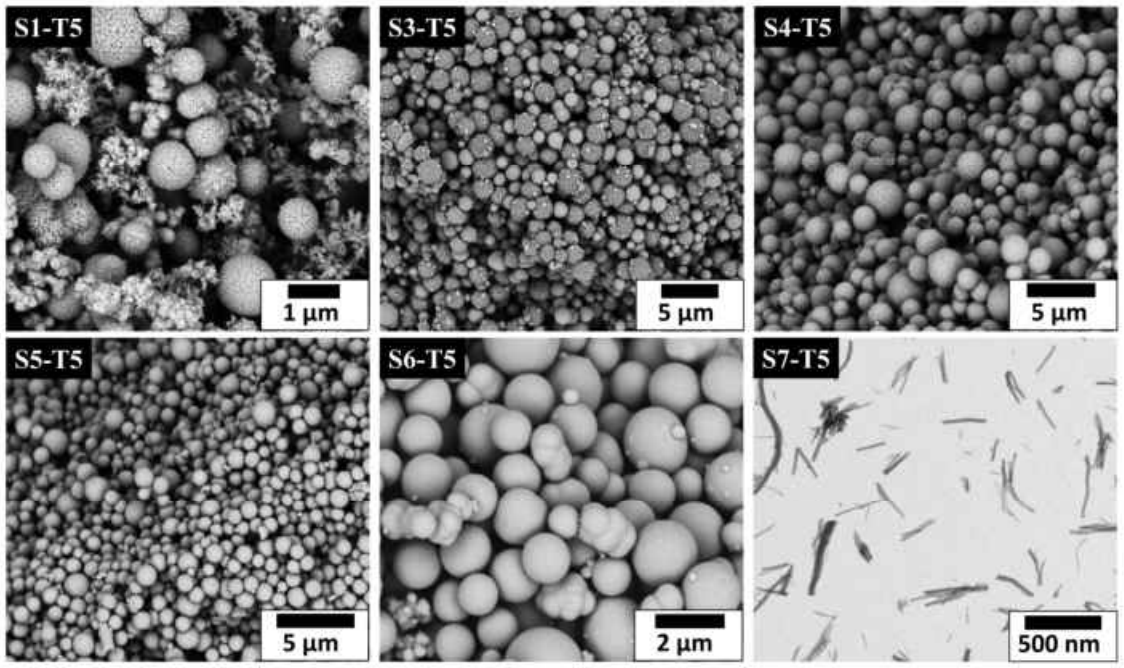

Figure A 155. Representative SEM and low magnification TEM images of the samples after heat treatment at 500 °C for 24 h: (S1-T5) $Mo_{0.5}W_{0.5}O_{2.1}$, (S3-T5) $Mo_{0.75}W_{0.25}O_{2.4}$, (S4-T5) $Mo_{0.85}W_{0.15}O_{2.6}$, (S5-T5) $Mo_{0.89}W_{0.11}O_{2.7}$, (S6-T5) MoO_{3-x} and (S7-T5) $W_{18}O_{49}$.

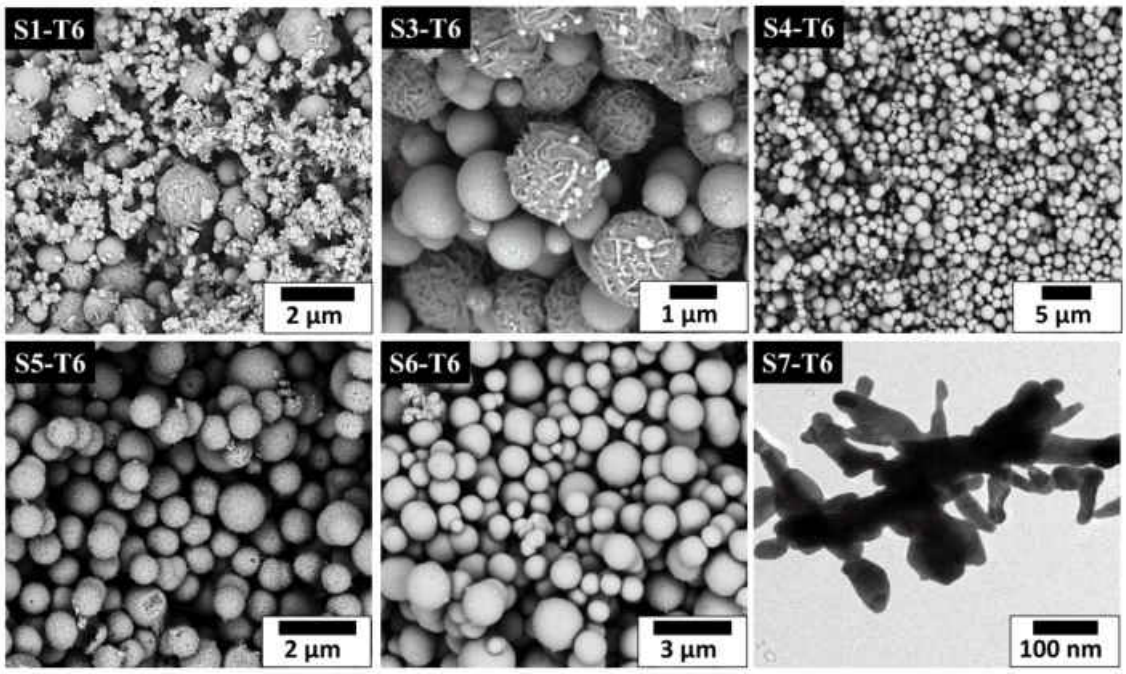

Figure A 156. Representative SEM and low magnification TEM images of the samples after heat treatment at 600 °C for 24 h: (S1-T6) $Mo_{0.5}W_{0.5}O_{2.1}$, (S3-T6) $Mo_{0.75}W_{0.25}O_{2.4}$, (S4-T6) $Mo_{0.85}W_{0.15}O_{2.6}$, (S5-T6) $Mo_{0.89}W_{0.11}O_{2.7}$, (S6-T6) MoO_{3-x} and (S7-T6) $W_{18}O_{49}$.

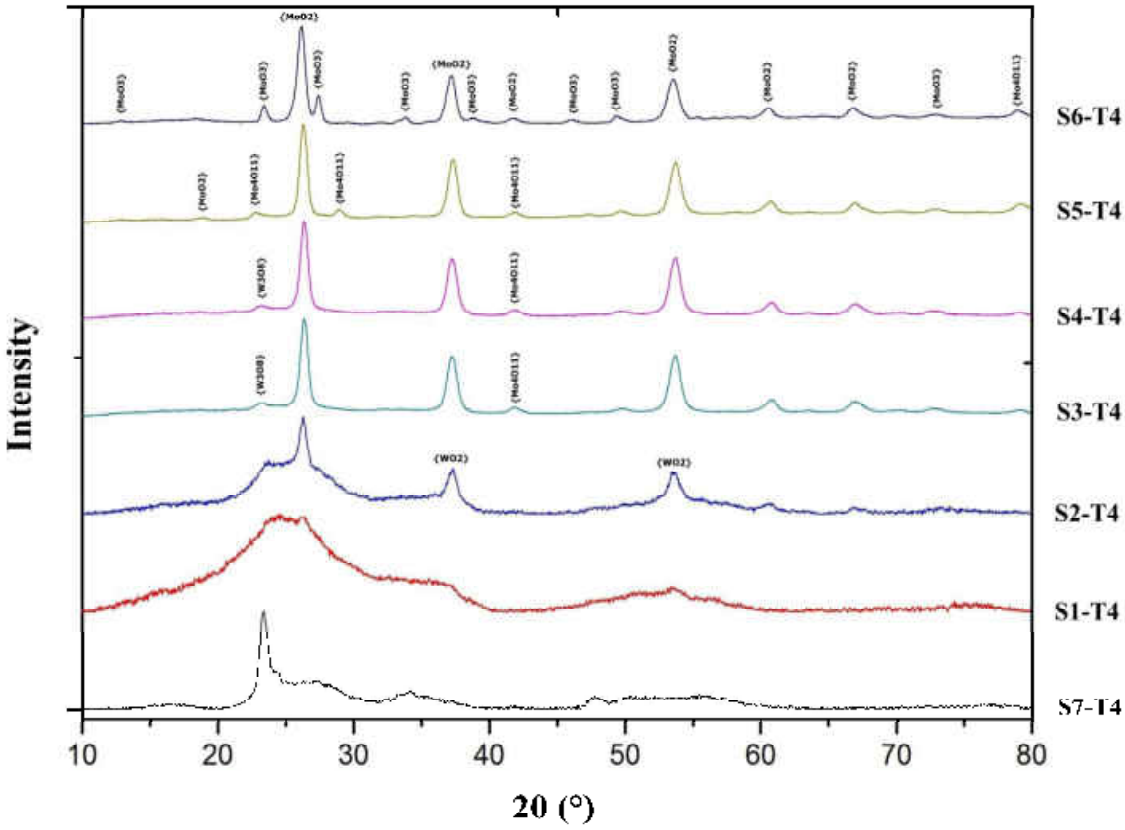

Figure A 157. Representative XRD patterns of the samples after heat treatment at 400 °C for 24 h: (S1-T4) $Mo_{0.5}W_{0.5}O_{2.1}$, (S2-T4) $Mo_{0.62}W_{0.38}O_{2.3}$, (S3-T4) $Mo_{0.75}W_{0.25}O_{2.4}$, (S4-T4) $Mo_{0.85}W_{0.15}O_{2.6}$, (S5-T4) $Mo_{0.89}W_{0.11}O_{2.7}$, (S6-T4) MoO_{3-x} and (S7-T4) $W_{18}O_{49}$.

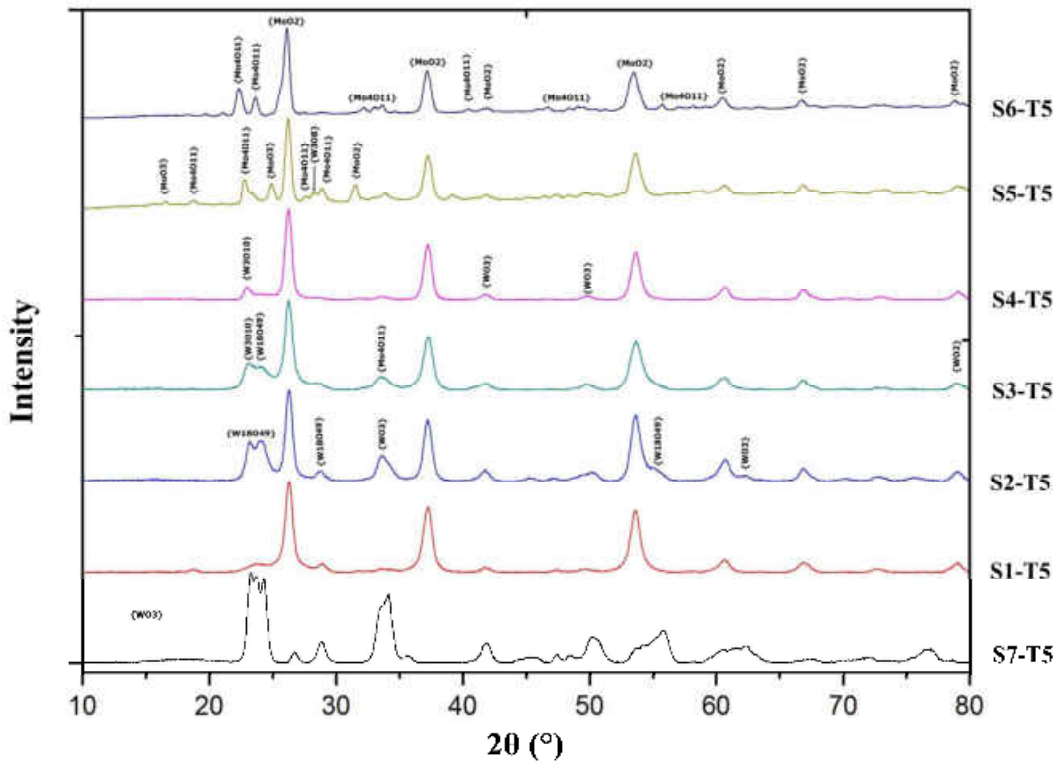

Figure A 158. Representative XRD patterns of the samples after heat treatment at 500 °C for 24 h: (S1-T5) $Mo_{0.5}W_{0.5}O_{2.1}$, (S2-T5) $Mo_{0.62}W_{0.38}O_{2.3}$, (S3-T5) $Mo_{0.75}W_{0.25}O_{2.4}$, (S4-T5) $Mo_{0.85}W_{0.15}O_{2.6}$, (S5-T5) $Mo_{0.89}W_{0.11}O_{2.7}$, (S6-T5) MoO_{3-x} and (S7-T5) $W_{18}O_{49}$.

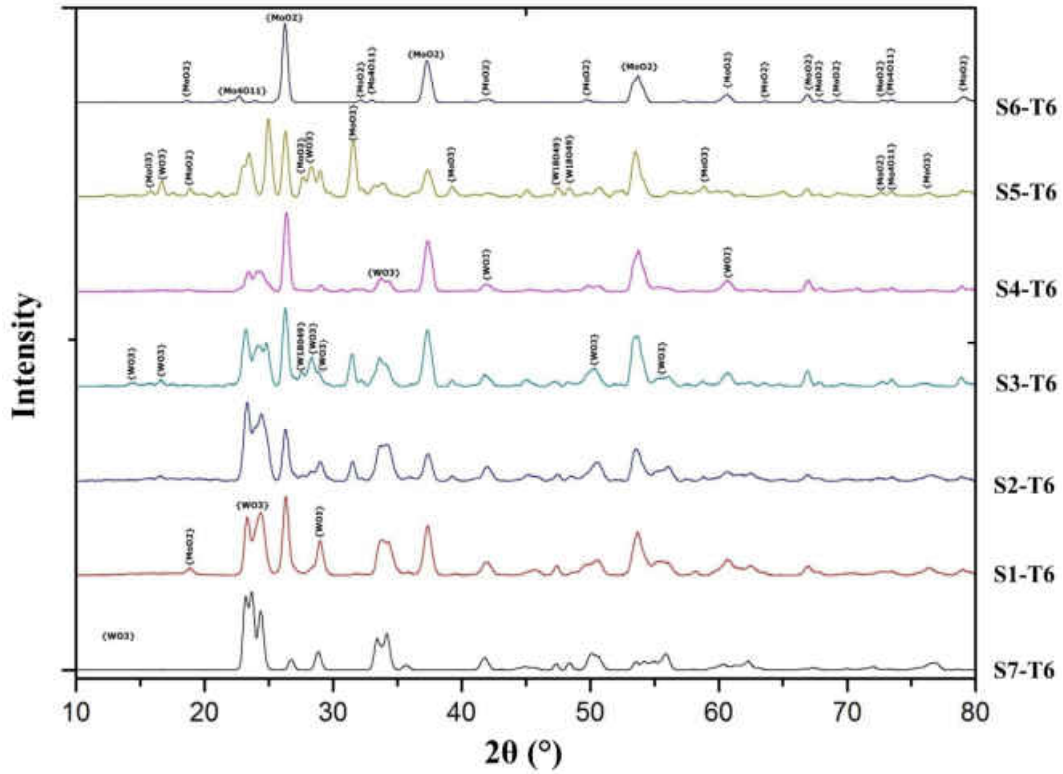

Figure A 159. Representative XRD patterns of the samples after heat treatment at 600 °C for 24 h: (S1-T6) $Mo_{0.5}W_{0.5}O_{2.1}$, (S2-T6) $Mo_{0.62}W_{0.38}O_{2.3}$, (S3-T6) $Mo_{0.75}W_{0.25}O_{2.4}$, (S4-T6) $Mo_{0.85}W_{0.15}O_{2.6}$, (S5-T6) $Mo_{0.89}W_{0.11}O_{2.7}$, (S6-T6) MoO_{3-x} and (S7-T6) $W_{18}O_{49}$.

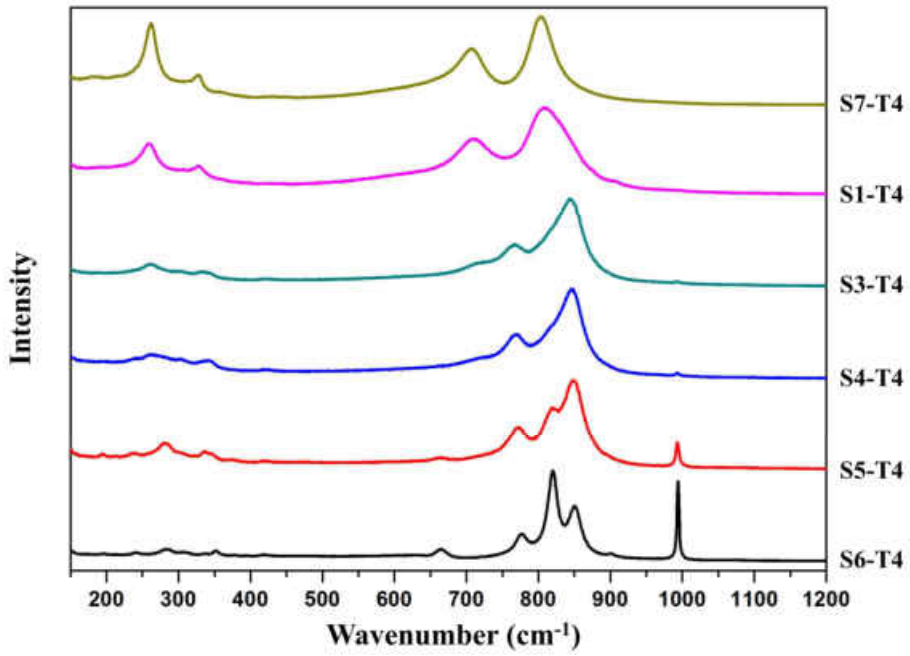

Figure 160. Representative Raman spectra of the samples after heat treatment at 400 °C for 24 h: (S1-T4) $Mo_{0.5}W_{0.5}O_{2.1}$, (S3-T4) $Mo_{0.75}W_{0.25}O_{2.4}$, (S4-T4) $Mo_{0.85}W_{0.15}O_{2.6}$, (S5-T4) $Mo_{0.89}W_{0.11}O_{2.7}$, (S6-T4) MoO_{3-x} and (S7-T4) $W_{18}O_{49}$.

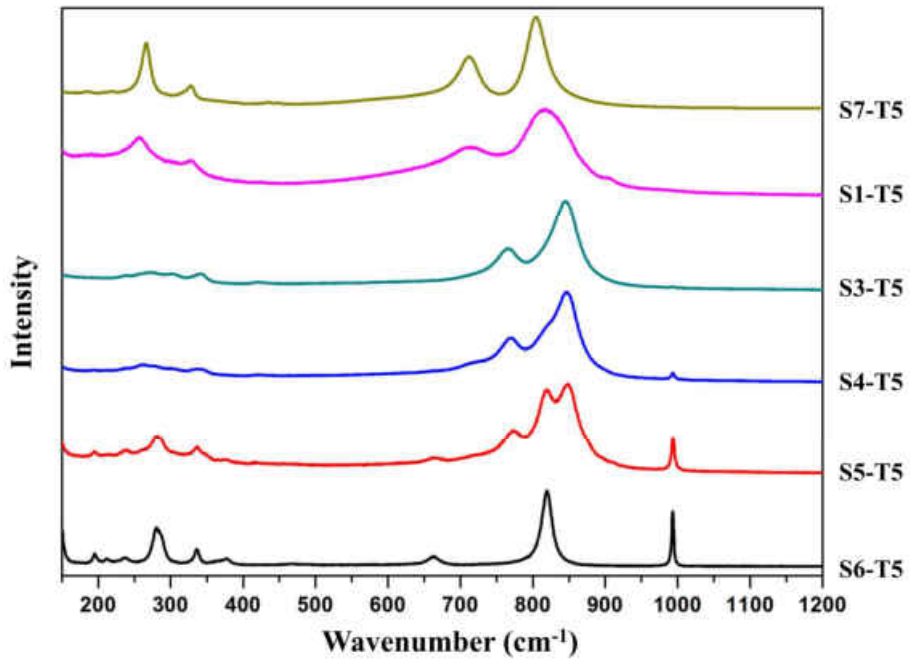

Figure A 161. Representative Raman spectra of the samples after heat treatment at 500 °C for 24 h: (S1-T5) $Mo_{0.5}W_{0.5}O_{2.1}$, (S3-T5) $Mo_{0.75}W_{0.25}O_{2.4}$, (S4-T5) $Mo_{0.85}W_{0.15}O_{2.6}$, (S5-T5) $Mo_{0.89}W_{0.11}O_{2.7}$, (S6-T5) MoO_{3-x} and (S7-T5) $W_{18}O_{49}$.

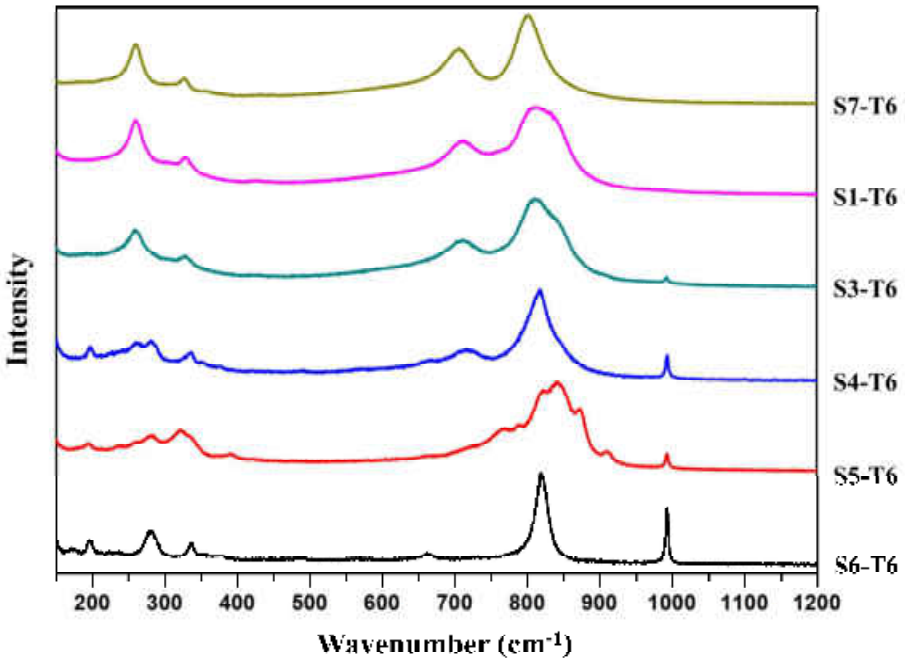

Figure A 162. Representative XRD patterns of the samples after heat treatment at 600 °C for 24 h: (S1-T6) $Mo_{0.5}W_{0.5}O_{2.1}$, (S3-T6) $Mo_{0.75}W_{0.25}O_{2.4}$, (S4-T6) $Mo_{0.85}W_{0.15}O_{2.6}$, (S5-T6) $Mo_{0.89}W_{0.11}O_{2.7}$, (S6-T6) MoO_{3-x} and (S7-T6) $W_{18}O_{49}$.

8.1.2. Photoelectrocatalysis Results

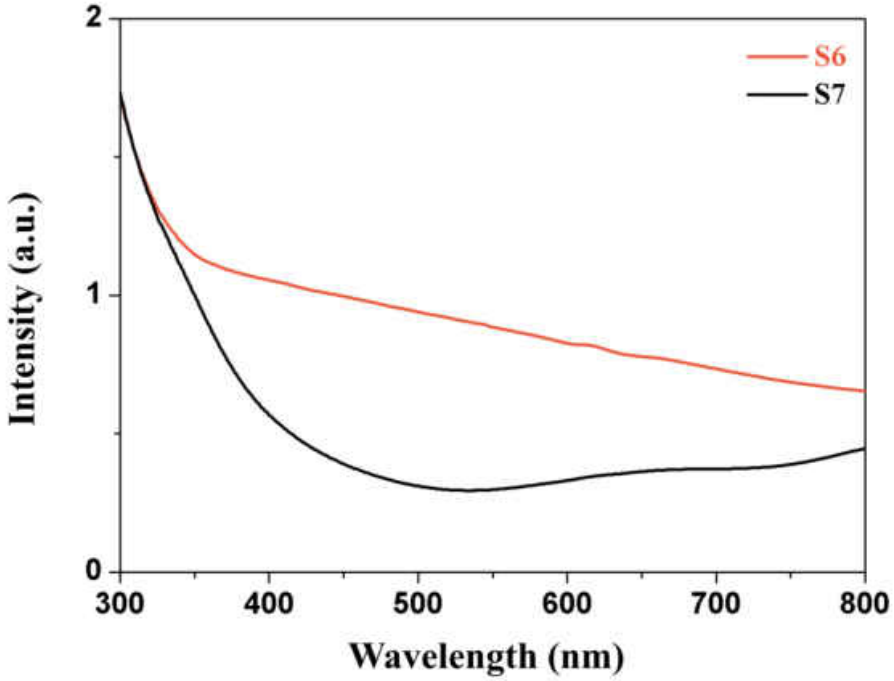

Figure A 163. UV-Vis absorption spectra of the as-synthesized MoO_{3-x} microspheres (S6) and $W_{18}O_{49}$ nanowires (S7), measured as 1 mg/mL solution in water.

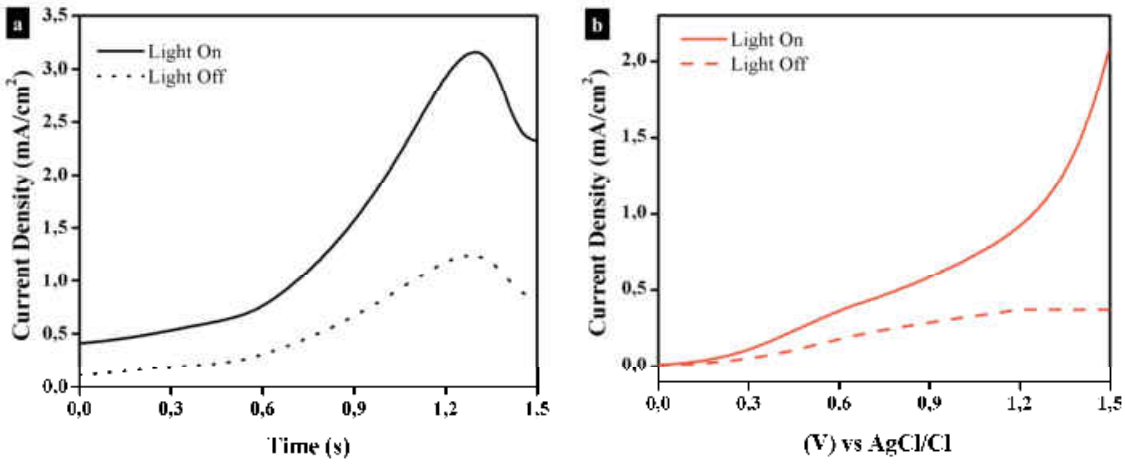

Figure A 164. Photocurrent-voltage responses of the MoO_{3-x} microspheres (a) and $W_{18}O_{49}$ nanowires (b) under chopped 1 SUN illumination in 0.5 M Na_2SO_4 electrolyte solution.

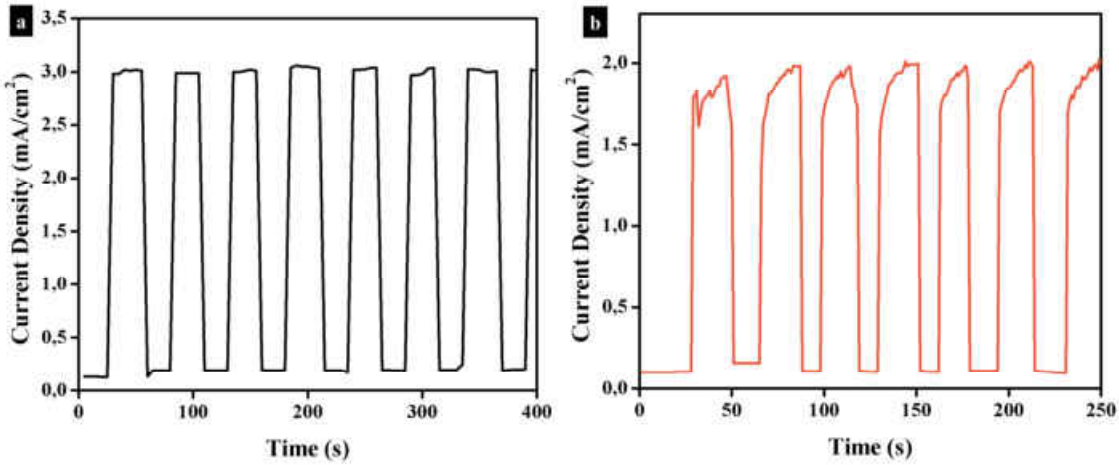

Figure A 165. Photocurrent-time responses measurements vs. SCE for the MoO_{3-x} microspheres (a) and $W_{18}O_{49}$ nanowires (b) electrode under a potential of 1.23 V.

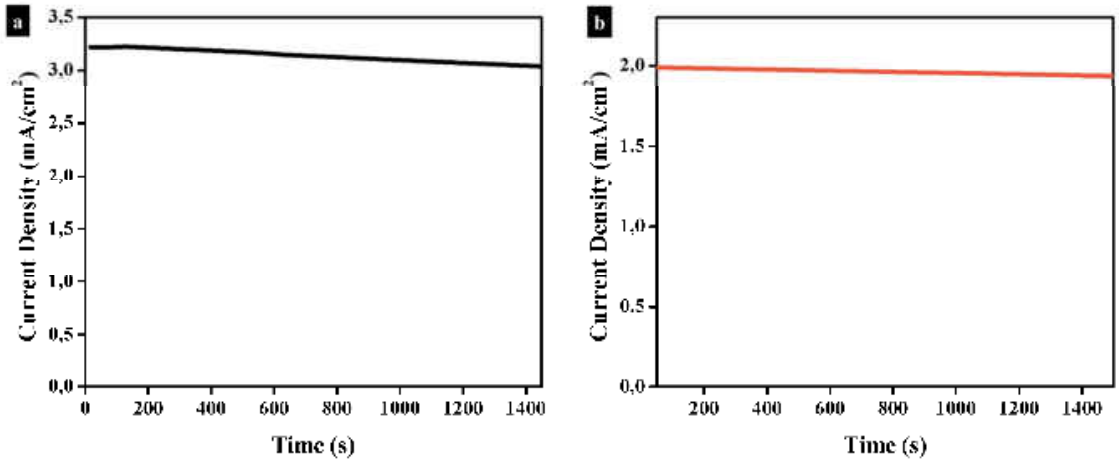

Figure A 166. Chronoamperometry analysis of the as-prepared photoanodes of MoO_{3-x} microspheres (a) and $W_{18}O_{49}$ nanowires (b).

8.1.3. Sulfoxidation Results

Table A 12. Relative composition of the reaction mixture of TA oxidation, directly after the addition of 1 eq H_2O_2, with the appropriate catalyst and a reference sample without particle addition.

	directly after addition of H_2O_2			
Sample	**Anisole [%]**	**Sulfoxide [%]**	**Sulfone [%]**	**Sum**
MoO_{3-x}	91.1	3.9	0	100
$Mo_{0.5}W_{0.5}O_{2.1}$	57.4	42.6	0	100
$Mo_{0.62}W_{0.48}O_{2.3}$	86.2	13.8	0	100
$Mo_{0.75}W_{0.25}O_{2.4}$	76.3	23.7	0	100
$Mo_{0.85}W_{0.15}O_{2.6}$	78.2	21.8	0	100
$Mo_{0.89}W_{0.11}O_{2.7}$	91.9	8.1	0	100
$W_{18}O_{49}$	84.3	15.7	0	100
without particles	100	0	0	100

Table A 13. Relative composition of the reaction mixture of TA oxidation with 1 eq H_2O_2, after 24 h reaction time, with the appropriate catalyst and a reference sample without particle addition.

	after 24 h			
Sample	**Anisole [%]**	**Sulfoxide [%]**	**Sulfone [%]**	**Sum**
MoO_{3-x}	0	82.4	17.6	100
$Mo_{0.5}W_{0.5}O_{2.1}$	0	66.5	33.5	100
$Mo_{0.62}W_{0.48}O_{2.3}$	0	76.9	23.1	100
$Mo_{0.75}W_{0.25}O_{2.4}$	0	77.4	22.6	100
$Mo_{0.85}W_{0.15}O_{2.6}$	0	73.8	26.2	100
$Mo_{0.89}W_{0.11}O_{2.47}$	3.1	88.6	8.3	100
$W_{18}O_{49}$	1.7	80.2	18.1	100
without particles	18.0	82.0	0	100

Table A 14. Relative composition of the reaction mixture of TA oxidation with 1 eq H_2O_2, after 48 h reaction time, with the appropriate catalyst and a reference sample without particle addition.

	after 48 h			
Sample	**Anisole [%]**	**Sulfoxide [%]**	**Sulfone [%]**	**Sum**
MoO_{3-x}	0	62.2	37.8	100
$Mo_{0.5}W_{0.5}O_{2.1}$	0	37.6	62.4	100
$Mo_{0.62}W_{0.48}O_{2.3}$	0	50.2	49.8	100
$Mo_{0.75}W_{0.25}O_{2.4}$	0	46.2	53.8	100
$Mo_{0.85}W_{0.15}O_{2.6}$	0	63.0	37.0	100
$Mo_{0.89}W_{0.11}O_{2.47}$	0	70.3	29.7	100
$W_{18}O_{49}$	0	54.6	45.4	100
without particles	0	100	0	100

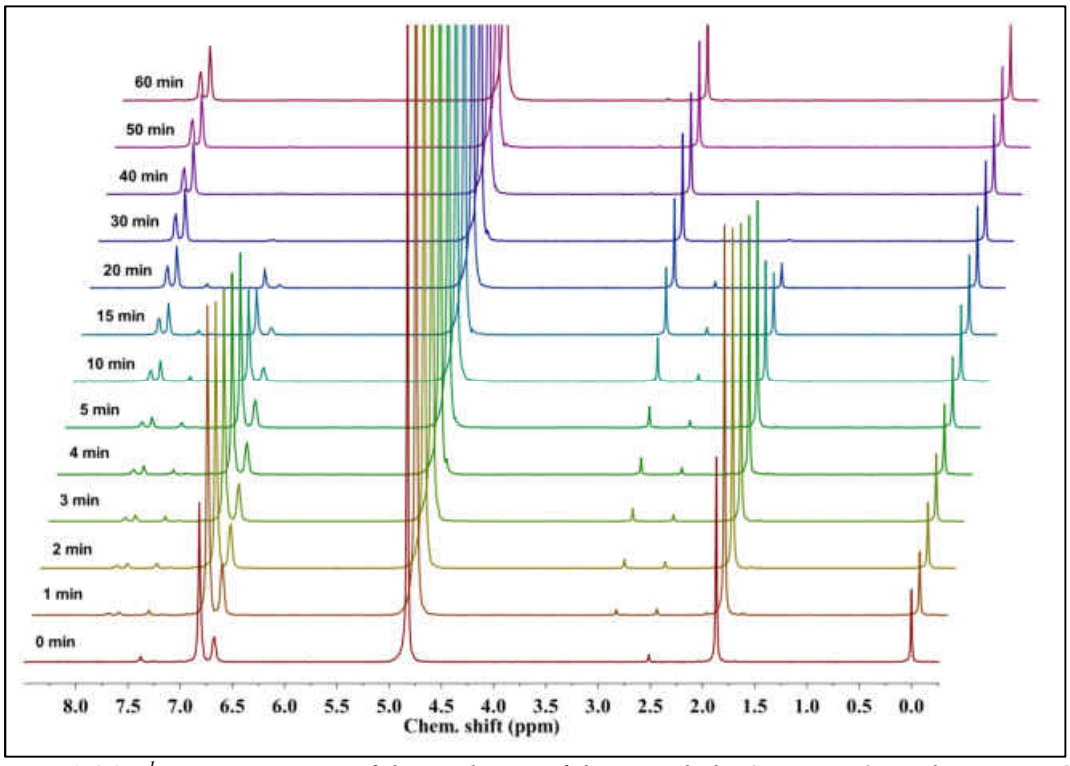

Figure A 167. ^{1}H-NMR spectra of the oxidation of thioanisole by 0.5 eq H_2O_2 and $Mo_{0.5}W_{0.5}O_{2.1}$ microparticles as catalyst, shown after different periods of time.

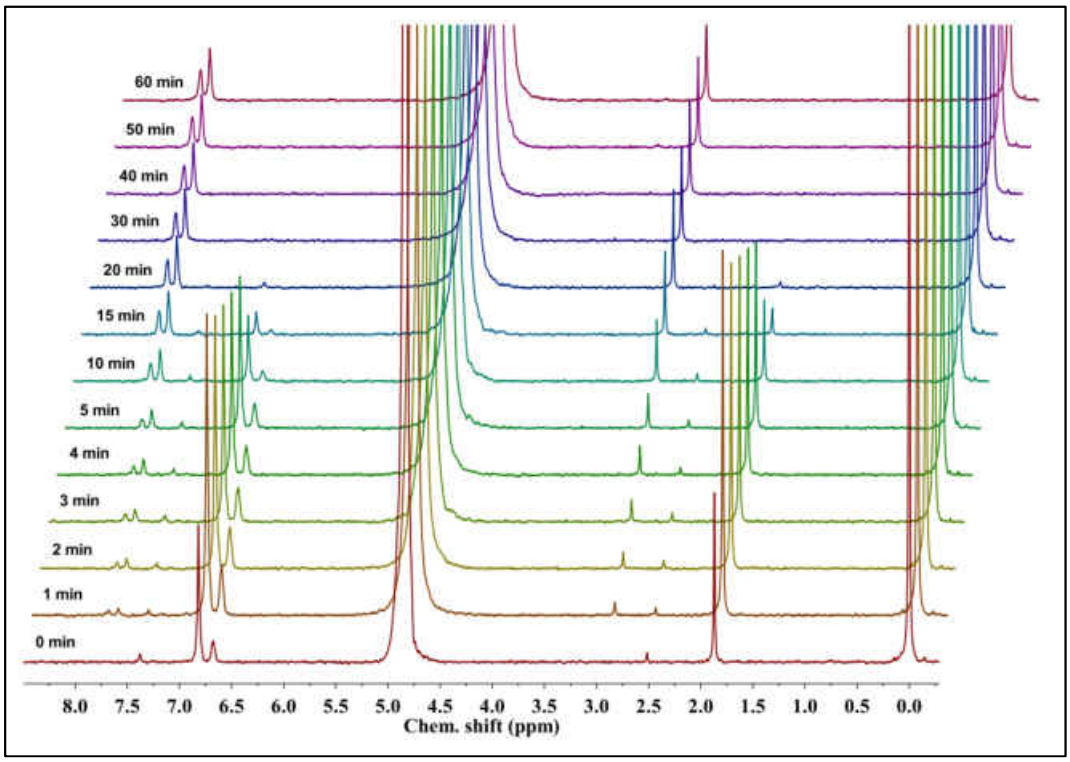

Figure A 168. ^{1}H-NMR spectra of the oxidation of thioanisole by 2 eq H_2O_2 and $Mo_{0.5}W_{0.5}O_{2.1}$ microparticles as catalyst, shown after different periods of time.

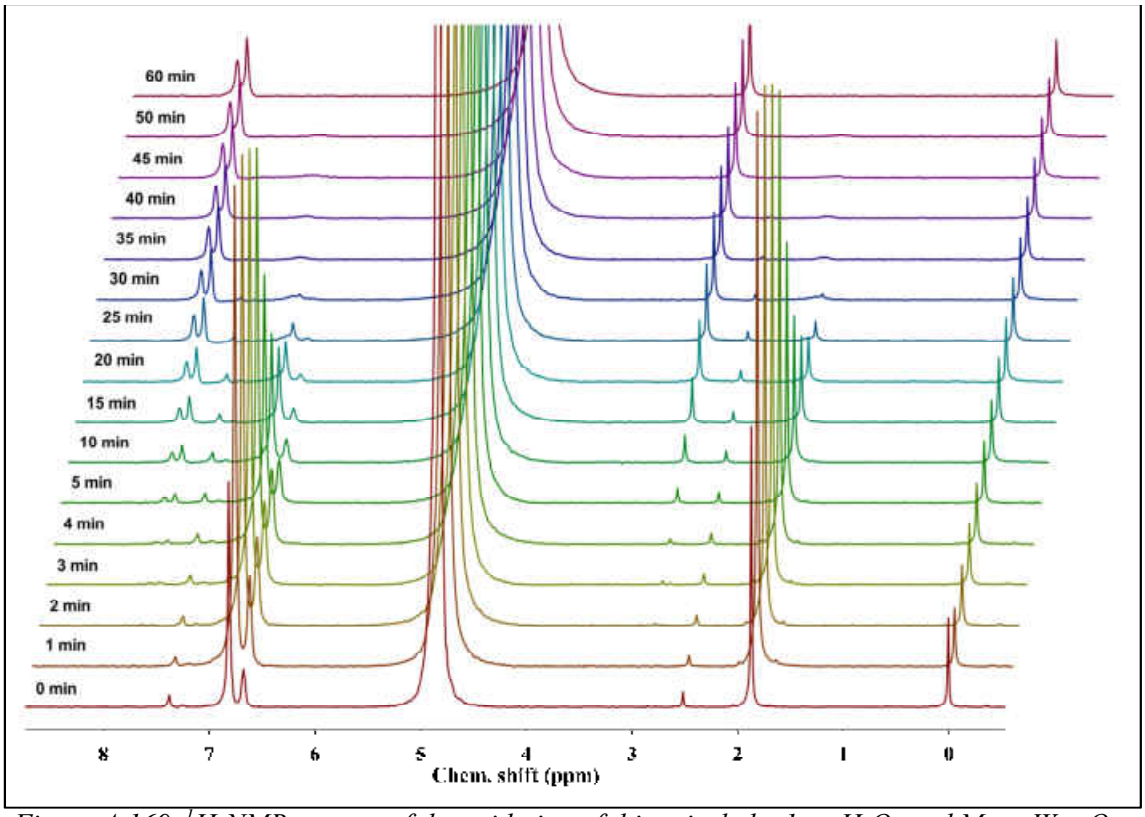

Figure A 169. ^{1}H-NMR spectra of the oxidation of thioanisole by 1 eq H_2O_2 and $Mo_{0.62}W_{0.38}O_{2.3}$ microparticles as catalyst, shown after different periods of time.

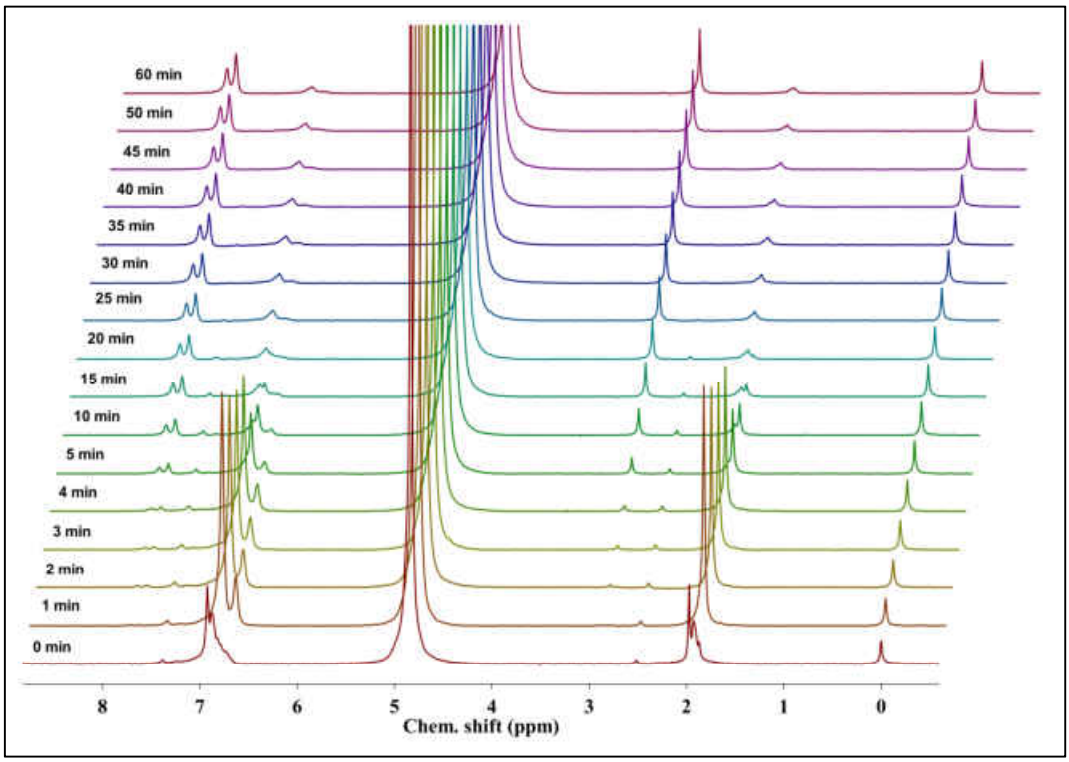

Figure A 170. ^{1}H-NMR spectra of the oxidation of thioanisole by 1 eq H_2O_2 and $Mo_{0.75}W_{0.25}O_{2.4}$ microparticles as catalyst, shown after different periods of time.

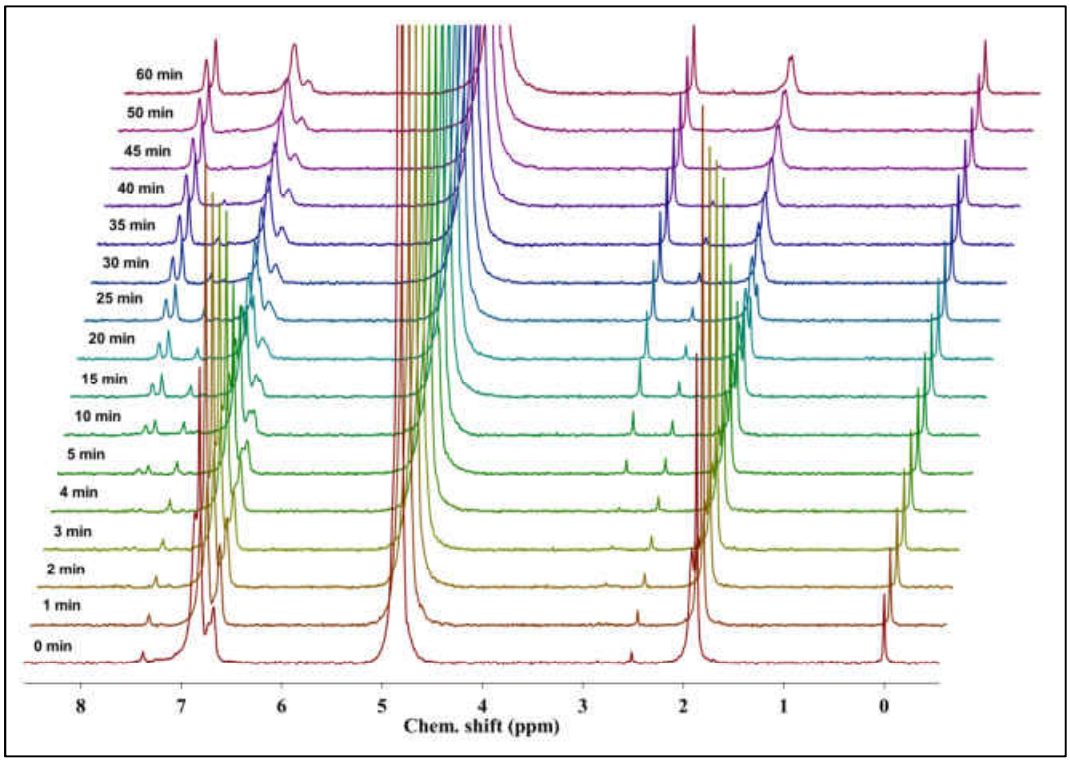

Figure A 171. ^{1}H-NMR spectra of the oxidation of thioanisole by 1 eq H_2O_2 and $Mo_{0.85}W_{0.15}O_{2.6}$ microparticles as catalyst, shown after different periods of time.

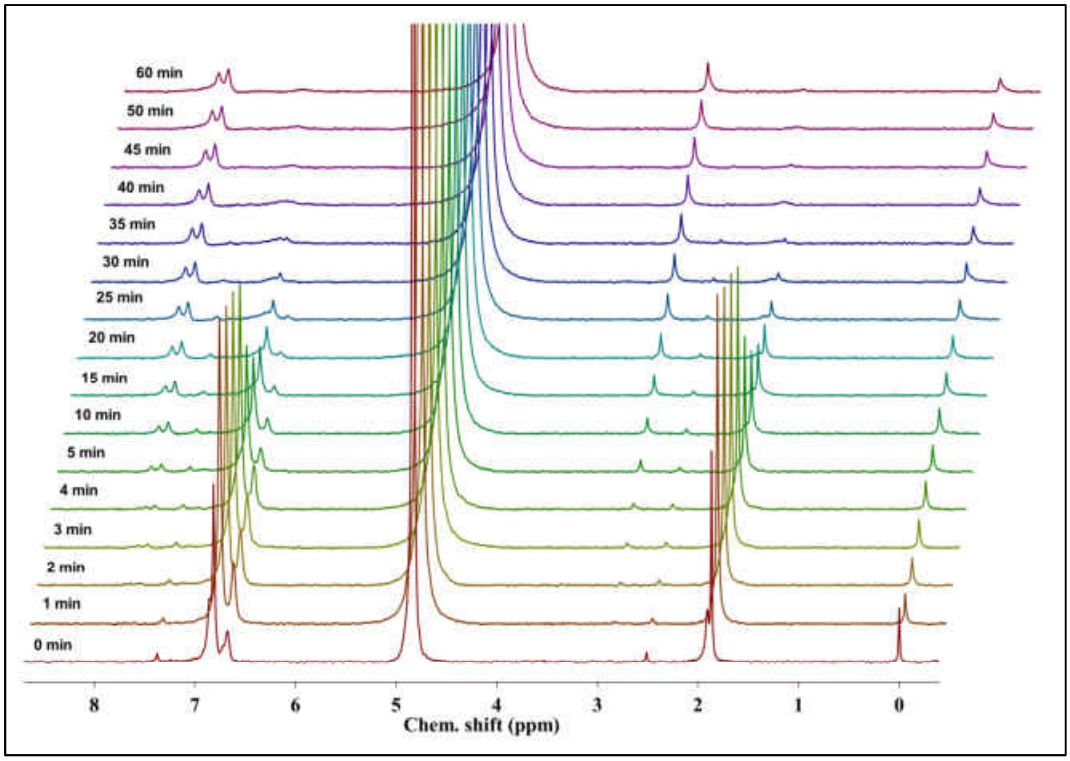

Figure A 172. ^{1}H-NMR spectra of the oxidation of thioanisole by 1 eq H_2O_2 and $Mo_{0.89}W_{0.11}O_{2.7}$ microparticles as catalyst, shown after different periods of time.

8.2 Additional Data for Iron Oxides (Chapter 5)

8.2.1. Particles Characterization

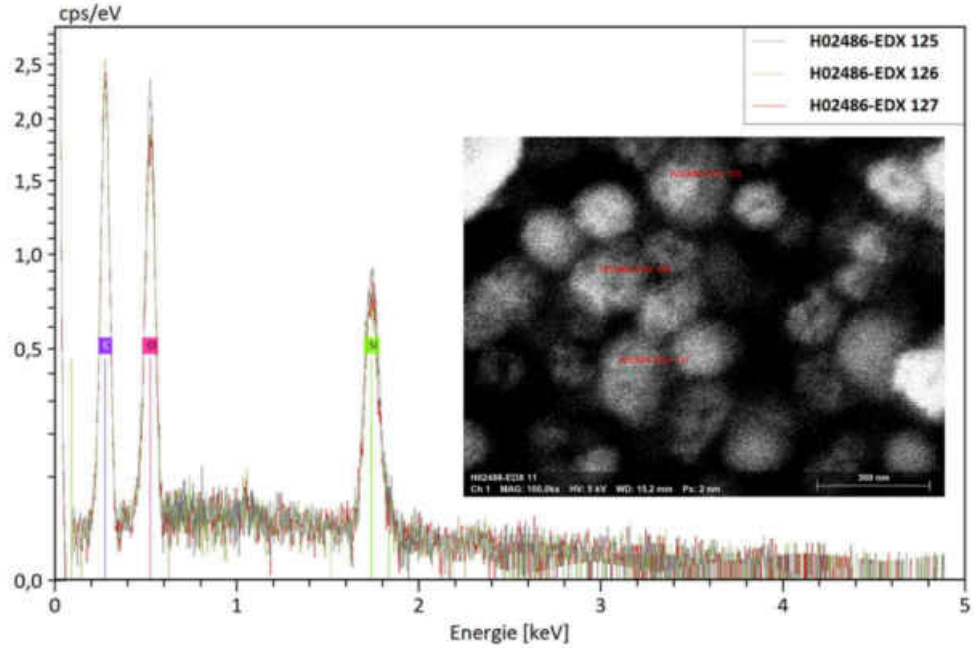

Figure A 173. EDS spectra measured on the particle shown in the STEM image. The sample was prepared from the product of the reaction at 200 °C for 12 h, with 30 mg NaF as etching agent.

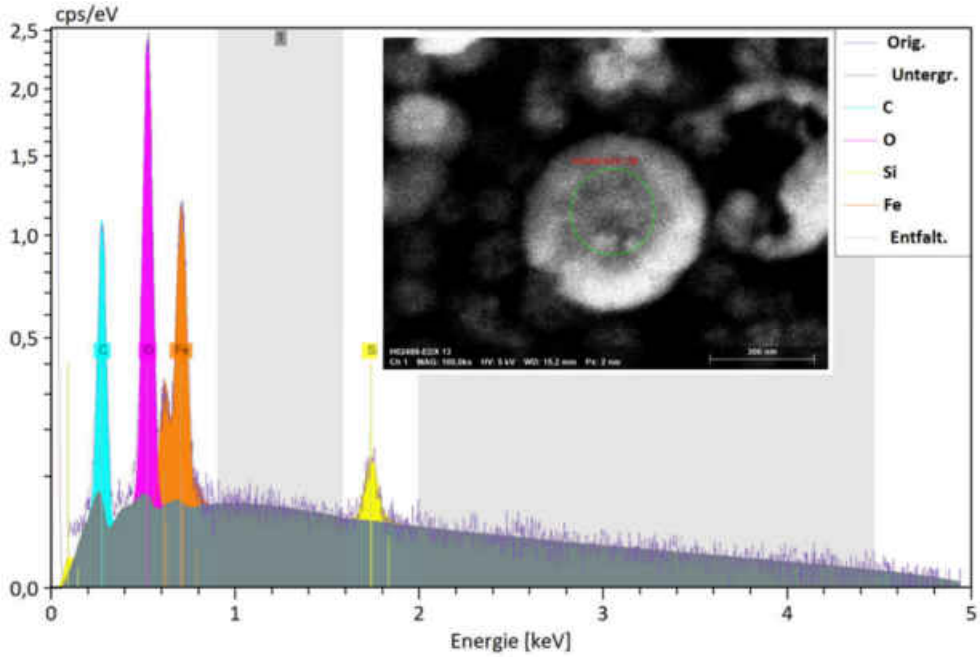

Figure A 174. EDS spectra measured on the particle shown in the STEM image. The sample was prepared from the product of the reaction at 200 °C for 12 h, with 30 mg NaF as etching agent.

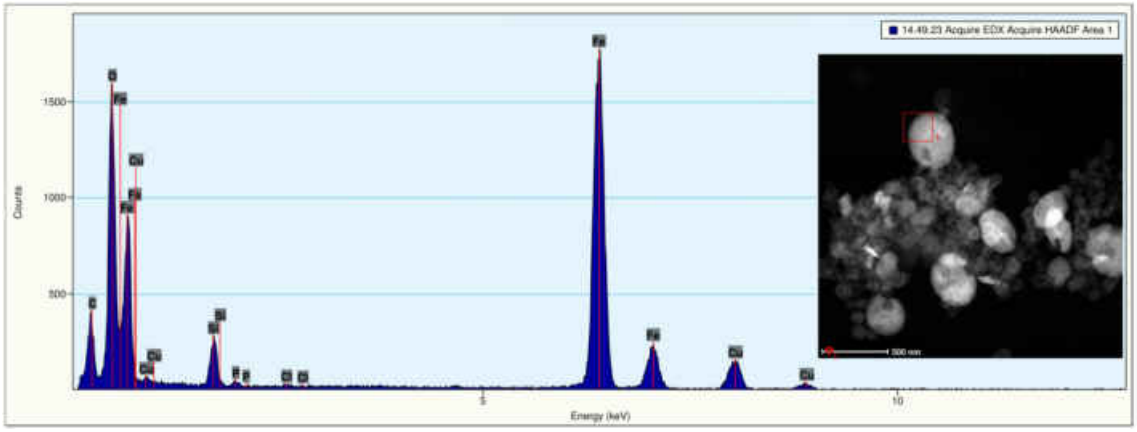

Figure A 175. EDS spectra measured on the particle shown in the STEM image. The sample was prepared from the product of the reaction at 200 °C for 24 h, with 30 mg NaF as etching agent.

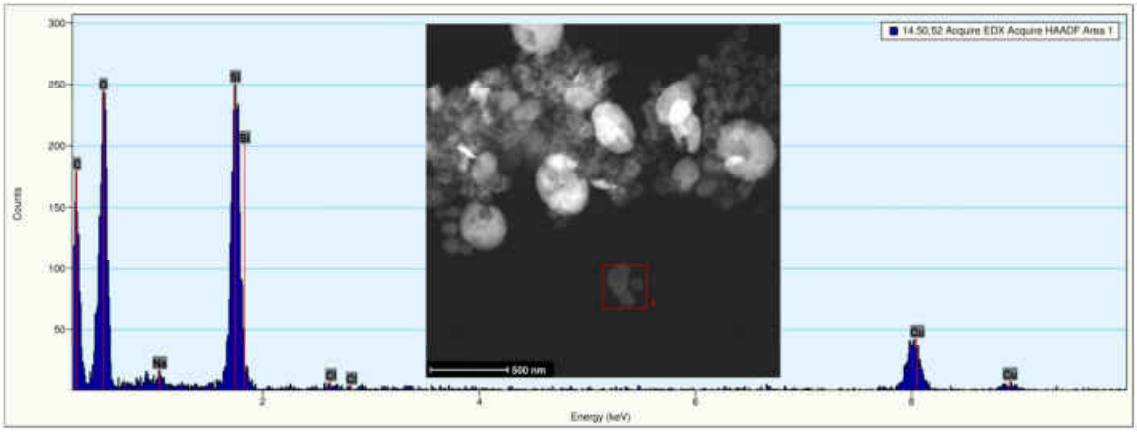

Figure A 176. EDS spectra measured on the particle shown in the STEM image. The sample was prepared from the product of the reaction at 200 °C for 24 h, with 30 mg NaF as etching agent.

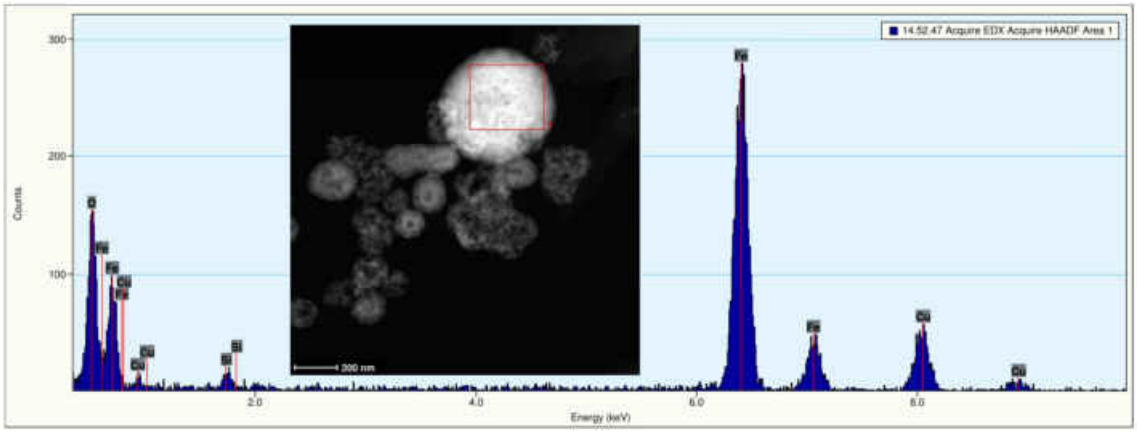

Figure A 177. EDS spectra measured on the particle shown in the STEM image. The sample was prepared from the product of the reaction at 200 °C for 48 h, with 30 mg NaF as etching agent.

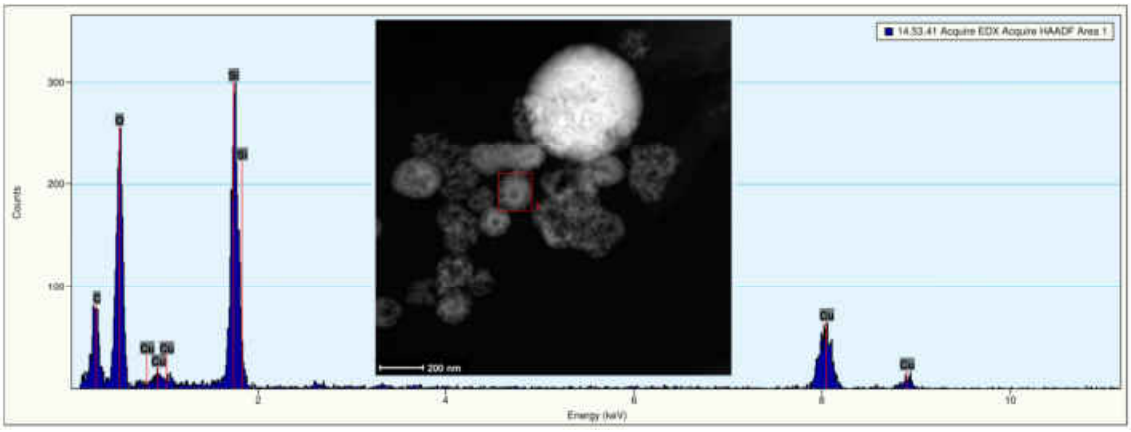

Figure A 178. EDS spectra measured on the particle shown in the STEM image. The sample was prepared from the product of the reaction at 200 °C for 48 h, with 30 mg NaF as etching agent.

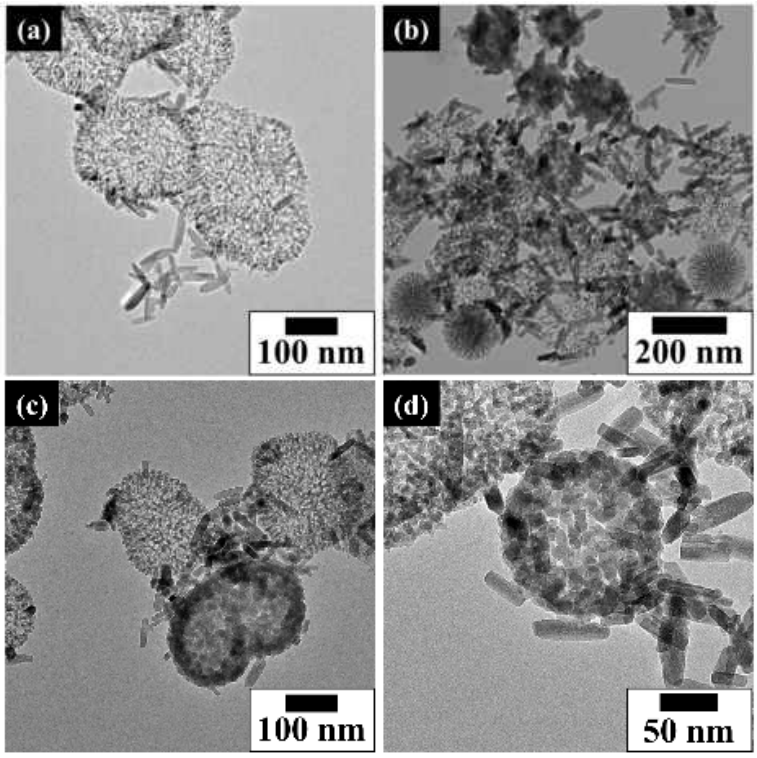

Figure A 179. (a-d) TEM images of silica-hematite particles, synthesized with 15 mg NaF at 200 °C for 2 h.

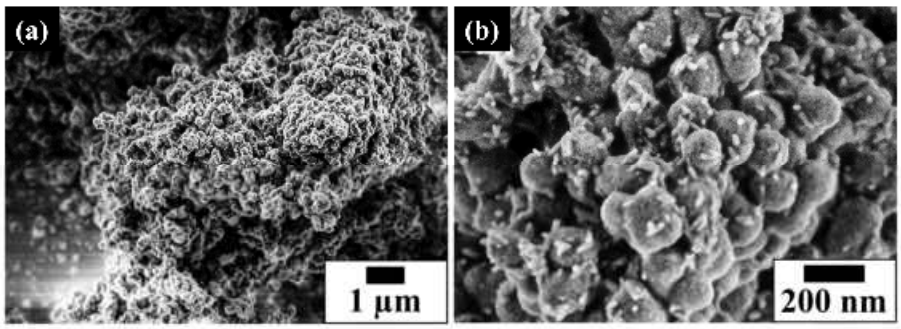

Figure A 180. (a,b) SEM images of silica-hematite particles, synthesized with 15 mg NaF at 200 °C for 2 h.

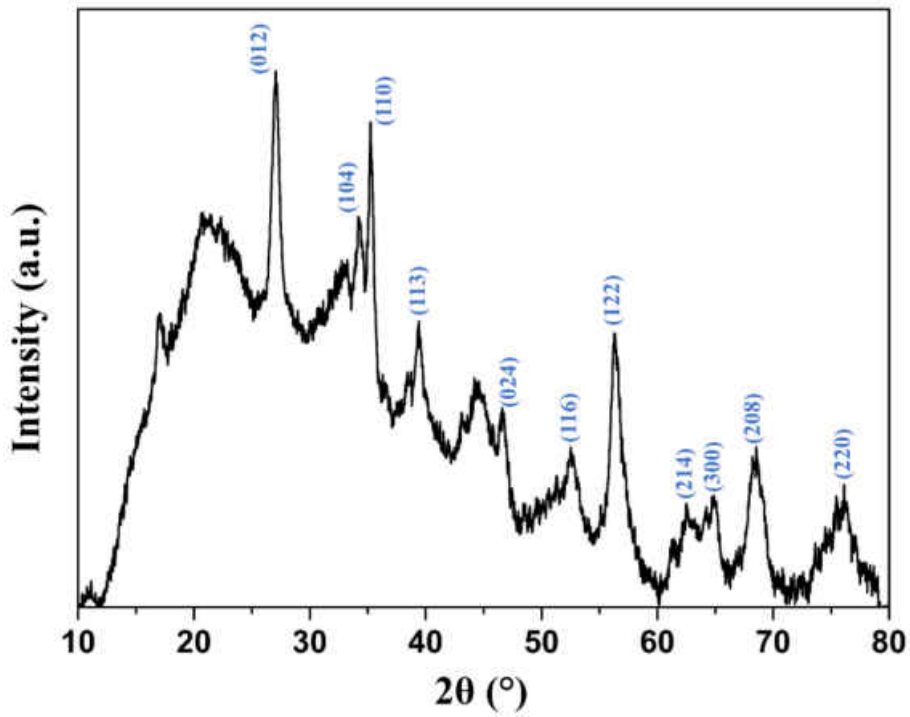

Figure A 181. Powder-XRD pattern of silica-hematite particles, synthesized with 15 mg NaF at 200 °C for 2 h.

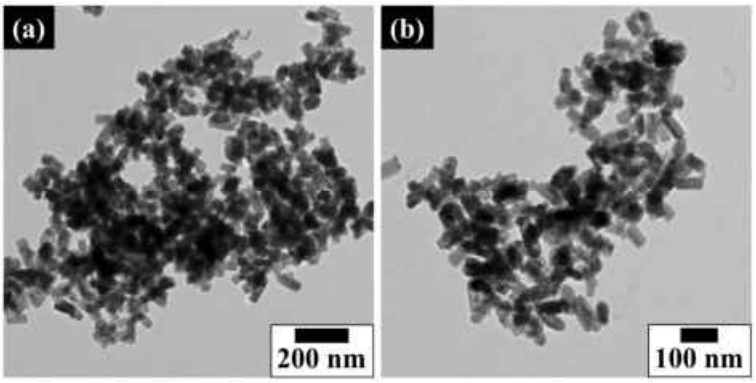

Figure A 182. (a, b) TEM images of silica-hematite particles, synthesized with 30 mg NaF at 200 °C for 2 h.

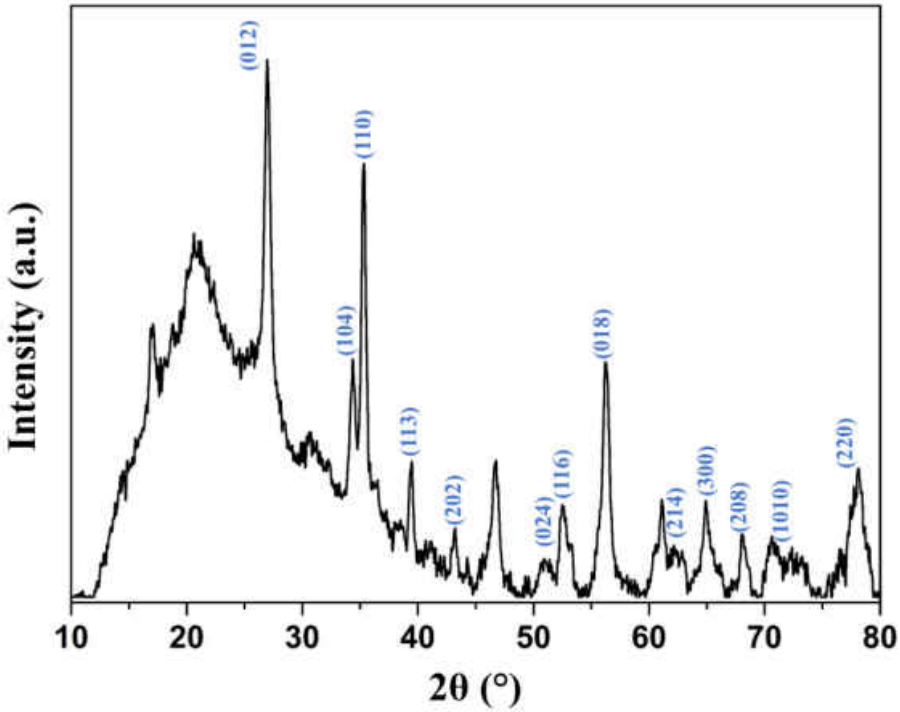

Figure A 183. Powder-XRD pattern of silica-hematite particles, synthesized with 30 mg NaF at 200 °C for 2 h.

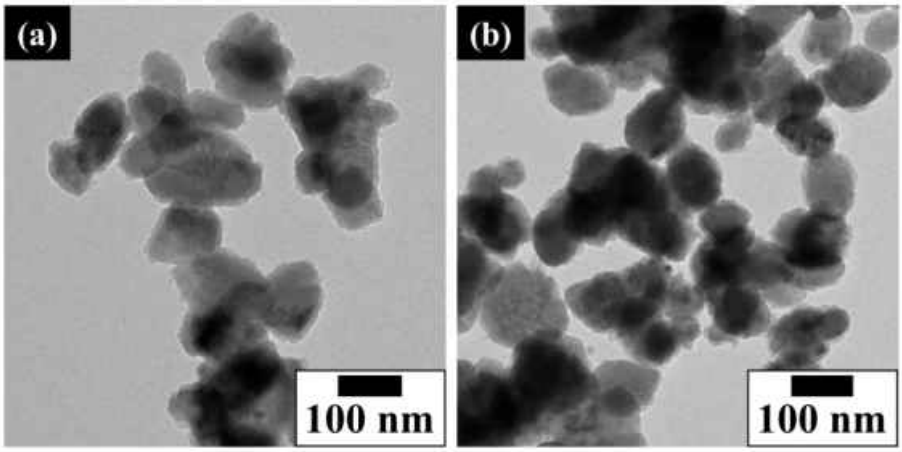

Figure A 184. (a, b) TEM images of silica-hematite particles, synthesized with 40 mg NaF at 200 °C for 2 h.

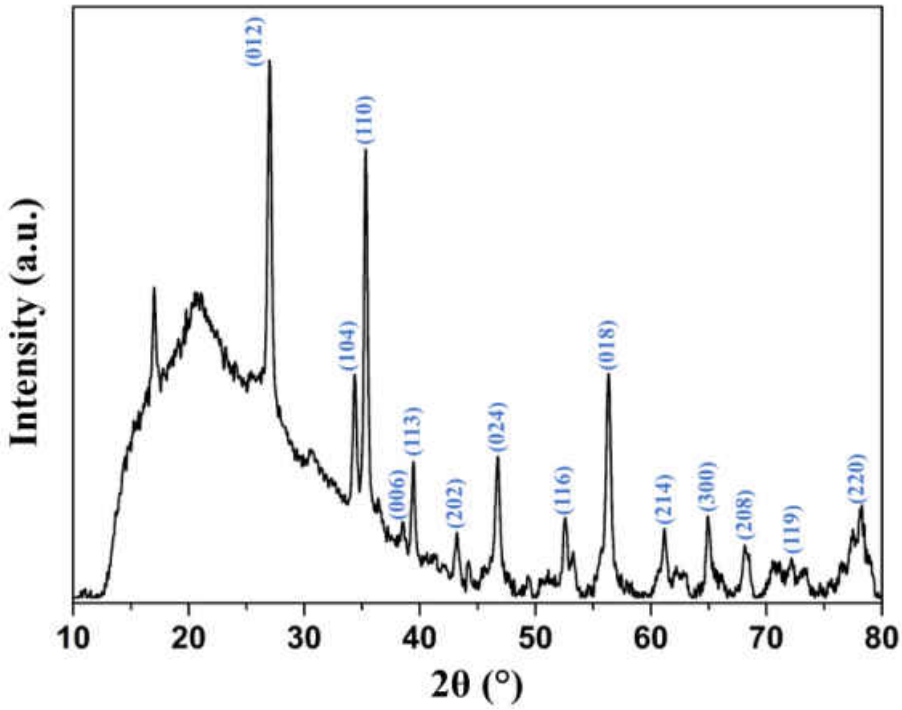

Figure A 185. Powder-XRD pattern of silica-hematite particles, synthesized with 40 mg NaF at 200 °C for 2 h.

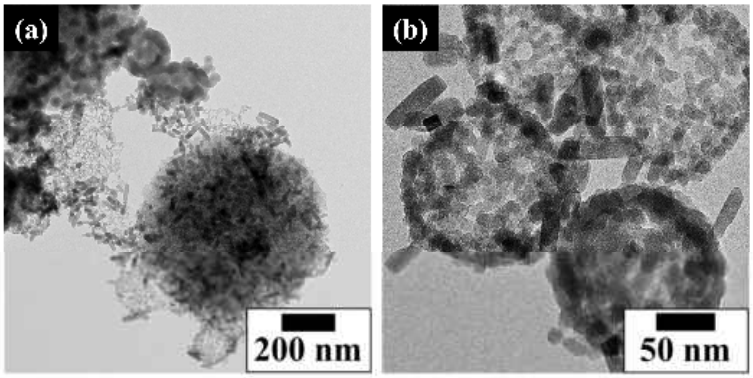

Figure A 186. (a, b) TEM images of silica-hematite particles, synthesized with 30 mg NaF at 200 °C for 4 h.

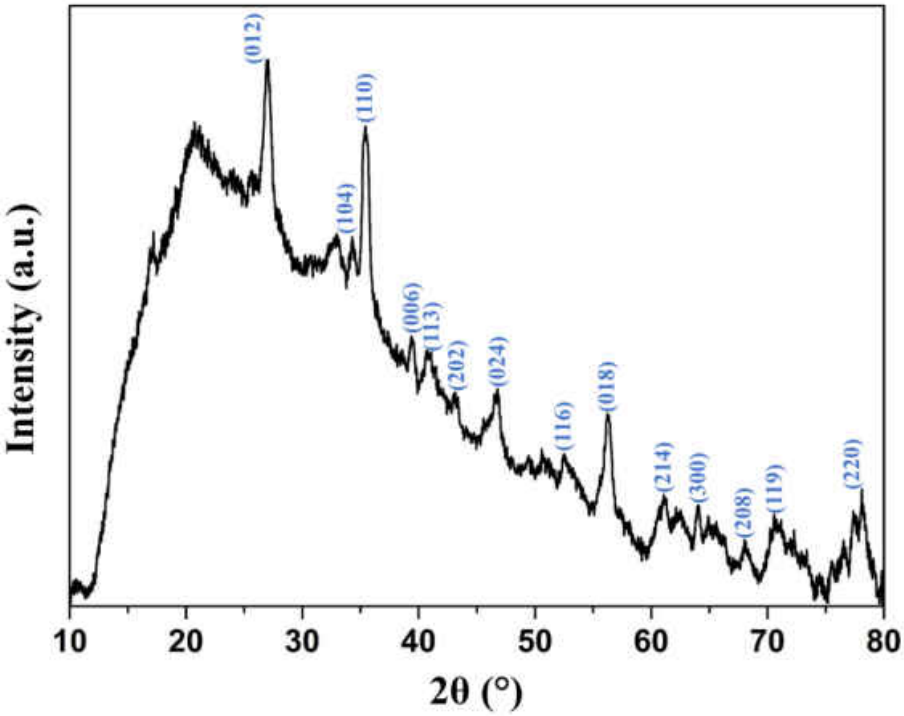

Figure A 187. Powder-XRD pattern of silica-hematite particles, synthesized with 30 mg NaF at 200 °C for 4 h.

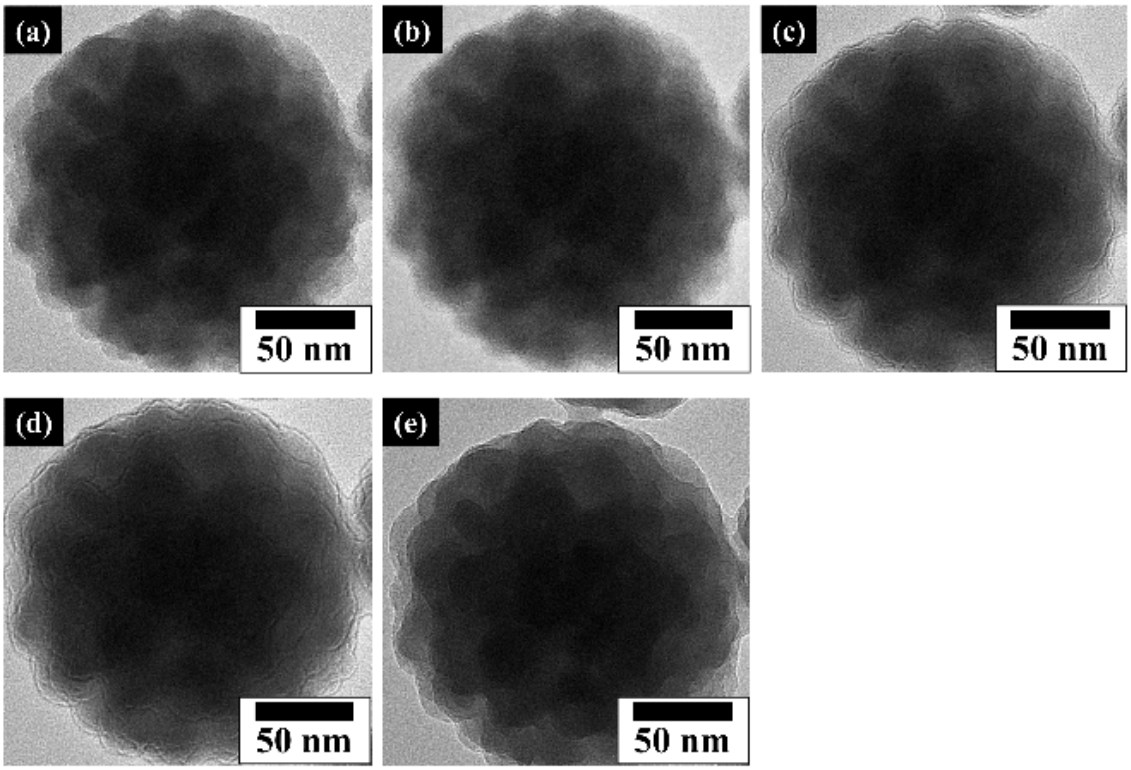

Figure A 188. TEM focus-defocus series of a single SHP, which was synthesized with 30 mg NaF at 200 °C for 6 h.

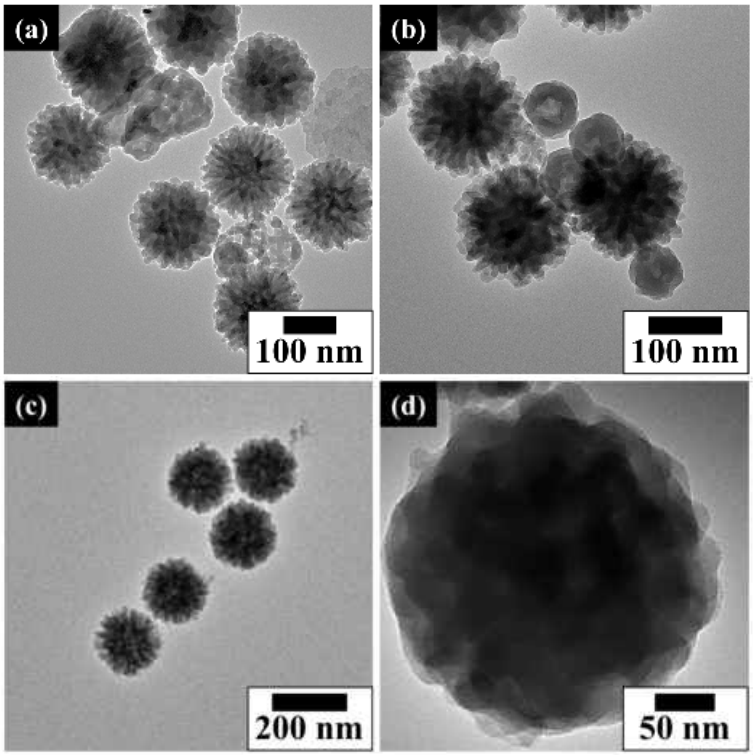

Figure A 189. (a-d) TEM images of silica-hematite particles, synthesized with 30 mg NaF at 200 °C for 8 h.

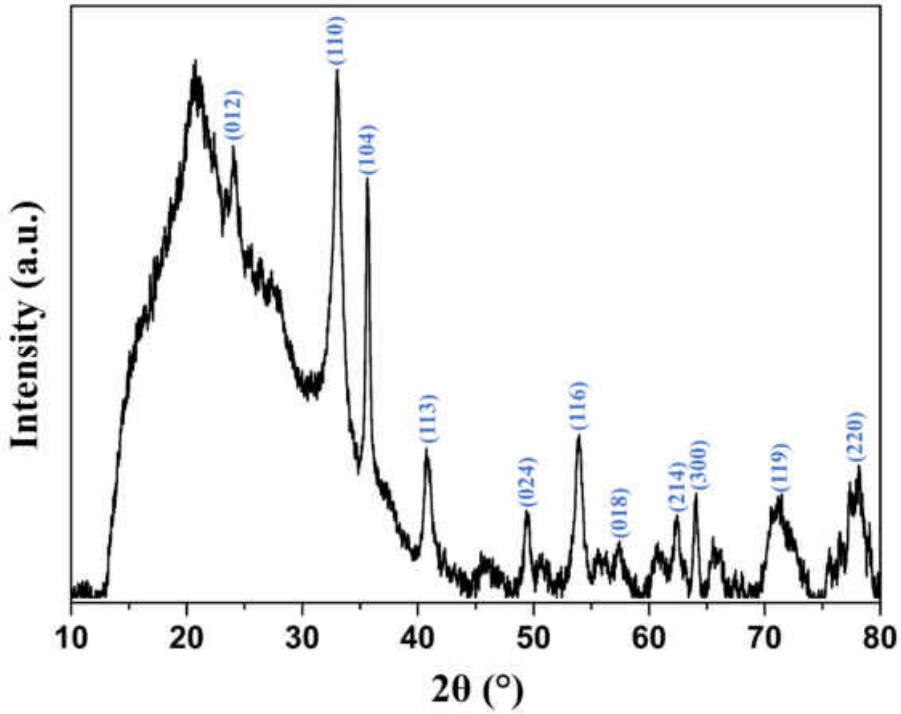

Figure A 190. Powder-XRD pattern of silica-hematite particles, synthesized with 30 mg NaF at 200 °C for 8 h.

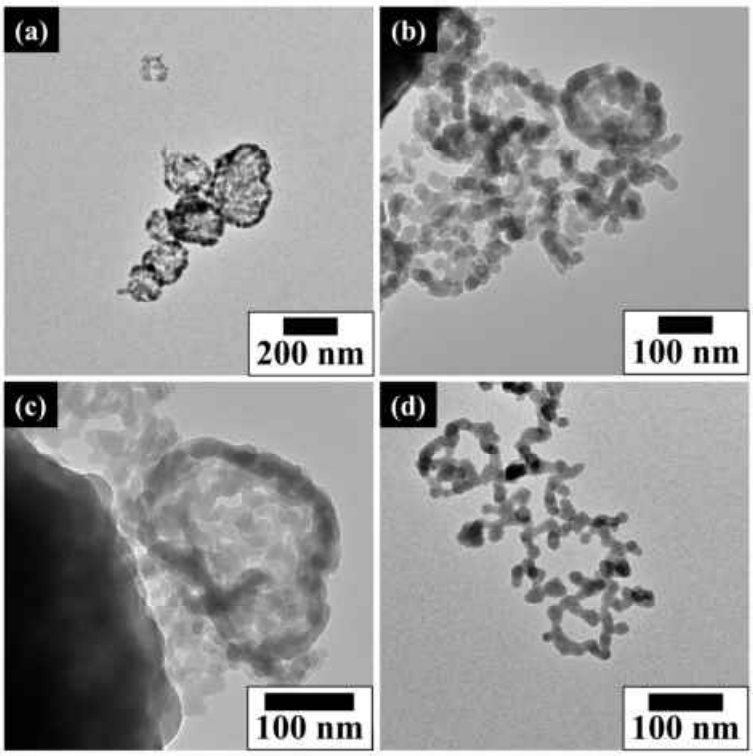

Figure A 191. (a-d) TEM images of silica-hematite particles, synthesized with 40 mg NaF at 200 °C for 48 h.

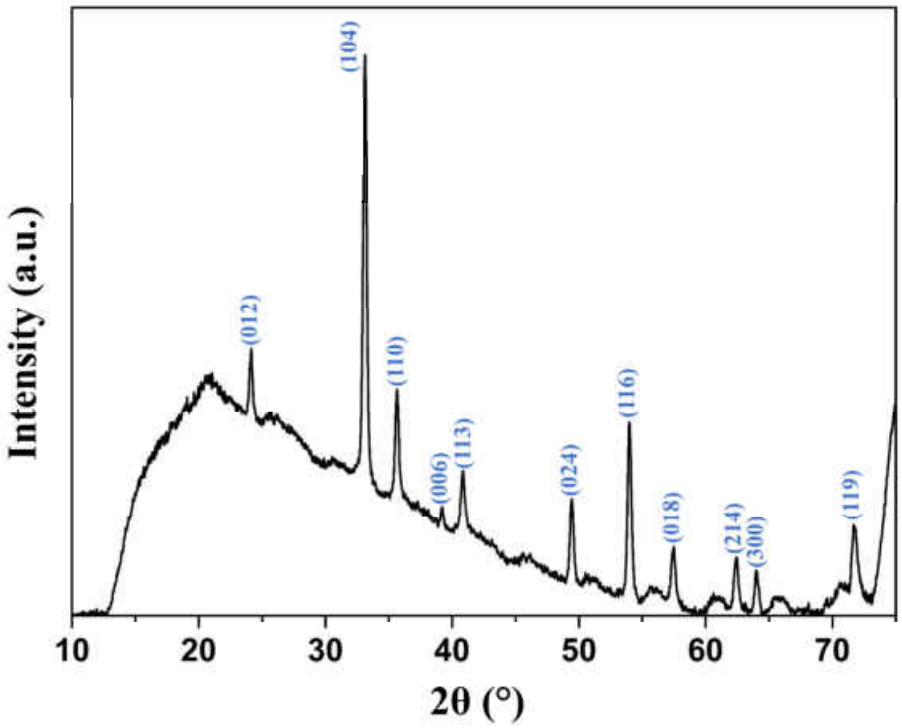

Figure A 192. Powder-XRD pattern of silica-hematite particles, synthesized with 40 mg NaF at 200 °C for 48 h.

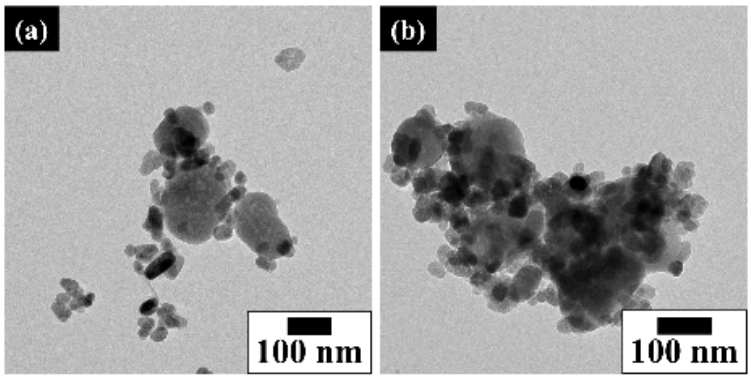

Figure A 193. (a, b) TEM images of silica-hematite particles, synthesized with 100 mg NaF at 200 °C for 48 h.

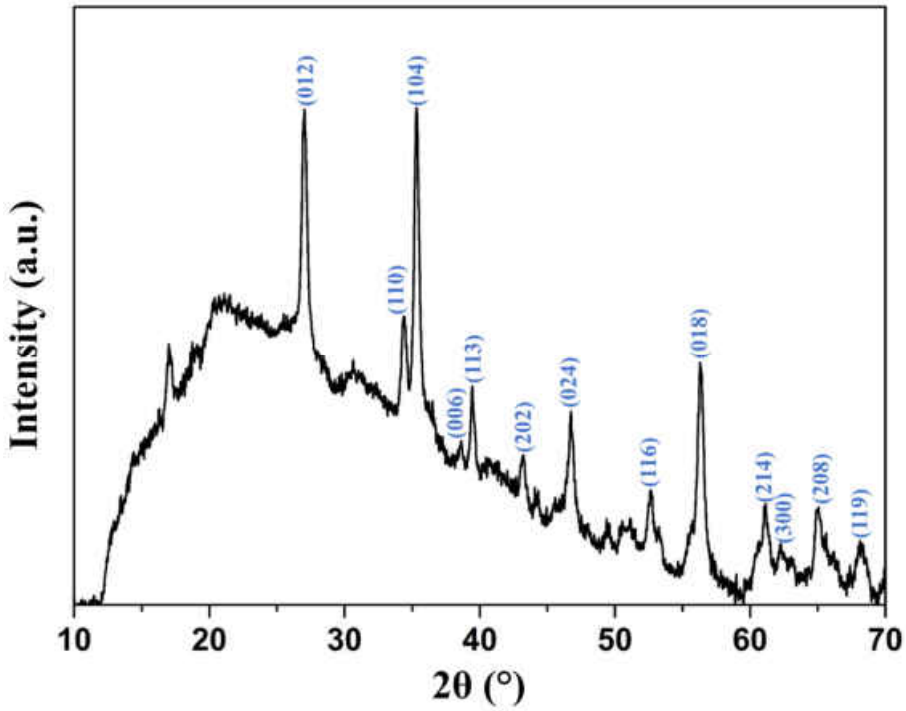

Figure A 194. Powder-XRD pattern of silica-hematite particles, synthesized with 100 mg NaF at 200 °C for 48 h.

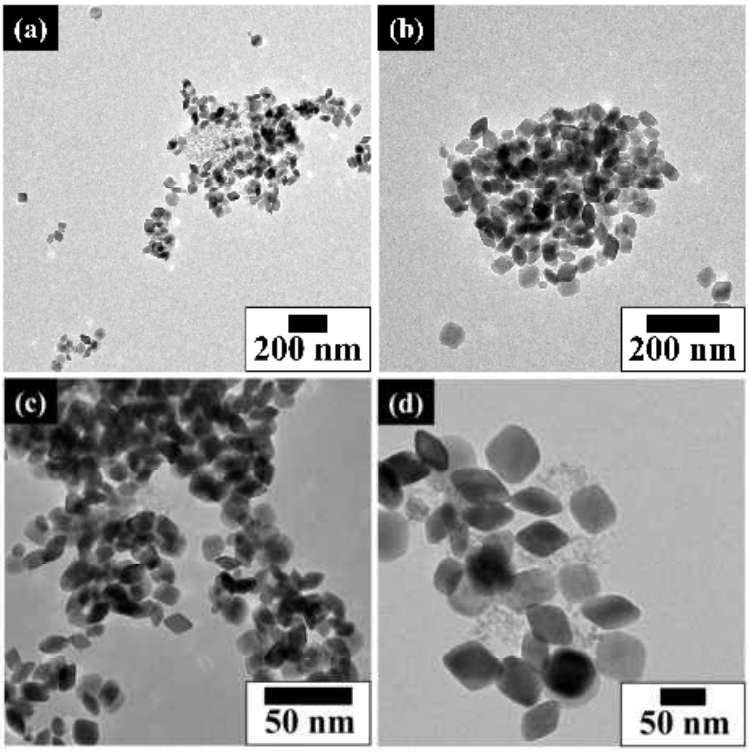

Figure A 195. TEM images of the reference experiment with iron precursor and silica template, but without NaF.

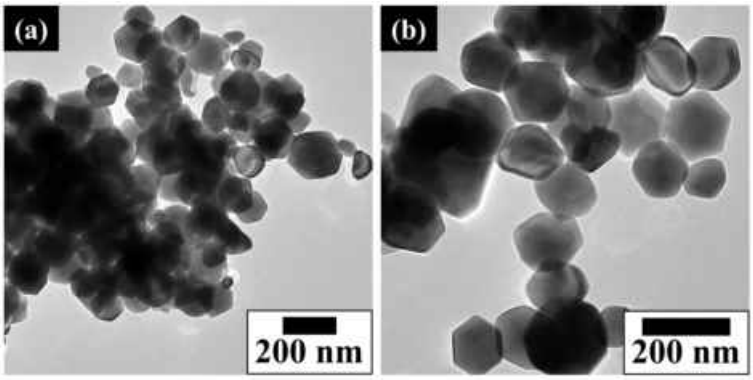

Figure A 196. TEM images of the reference experiment (200 °C/48 h) with iron precursor and 15 mg NaF, but without silica template.

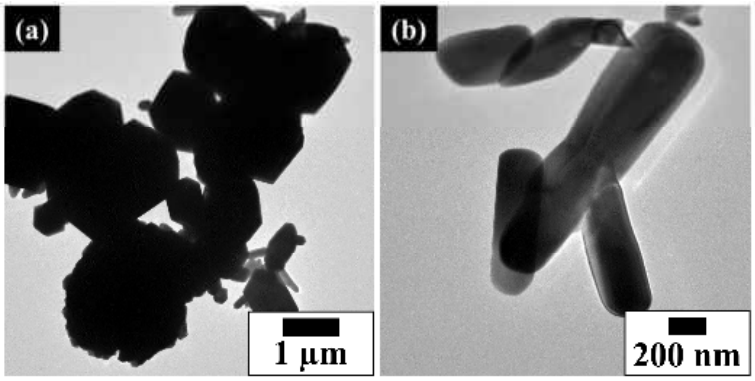

Figure A 197. TEM images of the reference experiment (200 °C/48 h) with iron precursor and 30 mg NaF, but without silica template.

8.2.2. Fitting Curves of Rhodamine B Degradation

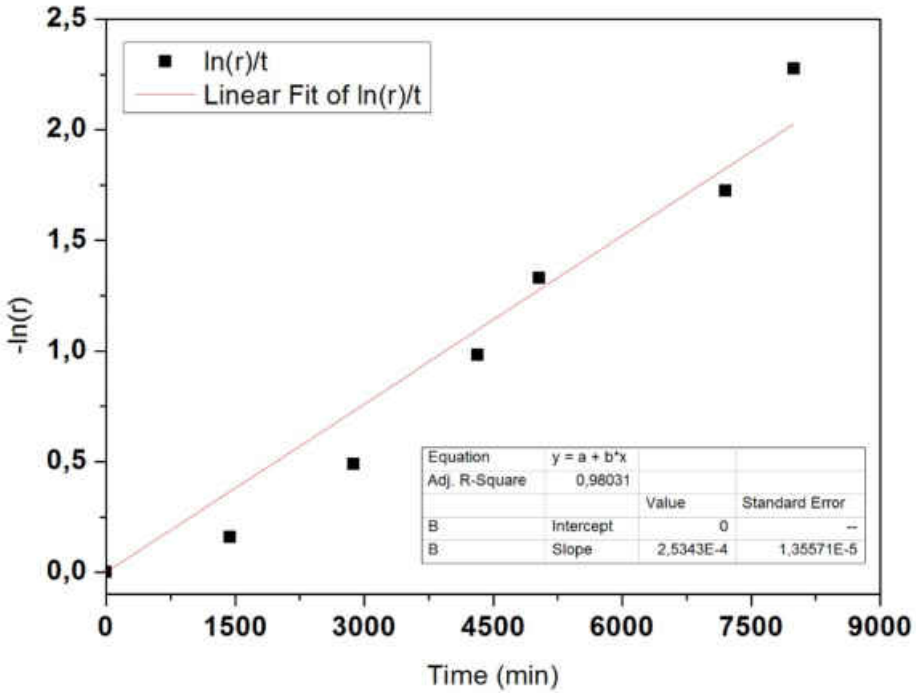

Figure A 198. Relationship of ln(r) and reaction time for the degradation of RhB with H_2O_2 only. The values of the linear curve fitting are summarized in the inset.

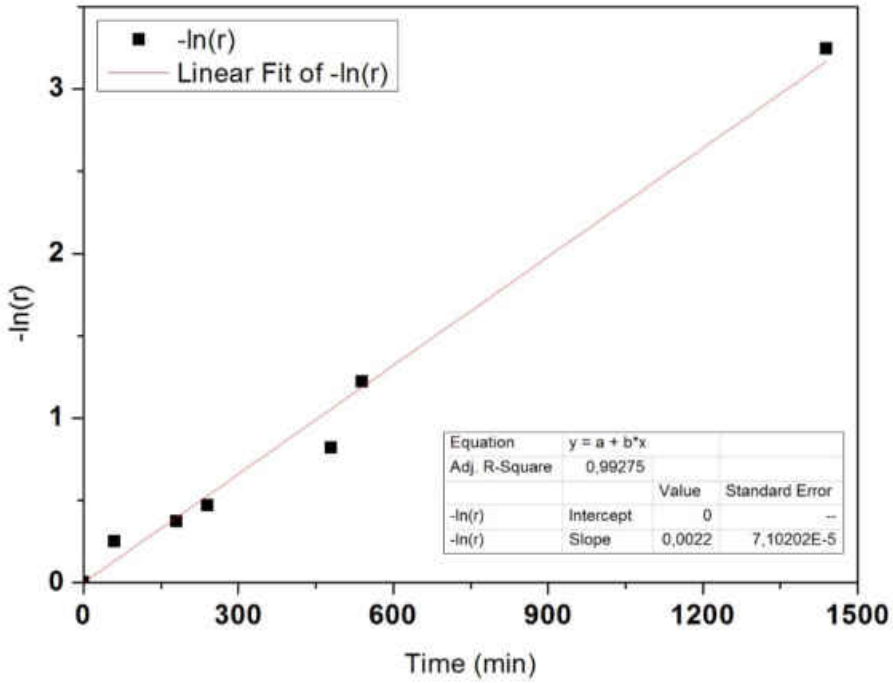

Figure A 199. Relationship of ln(r) and reaction time for the degradation of RhB with SHP-48h and H_2O_2. The values of the linear curve fitting are summarized in the inset.

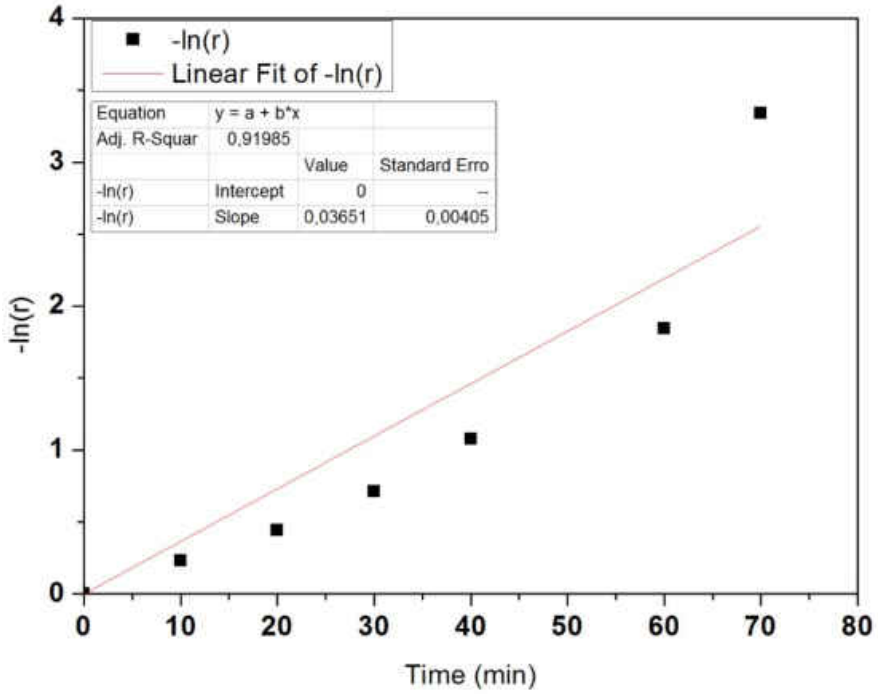

Figure A 200. Relationship of ln(r) and reaction time for the degradation of RhB with HP and H_2O_2. The values of the linear curve fitting are summarized in the inset.

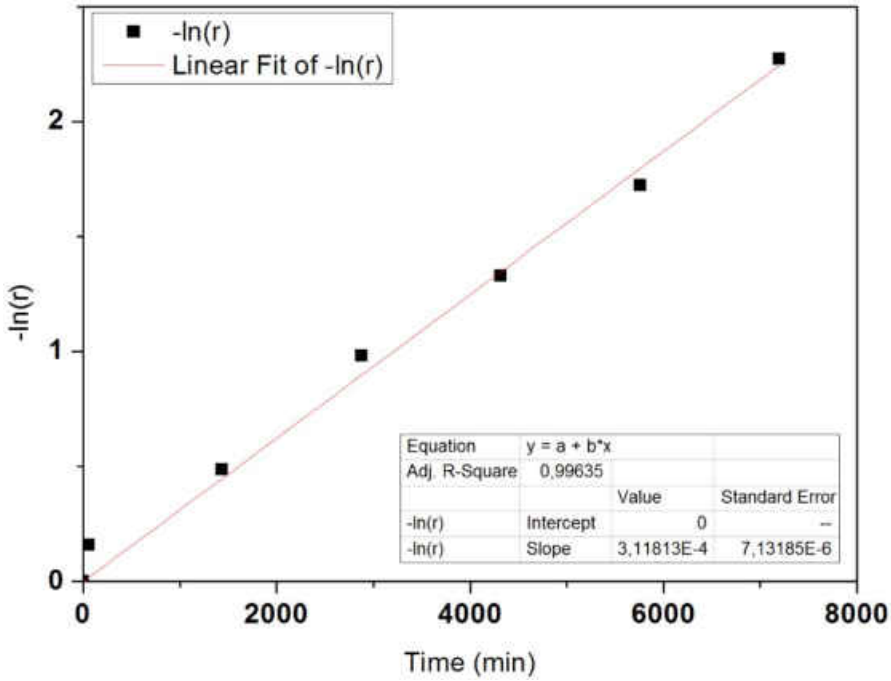

Figure A 201. Relationship of ln(r) and reaction time for the degradation of RhB with MSN and H_2O_2. The values of the linear curve fitting are summarized in the inset.

8.3. Additional Data for TMCs (Chapter 6)

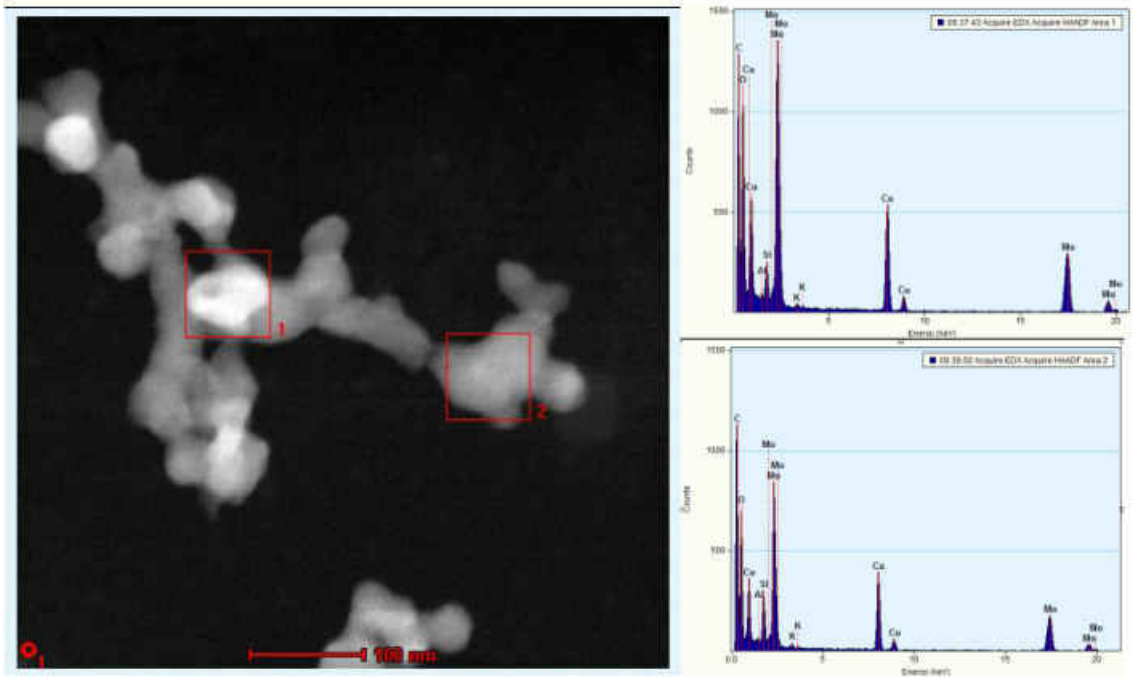

Figure A 202. STEM image of MoO_xS_{2-x} nanoflakes and the EDX spectra of the selected areas.

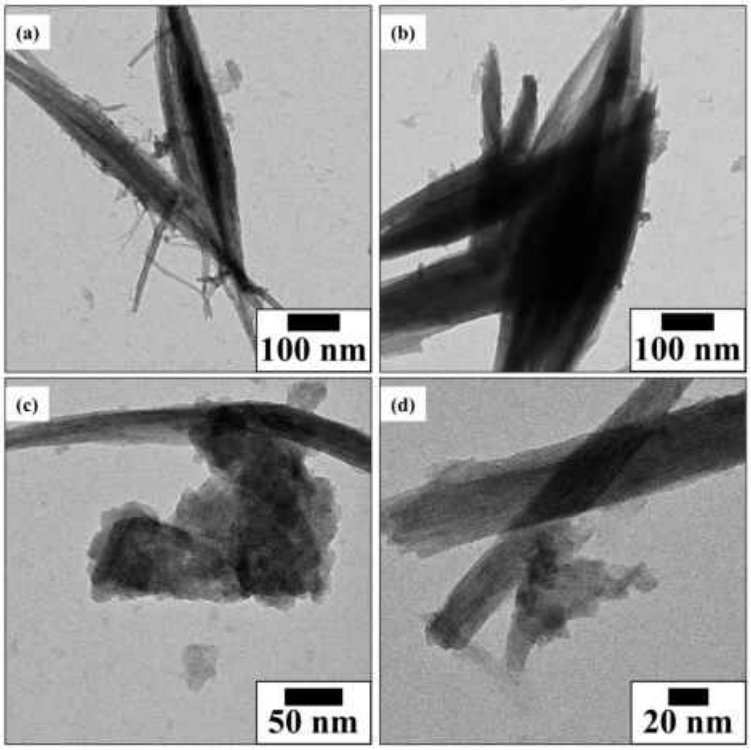

Figure A 203. TEM images of the particles obtained from the exfoliation of purified $(NH_4)[Mo_3S_{13}]$ in benzyl alcohol.

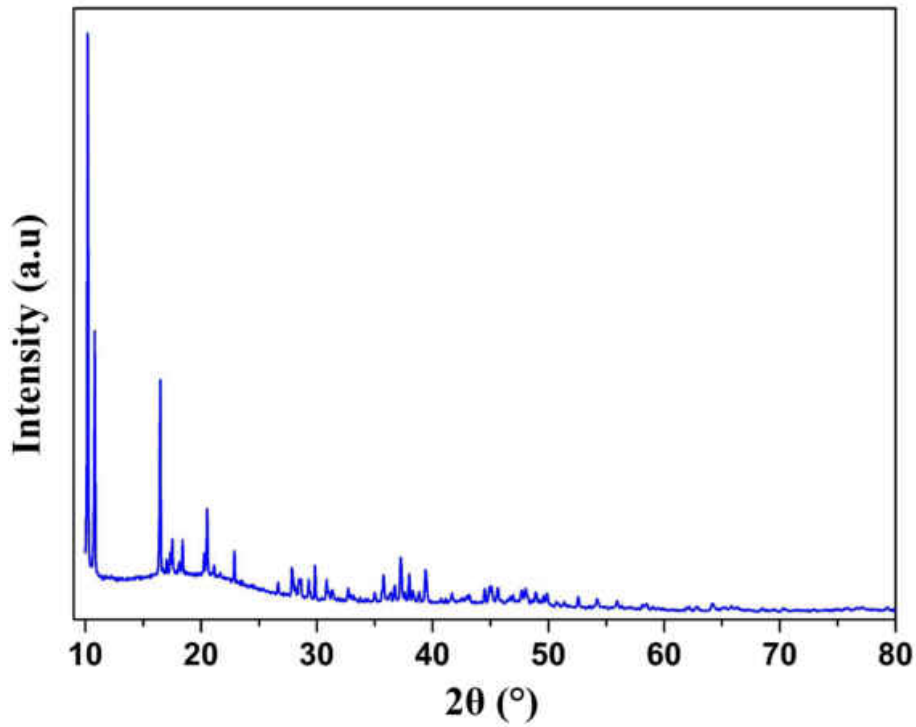

Figure A 204. XRD pattern of the particles obtained from the exfoliation of purified $(NH_4)[Mo_3S_{13}]$ in benzyl alcohol.

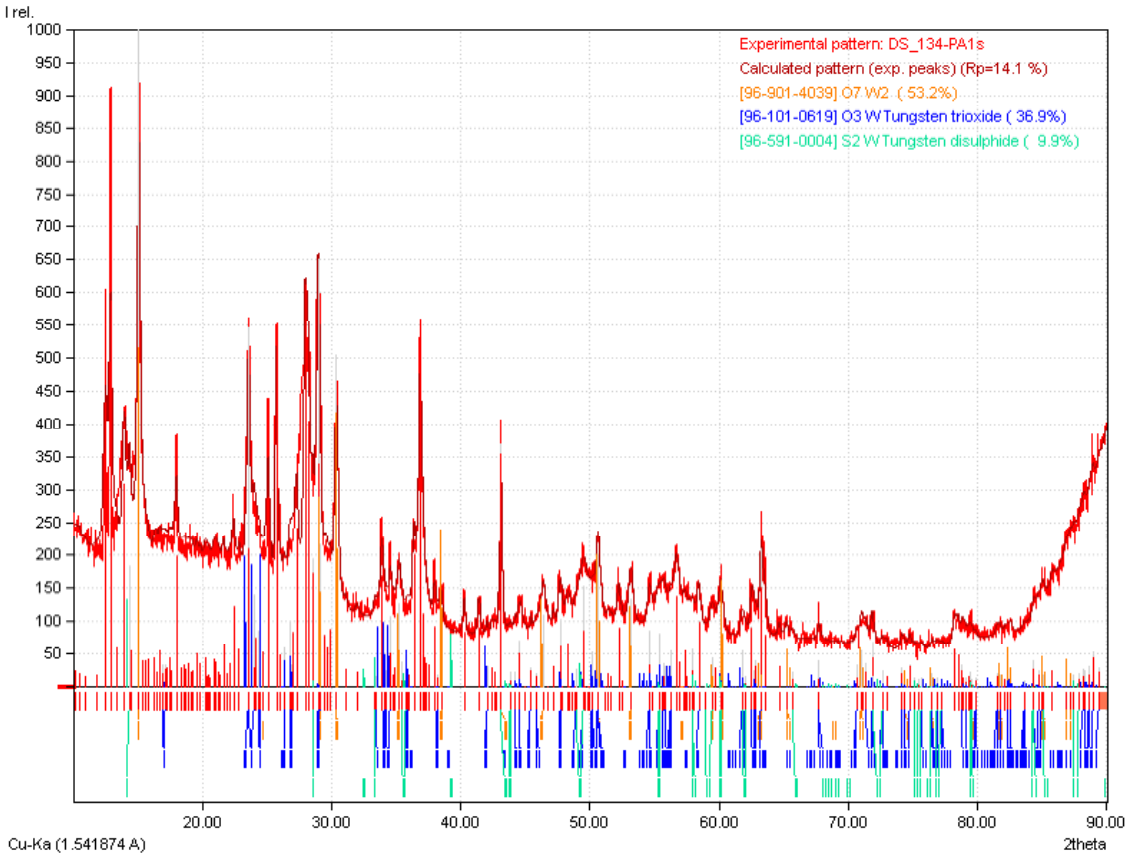

Figure A 205. XRD pattern of the WO_xS_{2-x} nanoflakes obtained from benzyl alcohol synthesis. The profile fitting and indexing was done with MATCH! (Version 3.4.2. Build 96, by H. Putz).

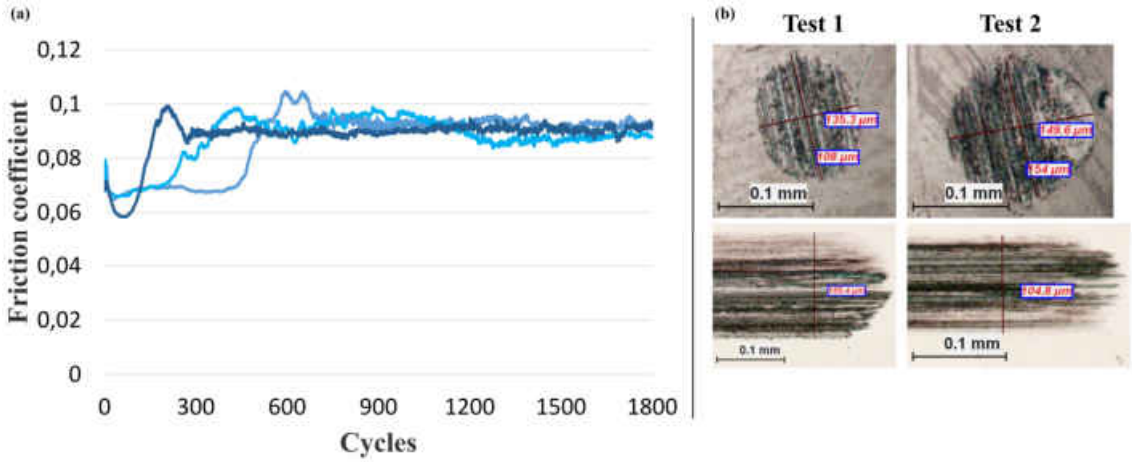

Figure A 206. (a) Measurements of friction coefficient for MoS_x nanosheets in three different runs, (b) digital photographs of the worn surfaces for the first two runs with MoS_x nanosheets as additives to PAO6.

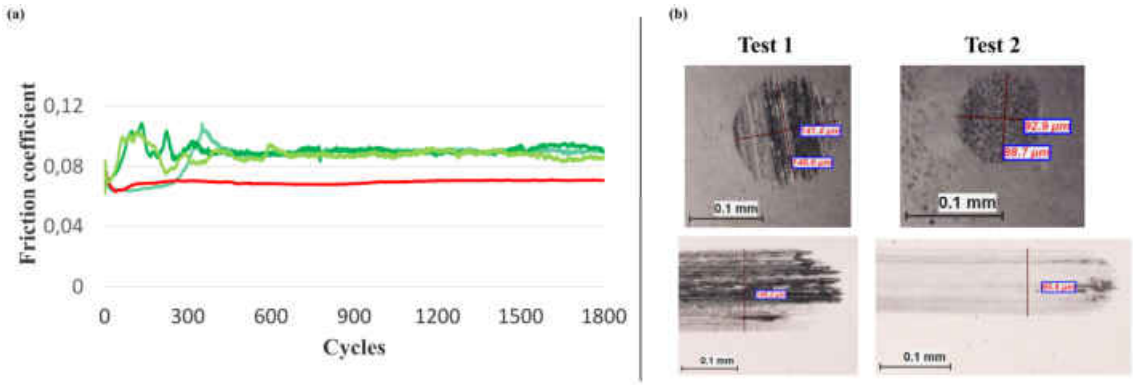

Figure A 207. (a) Measurements of friction coefficient for WSx nanosheets in four different runs, (b) digital photographs of the worn surfaces for the first two runs with WSx nanosheets as additives to PAO6.

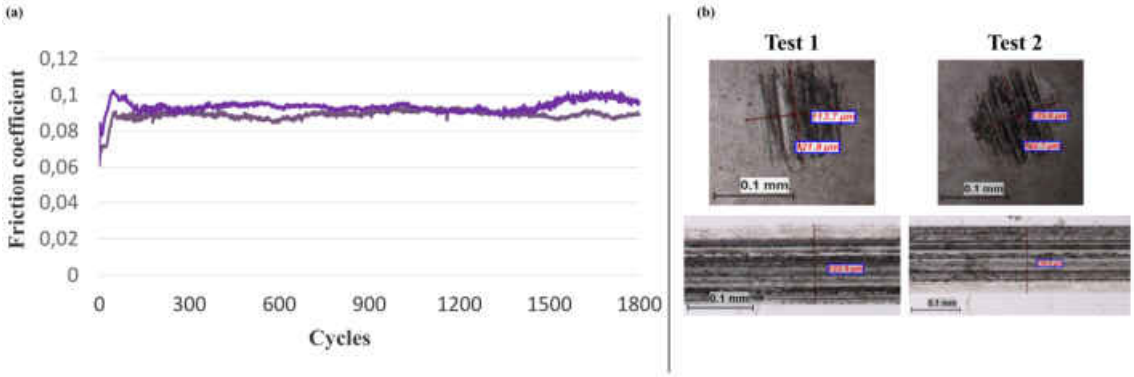

Figure A 208. (a) Measurements of friction coefficient for MoWSx nanosheets in two different runs, (b) digital photographs of the worn surfaces for the two runs with MoWSx nanosheets as additives to PAO6.

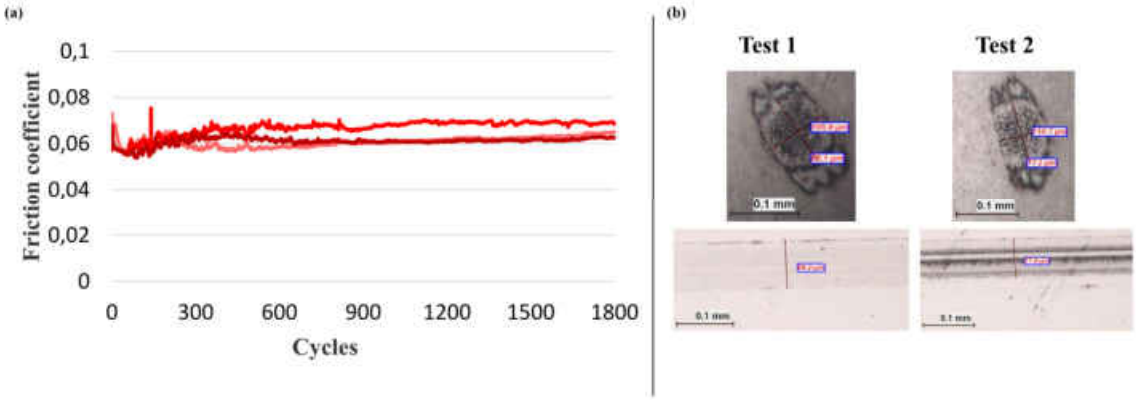

Figure A 209. (a) Measurements of friction coefficient for MoOSx nanoflakes in three different runs, (b) digital photographs of the worn surfaces for the first two runs with MoOSx nanoflakes as additives to PAO6.

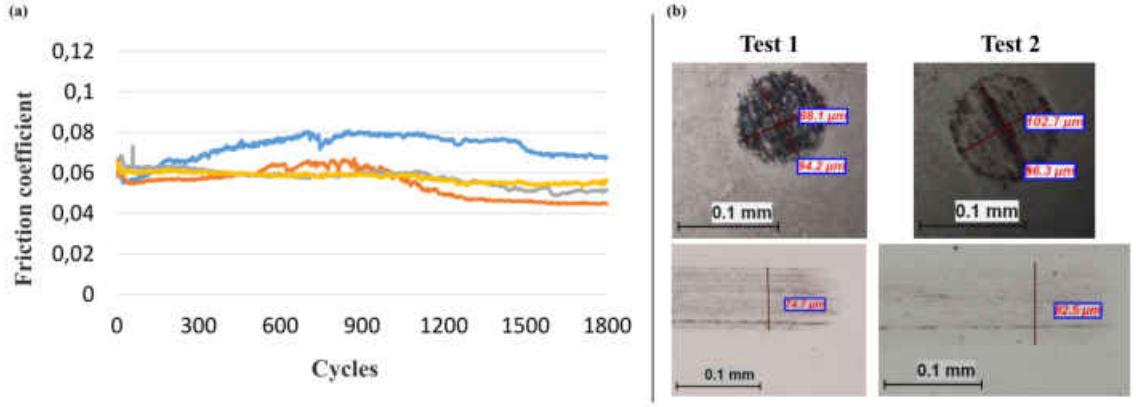

Figure A 210. (a) Measurements of friction coefficient for WS_2 fullerenes in four different runs, (b) digital photographs of the worn surfaces for the first two runs with WS_2 fullerenes as additives to PAO6.

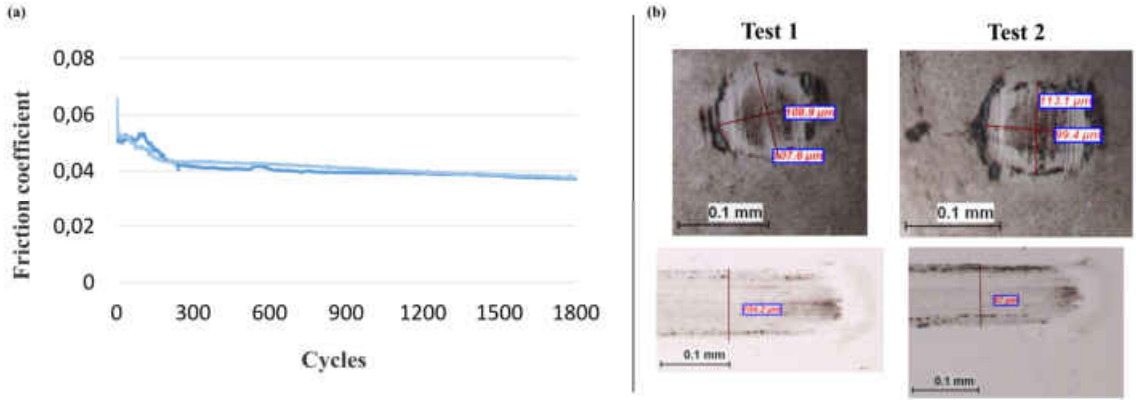

Figure A 211. (a) Measurements of friction coefficient for WOS_x nanoflakes in two different runs, (b) digital photographs of the worn surfaces for the two runs with WOS_x nanoflakes as additives to PAO6.

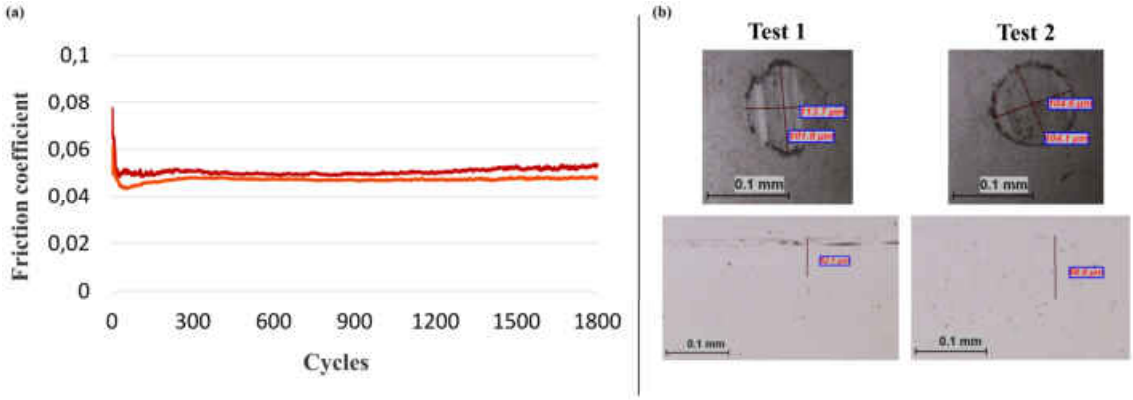

Figure A 212. (a) Measurements of friction coefficient for WS_2 nanotubes in two different runs, (b) digital photographs of the worn surfaces for the first two runs with WS_2 nanotubes as additives to PAO6.